

Copper Sulfide Nanoparticles

Synthesis, Characterization and Catalysis

PhD thesis, Utrecht University, the Netherlands, August 2020

ISBN: 978-94-6380-900-9

Printed by: ProefschriftMaken || www.proefschriftmaken.nl

The work described in this thesis was performed in the Condensed Matter and Interfaces group and Inorganic Chemistry and Catalysis group, which are part of the Debye Institute for Nanomaterials Science, at Utrecht University.

Copper Sulfide Nanoparticles

Synthesis, Characterization and Catalysis

Kopersulfide nanodeeltjes

Synthese, karakterisatie en katalyse
(met een samenvatting in het Nederlands)

Proefschrift

ter verkrijging van de graad van doctor aan de Universiteit Utrecht op gezag van de rector magnificus, prof. dr. H.R.B.M. Kummeling, ingevolge het besluit van het college voor promoties in het openbaar te verdedigen op

woensdag 2 september 2020
des middags te 4.15 uur

door

Christina Heiltje Martina van Oversteeg

geboren op 2 mei 1992
te Muscat, Oman

Promotor: Prof. dr. P.E. de Jongh
Copromotor: Dr. C. de Mello Donegá

This work was supported by the Netherlands Center for Multiscale Catalytic Energy Conversion (MCEC), an NWO Gravitation program funded by the Ministry of Education, Culture and Science of the government of the Netherlands.

Table of Contents

Chapter 1	1
Introduction	
Chapter 2	21
Water dispersible Cu _{2-x} S nanocrystals via ligand exchange of 1-dodecanethiol	
Chapter 3	49
The synthesis and formation mechanism of Cu _{2-x} S/CuInS ₂ heteronanocrystals	
Chapter 4	75
The preparation of silica supported Cu _{2-x} S nanoparticles	
Chapter 5	97
Challenges and guidelines in heterogeneous liquid-phase photocatalysis	
Chapter 6	121
Cu _{2-x} S derived nanoparticles supported on carbon for the electrocatalytic reduction of CO ₂	
Chapter 7	143
Summary and outlook	
Chapter 8	149
Nederlandse samenvatting	
List of publications and conference contributions	158
Acknowledgements	160
About the author	163



Chapter 1

Introduction

1 Introduction

The composition-dependent material properties of copper sulfide have attracted interest for their use in a variety of applications, such as biomedical sensing,^{1–3} photothermal therapy,^{2–4} photovoltaic and plasmonic devices^{5–8} and photo- and electrocatalysis.^{9–18} In this thesis, the synthesis of copper sulfide nanoparticles and their potential for applications in photo- and electrocatalysis is explored. This chapter provides a brief background on the topics discussed and ends with an outline of the thesis.

1.1 Copper sulfide

Copper sulfide consists of a family of chemical compounds with the formula Cu_{2-x}S ($0 \leq x \leq 1$), where x indicates the degree of copper deficiency with respect to the fully stoichiometric compound. Copper sulfide has a rich phase diagram and exists in a variety of equilibrium crystal structures, such as monoclinic low-chalcocite Cu_2S , hexagonal high-chalcocite Cu_2S , monoclinic djurleite $\text{Cu}_{1.94}\text{S}$, hexagonal digenite $\text{Cu}_{1.8}\text{S}$, monoclinic roxbyite $\text{Cu}_{1.78}\text{S}$, orthorhombic anilite $\text{Cu}_{1.75}\text{S}$ and hexagonal covellite CuS .^{19,20} Most of these Cu_{2-x}S phases occur as minerals in nature.²⁰

The two most well-known copper sulfides are chalcocite (Cu_2S) and covellite (CuS) (Figure 1.1). Chalcocite originates from the Greek word *Chalkos*, which means copper, and has a dark grey to black color (Figure 1.1a).²¹ It is an important copper ore due to its high copper content and worldwide abundancy, and has been mined for centuries.²² The crystal structure of chalcocite is shown in Figure 1.1b and is based on a hexagonal close packing of sulfur atoms, with copper (Cu^+) atoms occupying mainly triangular interstices.^{20,23,24}

Covellite (CuS) is named after Niccolo Covelli, who first discovered the mineral at Mount Vesuvius in Italy.^{25,26} It has a limited abundancy, and typically originates from oxidation of other copper sulfide deposits, such as chalcopyrite (CuFeS_2).²⁵ CuS has a indigo-blue to black color and is highly iridescent (Figure 1.1c).²⁶ Figure 1d shows the crystal structure of CuS .²⁷ The structure can be described by stacked trilayers that consist of a layer of triangular CuS_3 units sandwiched between two layers of CuS_4 tetrahedra. The trilayers are connected to adjacent trilayers by disulfide bonds.^{28,29} Interestingly, the oxidation state of copper in the CuS system is highly debated. Even though the stoichiometry suggests the presence of divalent copper, several studies provide considerable evidence that the oxidation state of copper in all Cu_{2-x}S phases is monovalent.^{30–34} Here, CuS is considered as $(\text{Cu}^+)_3(\text{S}_2)^{2-}\text{S}$, where some of the sulfur atoms form S_2 pairs, while others are bound only to copper.³¹ In contrast, other studies indicate a combination of monovalent and divalent copper in CuS .^{35,36}

Cu_{2-x}S has an interesting electronic structure, in which the top of the valence band has a strong contribution from the sulfur p- and copper $3d^{10}$ orbitals, while the bottom of the conduction band has mainly contributions from the copper 4s and 4p orbitals.²⁹ In

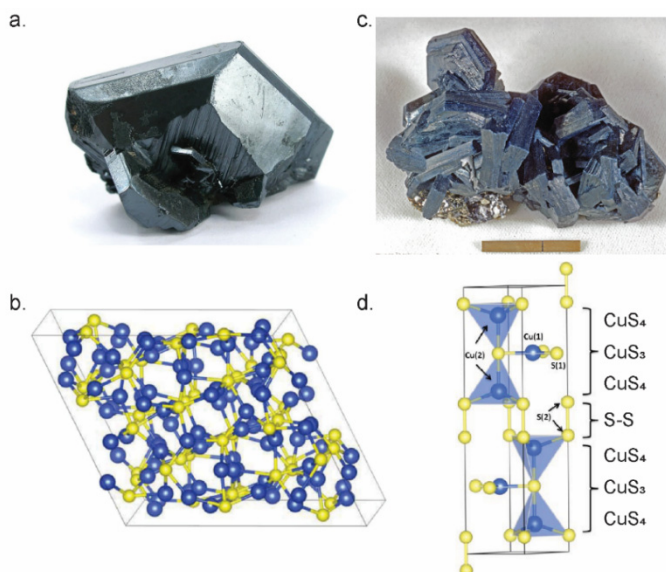


Figure 1.1 a) Chalcocite crystal²¹ and b) corresponding crystal structure. c) A covellite crystal,²⁶ and d) corresponding crystal structure. The blue and yellow spheres are copper and sulfur atoms, respectively. Panel b is reprinted from ref [24], with the permission of AIP Publishing. Copyright 2012 American Institute of Physics. Panel d is reprinted with permission from ref [27]. Copyright 2014 American Chemical Society.

stoichiometric Cu_2S , the valence band is completely filled. When copper is extracted, forming copper deficient Cu_{2-x}S compounds, holes are left in the top of the valence band. The presence of these holes influences the material properties.

For example, the effective bandgap of Cu_{2-x}S is affected by the concentration of holes in the valence band. The bandgap of a material can be defined as the photon energy needed to promote an electron from the top of the valence band to the bottom of the conduction band. The presence of holes in the top of the valence band leads to an increase in the effective bandgap, because the energy of the highest occupied electron states is lowered. This effect is schematically represented in Figure 1.2a and is referred to as the Burstein-Moss effect.^{29,37–39} The bandgap of Cu_{2-x}S is thus highly dependent on its composition, ranging from 1.2 eV for chalcocite (Cu_2S) to 1.9 eV for covellite (CuS).^{19,40}

In the case of Cu_{2-x}S nanoparticles, the holes in the valence band can give rise to a localized surface plasmon resonance (LSPR) absorption in the infrared region.⁶ This LSPR absorption originates from a collective oscillation of the holes in phase with the external electric field.²⁹ The frequency and intensity of the LSPR strongly depend on the free carrier concentration and thus on the composition of the Cu_{2-x}S nanoparticles.⁴¹ Figure 1.2b shows absorption spectra of Cu_{2-x}S nanoparticles with different compositions, indicating that with increasing copper concentration, *i.e.*, decreasing hole concentration, the LSPR absorption decreases in intensity and shifts to longer wavelengths.

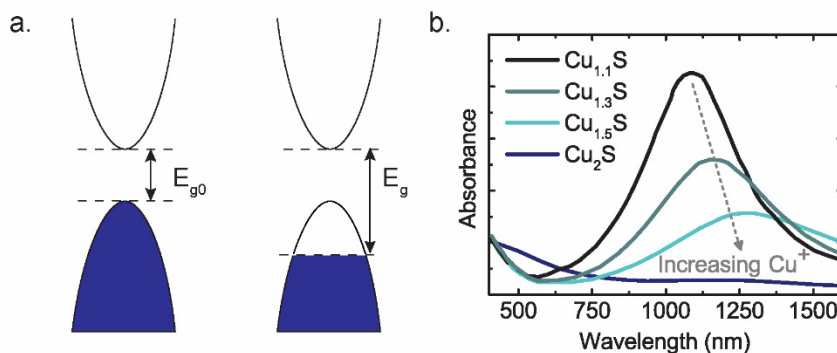


Figure 1.2 a) Representation of the band positions for Cu_2S and Cu_{2-x}S illustrating the increase of the effective bandgap with increasing amount of Cu-vacancies. Reprinted (adapted) with permission from ref [29]. Copyright 2014 The Royal Society of Chemistry. **b)** Optical absorption spectra of Cu_{2-x}S nanoparticles with different stoichiometries illustrating the dependence of the LSPR absorption on the Cu_{2-x}S composition. Reprinted (adapted) with permission from ref [41]. Copyright 2013 American Chemical Society.

1.2 Nanoparticles

The focus of this work is on Cu_{2-x}S nanoparticles. Nanoparticles are very small particles with dimensions ranging from 1 to 100 nanometers (nm), where one nm is equal to one billionth of a meter. As a comparison, 1 nm is about 100,000 times thinner than a sheet of paper. A nanoparticle consists roughly of about 100-10,000 atoms.⁴² Nanoparticles of Cu_{2-x}S have been successfully synthesized with a wide variety in size and shape, including nanospheres,⁴³⁻⁴⁵ nanoflowers,^{17,46} nanorods,⁴⁷ nanoplatelets^{45,47-49} and nanosheets.⁵⁰

Nanoparticles are attractive in chemistry due to their small size and resulting properties. In catalysis, reaction takes place at the surface of the catalyst. The smaller a particle, the larger the fraction of its atoms that are located at its surface, resulting in a high surface-to-volume ratio. This is illustrated in Figure 1.3a, which shows that the total surface area of small cubes is much larger than that of one big cube with the same total volume. In addition, the surface atoms differ from atoms in the interior of the particle as they have fewer chemical bonds with neighboring atoms, and consequently a higher free energy. This high free energy makes surface atoms more reactive.

Besides surface effects, the small size of nanoparticles leads to changes in their electronic structure. The electronic structure of a nanoparticle lies somewhere in between that of a molecule and of bulk material ($\sim 10^{22}$ atoms/cm³) (Figure 1.3b).⁵¹⁻⁵³ It consists of a valence- and conduction-band with discrete energy levels near the band edges. In a semiconductor, the valence- and conduction-band are separated by an energy gap of forbidden states, referred to as the band gap. When a semiconductor is irradiated with

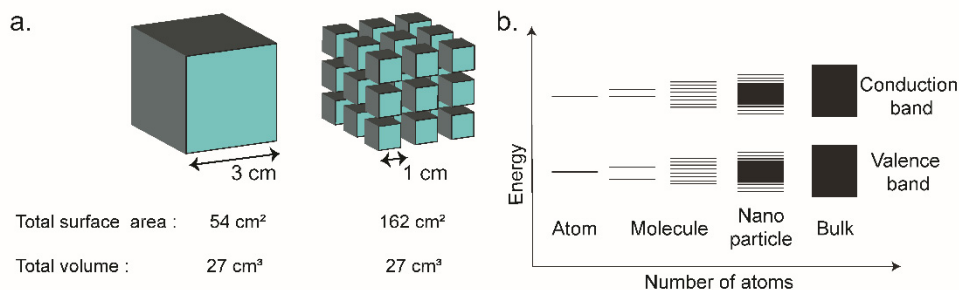


Figure 1.3 Size effects in nanoparticles **a)** Schematic representation of the increase in surface area when using 27 small particles instead of 1 big particle with the same volume. **b)** Band formation with increasing number of atoms according to the linear combination of atomic orbitals theory. Nanoparticles consist of a valence and conduction band with discrete energy levels near the band edges. Reprinted (adapted) with permission from ref [53]. Copyright 1996 The American Association for the Advancement of Science.

light that has an energy that is equal to or higher than the bandgap of the material, a negatively charged electron can be excited from the valence band to the conduction band, leaving behind a positively charged hole in the valence band. This electron-hole pair is referred to as an exciton. The spatial extension of the exciton is referred to as the exciton Bohr radius, and is a length characteristic for the material. When the size of a nanoparticle approaches this characteristic length, the exciton is confined in the nanoparticle, leading to an increase in its kinetic energy. As a consequence of this confinement, the bandgap increases. The bandgap of Cu_{2-x}S thus depends not only on its composition (see Section 1.1. above), but also on the size of the material via the quantum confinement effect. Although the value of the exciton Bohr radius of Cu_{2-x}S is under debate, several studies reported quantum confinement effects for Cu_{2-x}S nanoparticles with sizes around 10 nm and smaller.⁴⁰

1.3 Synthesis methods for Cu_{2-x}S nanoparticles

As the catalytic and electronic properties depend on nanoparticle composition, size and shape, having monodisperse samples is important. In this thesis we describe nanoparticles synthesized by either colloidal synthesis or incipient wetness impregnation. These methods are introduced below.

1.3.1 Colloidal synthesis

Colloidal synthesis methods are attractive as they allow for a high degree of control over the size, shape and composition of the nanoparticles.^{42,54} In colloidal synthesis, nanoparticles are grown in a liquid-phase and the product nanoparticles are obtained as colloidal suspension. This means that the nanoparticles are uniformly distributed in the solvent, without directly sinking to the bottom.⁵⁵

Figure 1.4 shows the different stages of colloidal synthesis.⁵⁶ In the first stage, referred to as the pre-nucleation stage, precursors react to form monomers. Examples of such precursors are inorganic salts and organometallic compounds. The formed monomers are the building blocks of nanocrystals. For example, $\text{Cu}_2\text{-xS}$ nanoparticles are formed by many Cu-S monomers. The sudden availability of a high concentration of monomers leads to monomer supersaturation, in which the concentration of monomers is higher than the solubility limit. During supersaturation, clusters of monomers, *i.e.*, the subcritical crystal nuclei, are formed. These subcritical nuclei can grow to larger nuclei, shrink to smaller nuclei or dissolve back to monomers. During the nucleation stage, nuclei grow larger than the critical radius, the size at which the nuclei are viable to grow to mature nanoparticles. During this stage, monomers are consumed and hence there will no longer be supersaturation. Consequently, the nucleation rate decreases and the remaining monomers in solution are now only used for growth of the already existing nuclei. Nanoparticle growth can occur via the addition of monomers to existing nuclei, coalescence of small particles or a combination of both processes.

Surfactants, or organic ligands, are present during the colloidal synthesis and influence the nucleation rates.⁴² Surfactants typically consist of an apolar hydrocarbon tail and a polar headgroup that can bind to the monomers and nuclei. The surfactants influence the size, shape and composition of the nanocrystals as they can affect the monomer

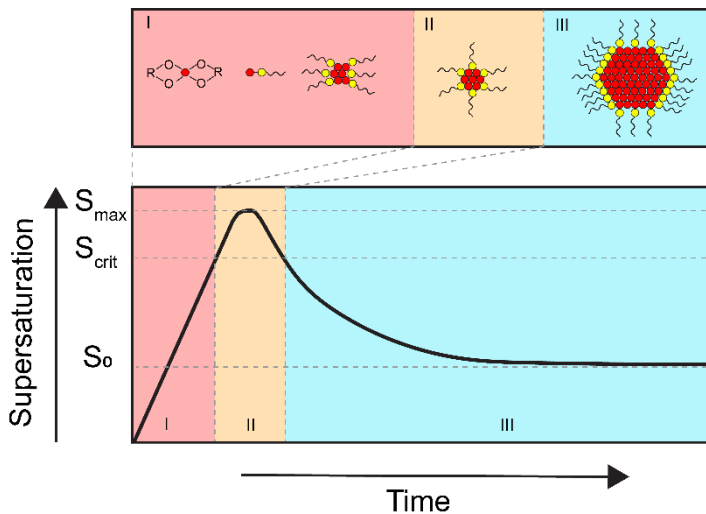


Figure 1.4 Evolution of the degree of supersaturation S over time with corresponding stages of colloidal nanocrystals synthesis. I) Induction, where metal precursors and ligands form monomers, that can subsequently form sub-critical nuclei, II) Nucleation, where the sub-critical nuclei are converted into nuclei that are capable of growing into mature nanocrystals and III) Growth, where the nuclei grow to mature nanocrystals. Reprinted (adapted) with permission from ref [52]. Copyright 2014 Springer-Verlag Berlin Heidelberg

reactivity and thereby the rate of monomer formation. Furthermore, the surfactant molecules dynamically bind to the monomer species and nuclei, thereby changing the stability of the monomers and consequently the nucleation rate. In addition, the surfactants can have a large impact on the growth rates and shape of the nanoparticles, as they may bind more strongly to certain facets, thereby determining the availability of surface sites.⁴² The surfactants have an important role not only during the synthesis, but also after, when they stabilize the nanoparticles in solution. However, when using colloidal nanoparticles in applications such as catalysis, the bulky organic ligands can influence catalytic performance by, for example, blocking the active catalyst species.⁵⁷⁻⁶¹ Therefore, ligand exchange procedures, in which the native ligands are replaced by alternatives that have no adverse effects in catalysis, are required. In chapter 2, such a ligand exchange procedure is described for strongly bound 1-dodecanethiol ligands on Cu_{2-x}S nanoparticles.

1.3.2 Incipient wetness impregnation to make supported nanoparticles

Supported nanoparticles are often used in catalysis. In the first place, the support can facilitate the preparation of small and uniformly distributed particles. In addition, the support can improve the mechanical and thermal stability of the catalyst and simplifies its handling (*e.g.*, separation of the catalyst and product stream).⁶² The most common catalyst support materials include silica, titanium dioxide, alumina, carbon and zeolites.⁶³ The properties of the support, such as thermal stability, electric conductivity and light absorption, determine which support material is most suitable for a certain application. For example, in photocatalysis, the absorption properties of the support material are of great importance, whereas in electrocatalysis a good electrical conductivity of the support is crucial.

Supported catalysts can be synthesized via various methods, among which incipient wetness impregnation.⁶² In this technique, a porous support, such as silica or carbon, is impregnated by a solution of the metal-precursor of interest. After the impregnation step, the material is dried to evaporate the solvent and heat treated to decompose the metal precursor and subsequently form metal oxide nanoparticles. The properties of the product nanoparticles can be influenced by the parameters used in the heat treatment. For example, the composition of the gas used during the heat treatment can influence the size or composition of the nanoparticles.⁶⁴⁻⁶⁶ Additional treatments can be performed to obtain *e.g.*, metal sulfide nanoparticles. Metal sulfide nanoparticles are often prepared by converting metal nanoparticles by a gas phase sulfidation, typically in $\text{H}_2\text{S}/\text{H}_2$ atmospheres at temperatures between 300-400°C.⁶⁷ In addition, metal sulfide nanoparticles can be obtained by a liquid-phase sulfidation. In Chapter 4, the preparation of silica supported copper sulfide nanoparticles via direct synthesis and via a liquid phase sulfidation of supported copper oxide nanoparticles is discussed in detail.

1.4 Catalysis with Copper Sulfide Nanoparticles

Due to their wide size, shape and composition tunability, natural abundance and low toxicity, Cu_{2-x}S nanoparticles have attracted increasing attention for applications in catalysis. In our work, the potential of Cu_{2-x}S nanoparticles as photo- and electrocatalysts is explored.

1.4.1 Photocatalysis

Photocatalysis is a process inspired by natural photosynthesis. Green plants harvest energy from sunlight and convert it into chemical energy, stored in carbohydrate molecules such as sugars. Similarly, in photocatalysis a semiconductor material (*i.e.*, the photocatalyst) absorbs light, which generates charge carriers (electrons and holes). These charge carriers can be used to drive redox reactions at the surface of the photocatalyst. Figure 1.5 schematically represents the photocatalysis process. A semiconductor has a band structure in which the conduction band and valence band are separated by a bandgap. If the semiconductor is irradiated with light that has an energy equal to or higher than the bandgap, electrons can be excited from the valence band to the conduction band, leaving behind positively charged holes in the valence band. The photogenerated charge carriers can recombine non-radiatively or radiatively, thereby releasing the energy as heat or photons, respectively. Alternatively, if the electrons and holes can reach the surface of the semiconductor, they can drive reduction and oxidation reactions of adsorbed species. The use of thin layers of material or nanoparticles is thus advantageous, as in this case the distance that the electrons and holes have to travel to reach the surface is small. Once the charge carriers have reached the surface, redox reactions only occur if the positions of the valence- and conduction band of the photocatalyst are aligned in a suitable manner with respect to the redox potentials of the reaction of interest. For a reduction reaction to occur, the conduction band edge has to

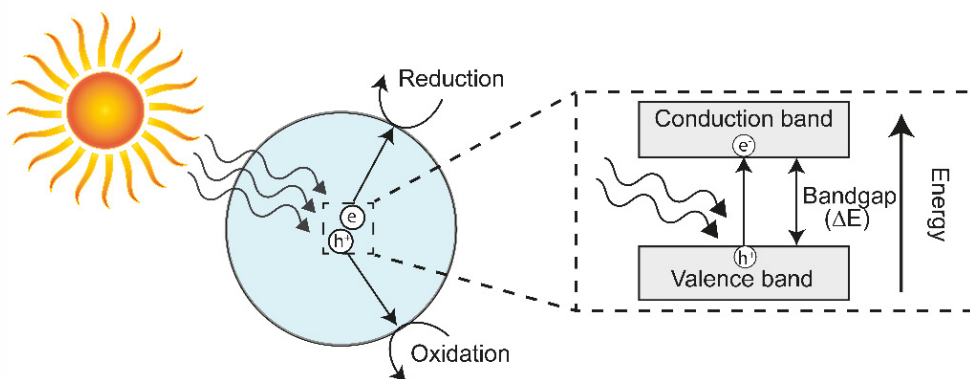
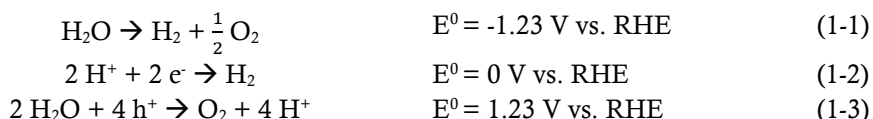


Figure 1.5 Schematic representation of a nanoparticle photocatalyst. The semiconductor nanoparticles can absorb (sun)light with an energy equal or higher than the bandgap, thereby exciting electrons from the valence to the conduction band. The photogenerated electron and hole can participate in redox reactions at the particle surface.

be more negative than the redox potential of this reaction, while for an oxidation reaction to occur, the valence band edge needs to be more positive than the redox potential of the reaction.

In general, two types of photocatalysis can be distinguished.^{68,69} Firstly, similar to 'classical' catalysis, a photocatalyst can reduce the activation energy of a chemical reaction and thereby accelerate a reaction that occurs spontaneously ($\Delta G < 0$). An example of this is the oxidative degradation of dye molecules. Degradation studies are often used to assess the performance of novel photocatalyst materials as the progress of the reaction is easy to follow due to the change of color. Their use is generally motivated by serving as model reactions for the decomposition of organic pollutants in waste water.⁷⁰⁻⁷² Frequently studied dyes in these type of reactions are methylene blue, methyl orange, malachite green and rhodamine B.⁷³

In addition, the term photocatalysis is used for reactions that are thermodynamically uphill ($\Delta G > 0$), but can proceed with light in the presence of a photocatalyst. This includes the production of solar fuels, where solar energy is converted into chemical energy. A well-known example here is photocatalytic water splitting, in which hydrogen and oxygen are produced by the cleavage of water, as described by Equation 1-1. The corresponding half-reactions are given in Equation 1-2 and Equation 1-3.



Although hydrogen production from water is a promising approach for the storage of renewable energy, photocatalytic water-splitting remains a challenge as there are only few photocatalysts with a suitable band positioning to drive both the hydrogen evolution reaction as well as the oxygen evolution reaction. Therefore, rather than overall water-splitting, a selective study of one of the half-reactions (Eq. 1-2 and 1-3) in the presence of a sacrificial agent is often used to examine the photocatalytic properties of novel materials.⁷⁴ Two individual photocatalysts that are each active for one of the half reactions (either H_2 -evolution or O_2 -evolution) can potentially be coupled to obtain Z-scheme photocatalysis and mimic overall water-splitting.⁷⁵

The bandgap of a photocatalyst is thus an important property. As discussed above, it should be sufficiently large to absorb photons with an energy large enough for the redox reaction to occur, but on the other hand should not be too large in order to efficiently absorb sunlight. In addition, the positions of the valence and conduction band should be compatible with the redox levels of the redox reaction of interest. The tunable bandgap of Cu_{2-x}S , ranging from 1.2 eV for Cu_2S to 1.9 eV for CuS , allows it to absorb a relatively large part of solar spectrum. Figure 1.6 gives a representation of the band positions of

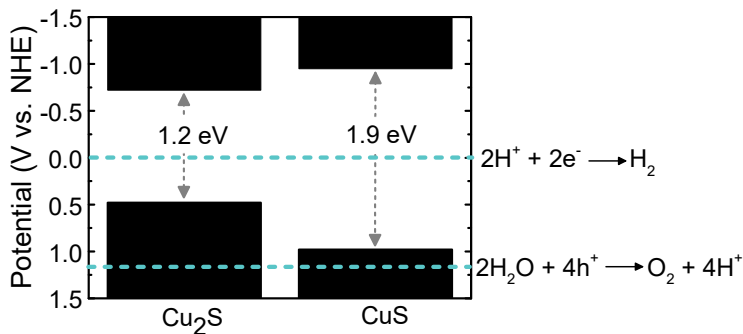


Figure 1.6 Representation of the band positions of Cu₂S and CuS illustrating the variation of the bandgap with Cu_{2-x}S composition. The blue dashed lines indicate the redox potentials of the H₂-evolution reaction and O₂-evolution reaction. The band positions are obtained from refs [76-78].

Cu₂S and CuS and the redox potentials of the H₂-evolution and O₂-evolution reactions.⁷⁶⁻⁷⁸ The conduction band edge of Cu_{2-x}S is more negative than the redox potential of the H₂-evolution reaction, indicating this reaction could proceed on Cu_{2-x}S. The redox potential of the O₂-evolution reaction is however more positive than the valence band edge of Cu_{2-x}S, making this reaction non-viable on Cu_{2-x}S. Several groups reported the use of Cu_{2-x}S as photocatalyst. For example, the photodegradation of dyes has been reported using Cu_{2-x}S photocatalysts with a variety of compositions and shapes, such as CuS nanoparticles,⁷⁹⁻⁸¹ Cu₂S nanoparticles,⁸²⁻⁸⁴ CuS nanotubes,⁸⁵⁻⁸⁷ Cu₂S microsponges⁸⁸ and CuS, Cu₂S and Cu_{1.8}S nanoflowers.⁸⁹⁻⁹¹ In addition, some studies reported the use of Cu_{2-x}S for photocatalytic hydrogen evolution in the presence of a sacrificial agent.^{9,92,93}

1.4.2 Electrocatalysis

An electrochemical reaction is driven by the passage of an electric current and involves the transfer of electrons between a solid electrode and reactants in solution. In electrocatalysis, the exchange current density of such an electrochemical reaction is altered by the addition of a catalyst. The catalyst may be the electrode itself, or can be deposited on the electrode. Figure 1.7 shows a schematic representation of an electrochemical cell, which has three main components: the anode, the cathode and the electrolyte. The anode is the electrode at which oxidation reactions occur, whereas reduction reactions take place at the cathode. The electrolyte is an ionically conducting medium connecting the anode with the cathode.

The electrochemical reduction of CO₂ using renewable electricity is considered a promising route to produce chemicals and fuels in a sustainable manner. Table 1.1 shows some half-reactions of products that can be formed by the reduction of CO₂ and corresponding redox potentials.⁹⁴ When looking at the possible half-reactions shown in Table 1.1, most of them include multiple electron- and proton transfer steps.

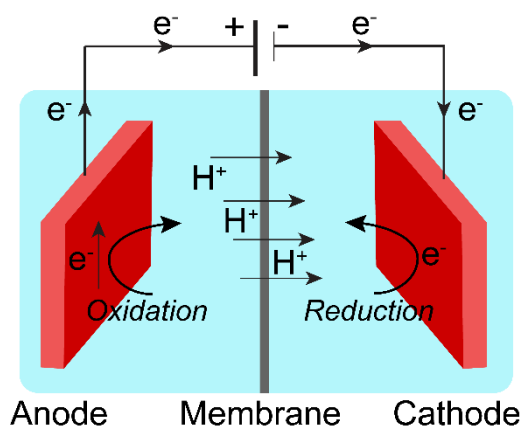


Figure 1.7 Schematic representation of an electrochemical cell used in electrocatalysis. Oxidation reactions occur at the anode, whereas reduction reactions occur at the cathode. The anode and cathode are connected by an ionically conducting electrolyte.

Furthermore, the redox potentials of the different products are very similar, making it difficult to selectively form one product. In addition, the redox potentials for the formation of CO₂ reduction products are similar to the redox potential for the hydrogen evolution reaction, making this a competing reaction. The electrochemical reduction of CO₂ is thus a complex process that requires a stable and efficient catalyst.⁹⁵

Over the last decade, great progress has been made in the development of electrocatalysts. The majority of electrocatalyst studied for the reduction of CO₂ are based on transition metals.^{95,96} For example, nanostructured gold and silver catalysts have shown to reduce CO₂ to CO with faradaic efficiencies over 90% at low overpotentials (<0.9 V vs. RHE).⁹⁷ In addition, copper catalysts have received significant attention due to their relatively low cost and unique ability to produce hydrocarbons and oxygenates.⁹⁸ However, the competing hydrogen evolution reaction (HER) at low overpotentials remains a challenge. More recently, the incorporation of sulfur in copper

Table 1.1 Selected half reactions and reduction potentials of CO₂ reduction reactions, along with that of the hydrogen evolution reaction. Reprinted with permission from ref [94]. Copyright 2014 American Chemical Society.

CO ₂ Reduction Half Reactions	[V] vs RHE
CO ₂ + H ₂ O + 2e ⁻ → CO + 2OH ⁻	-0.10
CO ₂ + H ₂ O + 2e ⁻ → HCOO ⁻ + OH ⁻	-0.03
CO ₂ + 5H ₂ O + 6e ⁻ → CH ₃ OH + 6OH ⁻	0.03
CO ₂ + 6H ₂ O + 8e ⁻ → CH ₄ + 8OH ⁻	0.17
2CO ₂ + 8H ₂ O + 12e ⁻ → C ₂ H ₄ + 12OH ⁻	0.08
H ₂ O Reduction Half Reaction	
2H ₂ O + 2e ⁻ → 2H ₂ + 2OH ⁻	0.0

electrodes has shown to modify their performance. Several experimental and theoretical studies have demonstrated that the presence of sulfur in the copper electrode steers the selectivity of the catalyst towards formate.^{12,99–102} In addition, Zhuang *et al.*, reported the production of ethanol, propanol and ethylene at intermediate overpotential (-0.95 V vs. RHE) using Cu₂S derived nanoparticles.¹³ An exploration of the influence of sulfur on copper electrocatalysts for the reduction of CO₂ is described in Chapter 6 of this thesis.

1.5 Outline of this thesis

1

The size-, shape- and composition dependent materials properties of Cu_{2-x}S, together with its abundance and relatively low toxicity, make it an interesting candidate for catalytic applications. In this thesis the synthesis and characterization of copper sulfide nanoparticles for applications in photo- and electrocatalysis is discussed.

In the first part (Chapters 2, 3 and 4), preparation methods for Cu_{2-x}S (hetero)nanoparticles are described. Colloidal synthesis methods allow a good control over the particle size, shape and composition. However, the organic ligands stabilizing the particles complicate their use in catalytic applications. Hence, ligand exchange procedures are often required. **Chapter 2** describes a ligand exchange procedure to replace strongly bound 1-dodecanethiol ligands on colloidal Cu_{2-x}S nanocrystals by alternative ligands. This ligand exchange procedure makes the nanocrystals dispersible in water and more accessible for reactants, and thus more applicable for catalysis.

As they are of potential interest as photocatalyst, **Chapter 3** describes the synthesis of Cu_{2-x}S/CuInS₂ heteronanocrystals via a seeded-injection strategy. The presence of a hetero-junction in these nanocrystals is expected to enhance the separation of the photogenerated charges, which can be beneficial in photocatalytic applications.

The use of a support material, such as carbon or silica, can improve the stability of nanoparticles and simplifies their handling (*e.g.*, in catalyst separation). In **Chapter 4** methods to synthesize supported Cu_{2-x}S nanoparticles are discussed. Besides a direct synthesis, a two-step approach is presented, in which supported CuO nanoparticles, prepared via incipient wetness impregnation, are converted into Cu_{2-x}S nanoparticles via a liquid phase sulfidation step. Depending on the sulfur source and reaction conditions used, different Cu_{2-x}S phases were prepared.

The original aim of the project was to investigate the effect of particle size, shape and composition of Cu_{2-x}S nanoparticles on their photocatalytic properties. However, along the way we found that Cu_{2-x}S nanoparticles show limited activity in photocatalytic dye degradation and H₂ evolution. In addition, conducting photocatalytic experiments proved to not always be straightforward, and experimental procedures and results reported in literature were not always reproducible. In **Chapter 5** various aspects of photocatalysis, including experimental techniques, data analysis, mechanistic insights and reporting of catalytic performance, are reviewed. Common pitfalls and practical

guidelines on how to reliably conduct, interpret and report photocatalytic experiments are discussed, based on experience from our own work on Cu_{2-x}S nanoparticles, as well as examples from literature.

Besides photocatalysis, the Cu_{2-x}S nanoparticles can be used in electrocatalysis. **Chapter 6** explores the use of carbon supported Cu_{2-x}S nanoparticles for the electrocatalytic reduction of CO_2 . Electrodes with good chemical contact were successfully prepared by spraying the carbon supported Cu_{2-x}S nanoparticles on a carbon paper substrate. Under reaction conditions, the Cu_{2-x}S nanoparticles are reduced to a metallic copper phase, that shows activity towards the reduction of CO_2 into formate.

Chapter 7 provides a summary of the thesis and a brief outlook for future work. Finally, a summary of the work in Dutch is provided in **Chapter 8**.

1.6 References

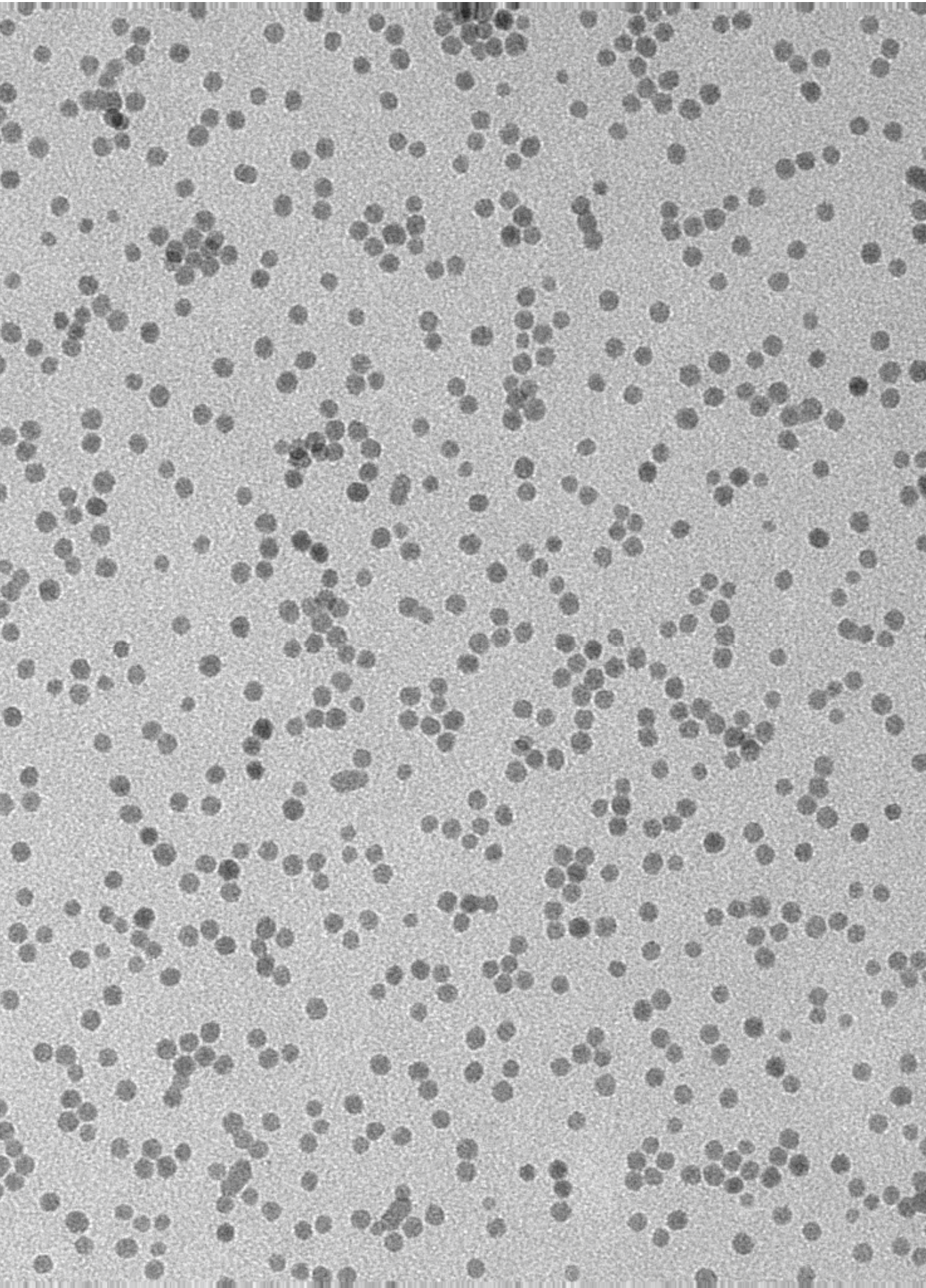
- (1) Goel, S.; Chen, F.; Ehlerding, E. B.; Cai, W. Intrinsically Radiolabeled Nanoparticles: An Emerging Paradigm. *Small* **2014**, *10*, 3825–3830.
- (2) Coughlan, C.; Ibáñez, M.; Dobrozhan, O.; Singh, A.; Cabot, A.; Ryan, K. M. Compound Copper Chalcogenide Nanocrystals. *Chem. Rev.* **2017**, *117*, 5865–6109.
- (3) Goel, S.; Chen, F.; Cai, W. Synthesis and Biomedical Applications of Copper Sulfide Nanoparticles: From Sensors to Theranostics. *Small* **2014**, *10*, 631–645.
- (4) Wang, S.; Riedinger, A.; Li, H.; Fu, C.; Liu, H.; Li, L.; Liu, T.; Tan, L.; Barthel, M. J.; Pugliese, G.; et al., Plasmonic Copper Sulfide Nanocrystals Exhibiting Near-Infrared Photothermal and Photodynamic Therapeutic Effects. *ACS Nano* **2015**, *9*, 1788–1800.
- (5) Zhao, Y.; Burda, C. Development of Plasmonic Semiconductor Nanomaterials with Copper Chalcogenides for a Future with Sustainable Energy Materials. *Energy Environ. Sci.* **2012**, *5*, 5564–5576.
- (6) Luther, J. M.; Jain, P. K.; Ewers, T.; Alivisatos, A. P. Localized Surface Plasmon Resonances Arising from Free Carriers in Doped Quantum Dots. *Nat. Mater.* **2011**, *10*, 361–366.
- (7) Abdelhady, A. L.; Ramasamy, K.; Malik, M. A.; O'Brien, P.; Haigh, S. J.; Raftery, J. New Routes to Copper Sulfide Nanostructures and Thin Films. *J. Mater. Chem.* **2011**, *21*, 17888–17895.
- (8) Van Der Stam, W.; Gudjonsdottir, S.; Evers, W. H.; Houtepen, A. J. Switching between Plasmonic and Fluorescent Copper Sulfide Nanocrystals. *J. Am. Chem. Soc.* **2017**, *139*, 13208–13217.
- (9) Ying Toe, C.; Zheng, Z.; Wu, H.; Scott, J.; Amal, R.; Hau Ng, Y. Transformation of Cuprous Oxide into Hollow Copper Sulfide Cubes for Photocatalytic Hydrogen Generation. *J. Phys. Chem. C* **2018**, *122*, 25.
- (10) Shao, P.; Ci, S.; Yi, L.; Cai, P.; Huang, P.; Cao, C.; Wen, Z. Hollow CuS Microcube Electrocatalysts for CO₂ Reduction Reaction. *ChemElectroChem* **2017**, *4*, 2593–2598.
- (11) Zhao, Z.; Peng, X.; Liu, X.; Sun, X.; Shi, J.; Han, L.; Li, G.; Luo, J. Efficient and Stable Electroreduction of CO₂ to CH₄ on CuS Nanosheet Arrays. *J. Mater. Chem. A* **2017**, *5*, 20239–20243.
- (12) Zhu, Q. G.; Sun, X. F.; Kang, X. C.; MA, J.; Qian, Q. L.; Han, B. X. Cu₂S on Cu Foam as Highly Efficient Electrocatalyst for Reduction of CO₂ to Formic Acid. *Acta Phys. - Chim. Sin.* **2016**, *32*, 261–266.
- (13) Zhuang, T.-T.; Liang, Z.-Q.; Seifitokaldani, A. Steering Post-C–C Coupling Selectivity Enables High Efficiency Electroreduction of Carbon Dioxide to Multi-Carbon Alcohols. *Nat. Catal.* **2018**, *1*, 421–428.
- (14) Chandra, M.; Bhunia, K.; Pradhan, D. Controlled Synthesis of CuS/TiO₂ Heterostructured Nanocomposites for Enhanced Photocatalytic Hydrogen Generation through Water Splitting. *Inorg. Chem.* **2018**, *57*, 4524–4533.
- (15) Huerta-Flores, A. M.; Torres-Martínez, L. M.; Moctezuma, E.; Singh, A. P.; Wickman, B. Green Synthesis of Earth-Abundant Metal Sulfides (FeS₂, CuS, and NiS₂) and Their Use as Visible-Light Active Photocatalysts for H₂ Generation and Dye Removal. *J. Mater. Sci. Mater. Electron.* **2018**, *29*, 11613–11626.
- (16) Chen, Y.; Qin, Z.; Wang, X.; Guo, X.; Guo, L. Noble-Metal-Free Cu₂S-Modified Photocatalysts for Enhanced Photocatalytic Hydrogen Production by Forming Nanoscale p-n Junction Structure. *RSC Advances* **2015**, *5*, 18159–18166.
- (17) Meng, X.; Tian, G.; Chen, Y.; Zhai, R.; Zhou, J.; Shi, Y.; Cao, X.; Zhou, W.; Fu, H. Hierarchical CuS Hollow Nanospheres and Their Structure-Enhanced Visible Light Photocatalytic Properties. *CrystEngComm* **2013**, *15*, 5144.
- (18) Kar, P.; Farsinezhad, S.; Zhang, X.; Shankar, K. Anodic Cu₂S and CuS Nanorod and Nanowall Arrays: Preparation, Properties and Application in CO₂ Photoreduction. *Nanoscale* **2014**, *6*, 14305–14318.
- (19) Van Der Stam, W.; Berends, A. C.; De Mello Donega, C. Prospects of Colloidal Copper Chalcogenide Nanocrystals. *ChemPhysChem* **2016**, *17*, 559–581.
- (20) Chakrabarti, D. J.; Laughlin, D. E. The Cu-S (Copper-Sulfur) System. *Bull. Alloy Phase Diagrams* **1983**, *4*, 254–271.
- (21) Chalcocite: Mineral information, data and localities. - Mindat.org <https://www.mindat.org/min-962.html> (accessed Feb 13, 2020).
- (22) Anthony, J. W.; Bideaux, R. A.; Bladh, K. W.; Nichols, M. C. Chalcocite, Handbook of Mineralogy, Mineralogical Society of America <http://www.handbookofmineralogy.org/pdfs/chalcocite.pdf> (accessed Nov 20, 2019).
- (23) Evans, H. T. The Crystal Structures of Low Chalcocite and Djurleite. *Zeitschrift für Krist. - New Cryst.*

- Struct.* **1979**, *150*, 299–320.
- (24) Xu, Q.; Huang, B.; Zhao, Y.; Yan, Y.; Noufi, R.; Wei, S. H. Crystal and Electronic Structures of Cu_xS Solar Cell Absorbers. *Appl. Phys. Lett.* **2012**, *100*, 061906.
- (25) Anthony, J. W.; Bideaux, R. A.; Bladh, K. W.; Nichols, M. C. Covellite, Handbook of Mineralogy, Mineralogical Society of America <http://www.handbookofmineralogy.org/pdfs/covellite.pdf> (accessed Nov 20, 2019).
- (26) Covellite: Mineral information, data and localities. <https://www.mindat.org/min-1144.html> (accessed Nov 20, 2019).
- (27) Morales-García, A.; Soares, A. L.; Dos Santos, E. C.; De Abreu, H. A.; Duarte, H. A. First-Principles Calculations and Electron Density Topological Analysis of Covellite (CuS). *J. Phys. Chem. A* **2014**, *118*, 5823–5831.
- (28) Casaca, A.; Lopes, E. B.; Gonçalves, A. P.; Almeida, M. Electrical Transport Properties of CuS Single Crystals. *J. Phys. Condens. Matter* **2012**, *24*, 015701.
- (29) Comin, A.; Manna, L. New Materials for Tunable Plasmonic Colloidal Nanocrystals. *Chem. Soc. Rev* **2014**, *43*, 3957–3975.
- (30) Goh, S. W.; Buckley, A. N.; Lamb, R. N. Copper(II) Sulfide? *Miner. Eng.* **2006**, *19*, 204–208.
- (31) Folmer, J. C. W.; Jellinek, F. The Valence of Copper in Sulphides and Selenides: An X-Ray Photoelectron Spectroscopy Study. *J. Less-Common Met.* **1980**, *76*, 153–162.
- (32) Rupp, H.; Weser, U. X-Ray Photoelectron Spectroscopy of Copper(II), Copper(I), and Mixed Valence Systems. *Bioinorg. Chem.* **1976**, *6*, 45–59.
- (33) Nakai, I.; Sugitani, Y.; Nagashima, K.; Niwa, Y. X-Ray Photoelectron Spectroscopic Study of Copper Minerals. *J. Inorg. Nucl. Chem.* **1978**, *40*, 789–791.
- (34) Folmer, J. C. W.; Jellinek, F.; Calis, G. H. M. The Electronic Structure of Pyrites, Particularly CuS_2 and $\text{Fe}_{1-x}\text{Cu}_x\text{Se}_2$: An XPS and Mössbauer Study. *J. Solid State Chem.* **1988**, *72*, 137–144.
- (35) Vegelius, J. R.; Kvashnina, K. O.; Hollmark, H.; Klintonberg, M.; Kvashnin, Y. O.; Soroka, I. L.; Werme, L.; Butorin, S. M. X-Ray Spectroscopic Study of Cu_2S , CuS , and Copper Films Exposed to Na_2S Solutions. *J. Phys. Chem. C* **2012**, *116*, 22293–22300.
- (36) Kumar, P.; Nagarajan, R.; Sarangi, R. Quantitative X-Ray Absorption and Emission Spectroscopies: Electronic Structure Elucidation of Cu_2S and CuS . *J. Mater. Chem. C* **2013**, *1*, 2448–2454.
- (37) Burstein, E. Anomalous Optical Absorption Limit in InSb . *Phys. Rev.* **1954**, *93*, 632–633.
- (38) Moss, T. S. The Interpretation of the Properties of Indium Antimonide. *Proc. Phys. Soc. Sect. B* **1954**, *67*, 775–782.
- (39) Lukashev, P.; Lambrecht, W. R. L.; Kotani, T.; Van Schilfgaarde, M. Electronic and Crystal Structure of Cu_{2-x}S : Full-Potential Electronic Structure Calculations. *Phys. Rev. B - Condens. Matter Mater. Phys.* **2007**, *76*, 195202.
- (40) Zhao, Y.; Pan, H.; Lou, Y.; Qiu, X.; Zhu, J.; Burda, C. Plasmonic Cu_{2-x}S Nanocrystals: Optical and Structural Properties of Copper-Deficient Copper(I) Sulfides. *J. Am. Chem. Soc.* **2009**, *131*, 4253–4261.
- (41) Xie, Y.; Riedinger, A.; Prato, M.; Casu, A.; Genovese, A.; Guardia, P.; Sottini, S.; Sangregorio, C.; Misztal, K.; Ghosh, S.; et al., Copper Sulfide Nanocrystals with Tunable Composition by Reduction of Covellite Nanocrystals with Cu^+ Ions. *J. Am. Chem. Soc.* **2013**, *135*, 17630–17637.
- (42) Donegá, C. D. M. Synthesis and Properties of Colloidal Heteronanocrystals. *Chem. Soc. Rev.* **2011**, *40*, 1512–1546.
- (43) Li, W.; Shavel, A.; Guzman, R.; Rubio-Garcia, J.; Flox, C.; Fan, J.; Cadavid, D.; Ibáñez, M.; Arbiol, J.; Morante, J. R.; et al., Morphology Evolution of Cu_{2-x}S Nanoparticles: From Spheres to Dodecahedrons. *Chem. Commun.* **2011**, *47*, 10332–10334.
- (44) Tang, A.; Qu, S.; Li, K.; Hou, Y.; Teng, F.; Cao, J.; Wang, Y.; Wang, Z. One-Pot Synthesis and Self-Assembly of Colloidal Copper(I) Sulfide Nanocrystals. *Nanotechnology* **2010**, *21*, 285602.
- (45) van der Stam, W.; Gradmann, S.; Altantzis, T.; Ke, X.; Baldus, M.; Bals, S.; de Mello Donega, C. Shape Control of Colloidal Cu_{2-x}S Polyhedral Nanocrystals by Tuning the Nucleation Rates. *Chem. Mater.* **2016**, *28*, 6705–6715.
- (46) Nekouei, F.; Nekouei, S.; Jashnsaz, O.; Pouzesh, M. Green Approach for In-Situ Growth of Highly-Ordered 3D Flower-like CuS Hollow Nanospheres Decorated on Nitrogen and Sulfur Co-Doped Graphene Bionanocomposite with Enhanced Peroxidase-like Catalytic Activity Performance for Colorimetric Biosensing of Glucose. *Mater. Sci. Eng. C* **2018**, *90*, 576–588.
- (47) Larsen, T. H.; Sigman, M.; Ghezlbash, A.; Doty, R. C.; Korgel, B. A. Solventless Synthesis of Copper Sulfide Nanorods by Thermolysis of a Single Source Thiolate-Derived Precursor. *J. Am. Chem. Soc.* **2003**, *125*, 5638–5639.
- (48) Li, X.; Shen, H.; Niu, J.; Li, S.; Zhang, Y.; Wang, H.; Li, L. S. Columnar Self-Assembly of Cu_2S Hexagonal Nanoplates Induced by Tin(IV)-X Complex as Inorganic Surface Ligand. *J. Am. Chem. Soc.* **2010**, *132*, 12778–12779.

- (49) Li, X.; Wang, M.; Shen, H.; Zhang, Y.; Wang, H.; Li, L. S. Inorganic Sn-X-Complex-Induced 1D, 2D, and 3D Copper Sulfide Superstructures from Anisotropic Hexagonal Nanoplate Building Blocks. *Chem. - A Eur. J.* **2011**, *17*, 10357–10364.
- (50) Van Der Stam, W.; Akkerman, Q. A.; Ke, X.; Van Huis, M. A.; Bals, S.; De, C.; Donega, M. Solution-Processable Ultrathin Size- and Shape-Controlled Colloidal Cu_{2-x}S Nanosheets. *Chem. Mater.* **2015**, *27*, 283–291.
- (51) Bawendi, M. The Quantum Mechanics Of Larger Semiconductor Clusters (Quantum Dots). *Annu. Rev. Phys. Chem.* **1990**, *41*, 477–496.
- (52) De Mello Donegá, C. *Nanoparticles: Workhorses of Nanoscience*; De Mello Donegá, C., Ed.; Springer-Verlag: Berlin Heidelberg, 2014.
- (53) Allivisatos, A. P. Semiconductor Clusters, Nanocrystals and Quantum Dots. *Science.* **1996**, *271*, 933–937.
- (54) Van Embden, J.; Chesman, A. S. R.; Jasieniak, J. J. The Heat-Up Synthesis of Colloidal Nanocrystals. *Chem. Mater.* **2015**, *27*, 2246–2285.
- (55) López-Esparza, R.; Balderas Altamirano, M. A.; Pérez, E.; Gama Goicochea, A. Importance of Molecular Interactions in Colloidal Dispersions. *Adv. Condens. Matter Phys.* **2015**, *2015*, 1–8.
- (56) LaMer, V. K.; Dinegar, R. H. Theory, Production and Mechanism of Formation of Monodispersed Hydrosols. *J. Am. Chem. Soc.* **1950**, *72*, 4847–4854.
- (57) Ben-Shahar, Y.; Scotognella, F.; Waiskopf, N.; Kriegel, I.; Dal Conte, S.; Cerullo, G.; Banin, U. Effect of Surface Coating on the Photocatalytic Function of Hybrid CdS-Au Nanorods. *Small* **2015**, *11*, 462–471.
- (58) Nag, A.; Kovalenko, M. V.; Lee, J. S.; Liu, W.; Spokoyny, B.; Talapin, D. V. Metal-Free Inorganic Ligands for Colloidal Nanocrystals: S²⁻, HS⁻, Se²⁻, HSe⁻, Te²⁻, HTe⁻, TeS₃²⁻, OH⁻, and NH₂⁻ as Surface Ligands. *J. Am. Chem. Soc.* **2011**, *133*, 10612–10620.
- (59) Donoeva, B.; de Jongh, P. E. Colloidal Au Catalyst Preparation: Selective Removal of Polyvinylpyrrolidone from Active Au Sites. *ChemCatChem* **2018**, *10*, 989–997.
- (60) Kodaimati, M. S.; Mcclelland, K. P.; He, C.; Lian, S.; Jiang, Y.; Zhang, Z.; Weiss, E. A. Viewpoint: Challenges in Colloidal Photocatalysis and Some Strategies for Addressing Them. *Inorg. Chem* **2018**, *57*, 3659–3670.
- (61) Niu, Z.; Li, Y. Removal and Utilization of Capping Agents in Nanocatalysis. *Chem. Mater.* **2014**, *26*, 72–83.
- (62) Munnik, P.; De Jongh, P. E.; De Jong, K. P. Recent Developments in the Synthesis of Supported Catalysts. *Chem. Rev.* **2015**, *115*, 6687–6718.
- (63) Pinna, F. Supported Metal Catalysts Preparation. *Catal. Today* **1998**, *41*, 129–137.
- (64) Munnik, P.; Wolters, M.; Gabrielsson, A.; Pollington, S. D.; Headdock, G.; Bitter, J. H.; De Jongh, P. E.; De Jong, K. P. Copper Nitrate Redispersion to Arrive at Highly Active Silica-Supported Copper Catalysts. *J. Phys. Chem. C* **2011**, *115*, 14698–14706.
- (65) Pompe, C. E.; van Uunen, D. L.; van der Wal, L. I.; van der Hoeven, J. E. S.; de Jong, K. P.; de Jongh, P. E. Stability of Mesocellular Foam Supported Copper Catalysts for Methanol Synthesis. *Catal. Today* **2019**, *334*, 79–89.
- (66) Wang, G.; van den Berg, R.; de Mello Donega, C.; de Jong, K. P.; de Jongh, P. E. Silica-Supported Cu₂O Nanoparticles with Tunable Size for Sustainable Hydrogen Generation. *Appl. Catal. B Environ.* **2016**, *192*, 199–207.
- (67) Weber, T.; Verhagen, J. C. M. C.; Weber, T.; Muijsers, J. C.; Van Wolput, J. H. M. C.; Verhagen, C. P. J.; Niemantsverdriet, J. W. Basic Reaction Steps in the Sulfidation of Crystalline MoO₃ to MoS₂, as Studied by X-Ray Photoelectron and Infrared Emission Spectroscopy. *J. Phys. Chem.* **1996**, *100*, 14144–14150.
- (68) Ohtani, B. Photocatalysis A to Z. What We Know and What We Do Not Know in a Scientific Sense. *J. Photochem. Photobiol. C Photochem. Rev.* **2011**, *11*, 157–178.
- (69) Zhu, S.; Wang, D. Photocatalysis: Basic Principles, Diverse Forms of Implementations and Emerging Scientific Opportunities. *Adv. Energy Mater.* **2017**, *7*, 1700841.
- (70) Byrne, C.; Subramanian, G.; Pillai, S. C. Recent Advances in Photocatalysis for Environmental Applications. *J. Environ. Chem. Eng.* **2018**, *6*, 3531–3555.
- (71) Bhatkhande, D. S.; Pangarkar, V. G.; Beenackers, A. A. C. M. Photocatalytic Degradation for Environmental Applications - A Review. *J. Chem. Technol. Biot.* **2002**, *77*, 102–116.
- (72) Gaya, U. I.; Abdullah, A. H. Heterogeneous Photocatalytic Degradation of Organic Contaminants over Titanium Dioxide: A Review of Fundamentals, Progress and Problems. *J. Photochem. Photobiol. C Photochem. Rev.* **2008**, *9*, 1–12.
- (73) Rochkind, M.; Pasternak, S.; Paz, Y. Using Dyes for Evaluating Photocatalytic Properties: A Critical Review. *Molecules* **2015**, *20*, 88–110.

- (74) Maeda, K. Photocatalytic Water Splitting Using Semiconductor Particles: History and Recent Developments. *J. Photochem. Photobiol. C Photochem. Rev.* **2011**, *12*, 237–268.
- (75) Wang, Z.; Li, C.; Domen, K. Recent Developments in Heterogeneous Photocatalysts for Solar-Driven Overall Water Splitting. *Chem. Soc. Rev.* **2019**, *48*, 2109–2125.
- (76) Liu, G.; Schulmeyer, T.; Brötz, J.; Klein, A.; Jaegermann, W. Interface Properties and Band Alignment of Cu₂S/CdS Thin Film Solar Cells. *Thin Solid Films* **2003**, *431–432*, 477–482.
- (77) Liu, G.; Schulmeyer, T.; Thissen, A.; Klein, A.; Jaegermann, W. In Situ Preparation and Interface Characterization of TiO₂/Cu₂S Heterointerface. *Appl. Phys. Lett.* **2003**, *82*, 2269–2271.
- (78) An, L.; Zhou, P.; Yin, J.; Liu, H.; Chen, F.; Liu, H.; Du, Y.; Xi, P. Phase Transformation Fabrication of a Cu₂S Nanoplate as an Efficient Catalyst for Water Oxidation with Glycine. *Inorg. Chem.* **2015**, *54*, 3281–3289.
- (79) Kapinus, E. I.; Viktorova, T. I.; Khalyavka, T. A. Photocatalytic Activity of Nanoparticles of Metal Sulfides in the Degradation of Organic Dyes. *Theor. Exp. Chem.* **2006**, *42*, 276–280.
- (80) Pal, M.; Mathews, N. R.; Sanchez-Mora, E.; Pal, U.; Paraguay-Delgado, F.; Mathew, X. Synthesis of CuS Nanoparticles by a Wet Chemical Route and Their Photocatalytic Activity. *J. Nanoparticle Res.* **2015**, *17*.
- (81) Ayodhya, D.; Venkatesham, M.; Santoshi kumari, A.; Reddy, G. B.; Ramakrishna, D.; Veerabhadram, G. Photocatalytic Degradation of Dye Pollutants under Solar, Visible and UV Lights Using Green Synthesised CuS Nanoparticles. *J. Exp. Nanosci.* **2016**, *11*, 418–432.
- (82) Mondal, G.; Bera, P.; Santra, A.; Jana, S.; Nath Mandal, T.; Mondal, A.; Il Seok cd, S.; Bera, P. Precursor-Driven Selective Synthesis of Hexagonal Chalcocite (Cu₂S) Nanocrystals: Structural, Optical, Electrical and Photocatalytic Properties. *New J. Chem. New J. Chem* **2014**, *38*, 4774–4782.
- (83) Shamraiz, U.; Badshah, A.; Hussain, R. A.; Nadeem, M. A.; Saba, S. Surfactant Free Fabrication of Copper Sulphide (CuS–Cu₂S) Nanoparticles from Single Source Precursor for Photocatalytic Applications. *J. Saudi Chem. Soc.* **2017**, *21*, 390–398.
- (84) Cao, Q.; Che, R.; Chen, N. Scalable Synthesis of Cu₂S Double-Superlattice Nanoparticle Systems with Enhanced UV/Visible-Light-Driven Photocatalytic Activity. *Appl. Catal. B Environ.* **2015**, *162*, 187–195.
- (85) Hai, Z.; Huang, J.; Remita, H.; Chen, J. Radiolytic Synthesis of CuS Nanotubes with Photocatalytic Activity under Visible Light. *Mater. Lett.* **2013**, *108*, 304–307.
- (86) Huang, J.; Wang, Y.; Gu, C.; Zhai, M. Large Scale Synthesis of Uniform CuS Nanotubes by a Sacrificial Templating Method and Their Application as an Efficient Photocatalyst. *Mater. Lett.* **2013**, *99*, 31–34.
- (87) Wang, X. Y.; Fang, Z.; Lin, X. Copper Sulfide Nanotubes: Facile, Large-Scale Synthesis, and Application in Photodegradation. *J. Nanoparticle Res.* **2009**, *11*, 731–736.
- (88) Liu, Y.; Deng, Y.; Sun, Z.; Wei, J.; Zheng, G.; Asiri, A. M.; Khan, S. B.; Rahman, M. M.; Zhao, D. Hierarchical Cu₂S Microsponges Constructed from Nanosheets for Efficient Photocatalysis. *Small* **2013**, *9*, 2702–2708.
- (89) Cheng, Z.; Wang, S.; Wang, Q.; Geng, B. A Facile Solution Chemical Route to Self-Assembly of CuS Ball-Flowers and Their Application as an Efficient Photocatalyst. *CrystEngComm* **2010**, *12*, 144–149.
- (90) Yang, Z. K.; Song, L. X.; Teng, Y.; Xia, J. Ethylenediamine-Modulated Synthesis of Highly Monodisperse Copper Sulfide Microflowers with Excellent Photocatalytic Performance. *J. Mater. Chem. A* **2014**, *2*, 20004–20009.
- (91) Song, C.; Yu, K.; Yin, H.; Zhang, Y.; Li, S.; Wang, Y.; Zhu, Z. Marigold-like Cu_x (x = 1.81, 2)S Nanocrystals: Controllable Synthesis, Field Emission, and Photocatalytic Properties. *Appl. Phys. A Mater. Sci. Process.* **2014**, *115*, 801–808.
- (92) Xu, M.; Wang, M.; Ye, T.; Liang, N.; Jin, L.; Zai, J.; Qian, X. Cube-in-Cube Hollow Cu₉S₅ Nanostructures with Enhanced Photocatalytic Activities in Solar H₂ Evolution. *Chem. – A Eur. J.* **2014**, *20*, 13576–13582.
- (93) Im, Y.; Kang, S.; Kim, K. M.; Ju, T.; Han, G. B.; Park, N. K.; Lee, T. J.; Kang, M. Dynamic Hydrogen Production from Methanol/Water Photo-Splitting Using Core@shell-Structured CuS@TiO₂ Catalyst Wrapped by High Concentrated TiO₂ Particles. *Int. J. Photoenergy* **2013**, *2013*.
- (94) Kuhl, K. P.; Hatsukade, T.; Cave, E. R.; Abram, D. N.; Kibsgaard, J.; Jaramillo, T. F. Electrocatalytic Conversion of Carbon Dioxide to Methane and Methanol on Transition Metal Surfaces. *J. Am. Chem. Soc.* **2014**, *136*, 14107–14113.
- (95) Birdja, Y. Y.; Pérez-Gallent, E.; Figueiredo, M. C.; Göttle, A. J.; Calle-Vallejo, F.; Koper, M. T. M. Advances and Challenges in Understanding the Electrocatalytic Conversion of Carbon Dioxide to Fuels. *Nat. Energy* **2019**, *4*, 732–745.
- (96) Hori, Y.; Wakebe, H.; Tsukamoto, T.; Koga, O. Electrocatalytic Process of CO Selectivity in

- Electrochemical Reduction of CO₂ at Metal Electrodes in Aqueous Media. *Electrochim. Acta* **1994**, *39*, 1833–1839.
- (97) Yin, Z.; Tayhas, G.; Palmore, R.; Sun, S.; Electrochemical Reduction of CO₂ Catalyzed by Metal Nanocatalysts. *Trends Chem.* **2019**, *1*, 739-750.
- (98) Nitopi, S.; Bertheussen, E.; Scott, S. B.; Liu, X.; Engstfeld, A. K.; Horch, S.; Seger, B.; Stephens, I. E. L.; Chan, K.; Hahn, C.; et al., Progress and Perspectives of Electrochemical CO₂ Reduction on Copper in Aqueous Electrolyte. *Chem. Rev.* **2019**, *119*, 7610–7672.
- (99) Deng, Y.; Huang, Y.; Ren, D.; Handoko, A. D.; Seh, Z. W.; Hirunsit, P.; Yeo, B. S. On the Role of Sulfur for the Selective Electrochemical Reduction of CO₂ to Formate on CuS_x Catalysts. *ACS Appl. Mater. Interfaces* **2018**, *10*, 28572–28581.
- (100) Shinagawa, T.; Larrazábal, G. O.; Martín, A. J.; Krumeich, F.; Pérez-Ramírez, J. Sulfur-Modified Copper Catalysts for the Electrochemical Reduction of Carbon Dioxide to Formate. *ACS Catal.* **2018**, *8*, 837–844.
- (101) Huang, Y.; Deng, Y.; Handoko, A. D.; Goh, G. K. L.; Yeo, B. S. Rational Design of Sulfur-Doped Copper Catalysts for the Selective Electroreduction of Carbon Dioxide to Formate. *ChemSusChem* **2018**, *11*, 320–326.
- (102) Phillips, K. R.; Katayama, Y.; Hwang, J.; Shao-Horn, Y. Sulfide-Derived Copper for Electrochemical Conversion of CO₂ to Formic Acid. *J. Phys. Chem. Lett.* **2018**, *9*, 4407–4412.



Chapter 2

Water dispersible Cu_{2-x}S nanocrystals
via ligand exchange of
1-dodecanethiol

Abstract: In colloidal Cu_{2-x}S nanocrystal synthesis, thiols are often used as organic ligands and sulfur source, as they yield high-quality nanocrystals. However, thiol ligands on Cu_{2-x}S nanocrystals are difficult to exchange, limiting the applications of these nanocrystals in (photo)catalysis. Here, we present an effective and facile procedure to exchange native 1-dodecanethiol on Cu_{2-x}S nanocrystals by 3-mercaptopropionic acid, 11-mercaptoundecanoic acid, and S^{2-} in formamide under inert atmosphere. The resulting hydrophilic Cu_{2-x}S nanocrystals have excellent colloidal stability in formamide. Furthermore, the size, shape and optical properties of the nanocrystals are not significantly affected by the ligand exchange. Water-dispersible Cu_{2-x}S nanocrystals are easily obtained by precipitation of the nanocrystals capped by S^{2-} , 3-mercaptopropionate or 11-mercaptoundecanoate from formamide, followed by redispersion in water. Interestingly, the ligand exchange rates for Cu_{2-x}S nanocrystals capped with 1-dodecanethiol depend on the preparation method, being much slower for Cu_{2-x}S nanocrystals prepared through heating-up than through hot-injection synthesis protocols. XPS studies reveal that the differences in the ligand exchange rates are due to the surface chemistry of the Cu_{2-x}S nanocrystals, where the nanocrystals prepared via hot-injection synthesis have a less dense ligand layer due to the presence of trioctylphosphine oxide during synthesis. A model is proposed that explains the observed differences in the ligand exchange rates. The facile ligand exchange procedures reported here enable the use of high-quality colloidal Cu_{2-x}S nanocrystals prepared in the presence of 1-dodecanethiol in (photo)catalytic applications.

2.1 Introduction

Colloidal synthesis methods allow for the preparation of monodisperse Cu_{2-x}S nanocrystals with uniform properties and hence are interesting for a variety of applications, such as such as biomedical sensing,¹⁻³ photothermal therapy,²⁻⁴ photovoltaic and plasmonic devices^{2,5-8} and photo- and electrocatalysis.^{2,5,9,10} The best known colloidal synthesis technique is hot-injection, in which the precursors are rapidly injected into a pre-heated reaction mixture containing the other reagents. The rapid injection leads to a high availability of monomers and hence a burst of nucleation, followed by further growth of the existing nuclei. Although hot-injection synthesis protocols are well-developed and can give nanocrystals with a large range of sizes, shapes and compositions, they usually only yield a small amount of product and cannot be easily scaled up, as factors like injection rate and mass and heat transport become less reproducible for larger reaction volumes.¹¹ An alternative to the hot-injection method is the so-called heating-up method, where all reagents are mixed in a reaction flask and heated to induce nucleation and growth of the nanocrystals. This method allows for a more reproducible and scalable synthesis, since factors such as injection rate and non-ideal mixing do not play a role.¹¹

As discussed in Chapter 1, organic ligands are important during colloidal synthesis as they allow for the high control over size, shape and composition of the nanocrystals by dynamically binding to the nanocrystal surface.¹² Furthermore, after synthesis they prevent aggregation of the nanocrystals by steric stabilization. These ligands usually

have a polar headgroup coordinating to the nanocrystal surface atoms through a donor atom (*e.g.*, S, N, O) and a long apolar hydrocarbon tail that stabilizes the nanocrystals in apolar solvents.¹⁵ Commonly used ligands include phosphines, amines and thiols. Though ligands are essential during and after synthesis, they lead to challenges when using the nanocrystals in applications. The apolar nature of the hydrocarbon chain prevents dispersion of the nanocrystals in water and other polar solvents, limiting their use in, *e.g.*, biomedical and photocatalytic applications. Furthermore, the bulky organic ligands can restrict interparticle conductivity and can render the nanocrystal surface inaccessible to reactants, hindering the use of the nanocrystals in optoelectronic, photovoltaic and photo- and electro-catalytic applications. As a consequence, ligand exchange is crucial to obtain colloidal nanocrystals suitable for a broad range of applications. Various procedures have been reported for ligand exchange on colloidal nanocrystals. For example, Nag *et al.*, reported the preparation of all-inorganic nanocrystals by replacing native organic ligands with inorganic ions such as S²⁻, HS⁻ and OH⁻.¹³ Kovalenko *et al.*, described the stabilization of colloidal nanocrystals in polar solvents by using molecular metal chalcogenide ligands, such as Sn₂S₆⁴⁻.^{14,15} By a subsequent heating step, the ligands could be converted into semiconducting phases, realizing conductive arrays of nanoparticles. Aqueous phase transfers have also been extensively reported using organic ligands such as 3-mercaptopropionic acid (MPA),¹⁶⁻²² 11-mercaptoundecanoic acid (MUA),²⁰⁻²⁴ cysteine²⁵ and various polymers.²⁶⁻²⁸

In Cu_{2-x}S nanocrystal synthesis, thiols are often used as ligands as they give high quality, monodisperse products.^{29,30} However, no effective ligand exchange procedures have been reported for Cu_{2-x}S and CuInS₂ nanocrystals prepared *via* direct synthesis in the presence of thiols.^{29,31-36} Xie *et al.*, reported the resistance of CuInS₂ nanocrystals obtained with thiol ligands towards a ligand exchange using MPA.³¹ Turo *et al.*, described the resistance of Cu_{2-x}S nanocrystals prepared with 1-dodecanethiol (DDT) towards ligand exchange procedures and attributed this to the presence of so-called crystal-bound thiols, where the thiols occupy high coordination number sites and are thus strongly bound to the nanocrystal.²⁹ A similar explanation has been given by other groups.³²⁻³⁴ More recently, Gromova *et al.*, reported on the difficulty of surface functionalization of CuInS₂ nanocrystals prepared in the presence of DDT. They attributed this to the presence of a ligand double layer on the nanocrystals surface, consisting of dodecanethiolate ligands and thioether species formed *in situ* during the heating-up synthesis in the presence of thiols.³⁵

In this chapter, we report on ligand exchange procedures for Cu_{2-x}S nanocrystals prepared by hot-injection and heating-up synthesis protocols in the presence of DDT. In contrast to the studies mentioned above,^{29,31-36} we developed procedures to replace DDT on Cu_{2-x}S nanocrystals with either MPA⁻, MUA⁻ or S²⁻ by performing the ligand exchange procedures under inert atmosphere in a highly polar solvent (formamide). In addition, we found that the ligand exchange rates are highly dependent on both the nature of the

replacing ligands (MPA⁻, MUA⁻ or S²⁻) and on the synthesis method used to produce the Cu_{2-x}S nanocrystals (*viz.*, hot-injection or heating-up). We propose a model for ligand exchange on thiolate capped Cu_{2-x}S nanocrystals that explains the observed differences. The ligand exchange protocols developed in this work present a facile way to achieve water-dispersible Cu_{2-x}S nanocrystals with, depending on the replacing ligand, accessible nanocrystal surfaces, making them more suitable for catalytic applications.

2.2 Experimental methods

2.2.1 Materials.

Copper(II) sulfate pentahydrate (CuSO₄ · 5H₂O, 99.999%), copper(I) acetate (CuAc, 97%), copper(I) chloride (CuCl, 99.995%), 1-dodecanethiol (DDT, ≥ 98%), oleic acid (OA, 90%), 1-octadecene (ODE, 90%), trioctylphosphine oxide (TOPO, 99%), oleylamine (OLAM, 70%), sodium sulfide (Na₂S), 11-mercaptoundecanoic acid (MUA, 98%), 3-mercaptopropionic acid (99%), tetramethylammonium hydroxide pentahydrate (TMAH, ≥ 97%), formamide (FA, 98%), chloroform, anhydrous toluene, methanol, butanol, ethanol, hexane and acetonitrile were purchased from Sigma-Aldrich. ODE and TOPO were degassed at 120 °C for 3 hours prior to use. Formamide was degassed at 120 °C for 2 hours prior to use. All other reagents were used as received.

2.2.2 Synthesis of colloidal DDT-capped Cu_{2-x}S nanocrystals by the heating-up method

Cu_{2-x}S nanocrystals of 12 nm diameter were synthesized according to the method described by van der Stam *et al.*,³⁷ 205 mg (0.8 mmol) CuSO₄·5H₂O, 7.5 mL DDT and 6 mL OA were mixed in a round-bottom flask. The mixture was gradually heated to 200 °C under nitrogen protection in a Schlenk line. Subsequently, the solution was kept at 200 °C for 2 hours. After that, the reaction mixture was washed three times by addition of an excess of methanol and butanol (1:1 ratio), followed by centrifugation at 2500 rpm for 5 minutes. The nanocrystals were redispersed in 10 mL anhydrous toluene.

2.2.3 Synthesis of colloidal Cu_{2-x}S nanocrystals by the hot-injection method

Cu_{2-x}S nanocrystals of various sizes were synthesized by adaptation of the method described by Xia *et al.*,²³ In a round-bottom flask, 0.13 g (1 mmol) Cu(I)Ac and 3.6 g (9.3 mmol) TOPO were added to 20 mL ODE. First, the mixture was degassed at 100 °C for 1 h. Subsequently, the flask was purged with nitrogen and subsequent steps of the synthesis were performed under nitrogen flow in a Schlenk line. The reaction mixture was heated to 210 °C. At 160 °C, 5 mL DDT was quickly injected into the flask. The nanocrystals were allowed to grow for 1 h at 210 °C. After reaction, the nanocrystals were washed using the method described above and redispersed in 10 mL anhydrous toluene.

2.2.4 Synthesis of colloidal OLAM-capped Cu_{2-x}S nanocrystals by the heating-up method

OLAM-capped Cu_{2-x}S nanocrystals of 7 nm diameter were synthesized in a Schlenk line under nitrogen protection according to a method described by Williamson *et al.*,³⁸ A S-OLAM precursor solution was prepared by dissolving 1.6 g (50 mmol) S in 7 mL OLAM and 3 mL ODE at 110 °C. The copper precursor solution was prepared by dissolving 6 g (60 mmol) CuCl in 42 mL OLAM and 18 mL ODE in a round-bottom flask at 110 °C. Both precursor solutions were cooled down to 50 °C, after which 6 mL of the S-OLAM precursor was added to the Cu-precursor solution. The mixture was left stirring at 50 °C for 5 minutes. Subsequently, the temperature was increased to 185 °C in 30 minutes and maintained for 2 h. After that the reaction mixture was cooled down using a water bath and addition of 60 mL hexane, which also decreased the viscosity of the mixture. The product was purified by washing with ethanol, followed by centrifugation at 2500 rpm for 5 minutes. The Cu_{2-x}S nanocrystals were redispersed in 75 mL *n*-hexane.

2.2.5 Ligand exchange using Na₂S

The phase transfer procedure using Na₂S was done using an adaptation of a method described by Nag *et al.*,¹³ For a typical ligand exchange, 1 mL Na₂S in formamide or demineralized water (5 mg/mL) was mixed with 1 mL of Cu_{2-x}S nanocrystals in toluene (~5 mg/mL). The experiments using formamide as the polar solvent were also performed under inert atmosphere in a nitrogen glovebox (≤ 6 ppm O₂). A biphasic system was formed, with the colorless Na₂S solution on the bottom and the black Cu_{2-x}S nanocrystals suspension in toluene on top (Figure 2.1). Upon ligand exchange of the native apolar ligands to sulfide, the black Cu_{2-x}S nanocrystals transferred to the polar formamide layer. Subsequently, the apolar layer was removed and the remaining polar phase containing the Cu_{2-x}S nanocrystals was washed with toluene to remove remaining apolar species. The Cu_{2-x}S nanocrystals were precipitated by adding an excess of acetonitrile, followed by centrifugation for 2 minutes at 2000 rpm. The purified sulfide-capped Cu_{2-x}S nanocrystals were redispersed in 2 mL degassed formamide and stored under nitrogen atmosphere.

2.2.6 Ligand exchange using MUA or MPA

The phase transfer procedure using MUA or MPA was based on a method described by Xia *et al.*,²³ 1.4 mmol MUA or MPA was dissolved in 30 mL demineralized H₂O or formamide. In the case of MUA, TMAH was added to increase the pH to 11 and deprotonate the MUA. In a typical ligand exchange, 4 mL of a Cu_{2-x}S nanocrystal suspension in toluene (~0.75 mg/L) was mixed with 5.8 mL of the MUA or MPA solutions. A two-layer system was formed, with the Cu_{2-x}S nanocrystals in toluene on the bottom and the polar MUA or MPA solution on top. The experiments using formamide as the polar solvent were also performed under inert atmosphere in a nitrogen glovebox (≤ 6 ppm O₂). The ligand exchange was successful when upon stirring the black

Cu_{2-x}S nanocrystals transferred to the polar phase. After centrifugation for 1 minute at 1000 rpm, the polar layer containing the Cu_{2-x}S nanocrystals was collected and washed by adding excess ethanol, followed by centrifugation for 5 min at 3000 rpm. The purified MUA- or MPA-capped Cu_{2-x}S nanocrystals were redispersed in demineralized water or formamide.

2.2.7 Structural characterization

Samples for transmission electron microscopy (TEM) analysis were prepared by drop-casting the Cu_{2-x}S nanocrystal suspension on a carbon-coated 200 mesh copper TEM grid. TEM analysis was performed using a FEI Tecnai-12 microscope operating at 120 kV or a FEI Technai-20 microscope operating at 200 kV.

Samples for x-ray diffraction (XRD) analysis were prepared by precipitating the Cu_{2-x}S nanocrystals with an antisolvent and subsequently drying the obtained powder under vacuum. The dried Cu_{2-x}S nanocrystal powder was spread over a Si wafer. XRD measurements were performed with a Bruker D2 Phaser, equipped with a Co K α x-ray source with a wavelength of 1.79026 Å.

ζ -Potential and dynamic light scattering (DLS) measurements were performed on a Zetasizer Nano ZS from Malvern Instruments using a dip cell with palladium electrodes with 2 mm spacing in a PCS1115 cuvette and a measurement angle of 173 °. Measurements were corrected by the instrument software for solvent (formamide or toluene), refractive index, temperature and viscosity. Measurements were done in the automatic mode and repeated 5 times for each sample in order to obtain reliable results.

2.2.8 X-ray photoelectron spectroscopy (XPS)

Sample preparation for x-ray photoelectron spectroscopy (XPS) was done under air-free conditions to prevent oxidation and chemisorption of CO₂ on the samples. Samples were mounted in a glovebox and transferred into the spectrometer in a vacuum transfer module. The as-synthesized samples with the original apolar ligands were drop casted on a clean tantalum sample holder in order to avoid the influence of carbon tape. Samples after ligand exchange to S²⁻ were dried under vacuum and stuck onto the tantalum sample holder as powder using carbon tape. XPS spectra were taken with Thermo Scientific K-Alpha spectrometer using a 72 W monochromated Al K α source ($h\nu = 1486.6$ eV). The x-rays were microfocused at the source to give a spot size on the sample of 400 μm in diameter. The analyzer was a double focusing 180° hemisphere with mean radius of 125 mm, run in constant analyzer energy (CAE) mode. The pass energy was set to 200 eV for survey scans and 50 eV for high resolution regions. Data analysis was done using CasaXPS software. Binding energies were calibrated by setting the lowest energy C 1s peak to 284.8 eV.

2.2.9 ³¹P-NMR spectroscopy

³¹P-NMR measurements were done on a reference solution of TOPO in ODE, the Cu_{2-x}S nanocrystal reaction mixture directly after synthesis and after washing for 3 times. The

reaction mixture and reference solution were both diluted with CDCl₃ to a concentration half of the original in order to perform a lock procedure. The washed sample was dried under vacuum overnight after the 3rd wash step and subsequently redispersed in CDCl₃. Measurements were performed on an Agilent MRF400 spectrometer at 25 °C and 161 MHz.

2.3 Results and Discussion

2.3.1 Ligand exchange procedures on Cu_{2-x}S nanocrystals prepared with thiols

Cu_{2-x}S nanocrystals were synthesized according to two previously described protocols, where DDT was used as both sulfur source and ligand (see Experimental Methods for details). In the first method, Cu_{2-x}S nanocrystals were synthesized using a hot-injection technique. DDT was injected into a mixture of Cu(I)acetate, trioctylphosphineoxide (TOPO) and 1-octadecene (ODE).^{23,39} During this synthesis, both TOPO and DDT ligands direct the growth of the nanocrystals.³⁹ These nanocrystals will hereafter be referred to as HI_DDT/TOPO. Cu_{2-x}S nanocrystals were also synthesized by heating CuSO₄·5H₂O, DDT and oleic acid (OA) to 200 °C in a so-called heating-up synthesis.³⁷ These nanocrystals will hereafter be referred to as HU_DDT.

To replace the native ligands on the Cu_{2-x}S nanocrystals and obtain water-dispersible Cu_{2-x}S nanocrystals, ligand exchange procedures using MPA, MUA, and S²⁻ (either from (NH₄)₂S or Na₂S), were studied. In a typical ligand exchange reaction a two-phase system was formed by combining the Cu_{2-x}S nanocrystals in an apolar solvent (*e.g.*, toluene) with an excess of the replacing ligand (MPA, MUA or S²⁻) in polar solvent (*e.g.*, water or formamide). The pH of the solutions containing MUA was increased to 11 using tetramethylammonium hydroxide (TMAH) in order to deprotonate the carboxylic acid group, thereby rendering the MUA water soluble. The solutions containing S²⁻ were also alkaline as the S²⁻ undergoes hydrolysis, forming HS⁻ and OH⁻. In contrast, the MPA solution has a low pH of 3 at the start of the ligand exchange experiments. Although not needed for the solubility of MPA in formamide or water, experiments using MPA were also performed at pH 11 to compare the different replacing ligands under identical conditions. No differences in phase transfer rate were observed between the MPA experiments carried out at low and high pHs. Therefore, for the sake of conciseness, only experiments using MPA at low pH are further discussed.

The success of the ligand exchange was evidenced by transfer of the Cu_{2-x}S nanocrystals from the apolar to the polar phase, as illustrated in Figure 2.1. Different experimental conditions were studied for the ligand exchange experiments. First, experiments were performed in air using water as the polar solvent. Subsequently, experiments were

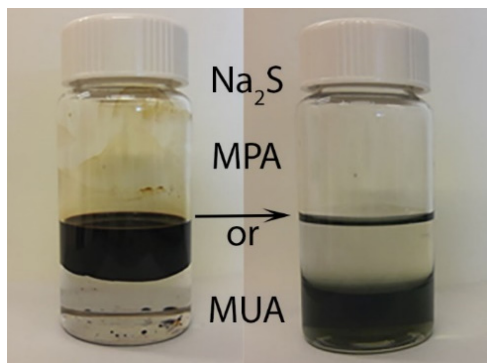


Figure 2.1 Photograph of a typical ligand-exchange procedure using a two-layer system of formamide (bottom layer) and toluene (top layer). The image on the left represents the system before ligand exchange, with black colloidal Cu_{2-x}S nanocrystals dispersed in the apolar toluene layer. In a successful ligand exchange using S^{2-} , MPA^- or MUA^- , the Cu_{2-x}S nanocrystals undergo a phase transfer from toluene to formamide upon exchange of the native 1-dodecanethiol ligands (image on the right).

performed in air, using formamide as the polar solvent. Lastly, experiments were performed under air-free conditions and using formamide as the polar solvent. The three different sets of experiments are discussed in more detail below.

At first, ligand exchange procedures were performed using water in air, as described elsewhere.^{13,23} Using this procedure, ligand exchange using MPA^- and S^{2-} (either from $(\text{NH}_4)_2\text{S}$ or Na_2S) as the replacing ligands was successful. However, the colloidal stability of the product nanocrystals was low and aggregates formed during the phase transfer process. In addition, the sample obtained using $(\text{NH}_4)_2\text{S}$ turned from black to blue after several hours, suggesting the formation of Cu^{2+} -ammonia complexes. Copper has a valency of +1 in the Cu_{2-x}S nanocrystals, but in the presence of oxygen, part of the Cu^+ ions may be oxidized to Cu^{2+} .^{29,40} In aqueous solution, the ammonium ion can dissociate into ammonia and a proton through $\text{NH}_4^+(\text{aq}) \rightleftharpoons \text{NH}_3(\text{aq}) + \text{H}^+(\text{aq})$. In the presence of $\text{NH}_3(\text{aq})$, Cu^{2+} can then form the stable $[\text{Cu}(\text{NH}_3)_4]^{2+}$ complex that has an intense violet-blue color.^{41,42} Due to the instability of the Cu_{2-x}S nanocrystals in the presence of $\text{NH}_3/\text{NH}_4^+$, $(\text{NH}_4)_2\text{S}$ was not used as S^{2-} source in further experiments. When using S^{2-} as the replacing ligand, both the HI_DDT/TOPO and the HU_DDT nanocrystals were transferred to the polar water phase upon stirring for about 5 hours. When MPA was used as the replacing ligand, both the HI_DDT/TOPO and the HU_DDT nanocrystals were transferred to the polar aqueous MPA solution upon stirring overnight. In contrast, when MUA was used as the replacing ligand, only partial transfer of the HI_DDT/TOPO nanocrystal was observed upon stirring overnight, while for the HU_DDT nanocrystals no phase transfer was observed, even after stirring for 3 days.

As the polarity of the solvent could influence the success of the ligand exchange by stabilizing charged intermediates, the ligand exchange was also performed using formamide as the polar solvent under ambient conditions. Formamide has a higher polarity ($\epsilon = 106$) than water ($\epsilon = 80$).¹³ However, upon stirring for several hours, the color of the MUA and Na₂S solution layers changed from colorless to black and then to violet-blue, while the apolar phase initially containing the Cu_{2-x}S nanocrystals turned from black to colorless. This indicates that the Cu_{2-x}S nanocrystals were successfully transferred to the polar phase, but were not stable after the transfer. The dark blue color again suggests the formation of Cu²⁺ complexes, where formamide itself can act as the ligand. Complex formation between Cu²⁺ and formamide has been observed in oxidative and alkaline environments,⁴³ where Cu²⁺ leaking into solution from either Cu₂S⁴⁴ or copper foil^{45,46} was quickly coordinated by formamide. The blue color was also observed when using MPA, but only after storing the MPA-capped Cu_{2-x}S nanocrystals in formamide for several days in air. The alkaline nature of the solutions containing MUA or Na₂S when compared to the more acidic MPA solution when initiating the ligand exchange experiments can possibly explain the slower complex formation between Cu²⁺ and formamide observed in MPA solutions.⁴⁴

To prevent the oxidation of Cu⁺ to Cu²⁺ and the rapid complexation of Cu²⁺ by formamide, the ligand exchange experiments using formamide were performed under inert atmosphere in a nitrogen glovebox (≤ 6 ppm O₂). We found that under these conditions the native ligands on the Cu_{2-x}S nanocrystals could successfully be replaced with all three ligands (MPA⁻, MUA⁻ and S²⁻ from Na₂S). Colloidal stability in the polar formamide was obtained by binding the negatively charged MPA⁻, MUA⁻ or S²⁻ to the nanocrystal surface. The negative charge of the ligands was confirmed with ζ -potential measurements. Cu_{2-x}S nanocrystals prepared by hot-injection synthesis gave ζ -potentials of -44.4 mV, -31.1 mV and -34.9 mV for nanocrystals capped with S²⁻, MPA⁻ and MUA⁻, respectively (Figure 2.2a). For the Cu_{2-x}S nanocrystals prepared by heating-up synthesis, the ζ -potentials were -31.3 mV, -33.9 mV and -34.0 mV for nanocrystals capped with S²⁻, MPA⁻ and MUA⁻, respectively (Figure 2.2b). The resulting hydrophilic nanocrystals have a high colloidal stability and were stored in formamide inside the glovebox for several months without losing colloidal stability. To obtain water-dispersible Cu_{2-x}S nanocrystals, the particles were precipitated using acetonitrile as antisolvent and isolated by centrifugation, followed by redispersion in water. When dispersed in water, slight turbidity developed over time (on a time scale of hours), indicating that the colloidal stability of the hydrophilic nanocrystals in water is lower than in formamide. This difference in colloidal stability is ascribed to the polarity of the solvent, where the charged nanocrystals are better stabilized in the highly polar formamide ($\epsilon = 106$) than in the less polar water ($\epsilon = 80$).¹³

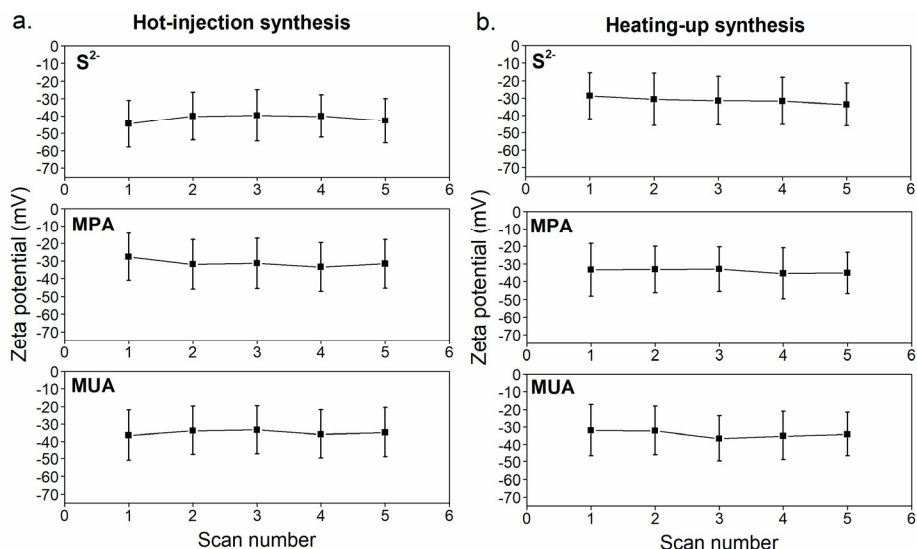


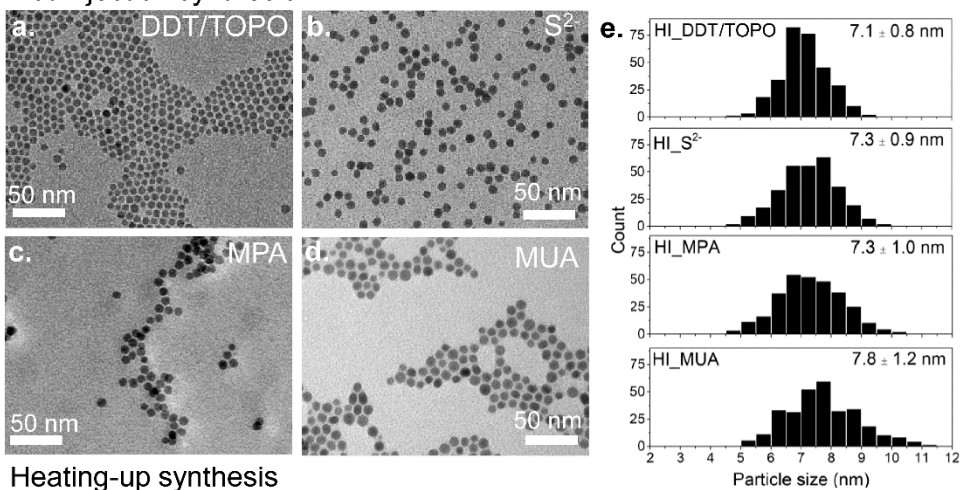
Figure 2.2 ζ -potential of Cu_{2-x}S nanocrystals in formamide prepared by a) hot-injection synthesis or b) heating-up synthesis and capped with S^{2-} , MPA or MUA, respectively.

2.3.2 Impact of ligand exchange on nanocrystal size, crystal structure and optical properties

Figure 2.3 shows transmission electron microscopy (TEM) images of the Cu_{2-x}S nanocrystals prepared by hot-injection synthesis and heating-up synthesis, both before (Figure 2.3a,f) and after ligand exchange with S^{2-} , MPA and MUA in formamide under inert atmosphere (Figure 2.3b,c,d,g,h,i). The corresponding particle size histograms (Figure 2.3e,j) show the size of the Cu_{2-x}S nanocrystals without the ligand layer. Before ligand exchange, a particle size of 7.1 ± 0.8 nm was found for the nanocrystals prepared by hot-injection synthesis, whereas the nanocrystals prepared by heating-up synthesis had a size of 12.3 ± 1.2 nm. TEM analysis shows that the size and shape of the nanocrystals were not significantly affected by exchanging the native DDT ligands by any of the replacing ligands.

In addition, the TEM images show that the nanocrystals assembled in organized arrays when dried on the TEM grid (Figure 2.3). The separation between the nanocrystals in such an array can be related to the organic ligands capping the nanocrystals. The interparticle distance was 1.7 ± 0.2 nm for both the as-synthesized sample prepared by hot-injection in the presence of TOPO and by heating-up synthesis without TOPO. This distance is very similar to the DDT chain length (*viz.*, 1.8 nm).⁴⁷ Upon ligand exchange with, *e.g.*, S^{2-} , the nanocrystals come in very close proximity to each other (Figure 2.3b,g). This can be explained by the replacement of 1-dodecanethiol by the smaller S^{2-} .

Hot-injection synthesis



Heating-up synthesis

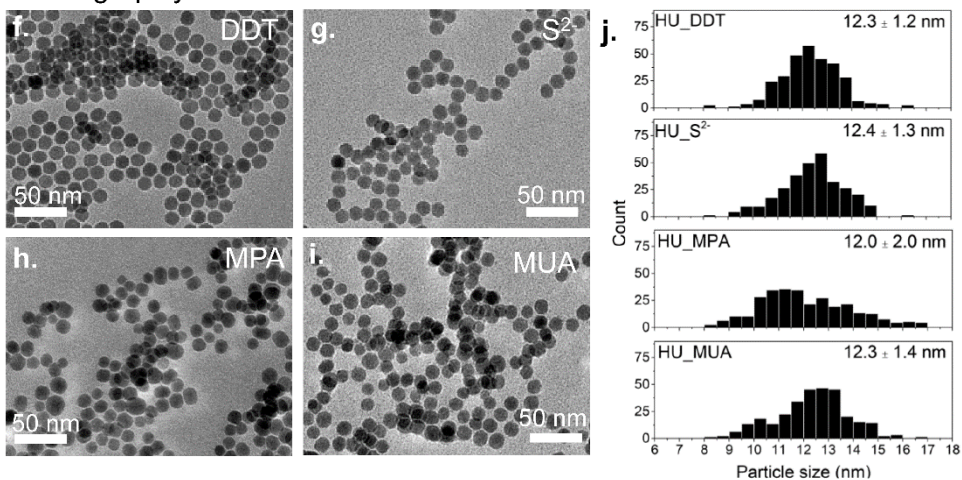


Figure 2.3 TEM images of Cu_{2-x}S nanocrystals prepared via hot-injection synthesis **a)** before and after ligand exchange with **b)** S^{2-} , **c)** MPA and **d)** MUA and **e)** corresponding particle size histograms. TEM images of Cu_{2-x}S nanocrystals prepared via heating-up synthesis **f)** before and after ligand exchange with **g)** S^{2-} , **h)** MPA and **i)** MUA and **j)** corresponding particle size histograms.

The crystal structure of the Cu_{2-x}S nanocrystals before and after ligand exchange was investigated using x-ray diffraction (XRD) (Figure 2.4). Prior to ligand exchange, the nanocrystals prepared by both hot-injection and heating-up synthesis can be identified as chalcocite ($\text{Cu}_{1.997-2.0}\text{S}$) or djurleite ($\text{Cu}_{1.94}\text{S}$). Based on the XRD patterns, no distinction can be made between these two phases. However, as the copper-deficient djurleite phase is more thermodynamically stable due to its lower crystallographic symmetry compared to the chalcocite phase, the nanocrystals are likely in the djurleite phase.⁸ After ligand exchange with S^{2-} and phase transfer to formamide, the Cu_{2-x}S nanocrystals remain in the djurleite phase (Figure 2.4c). However, after phase transfer to water and exposure to air the nanocrystals partially oxidized to a roxbyite ($\text{Cu}_{1.81}\text{S}$) phase (Figure 2.4a,b). This can be explained by the formation of copper vacancies under oxygen. In this phase, the copper atoms in the Cu_{2-x}S nanocrystal remain in the +1 oxidation state, whereas the

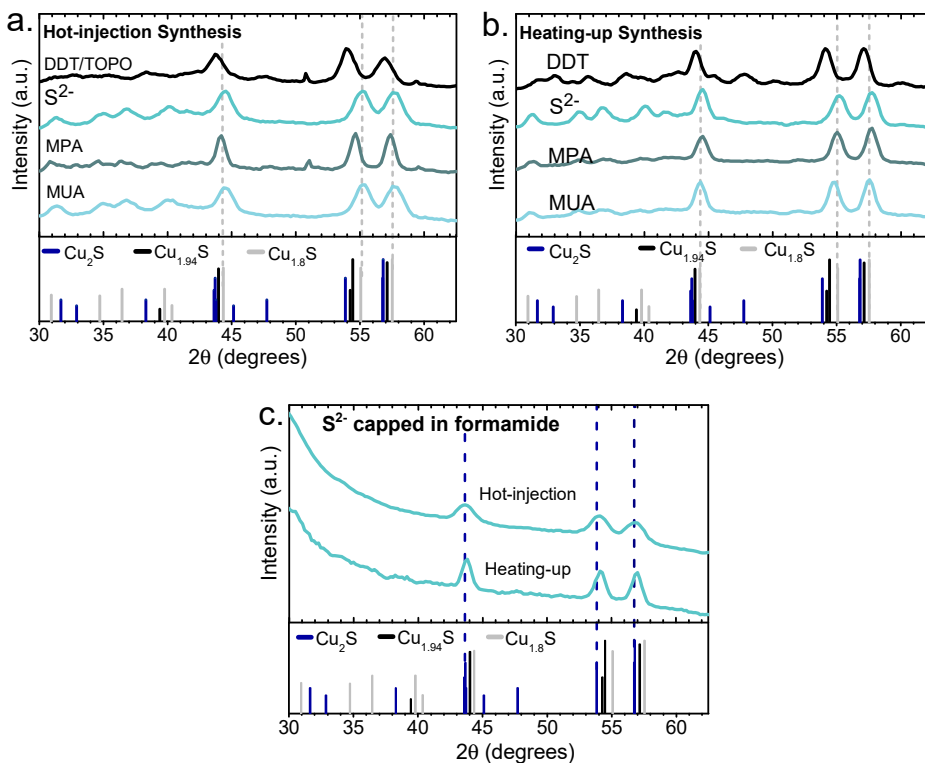


Figure 2.4 a) X-ray diffractograms of the Cu_{2-x}S nanocrystals prepared via hot-injection synthesis before (DDT/TOPO) and after ligand exchange procedures with S^{2-} , MPA and MUA and phase transfer to water. **b)** X-ray diffractograms of the Cu_{2-x}S nanocrystals prepared via heating-up synthesis before (DDT) and after ligand exchange procedures with S^{2-} , MPA and MUA and phase transfer to water. The dashed lines mark the position of the roxbyite peaks. **c)** X-ray diffractograms of the Cu_{2-x}S nanocrystals prepared via hot-injection synthesis after ligand exchange with S^{2-} , dried directly from formamide and handled and recorded under inert atmosphere.

formal valency of sulfur partially evolves from -2 to -1.⁴⁸ This partial oxidation was observed for both the samples prepared by hot-injection and by heating-up synthesis when replacing DDT with MUA or MPA using water as the polar solvent.

The absorption spectra of the Cu_{2-x}S nanocrystals before and after ligand exchange with S^{2-} , MPA and MUA are shown in Figure 2.5. Colloidal Cu_{2-x}S nanocrystals typically show a broad and featureless absorption with an onset in the visible region, accompanied by a lower energy tail,^{6,8,49} which can be ascribed to the presence of excess holes in the valence band (the so-called Urbach tail).¹³ Excess holes (*i.e.*, p-doping) are commonly observed in Cu-chalcogenide nanocrystals due to Cu-vacancies, and also give rise to a broad absorption band in the NIR due to localized surface plasmon resonances (LSPR) that emerge when the density of holes is sufficiently large (*i.e.*, when the concentration of Cu-vacancies is sufficiently high).^{6,8,49,59}

The absorption spectra of the Cu_{2-x}S nanocrystals prepared by hot-injection indeed show a clear absorption onset due to the band-edge absorption transition, and a weak tail towards longer wavelengths (Figure 2.5a). The absorption in the NIR is negligible, showing that LSPR bands are not present. These observations imply that the concentration of Cu-vacancies is very low, consistent with the observed crystal structure (Figure 2.4a). The absorption spectra after ligand exchange with S^{2-} , MPA or MUA are essentially unchanged, indicating that the optical properties of the Cu_{2-x}S nanocrystals are not affected by the ligand exchange.

The absorption spectrum of the Cu_{2-x}S nanocrystals prepared by heating-up is quite different, with a broad feature between 500-1000 nm that is not observed in the samples prepared by hot-injection (Figure 2.5b). This feature cannot be ascribed to a LSPR band because it occurs at too short wavelengths. In addition, the spectral position of this feature shifts after the sample is placed in a sonic bath. Hence, we ascribe this spectral

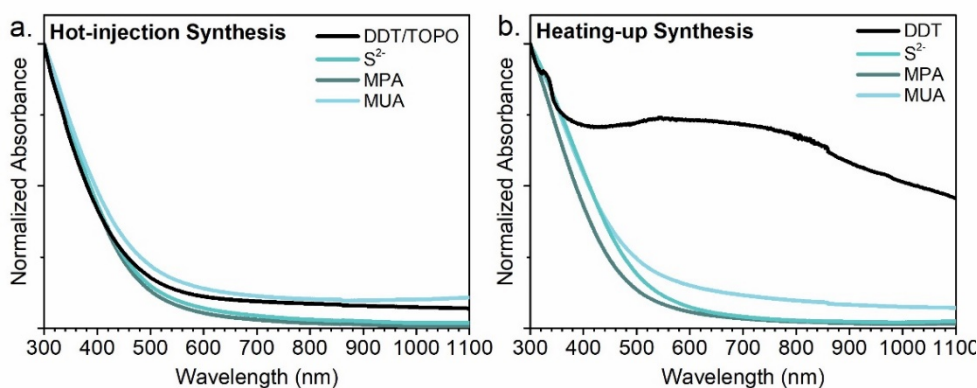


Figure 2.5 Absorption spectra of Cu_{2-x}S nanocrystals prepared by **a)** hot-injection synthesis, before (DDT/TOPO) and after ligand exchange with S^{2-} , MPA and MUA and prepared by **b)** heating-up synthesis, before (DDT/TOPO) and after ligand exchange with S^{2-} , MPA and MUA.

feature to light scattering due to the presence of nanocrystal aggregates.⁶ Importantly, upon ligand exchange with S^{2-} , MPA or MUA, this feature is no longer observed in the absorption spectrum, which shows instead the characteristic absorption of nearly stoichiometric $Cu_{2-x}S$ nanocrystals, being very similar to that of the nanocrystals synthesized by hot-injection. This is consistent with the fact that no aggregates are observed after the ligand exchange procedure in either of the samples. These observations confirm that the optical properties of the $Cu_{2-x}S$ nanocrystals are preserved upon ligand exchange and phase-transfer.

2.3.3 Dependence of the ligand exchange rates on the native and replacing ligand and synthesis method

The difficulty of ligand exchange on $Cu_{2-x}S$ nanocrystals has been ascribed to the presence of thiolate ligands at the nanocrystal surface.^{29,35} To verify whether other ligands are easier to replace, the ligand exchange procedures used for DDT-capped $Cu_{2-x}S$ nanocrystals were also performed on $Cu_{2-x}S$ nanocrystals capped by oleylamine. Oleylamine is expected to bind weakly to the $Cu_{2-x}S$ nanocrystal surface, because it is a relatively hard Lewis base and consequently will not have a strong interaction with the soft Lewis acid Cu^+ in the $Cu_{2-x}S$ nanocrystal. First, $Cu_{2-x}S$ nanocrystals of ~ 7 nm capped with oleylamine ligands were synthesized (Figure 2.6a). Similar to the $Cu_{2-x}S$ nanocrystals prepared with DDT, the obtained nanocrystals were in a djurleite ($Cu_{1.94}S$) crystal phase (Figure 2.6b).

As expected from their lower binding strength, oleylamine ligands on the $Cu_{2-x}S$ nanocrystals were rapidly replaced by MPA⁻, MUA⁻ and S^{2-} using the methods described above, leading to much faster phase transfer than observed for the DDT-capped $Cu_{2-x}S$ nanocrystals. For example, when replacing oleylamine for S^{2-} using Na_2S in formamide under inert atmosphere, phase transfer of the $Cu_{2-x}S$ nanocrystals from toluene to formamide occurred within minutes, while it took about one hour for DDT-capped $Cu_{2-x}S$ nanocrystals under the same conditions. However, whereas the size and shape of the nanocrystals were well preserved in ligand exchange procedures using S^{2-} as the replacing ligand on DDT-capped $Cu_{2-x}S$ nanocrystals (see Figure 2.3 above), the product nanocrystals from the oleylamine-capped $Cu_{2-x}S$ nanocrystals were highly aggregated (Figure 2.6c). A possible explanation for this observation is the fast rate of ligand exchange for the oleylamine-capped $Cu_{2-x}S$ nanocrystals. The fast stripping of the native ligands during the exchange could lead to an abrupt destabilization of the nanocrystals if the incoming S^{2-} ligands cannot provide sufficient charge stabilization of the nanocrystals fast enough, causing the nanocrystals to aggregate while at the interface between the two phases. This hypothesis is supported by the observation that when the bulkier MUA is used as the replacing ligand on the oleylamine-capped nanocrystals, the phase transfer was slower (on the order of hours) than when using S^{2-} (on the order of minutes) and the product nanocrystals did preserve their size and shape, with negligible

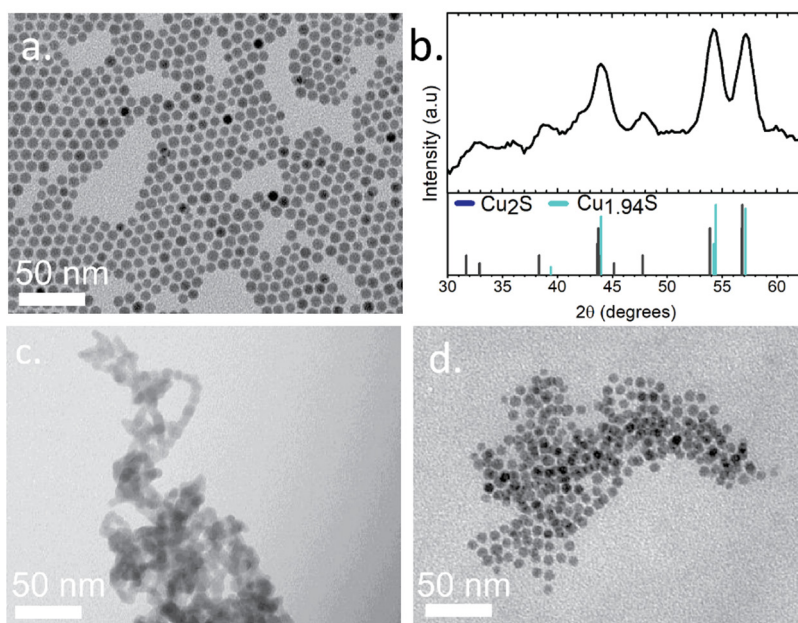


Figure 2.6 a) TEM image and b) X-Ray diffractogram of Cu_{2-x}S nanocrystals as-synthesized capped with oleylamine. TEM images of the oleylamine capped Cu_{2-x}S nanocrystals after ligand exchange with c) S^{2-} and d) MUA.

aggregation (Figure 2.6d). The negligible aggregation of the MUA⁻-capped Cu_{2-x}S nanocrystals can be ascribed to the ability of MUA⁻ ligands to provide both charge- and steric-stabilization, in contrast to S^{2-} ligands. The fast phase transfer observed for oleylamine-capped Cu_{2-x}S nanocrystals demonstrates that indeed oleylamine ligands are weakly bound to the Cu_{2-x}S nanocrystal surface and are thus more easily replaced than DDT ligands.

The native DDT ligands on the Cu_{2-x}S nanocrystals were replaced by all three ligands investigated when the ligand exchange was performed under inert atmosphere using formamide as polar solvent. However, a significant difference was observed in the kinetics of the ligand exchange for the three different replacing ligands. The kinetics of the ligand exchange was determined by the time it took for Cu_{2-x}S nanocrystals to transfer from the apolar to the polar phase. This phase-transfer only occurs after a sufficiently large number of apolar DDT molecules has been exchanged by polar ligands. The kinetics of the phase transfer process thus reflects the cumulative rates of a series of individual ligand exchange steps. The time it takes for phase-transfer to occur can then be directly related to the ligand exchange rates, being shorter for faster exchange rates. Therefore, we will discuss the kinetics of the phase-transfer in terms of ligand exchange rates. The ligand exchange was fastest when using S^{2-} . Here, phase transfer of the Cu_{2-x}S nanocrystals prepared by hot-injection synthesis was already observed upon stirring for

one hour. In contrast, ligand exchange was observed only after two hours for MPA and only after twelve hours for MUA. The same trend in ligand exchange rates with replacing ligand was observed for nanocrystals prepared by heating-up synthesis. The origin of the difference in the ligand exchange rates with the replacing ligands is discussed in more detail later. Besides the dependence of the ligand exchange rate on the replacing ligand, we found that the synthesis method of the Cu_{2-x}S nanocrystals (hot-injection with TOPO or heating-up without TOPO) also induced differences in the ligand exchange rates. The observed trend in all experiments was that the heating-up method gives Cu_{2-x}S nanocrystals that are more resistant towards ligand exchange than Cu_{2-x}S nanocrystals prepared by hot-injection synthesis with TOPO. To better understand this difference, additional experiments were performed.

2

A possible factor influencing the success of ligand exchange could be the formation of superstructures by self-organization of monodisperse nanocrystals. These superstructures could hinder the ligand exchange as the nanocrystals that are packed in the interior of the superlattices are shielded from the surroundings and thus from the incoming ligands. Besides single nanocrystals (Figure 2.3a,f), TEM evidenced the presence of these superstructures in both the samples prepared by hot-injection synthesis and by heating-up synthesis (Figure 2.7a). The presence of superstructures in the colloidal suspensions is verified using dynamic light scattering (DLS), where a hydrodynamic size of 1564 ± 316 nm and 932 ± 184 nm was observed for the samples prepared by heating-up and hot-injection, respectively (Figure 2.7b). Assuming a DDT chain length of 1.8 nm,⁵⁰ the size of the Cu_{2-x}S nanocrystals including ligand layer nanocrystals is ~ 16 nm for HU_DDT/TOPO and ~ 11 nm for HI_DDT. For both samples, the hydrodynamic size found by DLS was much larger than the size of the Cu_{2-x}S nanocrystals including the ligand shell, which indicates that large nanocrystal superstructures are present in the colloidal dispersion. The larger size of the

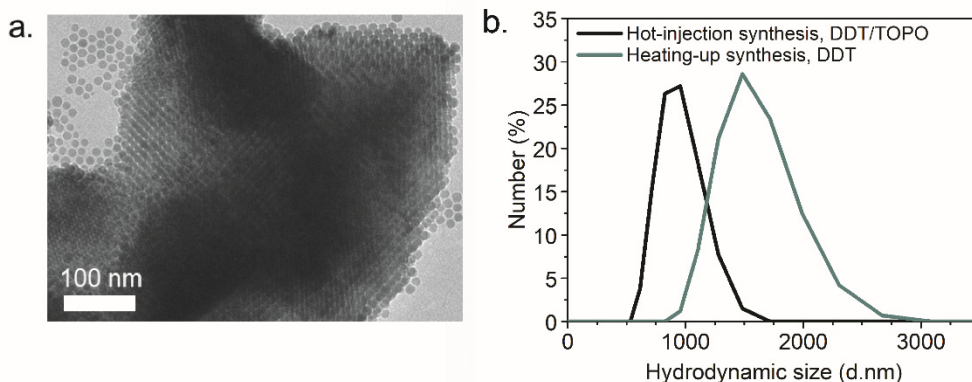


Figure 2.7 a) TEM image of a superstructure formed from monodisperse Cu_{2-x}S nanocrystals prepared by heating-up synthesis. **b)** Hydrodynamic size of Cu_{2-x}S nanocrystals in toluene prepared by either hot-injection synthesis or heating-up synthesis. The large hydrodynamic size indicates the presence of nanocrystal superstructures.

superstructures observed for the sample prepared by heating-up synthesis is attributed to the larger particle size. As can be seen from the hydrodynamic size distribution shown in Figure 2.7b, the large superstructures were predominant in both samples. Considering that superstructures were present in both samples, it is unlikely that the difference in the ligand exchange rates can be ascribed to their presence.

Another difference between the two samples is the size of the nanocrystals. Since the bond strength between ligand and nanocrystal has been reported to be size-dependent by several groups,^{51,52} we investigated the influence of the nanocrystal size on the rate of ligand exchange. To make nanocrystals similar in size, Cu_{2-x}S nanocrystals with a size of 11 nm were synthesized using the hot-injection method with TOPO by allowing for a longer reaction time (Figure 2.8). Subsequently, ligand exchange procedures using MUA in water were performed. In the ligand exchange experiments discussed above, the exchange using MUA in water occurred only for the 7 nm Cu_{2-x}S nanocrystals prepared by hot-injection synthesis in the presence of TOPO, upon stirring overnight. The 12 nm Cu_{2-x}S nanocrystals prepared by heating-up synthesis did not transfer to the aqueous phase, even after stirring for 3 days. In contrast, the 11 nm Cu_{2-x}S nanocrystals prepared by hot-injection in the presence of TOPO underwent phase-transfer from the apolar to the polar phase upon stirring overnight (Figure 2.8b). The ligand exchange rate was thus similar for 7 nm and 11 nm Cu_{2-x}S nanocrystals prepared by hot-injection synthesis. This demonstrates that the difference in the ligand exchange rates cannot be explained by nanocrystal size effects, nor by the presence of superstructures, and must thus be due to differences in the surface chemistry of the Cu_{2-x}S nanocrystals prepared by the two different synthesis methods.

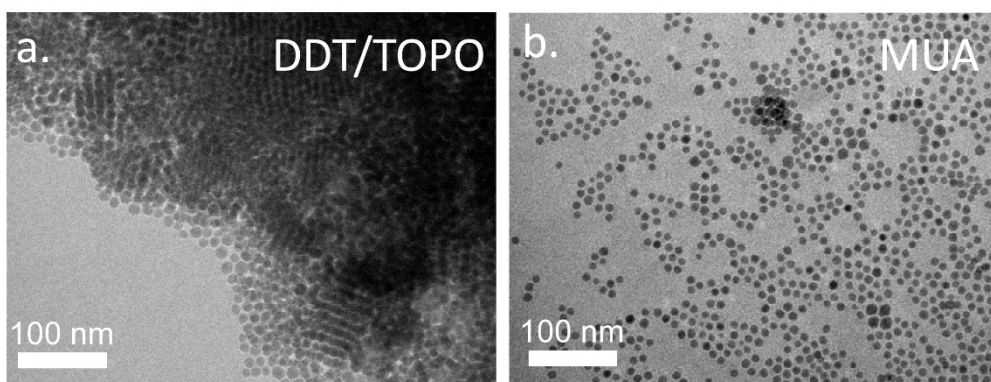


Figure 2.8 TEM images of Cu_{2-x}S nanocrystals of ~ 11 nm prepared by hot-injection synthesis, **a)** before and **b)** after ligand exchange with MUA in water.

2.3.4 Surface chemistry of the Cu_{2-x}S nanocrystals

As mentioned above, the nanocrystals prepared by hot-injection were synthesized in the presence of TOPO. TOPO is a widely used ligand in the synthesis of colloidal semiconductor nanocrystals, including Cu_{2-x}S and CuInS_2 , and is generally assumed to be present as a capping ligand at the nanocrystal surface after synthesis.^{23,53–55} Furthermore, Wang *et al.*, reported a shape controlling effect of TOPO in the synthesis of Cu_{2-x}S nanocrystals, which was attributed to preferential binding of TOPO onto (001) crystal facets, thereby facilitating anisotropic growth.³⁹ The presence of TOPO in combination with DDT at the surface of the nanocrystals synthesized by hot-injection could thus influence the ligand exchange rates. Therefore, we studied the surface species of the Cu_{2-x}S nanocrystals in more detail by means of x-ray photoelectron spectroscopy (XPS). Due to the limited escape depth of the generated photoelectrons, XPS is a surface sensitive technique and hence will be sensitive to probe the ligand layer around the nanocrystals and (part of) the Cu_{2-x}S nanocrystals as well.

Figure 2.9a shows the XPS survey scan of the as-prepared Cu_{2-x}S sample prepared via hot-injection synthesis in the presence of TOPO. It can be readily observed that none of the phosphorus core lines are observed, indicating the absence of TOPO at the nanocrystal surface. In addition, liquid phase ^{31}P -NMR was used to study the presence of TOPO bound to the nanocrystal surface in a sample taken directly after synthesis and of the same sample after washing with a mixture of methanol and butanol for three times (see Experimental Methods for details). Figure 2.9b shows the ^{31}P -NMR spectra of the unwashed sample and the sample washed three times. In the unwashed sample, a sharp resonance is present at a chemical shift of 48 ppm. By using a reference solution of TOPO in ODE, the resonance at 48 ppm is ascribed to TOPO. Ligands bound to nanocrystal surfaces typically show broad resonances due to solvent exclusion from the ligand shell and shorter relaxation times originating from the restricted mobility of the ligands when bound to the nanocrystal surface.^{56–60} Hence, the sharp resonance observed for the unwashed sample indicates that after synthesis no significant amount of TOPO is strongly bound to the nanocrystal surface, but instead TOPO is present as free ligand in solution. The sample analyzed after three wash steps shows no resonances in the ^{31}P -NMR spectrum, indicating that washing successfully removes free TOPO ligands from the nanocrystals dispersion and also bound TOPO from the nanocrystal surface.

The absence of TOPO species at the nanocrystal surface after synthesis and washing, in combination with the finding that TOPO acts as a shape-directing ligand in Cu_{2-x}S nanocrystal synthesis,³⁹ suggest that TOPO binds only weakly and dynamically to the nanocrystal surface during the synthesis and therefore does not end up at the nanocrystal surface in the equilibrium structure formed after synthesis and washing. The weak bond between TOPO and the nanocrystal surface can be rationalized in terms of Lewis acid-base interaction.^{12,13} TOPO binds through its oxygen lone pair to the Cu^+ in the Cu_{2-x}S

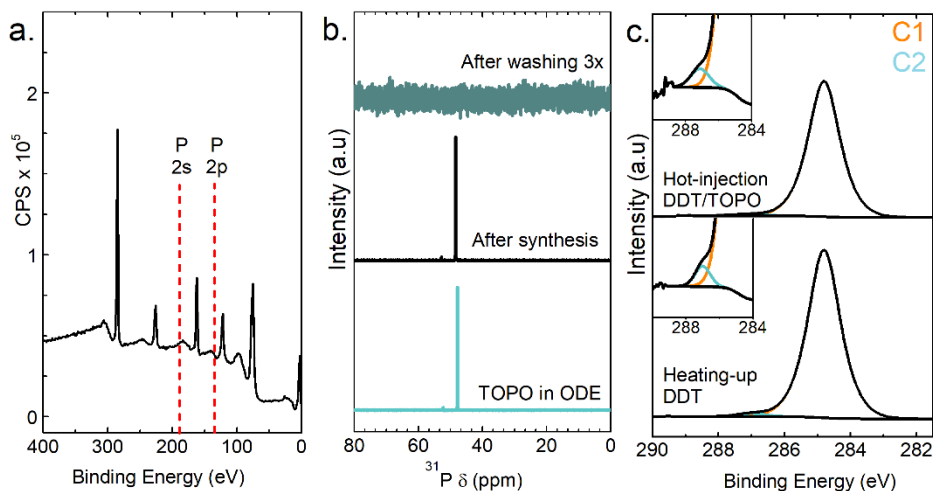


Figure 2.9 a) Zoom in of the XPS survey scan of the as-synthesized Cu_{2-x}S nanocrystals prepared by hot-injection synthesis. The red lines indicate the binding energy at which a phosphorus signal would be observed (left: P2s, right: P2p). The absence of peaks in this region confirms the absence of phosphorus in this sample. b) ^{31}P -NMR spectra of TOPO in ODE (reference) and of as-synthesized Cu_{2-x}S nanocrystals prepared by hot-injection in the presence of TOPO and after washing with a methanol/butanol mixture for 3 times. For the washed sample, even upon zooming-in no ^{31}P resonances are observed. c) XPS spectra of the C 1s region of as-synthesized Cu_{2-x}S nanocrystals, prepared by hot-injection (top) and heating-up (bottom) synthesis protocols. The fits of the first and second carbon components (C1 and C2) are shown in orange and blue, respectively.

nanocrystal. Since oxygen is a hard Lewis base and Cu^+ a soft Lewis acid, the interaction between the two species will be weak. In contrast, TOPO binds to the surface of *e.g.*, CuInS_2 nanocrystals,^{63,64} which can be explained by the fact that In^{3+} is a strong Lewis acid and will thus bind more strongly to the strong Lewis base oxygen.

Besides TOPO, acetate was added during the hot-injection synthesis (as $\text{Cu}(\text{I})$ acetate) and hence could be present as a weakly binding ligand on the Cu_{2-x}S nanocrystals. Additionally, in the heating-up synthesis, oleic acid is used as solvent and coordinating ligand and can consequently be present in the sample. To identify the carbon species present in the as-synthesized samples high-resolution XPS studies on the carbon 1s core line were performed (Figure 2.9c). In the Cu_{2-x}S nanocrystals prepared by hot-injection, carbon species can originate from the thiolate ligands, 1-octadecene or from acetate in the copper(I)acetate precursor. For the Cu_{2-x}S nanocrystals prepared by heating-up, carbon species can originate either from the thiolate ligands or from oleic acid used in the synthesis. Other solvents and antisolvents used during the synthesis and washing-up procedures have low boiling points and consequently will have evaporated in the ultra-high vacuum applied during the XPS measurements.

For both samples, C 1s peaks are observed at a binding energy of 284.8 eV and 287.0 eV. The peak at a binding energy of 284.8 eV is ascribed to carbon atoms in an aliphatic

chain (C-C) either originating from the thiolate ligands, 1-octadecene, oleic acid or adventitious carbon.⁶¹⁻⁶⁴ The peak at a binding energy of 287.0 eV is present for both species and is ascribed to carbon bound to sulfur in thiolates.⁶¹ Both the acetate and oleic acid species will give rise to a C 1s peak originating from carboxylate species (O=C-O) at slightly higher binding energies in the range of 288.1-289.1 eV.⁶¹⁻⁶⁵ As no peaks are present in this region in the C 1s spectrum of both samples, we conclude that there was no significant amount of acetate or oleic acid present. Moreover, these results show that both types of as-synthesized nanocrystals were capped solely by thiol ligands.

To further investigate the surface of the Cu_{2-x}S nanocrystals, high-resolution XPS studies on the sulfur 2p core line were performed (Figure 2.10). The as-synthesized nanocrystals capped with the thiol species were compared to the S 2p regions of the nanocrystals after ligand exchange with S^{2-} . For a single sulfur component, a set of spin-orbit coupled peaks ($2p_{3/2}$ and $2p_{1/2}$) is expected with an intensity ratio of 1:2 and a spin-orbit coupling split of ~ 1.2 eV. The S 2p regions of the as-synthesized samples clearly exhibited a second component and were therefore fitted using two sets of spin-orbit coupled peaks. In agreement with recent studies,^{29,61} we ascribe the component at a S $2p_{3/2}$ binding energy of 161.5 eV to sulfur in the Cu_{2-x}S nanocrystal lattice and possibly crystal-bound thiolate

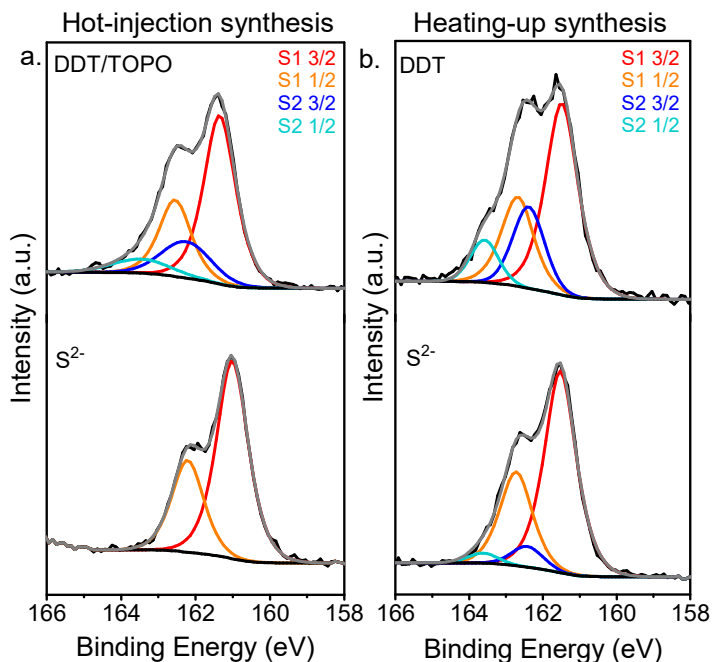


Figure 2.10 XPS of the sulfur 2p region of Cu_{2-x}S nanocrystals before and after ligand exchange with S^{2-} prepared by **a)** hot-injection and **b)** heating-up synthesis protocols. The black lines indicate the experimental data. The fits of the first sulfur component are shown in red and orange and the fit of the second sulfur component is shown in blue and light blue.

ligands. In the crystal-bound thiolate ligands, sulfur atoms are bound into higher coordination sites within the crystal lattice and hence the binding energy is very similar to the sulfides in the Cu_{2-x}S nanocrystal.²⁹ The second component has a higher S 2p_{3/2} binding energy of 162.4 eV and hence is ascribed to a sulfur species different from the sulfur in the Cu_{2-x}S lattice. The identical binding energy of 162.4 eV observed for the second sulfur component in the samples prepared by different synthesis methods suggests that the second sulfur component originates from the same sulfur species in both samples. This second Sulfur 2p component can be ascribed to surface-bound thiolate (*i.e.*, thiolate bound to surface sites with lower coordination numbers), as described by Turo *et al.*,²⁹ Other sulfur species possibly associated to this high binding energy S 2p component are thioethers forming a ligand double layer, similar to that recently described by Gromova *et al.*, for CuInS₂ nanocrystals prepared by a heating-up synthesis in the presence of DDT.³⁵

For the Cu_{2-x}S nanocrystals prepared by hot-injection in the presence of TOPO, the second sulfur component holds 9% of the total sulfur species, whereas this is 28% for the nanocrystals prepared by heating-up synthesis in the absence of TOPO. This suggests a denser layer of surface-bound thiolate species or thioether species around the nanocrystals prepared by the heating-up synthesis. Figure 2.10 (bottom) shows the high-resolution XPS spectra in the S 2p region of the Cu_{2-x}S nanocrystals after ligand exchange with S²⁻. For the nanocrystals prepared by hot-injection, the S 2p feature is best fitted with a single set of spin-orbit coupled peaks. Upon ligand exchange with S²⁻, the second component originating from the ligand layer is thus completely removed. In contrast, the second set of spin-orbit coupled peaks is still clearly present for the nanocrystals prepared by heating-up, indicating only partial removal of the surface-bound alkanethiols. The trend of ligand removal found with XPS studies correlates with the success and kinetics of the ligand exchange procedures discussed above, where it was found that DDT molecules on Cu_{2-x}S nanocrystals prepared by hot-injection in the presence of TOPO were more easily exchanged by the replacing ligands.

2.3.5 Model for ligand exchange on DDT-capped Cu_{2-x}S nanocrystals.

Based on the observations above we propose a model for the ligand exchange that explains the observed differences in the exchange rates (Figure 2.11). In the ligand exchange protocol developed in our work a two layer system is formed in which the apolar layer contains the Cu_{2-x}S nanocrystals capped by the native thiolate ligands and the polar formamide layer contains the replacing negatively charged ligands (MPA⁻, MUA⁻ or S²⁻) and, later in the process, also the negatively charged Cu_{2-x}S nanocrystals capped with the replacing ligands. As the two solvents are immiscible, and the replacing

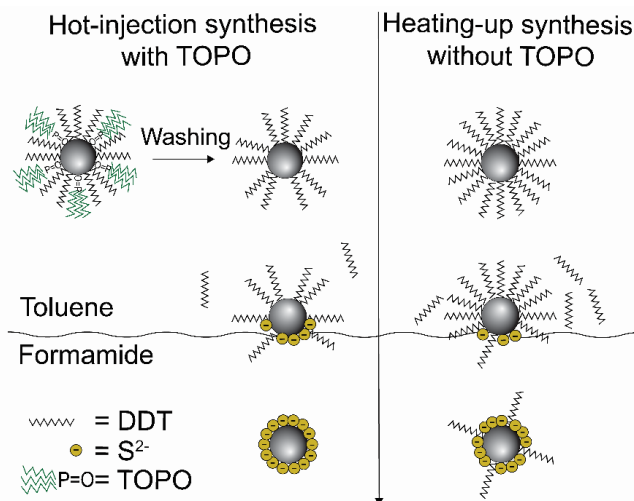


Figure 2.11 Schematic illustration of a ligand exchange of DDT for S²⁻ and subsequent phase transfer from apolar toluene to polar formamide. The Cu_{2-x}S nanocrystals prepared by hot-injection synthesis have a less dense ligand layer than the nanocrystals prepared by heating-up synthesis due to the removal of TOPO from the surface of the nanocrystal after synthesis and washing. Consequently, the nanocrystal surface is more accessible to the incoming ligands, resulting in a faster ligand exchange. Upon ligand exchange on nanocrystals prepared by hot-injection synthesis, all thiolate ligands are removed from the nanocrystal surface. In contrast, upon ligand exchange on nanocrystals prepared by heating-up synthesis, some thiolate ligands remain on the surface.

ligands and the charged nanocrystals do not disperse in the apolar phase, while the nanocrystals with the native DDT ligands do not disperse in the polar phase, the ligand exchange must necessarily take place at the interface between the polar and the apolar layers.

The native DDT ligand is bound to the nanocrystal surface through its sulfur atom that donates an unshared electron pair and coordinates to the Cu⁺.¹² In the ligand exchange reactions, the negatively charged replacing ligand (MPA⁻, MUA⁻ or S²⁻) will coordinate its electron-rich sulfur species to the Cu⁺ site on the nanocrystal,¹³ thereby weakening the bond between the Cu⁺ and the donor sulfur atom of the DDT ligands, which will eventually force the native thiolate ligand to leave the nanocrystal surface. When part of the native ligands are exchanged for charged species, the nanocrystals will be trapped at the interface since they will become charged (Figure 2.11). If most native ligands are exchanged for charged replacing ligands, thereby making the nanocrystal sufficiently negatively charged, the nanocrystal will transfer to the polar solvent (Figure 2.11). As described above, we found that the polarity of the solvent influences the success of ligand exchange. This can be understood by the good ability of the highly polar formamide to shield the charged intermediates. Similarly, the higher stability of the nanocrystals in

solvents with higher polarity (*e.g.*, formamide) results from the better shielding of the charged nanocrystals.

The observed dependence of the ligand exchange rate on the incoming ligand (*viz.*, highest for S²⁻, followed by MPA⁻ and then MUA⁻), can be rationalized in terms of the accessibility of the nanocrystal surface due to variable degrees of steric hindrance. The hydrophobic ligand layer at the nanocrystal surface acts as a barrier around the nanocrystal. The small S²⁻ ions can more easily diffuse through this hydrophobic layer and reach the surface Cu⁺ sites, whereas the bulky MUA molecule cannot easily access the surface sites, which results in much slower ligand exchange rates.

The observed difference in the ligand exchange rates for the Cu_{2-x}S nanocrystals prepared by hot-injection or heating-up can be explained by the ligand layer at the surface of the nanocrystals. Although we cannot identify the exact nature of the ligand layer, the XPS studies discussed above indicate a denser layer of thiolate ligands around Cu_{2-x}S nanocrystals prepared by the heating-up synthesis, *i.e.*, in the absence of TOPO. The fact that the native ligand layer is less dense for the nanocrystals prepared through the hot-injection method can be understood from the synthesis conditions used. In the hot-injection synthesis, TOPO is used as a coordinating ligand. As has been shown by Wang *et al.*, TOPO has a shape directing effect in the synthesis of Cu_{2-x}S nanocrystals, implying that it dynamically binds to the nanocrystals surface during its growth.³⁹ The bulky nature of TOPO will thus prevent the formation of a dense layer of thiolates around the growing Cu_{2-x}S nanocrystals. As shown by the XPS and ³¹P-NMR studies discussed above, TOPO is no longer present on the Cu_{2-x}S nanocrystals after the synthesis, implying that it has been removed from the surface, thereby leaving vacant sites on the nanocrystal surface. Consequently, the Cu_{2-x}S nanocrystals prepared by hot-injection synthesis in the presence of TOPO have a less dense layer of thiolate ligands at the nanocrystal surface than nanocrystals prepared by the heating-up synthesis. The denser, hydrophobic native ligand layer at the surface of the nanocrystals prepared by the heating-up method will make the surface sites less accessible for the charged incoming ligands and hence will significantly slow down the ligand exchange kinetics.

Additionally, Cu_{2-x}S nanocrystals prepared by hot-injection show a single sulfur species upon ligand exchange with S²⁻, indicating that all surface-bound thiolate ligands are removed from the nanocrystal surface upon ligand exchange. In contrast, nanocrystals prepared using heating-up synthesis show residual surface-bound thiolate species at their surface upon ligand exchange (see Figure 2.10 and XPS discussion above). Consequently, the nanocrystals are likely capped with a combination of remaining thiolate species and sulfides, as is schematically represented in Figure 2.11. However, since the nanocrystals do show colloidal stability in formamide, the nanocrystal surface is covered by sufficient negatively charged sulfide anions to stabilize the nanocrystals in formamide.

2.4 Conclusions

In this chapter we present effective ligand exchange procedures of DDT on Cu_{2-x}S nanocrystals for MPA^- , MUA^- , and S^{2-} from Na_2S in formamide under inert atmosphere. In this manner, colloidal Cu_{2-x}S nanocrystals more suitable for (photo)catalytic applications could be obtained. The ligand exchange procedures did not significantly affect the size, shape and optical properties of the nanocrystals. The resulting hydrophilic Cu_{2-x}S nanocrystals have excellent colloidal stability in formamide. Water-dispersible Cu_{2-x}S nanocrystals can be easily obtained by precipitation of the nanocrystals, followed by redispersion in water. In addition, the ligand exchange rates for DDT-capped Cu_{2-x}S nanocrystals depended on the preparation method, being much slower for Cu_{2-x}S nanocrystals prepared by heating-up than by hot-injection synthesis. XPS studies revealed that the differences in the ligand exchange rates can be attributed to the surface chemistry of the Cu_{2-x}S nanocrystals, where nanocrystals prepared by heating-up synthesis had a denser ligand layer in comparison to nanocrystals prepared by hot-injection in the presence of TOPO. The less dense native thiolate ligand layer on the surface of the nanocrystals prepared by hot-injection originates from the presence of TOPO during the synthesis, which prevents the formation of a dense thiolate layer around the nanocrystals during their growth, thus leaving vacant surface sites after being removed upon washing after the synthesis. The dense native thiolate ligand layer makes the nanocrystal surface less accessible for the charged incoming ligands, hence significantly slowing down the ligand exchange rates. The facile ligand exchange procedures developed in our work open up opportunities for the use of high-quality colloidal Cu_{2-x}S nanocrystals prepared with thiols in various applications, such as catalysis, photothermal therapy, or solution-processable devices (flexible conductive films, sensors, solar cells).

2.5 Acknowledgements

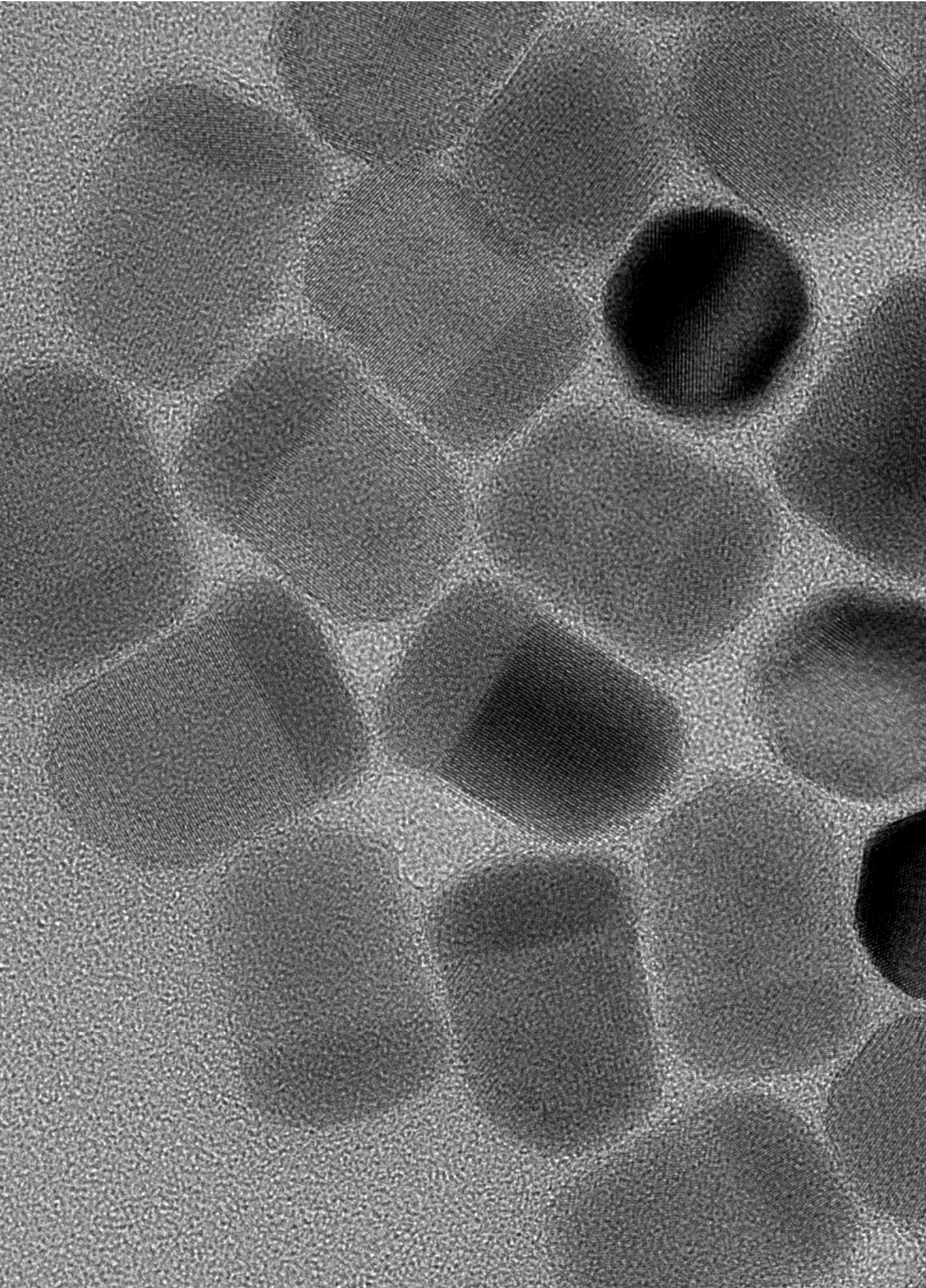
We are grateful to Freddy Oropeza (TU Eindhoven) for his help in performing the XPS measurements and useful discussions. Jan Philip Hofmann (TU Eindhoven) and Emiel Hensen (TU Eindhoven) are also acknowledged for their assistance in the XPS measurements. In addition, Johann Jastrzebski (Utrecht University) is thanked for his assistance with ^{31}P -NMR measurements.

2.6 References

- (1) Goel, S.; Chen, F.; Ehlerding, E. B.; Cai, W. Intrinsically Radiolabeled Nanoparticles: An Emerging Paradigm. *Small* **2014**, *10*, 3825–3830.
- (2) Coughlan, C.; Ibáñez, M.; Dobrozhan, O.; Singh, A.; Cabot, A.; Ryan, K. M. Compound Copper Chalcogenide Nanocrystals. *Chem. Rev.* **2017**, *117*, 5865–6109.
- (3) Goel, S.; Chen, F.; Cai, W. Synthesis and Biomedical Applications of Copper Sulfide Nanoparticles: From Sensors to Theranostics. *Small* **2014**, *10*, 631–645.
- (4) Wang, S.; Riedinger, A.; Li, H.; Fu, C.; Liu, H.; Li, L.; Liu, T.; Tan, L.; Barthel, M. J.; Pugliese, G.; et al., Plasmonic Copper Sulfide Nanocrystals Exhibiting Near-Infrared Photothermal and Photodynamic Therapeutic Effects. *ACS Nano* **2015**, *9*, 1788–1800.
- (5) Zhao, Y.; Burda, C. Development of Plasmonic Semiconductor Nanomaterials with Copper Chalcogenides for a Future with Sustainable Energy Materials. *Energy Environ. Sci.* **2012**, *5*, 5564–5576.
- (6) Luther, J. M.; Jain, P. K.; Ewers, T.; Alivisatos, A. P. Localized Surface Plasmon Resonances Arising from Free Carriers in Doped Quantum Dots. *Nat. Mater.* **2011**, *10*, 361–366.
- (7) Abdelhady, A. L.; Ramasamy, K.; Malik, M. A.; O'Brien, P.; Haigh, S. J.; Raftery, J. New Routes to Copper Sulfide Nanostructures and Thin Films. *J. Mater. Chem.* **2011**, *21*, 17888–17895.
- (8) Van Der Stam, W.; Gudjonsdottir, S.; Evers, W. H.; Houtepen, A. J. Switching between Plasmonic and Fluorescent Copper Sulfide Nanocrystals. *J. Am. Chem. Soc.* **2017**, *139*, 13208–13217.
- (9) Shao, P.; Ci, S.; Yi, L.; Cai, P.; Huang, P.; Cao, C.; Wen, Z. Hollow CuS Microcube Electrocatalysts for CO₂ Reduction Reaction. *ChemElectroChem* **2017**, *4*, 2593–2598.
- (10) Zhao, Z.; Peng, X.; Liu, X.; Sun, X.; Shi, J.; Han, L.; Li, G.; Luo, J. Efficient and Stable Electroreduction of CO₂ to CH₄ on CuS Nanosheet Arrays. *J. Mater. Chem. A* **2017**, *5*, 20239–20243.
- (11) Van Embden, J.; Chesman, A. S. R.; Jasieniak, J. J. The Heat-Up Synthesis of Colloidal Nanocrystals. *Chem. Mater.* **2015**, *27*, 2246–2285.
- (12) Donegá, C. D. M. Synthesis and Properties of Colloidal Heteronanocrystals. *Chem. Soc. Rev.* **2011**, *40*, 1512–1546.
- (13) Nag, A.; Kovalenko, M. V.; Lee, J. S.; Liu, W.; Spokoyny, B.; Talapin, D. V. Metal-Free Inorganic Ligands for Colloidal Nanocrystals: S²⁻, HS⁻, Se²⁻, HSe⁻, Te²⁻, HTe⁻, TeS₃²⁻, OH⁻, and NH₂⁻ as Surface Ligands. *J. Am. Chem. Soc.* **2011**, *133*, 10612–10620.
- (14) Kovalenko, M. V.; Scheele, M.; Talapin, D. V. Colloidal Nanocrystals with Molecular Metal Chalcogenide Surface Ligands. *Science* **2009**, *324*, 1417–1420.
- (15) Kovalenko, M. V.; Bodnarchuk, M. I.; Zaumseil, J.; Lee, J. S.; Talapin, D. V. Expanding the Chemical Versatility of Colloidal Nanocrystals Capped with Molecular Metal Chalcogenide Ligands. *J. Am. Chem. Soc.* **2010**, *132*, 10085–10092.
- (16) Gugula, K.; Stegemann, L.; Cywiński, P. J.; Strassert, C. A.; Bredol, M. Facile Surface Engineering of CuInS₂/ZnS Quantum Dots for LED down-Converters. *RSC Adv.* **2016**, *6*, 10086–10093.
- (17) Wuister, S. F.; De Mello Donegá, C.; Meijerink, A. Luminescence Temperature Antiquenching of Water-Soluble CdTe Quantum Dots: Role of the Solvent. *J. Am. Chem. Soc.* **2004**, *126*, 10397–10402.
- (18) Bagaria, H. G.; Ada, E. T.; Shamsuzzoha, M.; Nikles, D. E.; Johnson, D. T. Understanding Mercapto Ligand Exchange on the Surface of FePt Nanoparticles. *Langmuir* **2006**, *22*, 7732–7737.
- (19) Chan, W. C. W.; Nie, S. Quantum Dot Bioconjugates for Ultrasensitive Nonisotopic Detection. *Adv. Sci.* **2009**, *281*, 2016–2018.
- (20) Algar, W. R.; Krull, U. J. Luminescence and Stability of Aqueous Thioalkyl Acid Capped CdSe/ZnS Quantum Dots Correlated to Ligand Ionization. *ChemPhysChem* **2007**, *8*, 561–568.
- (21) Aldana, J.; Wang, Y. A.; Peng, X. Photochemical Instability of CdSe Nanocrystals Coated by Hydrophilic Thiols. *J. Am. Chem. Soc.* **2001**, *123*, 8844–8850.
- (22) Ben-Shahar, Y.; Scotognella, F.; Waiskopf, N.; Kriegel, I.; Dal Conte, S.; Cerullo, G.; Banin, U. Effect of Surface Coating on the Photocatalytic Function of Hybrid CdS-Au Nanorods. *Small* **2015**, *11*, 462–471.
- (23) Xia, C.; Meeldijk, J. D.; Gerritsen, H. C.; de Mello Donegá, C. Highly Luminescent Water-Dispersible NIR-Emitting Wurtzite CuInS₂/ZnS Core/Shell Colloidal Quantum Dots. *Chem. Mater.* **2017**, *29*, 4940–4951.
- (24) Zhao, C.; Bai, Z.; Liu, X.; Zhang, Y.; Zou, B.; Zhong, H. Small GSH-Capped CuInS₂ Quantum Dots: MPA-Assisted Aqueous Phase Transfer and Bioimaging Applications. *ACS Appl. Mater. Interfaces* **2015**, *7*, 17623–17629.
- (25) Tamang, S.; Beaune, G.; Texier, I.; Reiss, P. Aqueous Phase Transfer of InP/ZnS Nanocrystals Conserving Fluorescence and High Colloidal Stability. *ACS Nano* **2011**, *5*, 9392–9402.

- (26) Nann, T. Phase-Transfer of CdSe@ZnS Quantum Dots Using Amphiphilic Hyperbranched Polyethylenimine. *Chem. Commun.* **2005**, 1735–1736.
- (27) Ben-Shahar, Y.; Scotognella, F.; Waiskopf, N.; Kriegel, I.; Dal Conte, S.; Cerullo, G.; Banin, U. Effect of Surface Coating on the Photocatalytic Function of Hybrid CdS-Au Nanorods. *Small* **2015**, *11*, 462–471.
- (28) Lees, E. E.; Nguyen, T. L.; Clayton, A. H. A.; Mulvaney, P. The Preparation of Colloidally Stable, Water-Soluble, Biocompatible, Semiconductor Nanocrystals with a Small Hydrodynamic Diameter. *ACS Nano* **2009**, *3*, 1121–1128.
- (29) Turo, M. J.; Macdonald, J. E. Crystal-Bound vs Surface-Bound Thiols on Nanocrystals. *ACS Nano* **2014**, *8*, 10205–10213.
- (30) Chen, L.; Li, G. Functions of 1-Dodecanethiol in the Synthesis and Post-Treatment of Copper Sulfide Nanoparticles Relevant to Their Photocatalytic Applications. *ACS Appl. Nano Mater.* **2018**, *1*, 4587–4593.
- (31) Xie, R.; Rutherford, M.; Peng, X. Formation of High-Quality I-III-VI Semiconductor Nanocrystals by Tuning Relative Reactivity of Cationic Precursors. *J. Am. Chem. Soc.* **2009**, *131*, 5691–5697.
- (32) So, D.; Konstantatos, G. Thiol-Free Synthesized Copper Indium Sulfide Nanocrystals as Optoelectronic Quantum Dot Solids. *Chem. Mater.* **2015**, *27*, 8424–8432.
- (33) Pan, Z.; Mora-Sero, I.; Shen, Q.; Zhang, H.; Li, Y.; Zhao, K.; Wang, J.; Zhong, X.; Bisquert, J. High-Efficiency Green Quantum Dot Solar Cells. *J. Am. Chem. Soc.* **2014**, *136*, 9203–9210.
- (34) Akdas, T.; Distaso, M.; Kuhri, S.; Winter, B.; Birajdar, B.; Spiecker, E.; Guldi, D. M.; Peukert, W. The Effects of Post-Processing on the Surface and the Optical Properties of Copper Indium Sulfide Quantum Dots. *J. Colloid Interface Sci.* **2015**, *445*, 337–347.
- (35) Gromova, M.; Lefrancois, A.; Vaure, L.; Agnese, F.; Aldakov, D.; Maurice, A.; Djurado, D.; Lebrun, C.; de Geyer, A.; Schulli, T. U.; et al., Growth Mechanism and Surface State of CuInS₂ Nanocrystals Synthesized with Dodecanethiol. *J. Am. Chem. Soc.* **2017**, *139*, 15748–15759.
- (36) Robinson, E. H.; Turo, M. J.; Macdonald, J. E. Controlled Surface Chemistry for the Directed Attachment of Copper(I) Sulfide Nanocrystals. *Chem. Mater.* **2017**, *29*, 3854–3857.
- (37) Van Der Stam, W.; Berends, A. C.; Rabouw, F. T.; Willhammar, T.; Ke, X.; Meeldijk, J. D.; Bals, S.; De Mello Donega, C. Luminescent CuInS₂ Quantum Dots by Partial Cation Exchange in Cu_{2-x}S Nanocrystals. *Chem. Mater.* **2015**, *27*, 621–628.
- (38) Williamson, C. B.; Nevers, D. R.; Hanrath, T.; Robinson, R. D. Prodigious Effects of Concentration Intensification on Nanoparticle Synthesis: A High-Quality, Scalable Approach. *J. Am. Chem. Soc.* **2015**, *137*, 15843–15851.
- (39) Wang, Y.; Hu, Y.; Zhang, Q.; Ge, J.; Lu, Z.; Hou, Y.; Yin, Y. One-Pot Synthesis and Optical Property of Copper(I) Sulfide Nanodisks. *Inorg. Chem.* **2010**, *49*, 6601–6608.
- (40) Wen, X.; Zhang, W.; Yang, S.; Dai, Z. R.; Wang, Z. L. Solution Phase Synthesis of Cu(OH)₂Nanoribbons by Coordination Self-Assembly Using Cu₂S Nanowires as Precursors. *Nano Lett.* **2002**, *2*, 1397–1401.
- (41) Trevani, L. N.; Roberts, J. C.; Tremaine, P. R. Copper(II)-Ammonia Complexation Equilibria in Aqueous Solutions at Temperatures from 30 to 250 Degrees C by Visible Spectroscopy. *J. Solution Chem.* **2001**, *30*, 585–622.
- (42) Lambie, G.; Moen, A.; Nicholson, D. G. Structure of the Diamminecopper(II) Ion in Solution An X-Ray Absorption Spectroscopic Study. *J. Chem. Soc. Faraday Trans* **1994**, *90*, 2211–2213.
- (43) Sano, M.; Maruo, T.; Yamatera, H. Structural Determination of Solvated Copper Species in Formamide Solution by EXAFS. *J. Chem. Phys.* **1988**, *89*, 1185–1187.
- (44) Nisar Ansari, M.; Khan, S. H.; Aziz Khan, A. Polarographic Studies on Copper(II)-Formamide Complex in Alkaline Medium. *J. Electroanal. Chem.* **1970**, *28*, 450–452.
- (45) Xu, J.; Xue, D.; Zhu, Y. Room Temperature Synthesis of Curved Ammonium Copper Molybdate Nanoflake and Its Hierarchical Architecture. *J. Phys. Chem. B* **2006**, *110*, 17400–17405.
- (46) Zhang, Z.; Shao, X.; Yu, H.; Wang, Y.; Han, M. Morphosynthesis and Ornamentation of 3D Dendritic Nanoarchitectures. *Chem. Mater.* **2005**, *17*, 332–336.
- (47) Ling Lou, J.; Wei Shiu, H.; Yueh Chang, L.; Ping Wu, C.; Soo, Y.-L.; Chen, C.-H. Preparation and Characterization of an Ordered 1-Dodecanethiol Monolayer on Bare Si(111) Surface. *Langmuir.* **2011**, *27*, 3436–3441.
- (48) Xie, Y.; Riedinger, A.; Prato, M.; Casu, A.; Genovese, A.; Guardia, P.; Sottini, S.; Sangregorio, C.; Miszta, K.; Ghosh, S.; et al., Copper Sulfide Nanocrystals with Tunable Composition by Reduction of Covellite Nanocrystals with Cu⁺ Ions. *J. Am. Chem. Soc.* **2013**, *135*, 17630–17637.
- (49) Zhao, Y.; Pan, H.; Lou, Y.; Qiu, X.; Zhu, J.; Burda, C. Plasmonic Cu_{2-x}S Nanocrystals: Optical and Structural Properties of Copper-Deficient Copper(I) Sulfides. *J. Am. Chem. Soc.* **2009**, *131*, 4253–4261.

- (50) Hinterwirth, H.; Kappel, S.; Waitz, T.; Prohaska, T.; Lindner, W.; Lämmerhofer, M. Quantifying Thiol Ligand Density of Self-Assembled Monolayers on Gold Nanoparticles by Inductively Coupled Plasma-Mass Spectrometry. *ACS Nano* **2013**, *7*, 1129–1136.
- (51) Aldana, J.; Lavelle, N.; Wang, Y.; Peng, X. Size-Dependent Dissociation PH of Thiolate Ligands from Cadmium Chalcogenide Nanocrystals. *J. Am. Chem. Soc.* **2005**, *127*, 2496–2504.
- (52) Schrier, J.; Wang, L. W. On the Size-Dependent Behavior of Nanocrystal-Ligand Bonds. *J. Phys. Chem. B* **2006**, *110*, 11982–11985.
- (53) Asgary, S.; Mirabbaszadeh, K.; Nayebi, P.; Emadi, H. Synthesis and Investigation of Optical Properties of TOPO-Capped CuInS₂ Semiconductor Nanocrystal in the Presence of Different Solvent. *Mater. Res. Bull.* **2014**, *51*, 411–417.
- (54) Kruszynska, M.; Borchert, H.; Parisi, J.; Kolny-Olesiak, J. Investigations of Solvents and Various Sulfur Sources Influence on the Shape-Controlled Synthesis of CuInS₂ Nanocrystals. *J. Nanoparticle Res.* **2011**, *13*, 5815–5824.
- (55) Kruszynska, M.; Borchert, H.; Bachmatiuk, A.; Rummeli, M. H.; Büchner, B.; Parisi, J.; Kolny-Olesiak, J. Size and Shape Control of Colloidal Copper(I) Sulfide Nanorods. *ACS Nano* **2012**, *6*, 5889–5896.
- (56) Hens, Z.; Martins, J. C. A Solution NMR Toolbox for Characterizing the Surface Chemistry of Colloidal Nanocrystals. *Chem. Mater.* **2013**, *25*, 1211–1221.
- (57) Owen, J. S.; Park, J.; Trudeau, P. E.; Alivisatos, A. P. Reaction Chemistry and Ligand Exchange at Cadmium-Selenide Nanocrystal Surfaces. *J. Am. Chem. Soc.* **2008**, *130*, 12279–12281.
- (58) Kopping, J. T.; Patten, T. E. Identification of Acidic Phosphorus-Containing Ligands Involved in the Surface Chemistry of CdSe Nanoparticles Prepared in Tri-N-Octylphosphine Oxide Solvents. *J. Am. Chem. Soc.* **2008**, *130*, 5689–5698.
- (59) Becerra, L. R.; Murray, C. B.; Griffin, R. G.; Bawendi, M. G. Investigation of the Surface Morphology of Capped CdSe Nanocrystallites by ³¹P Nuclear Magnetic Resonance. *J. Chem. Phys.* **1994**, *100*, 3297–3300.
- (60) De Roo, J.; Yazdani, N.; Drijvers, E.; Lauria, A.; Maes, J.; Owen, J. S.; Driessche, I. Van; Niederberger, M.; Wood, V.; Martins, J. C.; et al., Probing Solvent–Ligand Interactions in Colloidal Nanocrystals by the NMR Line Broadening. *Chem. Mater.* **2018**, *30*, 5485–5492.
- (61) Berends, A. C.; Van Der Stam, W.; Hofmann, J. P.; Bladt, E.; Meeldijk, J. D.; Bals, S.; De Mello Donega, C. Interplay between Surface Chemistry, Precursor Reactivity, and Temperature Determines Outcome of ZnS Shelling Reactions on CuInS₂ Nanocrystals. *Chem. Mater.* **2018**, *30*, 2400–2413.
- (62) Watts, J. F.; Leadley, S. R.; Castle, J. E.; Blomfield, C. J. Adsorption of PMMA on Oxidized Al and Si Substrates: An Investigation by High-Resolution X-Ray Photoelectron Spectroscopy. *Langmuir* **2000**, *16*, 2292–2300.
- (63) Wilson, D.; Langell, M. A. XPS Analysis of Oleylamine/Oleic Acid Capped Fe₃O₄ Nanoparticles as a Function of Temperature. *Appl. Surf. Sci.* **2014**, *303*, 6–13.
- (64) Zhang, L.; He, R.; Gu, H. C. Oleic Acid Coating on the Monodisperse Magnetite Nanoparticles. *Appl. Surf. Sci.* **2006**, *253*, 2611–2617.
- (65) Wagener, K.; Batich, C.; Kirsch, B.; Wanigatunga, S. Chain Propagation/Step Propagation Polymerization. III. An XPS Investigation of Poly(Oxyethylene)-b-Poly(Pivalolactone) Telechelomer. *J. Polym. Sci. Part A Polym. Chem.* **1989**, *27*, 2625–2631.



Chapter 3

The synthesis and formation mechanism of $\text{Cu}_{2-x}\text{S}/\text{CuInS}_2$ heteronanocrystals

Abstract: Colloidal heteronanocrystals are attracting increasing attention, as they allow for the synergistic combination of properties of different materials within one single nanocrystal. By coupling semiconductors with different compositions in one particle, spatial separation of the photogenerated electron and hole can be enhanced, which can improve the efficiency of the heteronanocrystals as photocatalysts. Besides the composition of the semiconductors, the design of the heteronanocrystals is of crucial importance, as it needs to allow for the photogenerated charge carriers to reach the particle surface. In this chapter, we developed a two-step synthesis route to form $\text{Cu}_{2-x}\text{S}/\text{CuInS}_2$ heteronanocrystals with tunable size, shape and composition. The heteronanocrystals are formed by injection of a solution of pre-formed Cu_{2-x}S seed nanocrystals in 1-dodecanethiol into a hot solution of indium-oleate. By varying the reaction time, heteronanocrystals with different sizes, shapes and compositions were obtained. We propose a model for the formation of these $\text{Cu}_{2-x}\text{S}/\text{CuInS}_2$ heteronanocrystals, in which the initial formation of the heteronanocrystals is attributed to a single step, thiolate-mediated cation exchange of Cu^+ for In^{3+} , that is followed by homoepitaxial growth of CuInS_2 on the pre-formed CuInS_2 surface. The outcome of the reaction strongly depends on the precursors in solution.

3.1 Introduction

Colloidal nanocrystals are attractive materials for various applications as they have unique size- and shape dependent properties.^{1,2} The interesting properties of these nanomaterials can be further extended by the use of heteronanocrystals (HNCs), where two (or more) materials are combined into one nanocrystal and share one or more interfaces.^{2,3} In this way, the optical, magnetic or catalytic properties of different materials can be synergistically combined into one particle. In addition, novel properties can arise, that can be tailored by the size, shape and composition of each part of the HNC.

The optoelectronic properties of HNCs are determined by the bandgap and band alignment of the materials comprising the HNC. Depending on the band alignment of the materials at the hetero-interface, different charge carrier localization regimes can be distinguished, namely type-I, type-I^{1/2} and type-II (Figure 3.1a).⁴ In type-I HNCs, both charge carriers are confined in the same component of the HNC. In type-I^{1/2} HNCs, one of the charge carriers is delocalized over the whole HNC, while the other charge carrier is confined in only one of the components. This leads to a smaller overlap of the electron and hole wavefunctions, resulting in longer exciton lifetimes. In type-II HNCs, the photogenerated electron and hole are spatially separated in different components of the HNC, again leading to longer exciton lifetimes. The band offsets are thus an important parameter in the design of HNCs with favorable optoelectronic properties, and can be tailored by the composition of each component in the HNC. In addition, the bandgap and consequently band offsets can be influenced by the size of each component via quantum confinement effects.

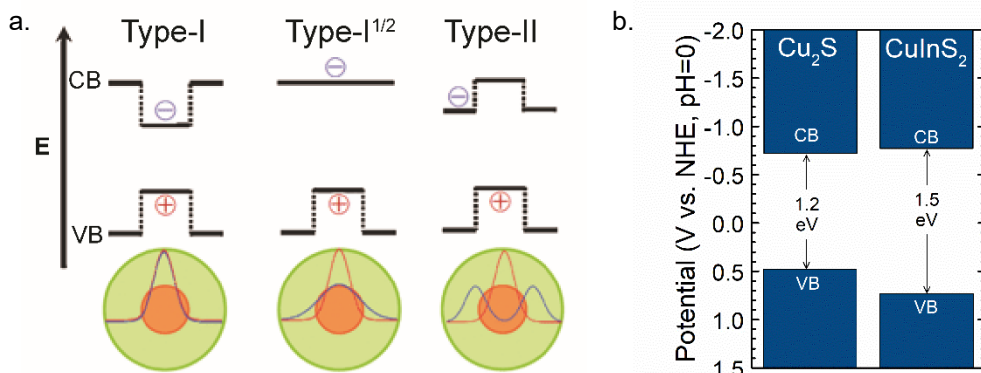


Figure 3.1 a) Schematic representation of the three charge carrier localization regimes that can occur in HNCs. In a type-I HNC the exciton is confined in one component of the HNC. In a type-I^{1/2} HNC, one of the charge carriers is confined in one component, whereas the other is delocalized over the whole HNC. In a type-II HNC the electron and hole are spatially separated. Reprinted with permission from ref [2]. Copyright 2011 The Royal Society of Chemistry **b)** Schematic representation of the valence- and conduction band edges and band gap energies of Cu_{2-x}S and CuInS_2 . Combining Cu_{2-x}S and CuInS_2 in a HNC can possibly lead to Type I^{1/2} charge carrier localization. The band positions are obtained from refs [35-37].

In photocatalysis, photogenerated charge carriers are used to promote redox reactions at the particle surface, as discussed in more detail in Chapter 1. Hence, the use of HNCs can be beneficial as they can provide spatially separated electrons and holes within a single nanoparticle after photoexcitation.^{2,4-8} This is advantageous for photocatalysis since it increases the exciton radiative lifetime, thereby kinetically favoring the redox reactions at the surface. The design of the HNC is crucial, as this determines the accessibility of the photogenerated charge carriers at the particle surface. For photocatalysis, where charge carriers are used in redox reaction taking place at the surface of the particle, morphologies such as heteronanorods or dumbbell nanorods are most suitable. In these morphologies both materials of the HNC comprise part of the surface of the particle, making both photogenerated carriers accessible. Concentric core-shell HNCs are less suitable, as in these morphologies (one of) the charge carriers formed upon photoexcitation can be confined to the core of the HNC.⁸⁻¹⁰ Several type-II HNCs, including CdSe-CdS dot-in-rod HNCs,¹¹⁻¹³ ZnSe-CdS dot-in-rod HNCs,¹⁴ ZnSe-CdS-ZnSe dumbbell nanorods¹⁵ and double heterojunction nanorods based on CdSe-CdS-ZnS¹⁶ have been shown to exhibit improved charge carrier separation. However, the majority of HNCs studied is based on cadmium, and hence alternative compositions that are more environmentally benign are needed.

As discussed in Chapter 1, Cu_{2-x}S is an attractive candidate for applications due its relatively low costs and low toxicity, especially when compared to cadmium-based alternatives. In addition, the favorable bandgap of Cu_{2-x}S , ranging from 1.2 eV for Cu_2S to 1.9 eV for CuS , makes it an interesting material for photovoltaic and photocatalytic applications. HNCs based on Cu_{2-x}S have already been synthesized with different compositions, such as $\text{Cu}_{2-x}\text{S-ZnS}$,¹⁷⁻²⁰ $\text{Cu}_{2-x}\text{S-MnS}$,²¹ $\text{Cu}_{2-x}\text{S-CdS}$,²² $\text{Cu}_{2-x}\text{S-PbS}$,²³ $\text{Cu}_{2-x}\text{S-In}_2\text{S}_3$,^{24,25} and $\text{Cu}_{2-x}\text{S/CuInS}_2$.²⁶⁻³⁴ Ternary CuInS_2 is an attractive second component for Cu_{2-x}S -based HNCs due to its similar crystal structure, and bulk band offsets that can lead to type-I^{1/2} charge carrier localization in HNCs (Figure 3.1b).³⁵⁻³⁷ Additionally, Cu_{2-x}S is a p-type semiconductor, while CuInS_2 is often n-type doped due to native defects.³⁸⁻⁴¹ Hence, an inter-particle heterojunction can be formed between the two materials that can improve the dissociation of the exciton and the spatial separation of the photogenerated electron and hole.⁵⁻⁷

$\text{Cu}_{2-x}\text{S/CuInS}_2$ HNCs were first unintentionally obtained as intermediates in the formation of CuInS_2 nanocrystals, which was found to proceed in multiple steps.²⁶⁻²⁸ First, Cu_{2-x}S nanocrystals nucleated, followed by the formation of rod-shaped $\text{Cu}_{2-x}\text{S/CuInS}_2$ HNCs and finally the conversion of the HNCs to pure CuInS_2 nanorods. Subsequent studies focused on the intentional synthesis of $\text{Cu}_{2-x}\text{S/CuInS}_2$ HNCs.^{29,31,32,34} To obtain the desired spatial separation of the photogenerated electrons and holes, strict control over the size, shape, hetero-architecture and hetero-interface of the $\text{Cu}_{2-x}\text{S/CuInS}_2$ HNCs is needed. Hence, the synthesis methods used are important.

Most of the studies on $\text{Cu}_{2-x}\text{S/CuInS}_2$ HNCs involve a one-pot synthesis approach, where all precursors were added in one reaction flask and subsequently heated to react and form the HNCs.^{26,28,29,31,32,34} An one-pot approach is appealing due to its simplicity, but the balance between the precursor reactivities is challenging, offering limited control over the reaction kinetics. The difference in reactivity of the cations forming the two parts of the HNCs is crucial as it must allow for separation between two stages in the synthesis: (1) the formation of Cu_{2-x}S , (2) the subsequent heteroepitaxial growth of CuInS_2 on the Cu_{2-x}S seed nanocrystals to form HNCs. To simplify this delicate reactivity balance, Kruszynska *et al.*, reported a one-pot, two-step synthesis, in which the sulfur-precursors were injected into a pre-heated mixture of the copper and indium precursors.²⁷ However, the control offered by this method over the size, shape, and composition of the intermediate $\text{Cu}_{2-x}\text{S/CuInS}_2$ HNCs is limited by the fact that the first step (*i.e.*, nucleation of Cu_{2-x}S nanocrystals) takes place under strongly changing physical-chemical conditions.

To truly separate the two steps in the formation of the HNCs, thereby further improving the control over the HNC size, shape and composition, we investigated the use of a two-step seeded-growth approach, similar to a method reported by Xia *et al.*, to synthesize $\text{CuInS}_2\text{-ZnS}$ dot-in-rod HNCs.⁴² We separated the two stages of the synthesis: first, the

Cu_{2-x}S seed nanocrystals were synthesized, and only in the second step they were mixed with indium and sulfur precursors to form $\text{Cu}_{2-x}\text{S}/\text{CuInS}_2$. The stability of Cu_{2-x}S seed nanocrystals at elevated temperature is low, especially in the presence of commonly used surfactants such as oleic acid.^{43,44} Therefore, the exposure of the Cu_{2-x}S seeds to high temperature prior to the HNC growth was minimized by injecting the pre-formed Cu_{2-x}S seed nanocrystals into a pre-heated indium-oleate mixture. Using this method, $\text{Cu}_{2-x}\text{S}/\text{CuInS}_2$ HNCs were obtained with a highly tunable size, shape and composition.

3.2 Experimental methods

3.2.1 Materials

Indium nitrate hydrate ($\text{In}(\text{NO}_3)_3 \cdot x \text{H}_2\text{O}$, 99.9%), Copper(I) acetate (CuOAc , 97%), Copper acetylacetonate ($\text{Cu}(\text{acac})_2$, 97%), 1-dodecanethiol (DDT, $\geq 98\%$), oleic acid (OA, 90%), oleylamine (OLAM, technical grade, 70%), anhydrous toluene, methanol, butanol and ethanol were purchased from Sigma-Aldrich and used as received.

3.2.2 Direct synthesis of $\text{Cu}_{2-x}\text{S}/\text{CuInS}_2$ HNCs

For comparison, $\text{Cu}_{2-x}\text{S}/\text{CuInS}_2$ HNCs were also prepared without using pre-formed Cu_{2-x}S seed nanocrystals. This method is referred to as direct synthesis (Figure 3.2a). First, 60.1 mg (0.20 mmol) $\text{In}(\text{NO}_3)_3 \cdot x \text{H}_2\text{O}$ was mixed with 4 mL (12.7 mmol) OA and degassed for 30 minutes at 120 °C. The $\text{In}(\text{NO}_3)_3$ -OA mixture was then heated to 240 °C under nitrogen protection. At 240 °C, a solution of 0.025 g (0.20 mmol) $\text{Cu}(\text{I})$ acetate in 5 mL DDT was rapidly injected and allowed to react for varying growth times to obtain $\text{Cu}_{2-x}\text{S}/\text{CuInS}_2$ HNCs of various sizes and shapes. The reaction mixture was quenched with toluene and washed with an excess of ethanol followed by centrifugation at 2750 rpm for 10 minutes. The $\text{Cu}_{2-x}\text{S}/\text{CuInS}_2$ HNCs were redispersed in toluene and stored in a glovebox.

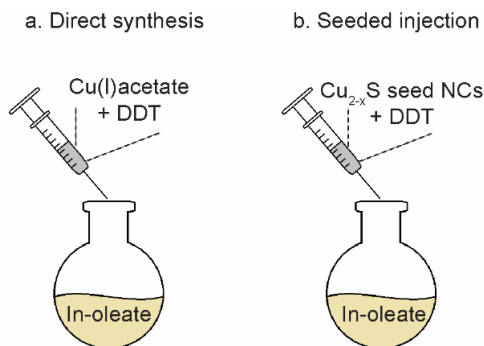


Figure 3.2 Schematic illustration of the synthesis methods. All experimental conditions are the same unless specified otherwise. **a)** In the direct synthesis, no pre-formed Cu_{2-x}S seed nanocrystals are used. This method was used as control experiment. **b)** To separate the two phases of HNC growth, a seeded-injection using pre-formed Cu_{2-x}S seed nanocrystals was investigated.

3.2.3 Seeded-injection synthesis of $\text{Cu}_{2-x}\text{S}/\text{CuInS}_2$ HNCs

In the seeded-injection synthesis, pre-formed Cu_{2-x}S seed nanocrystals were injected into a mixture of In-oleate (Figure 3.2b). First, Cu_{2-x}S seed nanocrystals were synthesized according to a method described by Tang *et al.*,⁴⁵ 0.79 g (3 mmol) $\text{Cu}(\text{acac})_2$, 15 mL OLAM and 15 mL DDT were mixed and gradually heated to 200 °C under N_2 protection using a Schlenk line. Subsequently, the mixture was kept at 200 °C for 2 hours. After that, the reaction mixture was naturally cooled down to room temperature. The mixture was washed three times by addition of an excess of methanol and butanol (1:1 ratio), followed by centrifugation at 2750 rpm for 10 minutes. The yielded nanocrystals were redispersed in 12 mL anhydrous toluene to form the Cu_{2-x}S seed nanocrystal stock solution.

Subsequently, 1 mL of the Cu_{2-x}S seed nanocrystal stock solution was precipitated using an excess of isometric methanol and butanol, followed by centrifugation at 2750 rpm for 10 minutes. The nanocrystals were redispersed in 5 mL DDT. 60.1 mg (0.20 mmol) $\text{In}(\text{NO}_3)_3 \cdot x \text{H}_2\text{O}$ was mixed with 4 mL OA and degassed for 30 minutes at 120 °C. The $\text{In}(\text{NO}_3)_3$ -oleic acid mixture was then heated to 240 °C under nitrogen protection in a Schlenk line. At 240 °C, the as-prepared Cu_{2-x}S seed nanocrystal solution was rapidly injected and allowed to react for varying growth times to obtain $\text{Cu}_{2-x}\text{S}/\text{CuInS}_2$ HNCs of various sizes and shapes. The reaction mixture was quenched with toluene and washed with an excess of ethanol and centrifugation. The $\text{Cu}_{2-x}\text{S}/\text{CuInS}_2$ HNCs were redispersed in toluene and stored in a glovebox.

3.2.4 Characterization

Samples for transmission electron microscopy (TEM) analysis were prepared by drop-casting the $\text{Cu}_{2-x}\text{S}/\text{CuInS}_2$ HNCs solution in toluene on carbon-coated 200 mesh copper TEM grids. TEM analysis was performed using a FEI-Technai 12 microscope operating at 100 kV or a FEI Technai 20 microscope operating at 200 kV. High resolution (HR)-TEM images and elemental maps were recorded using a FEI Talos F200x transmission electron microscope, operated at 200kV. Samples were prepared by dropcasting the nanocrystal solution in toluene on carbon coated aluminum grids.

Samples for x-ray diffraction (XRD) analysis were prepared by precipitating the Cu_{2-x}S or $\text{Cu}_{2-x}\text{S}/\text{CuInS}_2$ nanocrystals with an excess of methanol and butanol (1:1 ratio) followed by centrifugation for 10 minutes at 2750 rpm. The precipitate was then dried under vacuum. Subsequently the nanocrystal powder was spread over a Si wafer. XRD measurements at room temperature were performed with a Bruker D2 Phaser, equipped with a $\text{Co K}\alpha$ x-ray source with a wavelength of 1.79026 Å. The high temperature measurements were performed using a Bruker D8, equipped with a $\text{Co K}\alpha$ x-ray source with a wavelength of 1.79026 Å. These measurements were performed under an Argon flow at temperatures of 28, 50, 75, 90, 100, 110, 150, 200, 225, 240, 250 °C and after cooling down to room temperature. A heating ramp of 5 minutes was used.

3.3 Results and discussion

3.3.1 $\text{Cu}_{2-x}\text{S}/\text{CuInS}_2$ HNCs prepared by direct synthesis

$\text{Cu}_{2-x}\text{S}/\text{CuInS}_2$ HNCs had been previously obtained as intermediates in the synthesis of CuInS_2 NCs.^{26,27,32,33,46} In these methods, the HNCs were obtained directly from copper, indium and sulfur precursors and no pre-formed Cu_{2-x}S seed nanocrystals were used. In order to compare our seeded growth approach to these previously reported direct syntheses, we performed a direct synthesis, in which a mixture of Cu(I) acetate in DDT was injected into a pre-heated mixture of indium-oleate. Figure 3.3 shows the HNCs synthesized by direct synthesis with reaction times of 2, 3, 5, 10, 30 and 90 minutes. At short reaction times (2 minutes), Cu_{2-x}S nanocrystals formed first due to easier nucleation of the binary Cu_{2-x}S in comparison to ternary CuInS_2 . After 3-5 minutes of reaction time, the interparticle contrast observed in the TEM images indicates that HNCs are formed. With longer growth times (10-30 minutes), bottle-like nanocrystals are obtained, with a short Cu_{2-x}S part and an elongated CuInS_2 part. Eventually (reaction times > 60 minutes), the sharp interparticle contrast difference in TEM imaging is no longer observed, indicating a homogeneous CuInS_2 composition for the nanocrystals (Figure 3.3f). The complete conversion of the HNCs to CuInS_2 is in agreement with

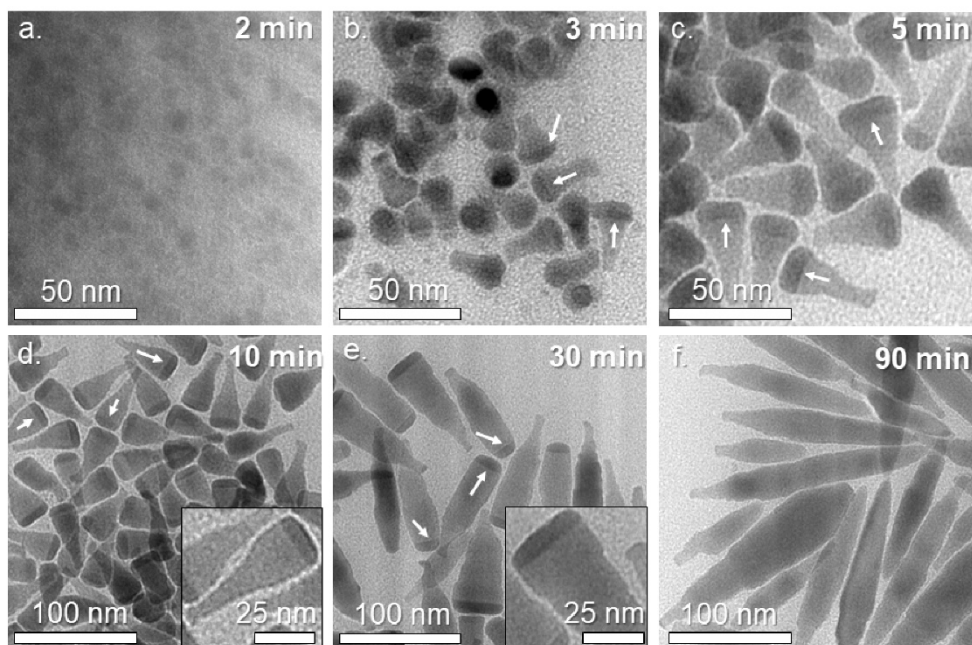


Figure 3.3 TEM images of $\text{Cu}_{2-x}\text{S}/\text{CuInS}_2$ HNCs prepared via direct synthesis without pre-formed seeds at 240 °C and with a reaction time of **a)** 2 minutes, **b)** 3 minutes, **c)** 5 minutes, **d)** 10 minutes, **e)** 30 minutes and **f)** 90 minutes. The images show that HNCs with irregular shapes can be formed by a direct synthesis. The white arrows indicate some of the heterointerfaces formed.

previous observations.^{26–28,32,34,46} The shape of the nanocrystals is irregular, suggesting a fast growth process under changing conditions. Consequently, the particle size and shape are rather polydisperse. To better control the heteroepitaxial growth of CuInS₂, thereby improving the quality of the Cu_{2-x}S/CuInS₂ heterointerface and the size and shape dispersion of the HNCs, we adapted the direct synthesis to a seeded-injection protocol. To this end, Cu_{2-x}S seed nanocrystals were prepared first.

3.3.2 Synthesis and structural characterization of the Cu_{2-x}S seed nanocrystals

Figure 3.4a shows a HR-TEM image of Cu_{2-x}S seed nanocrystals synthesized by a heating-up synthesis. The seed nanocrystals are shaped as platelets and have a diameter of 24.1 ± 1.2 nm and a thickness of 17.4 ± 0.9 nm. The crystal structure of the Cu_{2-x}S seeds was analyzed in detail using HR-TEM, indicating a monoclinic low-chalcocite structure. For bulk Cu_{2-x}S, it is known that the low-chalcocite structure undergoes a phase transformation into high-chalcocite at sufficiently high temperature.^{47–49} Whereas the high-chalcocite phase has a hexagonal close packing of sulfur ions very similar to the low-chalcocite phase, the structures differ from each other by the distribution of the Cu atoms. Low-chalcocite has a large unit cell with 96 molecule units, with each Cu atom in a unique site, whereas high-chalcocite has a hexagonal unit cell with only 2 molecule units, where the copper atoms randomly adopt a few possible high symmetry sites.⁴⁸ During the seeded injection procedure, the Cu_{2-x}S seed nanocrystals are injected into a hot indium-oleate solution at 240 °C and hence it is plausible that the monoclinic low-chalcocite phase transforms into a high-chalcocite phase. Therefore, the crystal structure

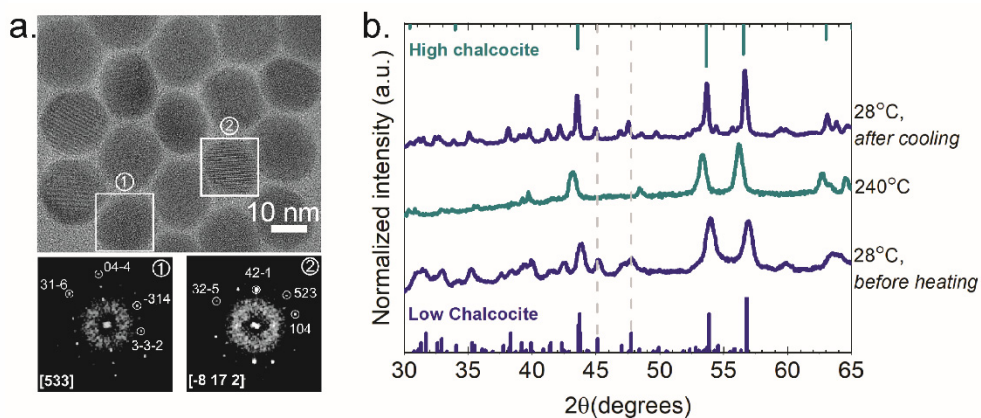


Figure 3.4 a) HRTEM images of Cu_{2-x}S seed nanocrystals. The panels 1 and 2 are the Fourier transform (FT) patterns of Cu_{2-x}S nanocrystals marked by white squares, which are indexed to monoclinic low chalcocite Cu_{2-x}S viewed along [533] and [-8 17 2] axis, respectively. The scale bar is 10 nm. **b)** XRD patterns of the Cu_{2-x}S nanocrystals at 28 °C before heating, at 240 °C and at after cooling back down to 28 °C. The diffraction patterns of low- and high-chalcocite are very similar, but can be distinguished by the additional diffractions observed for low-chalcocite at 2 θ values of e.g., 45° and 48° (dashed, grey lines).

of the Cu_{2-x}S seed nanocrystals was studied with XRD as function of temperature. Figure 3.4b shows the diffractograms of the Cu_{2-x}S seeds at a temperature of 28 °C, 240 °C and after cooling down to 28 °C. The diffractograms show that at 28 °C, the Cu_{2-x}S seed nanocrystals have the monoclinic low-chalcocite phase (PDF Card - 00-033-0490),⁵⁰ confirming the crystal structure found by HR-TEM analysis. At 240 °C, the diffractogram of the Cu_{2-x}S seed nanocrystals matches the reference pattern of high-chalcocite (PDF Card - 00-046-1195),⁵⁰ showing that the phase transition to the high-chalcocite indeed occurs. After cooling down to 28 °C, the diffractograms again confirm the presence of low-chalcocite, indicating the phase transition between low- and high chalcocite is reversible. This implies that the Cu_{2-x}S seed nanocrystals will likely change to the high-chalcocite crystal structure upon injection into the hot reaction mixture, and change back to the low-chalcocite phase when cooling down after the reaction is finished, even though the conditions in the reaction flask are different from those during the XRD measurements (*i.e.*, nanocrystals dispersed in a coordinating solvent instead of a dry powder).

3.3.3 $\text{Cu}_{2-x}\text{S}/\text{CuInS}_2$ heteronanocrystals prepared by seeded-injection

In the seeded-injection approach, the Cu_{2-x}S seed nanocrystals discussed above were injected in a hot solution of In-oleate to prepare $\text{Cu}_{2-x}\text{S}/\text{CuInS}_2$ HNCs. First, the influence of the reaction temperature on the growth of the HNCs was investigated by performing the seeded-injection synthesis at 200 °C, 240 °C and 260 °C and allowing the samples to react for 30 minutes (Figure 3.5). At a reaction temperature of 200 °C, small tear-shaped nanocrystals without any apparent interparticle contrast were obtained. In the TEM image of the sample synthesized at 240 °C, elongated nanocrystals with a contrast difference within the particles were observed (Figure 3.5b). This interparticle contrast difference suggests that the nanocrystals obtained at this temperature are heterostructured. Higher temperatures (Figure 3.5c) yield longer and thinner nanorods without any apparent contrast differences. This suggests that the nanocrystals consist of CuInS_2 only, indicating much faster reaction kinetics. Therefore, 240 °C was chosen as the

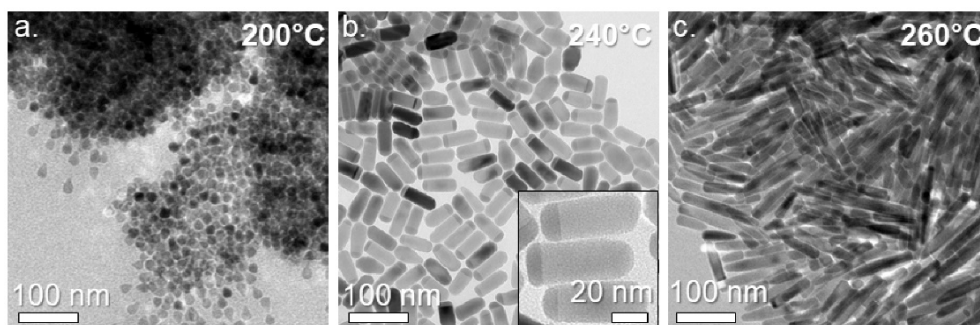


Figure 3.5 TEM images for nanoparticles prepared via the seeded-injection approach with a reaction time of 30 minutes and a reaction temperature of **a)** 200 °C, **b)** 240 °C and **c)** 260 °C.

reaction temperature for subsequent experiments since it leads to the formation of HNCs at a rate that is sufficiently slow to allow it to be followed in detail. By varying the reaction time at a temperature of 240 °C, heterostructures with different sizes, shapes and compositions could be formed. Detailed investigation of the $\text{Cu}_{2-x}\text{S}/\text{CuInS}_2$ HNCs formed with different reaction times indicated that the formation of the HNCs can be divided into different stages, which are discussed in more detail in the next sections.

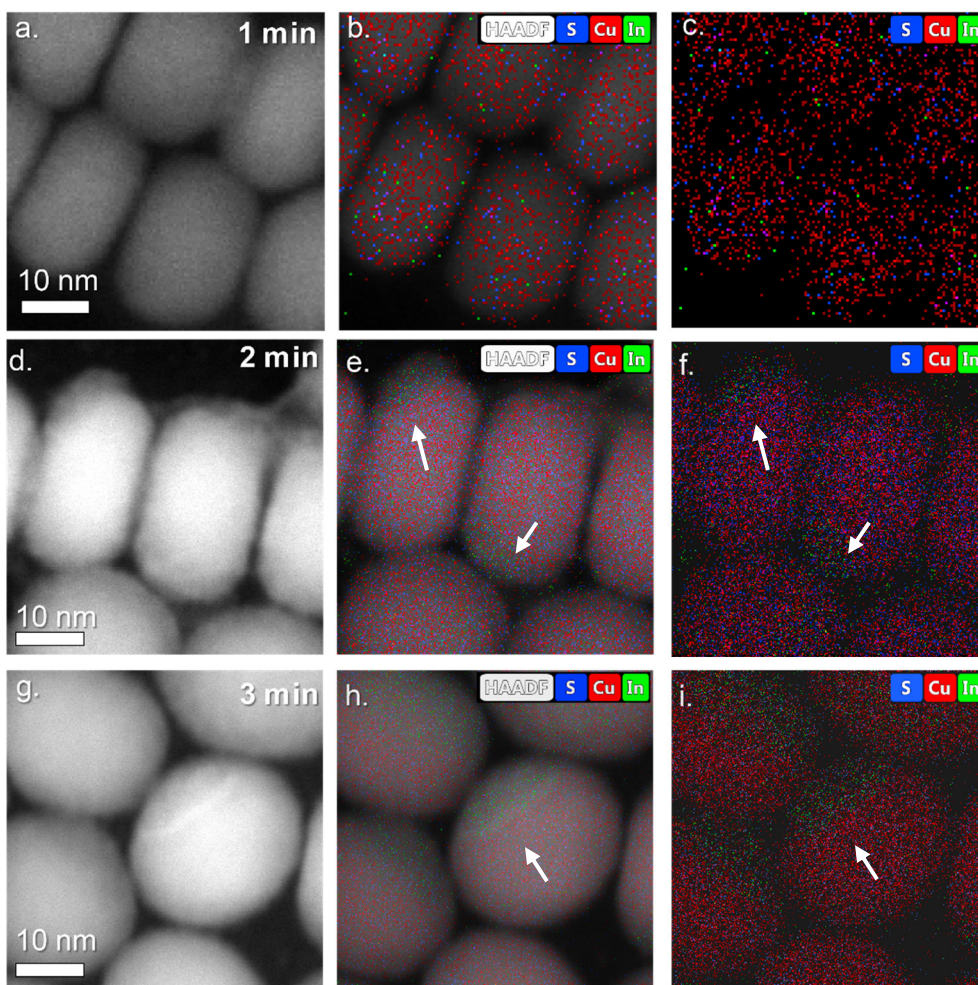


Figure 3.6 HAADF-STEM images and corresponding elemental maps of the $\text{Cu}_{2-x}\text{S}/\text{CuInS}_2$ HNCs formed by the injection of Cu_{2-x}S seed nanocrystals into a hot solution of indium-oleate. Samples after a reaction time of (a-c) 1 minute, (d-f) 2 minutes and (g-i) 3 minutes are shown. After 1 minute of reaction, no significant amount of indium was present in the nanocrystals, whereas after 2 and 3 minutes of reaction indium is clearly incorporated in the Cu_{2-x}S seed nanocrystals and heterointerfaces are formed, as indicated by the white arrows.

Figure 3.6 shows HAADF-STEM images and corresponding elemental maps of samples collected during the first 3 minutes of reaction after the injection of the Cu_{2-x}S seed nanocrystals. After 1 minute of reaction, the size and shape of the nanocrystals are very similar to those of the Cu_{2-x}S seed nanocrystals and no indium is observed in the particles or background of the image. After 2 minutes of reaction, the particle size and shape are still the same and almost all nanocrystals have an indium rich area (Figure 3.6d-f). After an additional minute of reaction, the indium rich area has clearly grown and a well-defined hetero-interface is visible. At the same time, the shape and size of the nanocrystals are not significantly changed. Figure 3.7 shows the length and diameter of the particles, obtained from TEM images, as a function of reaction time. This indeed shows that the length and diameter of the nanocrystals are not significantly changed during the first 3 minutes of reaction and are similar to that of the original Cu_{2-x}S seed nanocrystals.

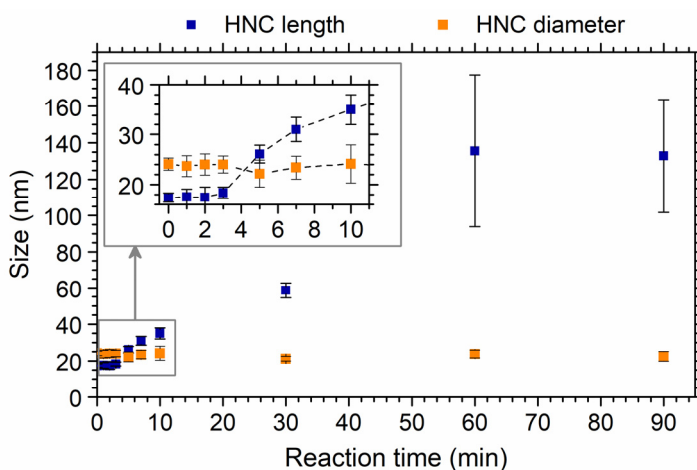


Figure 3.7 The average length and diameter of the HNCs obtained by varying the reaction time of the seeded injection synthesis. During the first 3 minutes of reaction, the length of the HNCs remains similar to that of the Cu_{2-x}S seed nanocrystals (shown at time= 0 min), while after 5 minutes the HNC length starts to increase. The HNC diameter shows no large variation with reaction time.

The incorporation of indium into the nanocrystals during the first 3 minutes of reaction, combined with the finding that the size and shape of the nanocrystals constant during this time, suggests that the first stage of the formation of $\text{Cu}_{2-x}\text{S}/\text{CuInS}_2$ HNCs occurs via a topotactic cation-exchange, rather than heteroepitaxial growth of CuInS_2 on the Cu_{2-x}S seed nanocrystals. During this cation-exchange In^{3+} ions diffuse into the nanocrystals and Cu^+ ions diffuse out of the nanocrystals into solution, while the size and shape of the Cu_{2-x}S seed nanocrystals are preserved. The Cu^+ extracted from the nanocrystals via this cation-exchange reaction in turn serves as Cu^+ source in later growth stages, as is discussed below. A similar observation was done by Zhou *et al.*, who attributed the initial formation of $\text{Cu}_{1.94}\text{S}-\text{MnS}$ HNCs to cation-exchange.²¹

With further extension of the reaction time, larger heterostructures were formed. Figure 3.8 shows TEM images of samples obtained after reaction times of 3, 5, 10, 30, 60 and 90 minutes. As can be seen from Figure 3.8, the size and shape of the nanocrystals start to change 5 minutes after injection of the Cu_{2-x}S seed nanocrystals, with the formation of acorn shaped nanocrystals and subsequently elongated rods with a clear interparticle contrast. While the length of the HNCs clearly increases with increasing reaction time, the diameter of the particles remains more or less the same (Figure 3.7). The evolution in size and shape of the nanocrystals shows that after 5 minutes a growth process is occurring, rather than cation exchange. In the final phase of the reaction, at reaction times >60 minutes, the sharp hetero-interface is no longer observed, indicating that the nanocrystals have a uniform composition. Furthermore, the size and shape of the particles do not significantly change upon increasing the reaction time from 60 to 90 minutes (Figure 3.7).

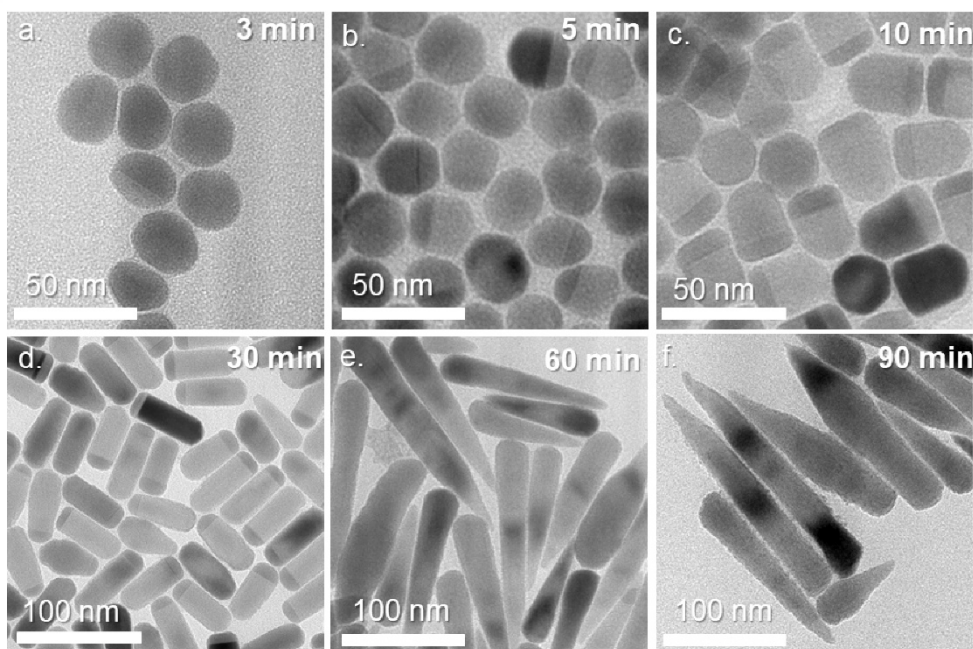


Figure 3.8 TEM images of $\text{Cu}_{2-x}\text{S}/\text{CuInS}_2$ HNCs formed by the injection of Cu_{2-x}S seed nanocrystals into a hot solution of indium-oleate and with a reaction time of **a)** 3 minutes, **b)** 5 minutes, **c)** 10 minutes, **d)** 30 minutes, **e)** 60 minutes and **f)** 90 minutes. The images show that after a reaction time of 3 minutes, the size of the HNCs clearly increases.

To investigate the origin of the contrast observed in the TEM images, elemental maps were obtained using STEM-EDX. Figure 3.9a-d show the elemental maps of the sample collected after a growth time of 10 minutes, which consists of acorn-shaped HNCs. The elemental maps of Cu, In, S and the combination map of Cu, In and S show that the tips of the particles contain no indium, whereas copper and sulfur are present in the whole nanocrystal. Sulfur is uniformly distributed over the whole particle and, as expected from

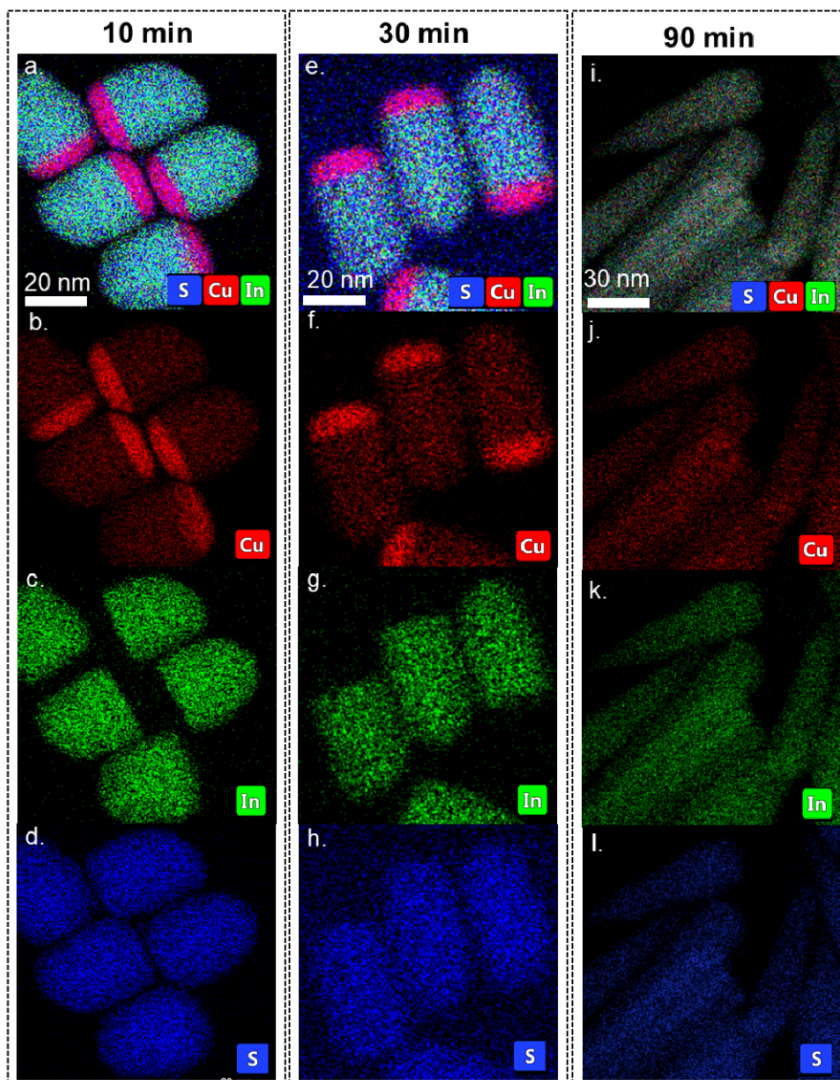


Figure 3.9 Elemental maps obtained by STEM-EDX of $\text{Cu}_{2-x}\text{S}/\text{CuInS}_2$ HNCs formed by the injection of Cu_{2-x}S seed nanocrystals into a hot solution of indium-oleate at 240°C and with a reaction time of (a-d) 10 minutes, (e-h) 30 minutes and (i-l) 90 minutes. The samples obtained with a reaction time of 10 and 30 minutes clearly show the Cu_{2-x}S and CuInS_2 segments. After 90 minutes of reaction, the HNCs are completely converted into CuInS_2 .

the copper to sulfur ratio of Cu_2S and CuInS_2 , copper is most abundant in the indium-poor tips. The HNCs thus consist of a short Cu_{2-x}S tip, with an elongated CuInS_2 segment. The elemental maps of the sample with a growth time of 30 minutes are shown in Figure 3.9d-f. Again, no indium is present in the tip of the structure, whereas copper and sulfur are present in the whole particle, confirming the formation of $\text{Cu}_{2-x}\text{S}/\text{CuInS}_2$ HNCs with a short Cu_{2-x}S tip and an elongated CuInS_2 segment. Interestingly, the volume of the CuInS_2 segment significantly increases from 10 to 30 minutes (Figure 3.8c,d and Figure 3.9a-h), while that of the Cu_{2-x}S tip remains essentially constant. Figure 3.9i-l show the elemental maps of the sample obtained after a reaction time of 90 minutes, and verify the full conversion of the HNCs into CuInS_2 in the final phase of reaction.

From the elemental maps obtained by STEM-EDX we obtained the chemical composition for the HNCs. Table 3.1 shows the elemental composition of two parts of the HNCs, namely the Cu_{2-x}S tip and the CuInS_2 segment, for the HNCs grown for 10 minutes and 30 minutes. After a reaction time of 10 minutes, the Cu_{2-x}S tip is composed of $\text{Cu}_{1.77}\text{S}$ with a negligible amount of indium, whereas after a reaction time of 30 minutes, the Cu_{2-x}S tip has a composition of $\text{Cu}_{0.99}\text{S}$. This implies that Cu^+ ions are extracted from the Cu_{2-x}S tip with increasing reaction time. The CuInS_2 segment has a stoichiometric composition of CuInS_2 after a reaction time of 10 minutes, and is slightly sulfur rich after a reaction time of 30 minutes. This can be explained by some additional sulfur originating from 1-dodecanethiol, that can be present on the particle surface as coordinating ligand.

Table 3.1 Atomic weight % of Cu, In and S in $\text{Cu}_{2-x}\text{S}/\text{CuInS}_2$ HNCs, formed by the injection of Cu_{2-x}S seed nanocrystals into a hot solution of indium-oleate at 240 °C and with a reaction time of 10 and 30 minutes. Corresponding atomic ratios are also shown. The data is obtained by quantitative analysis of the elemental maps in Figure 3.9a,e.

Reaction time	Element	Cu_{2-x}S Tip		CuInS_2 segment	
		Composition (at. %)	Ratio	Composition (at. %)	Ratio
10 minutes	Cu	63.6	1.77	24.2	0.98
	In	0.6	0.02	26.0	1.04
	S	35.8	1.00	49.8	2.00
30 minutes	Cu	49.0	0.99	18.8	0.63
	In	1.4	0.02	21.6	0.72
	S	49.6	1.00	59.6	2.00

The HNCs obtained after a reaction time of 10 and 30 minutes were further analyzed by the HR-TEM (Figure 3.10a). For both samples, the Cu_{2-x}S tips show a low chalcocite structure, whereas the elemental analysis indicated a copper to sulfur ratio consistent with covellite (CuS). The CuInS_2 part in the heterostructures can be identified as wurtzite CuInS_2 for both samples. The wurtzite CuInS_2 structure is a hexagonal structure with an hcp anionic sublattice. The growth of wurtzite CuInS_2 on the hexagonal chalcocite structure of the Cu_{2-x}S seed nanocrystals is favored since it requires little restructuring of the hexagonal sulfide lattice.⁵¹ Inset 1 in Figure 3.10a shows the Cu_{2-x}S part (red square) and CuInS_2 part (blue square) of a single $\text{Cu}_{2-x}\text{S}/\text{CuInS}_2$ HNC. The FT pattern of the Cu_{2-x}S part is consistent with [113] zone axis of the monoclinic low chalcocite Cu_2S while that of CuInS_2 part agrees well with the [010] zone axis of the wurtzite CuInS_2 . Inset 2 in Figure 3.10a shows the $\text{Cu}_{2-x}\text{S}/\text{CuInS}_2$ HNC projected along the [001] direction. The FT analysis suggests that CuInS_2 grows on either the top or bottom faces of the Cu_{2-x}S disks and develop along the [001] direction. Figure 3.10b shows the XRD patterns of the particles obtained after a reaction time of 30 minutes, confirming that the CuInS_2 parts of the nanocrystals have the hexagonal wurtzite CuInS_2 phase. Due to the small volume of the Cu_{2-x}S tips, no diffractions originating from the Cu_{2-x}S could be distinguished.

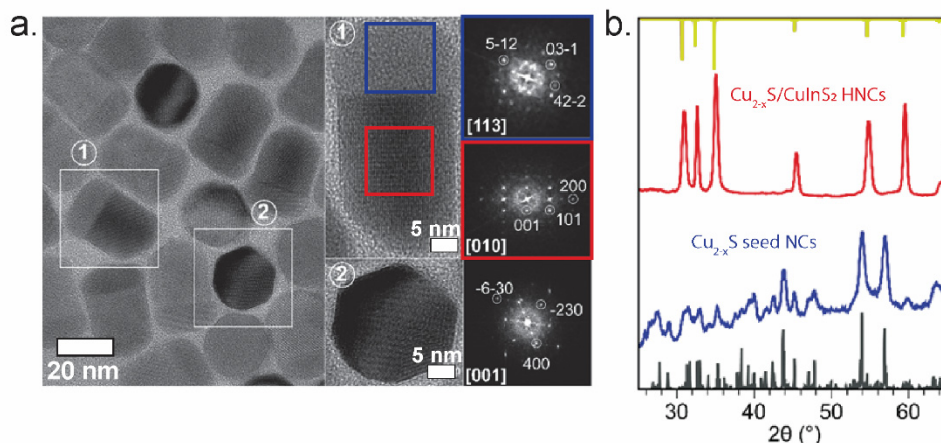


Figure 3.10 a) HRTEM image of $\text{Cu}_{2-x}\text{S}/\text{CuInS}_2$ HNCs. Panels 1 and 2 show the FT analyses of $\text{Cu}_{2-x}\text{S}/\text{CuInS}_2$ HNCs indicated with white squares 1 and 2, respectively. The FT patterns of panel 1 contain the Cu_{2-x}S part (red square) and CuInS_2 part (blue square) in a single $\text{Cu}_{2-x}\text{S}/\text{CuInS}_2$ HNC. Panel 2 is the $\text{Cu}_{2-x}\text{S}/\text{CuInS}_2$ HNC projected along the [001] direction. b) XRD pattern of the product $\text{Cu}_{2-x}\text{S}/\text{CuInS}_2$ HNCs (red line), which is in agreement with the standard XRD pattern of hexagonal wurtzite CuInS_2 (dark yellow line, top-axis). The XRD pattern of the Cu_{2-x}S seed nanocrystals (blue line) is shown for comparison and matches well with the standard XRD pattern of low chalcocite (black line, bottom axis).

3.3.4 The influence of the addition of extra Cu-precursors

In the seeded injection, the Cu_{2-x}S seed nanocrystals are the only source of copper in the reaction mixture. Therefore, the copper that is needed to grow the CuInS_2 part of the HNCs originates from the Cu_{2-x}S seed nanocrystals. We investigated whether the addition of extra copper ions can help preserve the Cu_{2-x}S tip and prevent formation of nanocrystals with a single CuInS_2 phase. In order to do so, the influence of different Cu-precursors, added to the reaction mixture in different concentrations, was investigated.

First, Cu(I)-acetate was added to the Cu_{2-x}S seed nanocrystals in DDT in different ratios. Figure 3.11a-d show the TEM images of $\text{Cu}_{2-x}\text{S}/\text{CuInS}_2$ HNCs synthesized at 240 °C with a reaction time of 30 minutes with Cu(I)acetate added in the Cu:In ratios 0:1, 0.5:1, 1:1 and 2:1. The addition of extra Cu(I) ions clearly influences the growth of the HNCs. In the presence of Cu(I)acetate in solution, the resulting HNCs are shorter and have a smaller CuInS_2 part, while the Cu_{2-x}S tips are more pronounced. However, as can be seen in Figure 3.11d, when the ratio 2:1 is used, separate, spherical nanocrystals are observed. These spherical nanocrystals are likely Cu_{2-x}S , due to the easy nucleation of the binary Cu_{2-x}S . This indicates that a too high Cu concentration leads to the secondary nucleation of Cu_{2-x}S nanocrystals.

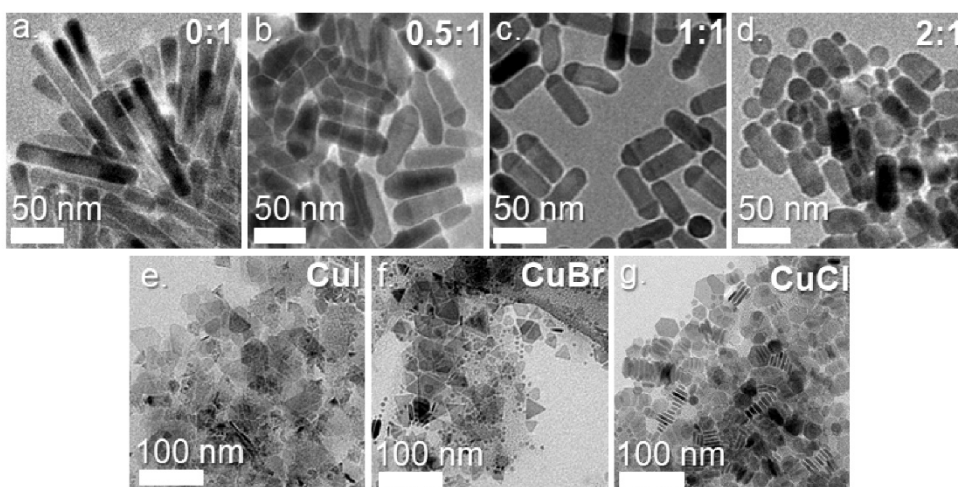


Figure 3.11 (a-d) TEM images of $\text{Cu}_{2-x}\text{S}/\text{CuInS}_2$ HNCs synthesized the injection of Cu_{2-x}S seed nanocrystals into a hot solution of indium-oleate at 240°C with a reaction time of 30 minutes and the addition of extra Cu(I)acetate with a Cu:In ratio of **a)** 0:1 **b)** 0.5:1 **c)** 1:1 and **d)** 2:1. The images show that the addition of extra Cu(I)acetate clearly influences the growth of the HNCs. **(e-g)** TEM images showing the formation of nanosheets by the addition of **e)** CuI, **f)** CuBr and **g)** CuCl to the seeded-injection at 240 °C and a reaction time of 30 minutes.

The addition of Cu-halides, such as CuI, CuBr and CuCl, was also investigated and resulted in the formation of nanosheets (Figure 3.11f-g). The formation of Cu_{2-x}S nanosheets by the addition of halides in the presence of Cu^+ and DDT was previously demonstrated by van der Stam *et al.*,⁵² Similarly, the formation of 2D sheets in the present case is attributed to interaction between the halide ions and the Cu^+ in the Cu-thiolate precursor, causing 2D constraints on the C-S thermolysis.

3.3.5 Formation mechanism

The injection of Cu_{2-x}S seed nanocrystals in an In-oleate solution starts a series of coupled reactions that ultimately lead to the formation of $\text{Cu}_{2-x}\text{S}/\text{CuInS}_2$ HNCs. The outcome of this chain of coupled reactions depends on a delicate kinetic balance between all the elementary steps involved, which is in turn determined by the changing reaction conditions, such as the concentrations of the different precursors. Based on the observations discussed above, we propose a model for the formation of $\text{Cu}_{2-x}\text{S}/\text{CuInS}_2$ HNCs via seeded-injection, which is schematically represented in Figure 3.12 and discussed in detail below.

In the first step of the reaction, at a temperature of 240 °C, the as-prepared Cu_{2-x}S seed nanocrystals dispersed in DDT are quickly injected. This leads to formation of In-thiolate complexes due to the injection of a large excess of DDT (step I, Figure 3.12). As evidenced by the EDX maps (Figure 3.6a), one minute after the injection of the $\text{Cu}_{2-x}\text{S}/\text{DDT}$ mixture, no indium is yet incorporated in the Cu_{2-x}S seed nanocrystals. The formation of the HNCs is thus not directly initiated upon injecting the Cu_{2-x}S seed nanocrystals, suggesting that first In-oleate must be converted to In-DDT complexes by reacting with the injected DDT.

Two minutes after the injection of the Cu_{2-x}S seed nanocrystals, a small corner of CuInS_2 is visible in most Cu_{2-x}S seeds (Figure 3.6d-f), indicating the formation of HNCs (Step II, Figure 3.12). The size and shape of the particles is however not significantly changed (Figure 3.7), indicating that the formation of the heterostructures is initiated by a topotactic cation-exchange reaction, where In^{3+} is incorporated into the crystal and Cu^+ is extracted from the nanocrystals, while the size and shape of the nanocrystal is preserved. Cation exchange requires a delicate balance of all reaction steps, *e.g.*, cleavage of the bond between the incoming cation (In^{3+}) and the thiolate ligand, formation of an In-S bond, followed by In^{3+} diffusion into the nanocrystal, formation of a bond between the host-cation (Cu^+) and the thiolate ligand, and cleavage of a Cu-S bond, and the diffusion of the Cu-thiolate complex from the nanocrystal into solution, leaving a Cu^+ -vacancy that must be filled by Cu^+ diffusing to the surface to allow the reaction to proceed.⁵¹ Ultimately, the driving force for the cation-exchange reaction is determined by reactivities and stabilities of both the parent and product nanocrystals, as well as of the cation complexes in solution.⁵¹

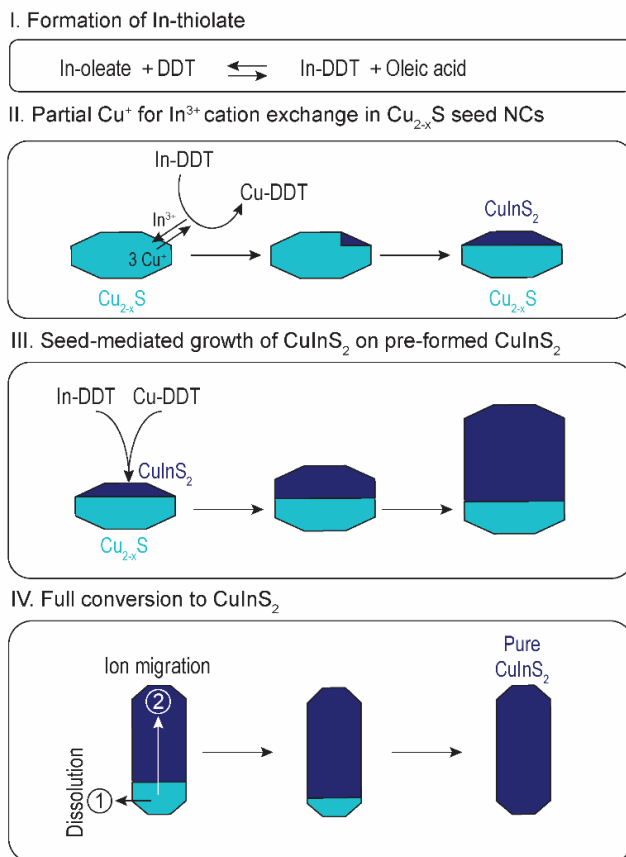


Figure 3.12 Schematic representation of the proposed formation mechanism for $\text{Cu}_{2-x}\text{S}/\text{CuInS}_2$ HNCs by injection of Cu_{2-x}S seed nanocrystals in a hot solution of In-oleate. In the 1st step, Cu_{2-x}S seed nanocrystals dispersed in DDT are injected, leading to the formation of In-thiolate complexes. Subsequently, the formation of the HNCs is initiated by single step, thiolate mediated Cu^+ for In^{3+} cation exchange (step II). The cation-exchange reaction is overtaken by the homoepitaxial growth of CuInS_2 on the pre-formed CuInS_2 surface (step III). Eventually the Cu_{2-x}S tips disappear and pure CuInS_2 nanocrystals are formed (step IV).

The delay prior to the start of the cation-exchange reaction can be explained by the requirement that first suitable precursors for the cation exchange reaction must be formed. Prior to the injection, indium is present as In-oleate, a stable complex of the hard Lewis acid In^{3+} ($\eta \sim 13 \text{ eV}$)⁵³ with the hard base oleate. In addition, Cu^+ is a soft Lewis acid ($\eta = 6.28 \text{ eV}$)⁵³ and hence oleate is not a suitable extracting ligand for Cu^+ , making the cation exchange unfavorable when only In-oleate is present. As discussed above, when the $\text{Cu}_{2-x}\text{S}/\text{DDT}$ mixture is injected, the large excess of DDT leads to the formation of In-thiolate complexes. According to the HSAB theory, In-thiolate is a less stable complex than In-oleate, while the formation of Cu(I)-thiolate is favored since thiolate is a soft Lewis base (absolute hardness thiolate $\eta \sim 6 \text{ eV}$)⁵⁴. This makes the

thiolate-mediated single step Cu^+ for In^{3+} exchange favorable, provided a sufficiently high concentration of In-thiolate is available.

Once one Cu^+ ion is exchanged for an In^{3+} ion, the valency of In (3+) will cause a charge imbalance in the nanocrystal, forcing two more Cu^+ ions out of the nanocrystal to balance the overall charge. This Cu^+ extraction leads to the formation of more Cu^+ vacancies in the nanocrystal, which in turn favors the diffusion of cations within the nanocrystal. The sufficiently high concentration of In-thiolate complexes will then lead to the incorporation of more In^{3+} , which in turn will force more Cu^+ ions to diffuse out of the nanocrystal, and so a cascade of reactions is started. This can also explain the observation that the cation-exchange always starts from one side of the nanocrystal: once the cation-exchange is initiated at a certain point, it is most likely to proceed here because of the cascade of reactions.^{55,56}

At longer reaction times (>5 minutes), the shape and size of the nanocrystals start to change, indicating that the reaction is no longer occurring via topotactic cation-exchange (Step III, Figure 3.12). Instead, the HNCs grow further via a seeded growth mechanism from Cu, In and S monomers in solution. The cation-exchange is thus terminated before the whole Cu_{2-x}S seed nanocrystal is converted into CuInS_2 . The heteroepitaxial growth of CuInS_2 directly on the Cu_{2-x}S seed nanocrystals is unfavorable due to the dynamic nature of the Cu_{2-x}S nanocrystal surface, in which the Cu^+ ions are very mobile.⁴⁸ The formation of a heteronanocrystal by cation-exchange in the 1st five minutes of reaction provides a stable CuInS_2 surface, onto which CuInS_2 can now readily grow from Cu, In and S precursors from solution through homoepitaxy. The homoepitaxial growth of CuInS_2 on this pre-formed CuInS_2 surface has a lower energy barrier than the cation-exchange. Therefore, the former outcompetes the latter for the limited supply of In-DDT complexes and the formation of the $\text{Cu}_{2-x}\text{S}/\text{CuInS}_2$ HNCs proceeds via seeded growth of CuInS_2 from precursors in solution.

As discussed above, the Cu_{2-x}S seed nanocrystals are the only source of Cu^+ ions for the formation of CuInS_2 . In the first phase of the reaction (cation-exchange), Cu^+ is extracted from the nanocrystals into solution, providing Cu^+ for the subsequent growth of CuInS_2 in the second phase. However, when looking at the volume of CuInS_2 segment after a reaction time of 30 minutes with respect to the volume of the original Cu_{2-x}S seed nanocrystals, the large increase in volume of the CuInS_2 in the HNCs suggests that, besides the Cu^+ in solution originating from the cation-exchange, additional Cu^+ must be present in solution. This additional Cu^+ likely originates from dissolution of part of the Cu_{2-x}S seed nanocrystals prior to the onset of the cation exchange and homoepitaxial growth phases. To verify if the Cu_{2-x}S seed nanocrystals are indeed susceptible to dissolution under these reaction conditions, a control experiment was performed in which the $\text{Cu}_{2-x}\text{S}/\text{DDT}$ mixture was injected into oleic acid at 240 °C. Figure 3.13 shows the TEM images of the Cu_{2-x}S seeds after 5 seconds, 1 minute and 5 minutes and

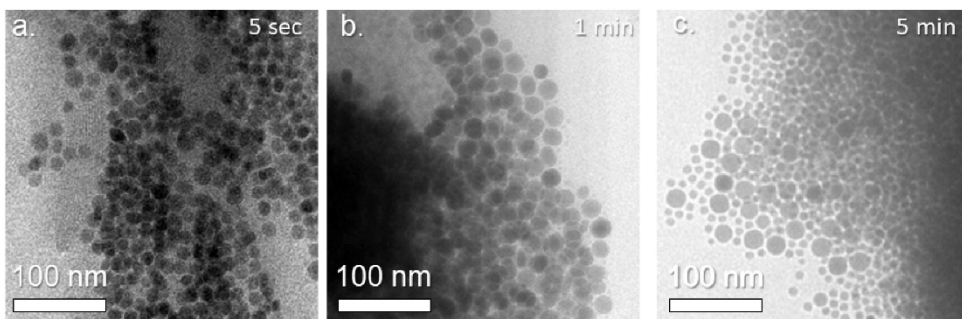


Figure 3.13 TEM figures of Cu_{2-x}S seed nanocrystals injected into oleic acid at 240°C after **a)** 5 seconds, **b)** 1 minute and **c)** 5 minutes.

indicates that the Cu_{2-x}S nanocrystals are indeed partially dissolved. Subsequently small Cu_{2-x}S particles are formed from the available Cu^+ and DDT in solution.

3

With even longer reaction times (>30 min), the Cu/S ratio in the Cu_{2-x}S tip of a single $\text{Cu}_{2-x}\text{S}/\text{CuInS}_2$ reduces from ~ 1.8 to ~ 1 (Table 3.1) and the volume of the Cu_{2-x}S part decreases and eventually disappears, forming CuInS_2 nanocrystals (Figure 3.9i-l). The reduction of Cu/S ratio indicates that Cu^+ ions for the growth of CuInS_2 originate not only from the dissolution of Cu_{2-x}S seed nanocrystals prior to the onset of the formation of CuInS_2 , but also from consumption of Cu_{2-x}S tips during the heteroepitaxial growth. The disappearance of Cu_{2-x}S tips and the formation of pure CuInS_2 nanocrystals can be explained by two possible pathways: (1) the depletion of Cu^+ ions by the growth of CuInS_2 leads to a low concentration of Cu^+ in solution, thereby eventually driving complete dissolution of the Cu_{2-x}S tips, which are then used to further grow the CuInS_2 ; (2) the Cu^+ ions in the Cu_{2-x}S lattice are highly mobile at high temperatures⁴⁹ and therefore migrate to the heterointerface to form CuInS_2 lattice. These pathways imply that the fate of the Cu_{2-x}S segment strongly depends on the available Cu^+ ions in the solution or in the Cu_{2-x}S seed nanocrystals.

Lastly, prolonged reaction times do not induce the conversion of CuInS_2 nanocrystals into In_2S_3 (Figure 3.9i-l), because the Cu^+ for In^{3+} cation exchange in Cu_{2-x}S nanocrystals is self-limited, as demonstrated in previous reports.^{51,54,57}

3.4 Conclusions

This chapter discussed a two-step synthesis route to form $\text{Cu}_{2-x}\text{S}/\text{CuInS}_2$ HNCs. The $\text{Cu}_{2-x}\text{S}/\text{CuInS}_2$ HNCs were obtained by injecting pre-formed Cu_{2-x}S seed nanocrystals, dispersed in 1-dodecanethiol, into a hot indium-oleate solution. By making use of pre-formed Cu_{2-x}S seed nanocrystals, the two stages of $\text{Cu}_{2-x}\text{S}/\text{CuInS}_2$ HNC growth were separated. This allowed for the formation of monodisperse HNCs with tunable size, shape and composition. Interestingly, elemental maps of the nanocrystals in the first few minutes of reaction suggest that the formation of the $\text{Cu}_{2-x}\text{S}/\text{CuInS}_2$ HNCs was initiated by a single-step, thiolate-mediated Cu^+ for In^{3+} exchange rather than by heteroepitaxial growth of CuInS_2 on the Cu_{2-x}S seed nanocrystals. At longer reaction times, the cation-exchange reaction was overtaken by homoepitaxial growth of CuInS_2 on the pre-formed CuInS_2 surface. The fate of the reaction and the resulting HNCs was strongly dependent on the concentration of Cu^+ and In^{3+} in solution. The good control over size, shape and composition of the HNCs offered by this method allowed for the formation of well-defined $\text{Cu}_{2-x}\text{S}/\text{CuInS}_2$ HNCs, that are of potential interest for photocatalytic applications.

3.5 Acknowledgements

The work in this chapter was performed in collaboration with Chenghui Xia. Anne Berends and Nienke Visser are thanked for the initial experiments on the synthesis of $\text{Cu}_{2-x}\text{S}/\text{CuInS}_2$ HNCs. Veerle Bogaards is thanked for synthesizing the samples used for the HR-TEM imaging of HNCs formed by reaction times of 10 and 30 minutes. Tim Spanjersberg is acknowledged for investigations of different reaction temperatures and the addition of extra copper precursors. Hans Meeldijk is thanked for his help with the HR-TEM imaging and elemental mapping. Dennie Wezendonk is acknowledged for his support with the high temperature XRD measurements.

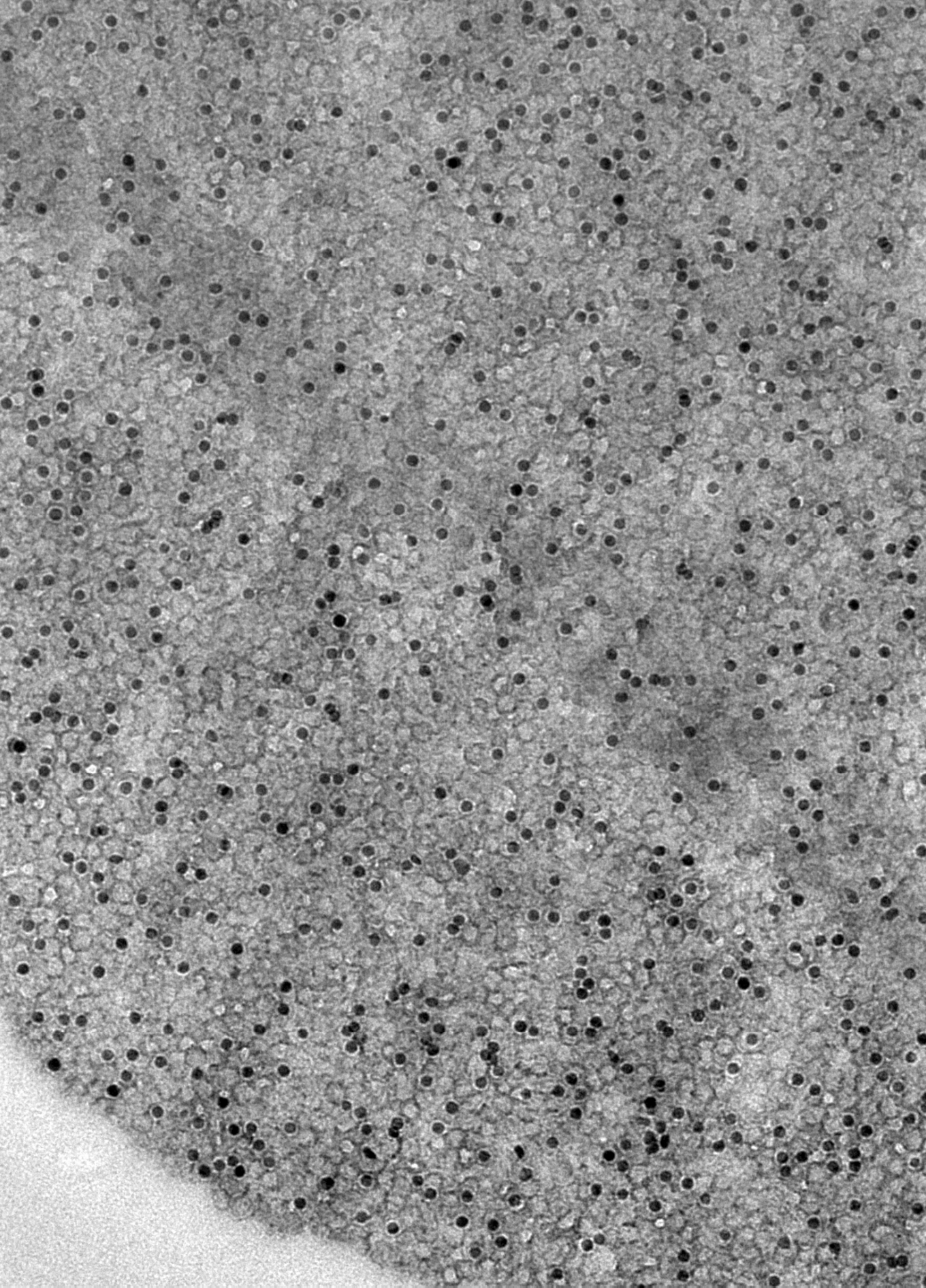
3.6 References

- (1) Van Der Stam, W.; Berends, A. C.; De Mello Donega, C. Prospects of Colloidal Copper Chalcogenide Nanocrystals. *ChemPhysChem* **2016**, *17*, 559–581.
- (2) Donegá, C. D. M. Synthesis and Properties of Colloidal Heteronanocrystals. *Chem. Soc. Rev.* **2011**, *40*, 1512–1546.
- (3) Costi, R.; Saunders, A. E.; Banin, U. Colloidal Hybrid Nanostructures: A New Type of Functional Materials. *Angew. Chemie Int. Ed.* **2010**, *49*, 4878–4897.
- (4) Rabouw, F. T.; de Mello Donega, C. Excited-State Dynamics in Colloidal Semiconductor Nanocrystals. *Top. Curr. Chem.* **2016**, *374*, 1–30.
- (5) Kodaimati, M. S.; McClelland, K. P.; He, C.; Lian, S.; Jiang, Y.; Zhang, Z.; Weiss, E. A. Viewpoint: Challenges in Colloidal Photocatalysis and Some Strategies for Addressing Them. *Inorg. Chem.* **2018**, *57*, 3659–3670.
- (6) Wu, K.; Lian, T. Quantum Confined Colloidal Nanorod Heterostructures for Solar-to-Fuel Conversion. *Chem. Soc. Rev.* **2016**, *45*, 3781–3810.
- (7) Zhu, H.; Lian, T. Wavefunction Engineering in Quantum Confined Semiconductor Nanoheterostructures for Efficient Charge Separation and Solar Energy Conversion. *Energy Environ. Sci.* **2012**, *5*, 9406–9418.
- (8) Casavola, M.; Buonsanti, R.; Caputo, G.; Cozzoli, P. D. Colloidal Strategies for Preparing Oxide-Based Hybrid Nanocrystals. *Eur. J. Inorg. Chem.* **2008**, *2008*, 837–854.
- (9) Cozzoli, P. D.; Pellegrino, T.; Manna, L. Synthesis, Properties and Perspectives of Hybrid Nanocrystal Structures. *Chem. Soc. Rev.* **2006**, *35*, 1195–1208.
- (10) Reiss, P.; Protière, M.; Li, L. Core/Shell Semiconductor Nanocrystals. *Small* **2009**, *5*, 154–168.
- (11) Bridewell, V. L.; Alam, R.; Karwacki, C. J.; Kamat, P. V. CdSe/CdS Nanorod Photocatalysts: Tuning the Interfacial Charge Transfer Process through Shell Length. *Chem. Mater.* **2015**, *27*, 5064–5071.
- (12) Rainò, G.; Stöferle, T.; Moreels, I.; Gomes, R.; Kamal, J. S.; Hens, Z.; Mahrt, R. F. Probing the Wave Function Delocalization in CdSe/CdS Dot-in-Rod Nanocrystals by Time-and Temperature-Resolved Spectroscopy. *ACS Nano* **2011**, *5*, 4031–4036.
- (13) Wu, K.; Rodríguez-Córdoba, W. E.; Liu, Z.; Zhu, H.; Lian, T. Beyond Band Alignment: Hole Localization Driven Formation of Three Spatially Separated Long-Lived Exciton States in CdSe/CdS Nanorods. *ACS Nano* **2013**, *7*, 7173–7185.
- (14) Dorfs, D.; Salant, A.; Popov, I.; Banin, U. ZnSe Quantum Dots within CdS Nanorods: A Seeded-Growth Type-II System. *Small* **2008**, *4*, 1319–1323.
- (15) Kirsanova, M.; Nemchinov, A.; Hewa-Kasakarage, N. N.; Schmall, N.; Zamkov, M. Synthesis of ZnSe/CdS/ZnSe Nanobarbells Showing Photoinduced Charge Separation. *Chem. Mater.* **2009**, *21*, 4305–4309.
- (16) Oh, N.; Kim, B. H.; Cho, S. Y.; Nam, S.; Rogers, S. P.; Jiang, Y.; Flanagan, J. C.; Zhai, Y.; Kim, J. H.; Lee, J.; et al. Double-Heterojunction Nanorod Light-Responsive LEDs for Display Applications. *Science* **2017**, *355*, 616–619.
- (17) Ye, H.; Tang, A.; Huang, L.; Wang, Y.; Yang, C.; Hou, Y.; Peng, H.; Zhang, F.; Teng, F. Facile One-Step Synthesis and Transformation of Cu(I)-Doped Zinc Sulfide Nanocrystals to Cu_{1.94}S-ZnS Heterostructured Nanocrystals. *Langmuir* **2013**, *29*, 8728–8735.
- (18) Han, S.-K.; Gong, M.; Yao, H.-B.; Wang, Z.-M.; Yu, S.-H. One-Pot Controlled Synthesis of Hexagonal-Prismatic Cu_{1.94}S-ZnS, Cu_{1.94}S-ZnS-Cu_{1.94}S, and Cu_{1.94}S-ZnS-Cu_{1.94}S-ZnS-Cu_{1.94}S Heteronanocrystals. *Angew. Chemie Int. Ed.* **2012**, *51*, 6365–6368.
- (19) Yi, L.; Tang, A.; Niu, M.; Han, W.; Hou, Y.; Gao, M. Synthesis and Self-Assembly of Cu_{1.94}S-ZnS Heterostructured Nanorods. *CrystEngComm* **2010**, *12*, 4124–4130.
- (20) Huang, F.; Wang, X.; Xu, J.; Chen, D.; Wang, Y. A Plasmonic Nano-Antenna with Controllable Resonance Frequency: Cu_{1.94}S-ZnS Dimeric Nanoheterostructure Synthesized in Solution. *J. Mater. Chem.* **2012**, *22*, 22614–22618.
- (21) Zhou, J.; Huang, F.; Xu, J.; Wang, Y. Cu_{1.94}S-MnS Dimeric Nanoheterostructures with Bifunctions: Localized Surface Plasmon Resonance and Magnetism. *CrystEngComm* **2013**, *15*, 4217–4220.
- (22) Regulacio, M. D.; Ye, C.; Hon Lim, S.; Bosman, M.; Polavarapu, L.; Ling Koh, W.; Zhang, J.; Xu, Q.-H.; Han, M.-Y. One-Pot Synthesis of Cu_{1.94}S-CdS and Cu_{1.94}S-Zn_xCd_{1-x}S Nanodisk Heterostructures. *J. Am. Chem. Soc.* **2011**, *133*, 2052–2055.
- (23) Cheng, H.; Huang, B.; Liu, Y.; Wang, Z.; Qin, X.; Zhang, X.; Dai, Y. An Anion Exchange Approach to Bi₂WO₆ Hollow Microspheres with Efficient Visible Light Photocatalytic Reduction of CO₂ to Methanol. *Chem. Commun.* **2012**, *48*, 9762–9764.

- (24) Choi, S. H.; Kim, E. G.; Hyeon, T. One-Pot Synthesis of Copper-Indium Sulfide Nanocrystal Heterostructures with Acorn, Bottle, and Larva Shapes. *J. Am. Chem. Soc.* **2006**, *128*, 2520–2521.
- (25) Han, W.; Yi, L.; Zhao, N.; Tang, A.; Gao, M.; Tang, Z. Synthesis and Shape-Tailoring of Copper Sulfide/Indium Sulfide-Based Nanocrystals. *J. Am. Chem. Soc.* **2008**, *130*, 13152–13161.
- (26) Connor, S. T.; Hsu, C. M.; Weil, B. D.; Aloni, S.; Cui, Y. Phase Transformation of Biphasic Cu₂S-CuInS₂ to Monophasic CuInS₂ Nanorods. *J. Am. Chem. Soc.* **2009**, *131*, 4962–4966.
- (27) Kruszynska, M.; Borchert, H.; Parisi, J.; Kolny-Olesiak, J. Synthesis and Shape Control of CuInS₂ Nanoparticles. *J. Am. Chem. Soc.* **2010**, *132*, 15976–15986.
- (28) Lu, X.; Zhuang, Z.; Peng, Q.; Li, Y. Controlled Synthesis of Wurtzite CuInS₂ Nanocrystals and Their Side-by-Side Nanorod Assemblies. *CrystEngComm* **2011**, *13*, 4039–4045.
- (29) Chang, J.-Y.; Cheng, C.-Y. Facile One-Pot Synthesis of Copper Sulfide-Metal Chalcogenide Anisotropic Heterostructures in a Noncoordinating Solvent. *Chem. Commun.* **2011**, *47*, 9089–9091.
- (30) Zhai, Y.; Flanagan, J. C.; Shim, M. Lattice Strain and Ligand Effects on the Formation of Cu_{2-x}S/I-III-VI₂ Nanorod Heterostructures through Partial Cation Exchange. *Chem. Mater.* **2017**, *29*, 6161–6167.
- (31) Li, Y.; Tang, A.; Liu, Z.; Peng, L.; Yuan, Y.; Shi, X.; Yang, C.; Teng, F. Formation of Uniform Carrot-like Cu₃₁S₁₆-CuInS₂ Heterostructures Assisted by Citric Acid at the Oil/Aqueous Interface. *Dalt. Trans.* **2018**, *47*, 67–73.
- (32) Li, J.; Bloemen, M.; Parisi, J.; Kolny-Olesiak, J. Role of Copper Sulfide Seeds in the Growth Process of CuInS₂ Nanorods and Networks. *ACS Appl. Mater. Interfaces* **2014**, *6*, 20535–20543.
- (33) Kruszynska, M.; Borchert, H.; Parisi, J.; Kolny-Olesiak, J. Investigations of Solvents and Various Sulfur Sources Influence on the Shape-Controlled Synthesis of CuInS₂ Nanocrystals. *J. Nanoparticle Res.* **2011**, *13*, 5815–5824.
- (34) Kolny-Olesiak, J. Synthesis of Copper Sulfide-Based Hybrid Nanostructures and Their Application in Shape Control of Colloidal Semiconductor Nanocrystals. *CrystEngComm* **2014**, *16*, 9381–9390.
- (35) Hashimoto, Y.; Takeuchi, K.; Ito, K. Band Alignment at CdS/CuInS₂ Heterojunction. *Appl. Phys. Lett.* **1995**, *67*, 980.
- (36) Liu, G.; Schulmeyer, T.; Thissen, A.; Klein, A.; Jaegermann, W. In Situ Preparation and Interface Characterization of TiO₂/Cu₂S Heterointerface. *Appl. Phys. Lett.* **2003**, *82*, 2269–2271.
- (37) Liu, G.; Schulmeyer, T.; Brötz, J.; Klein, A.; Jaegermann, W. Interface Properties and Band Alignment of Cu₂S/CdS Thin Film Solar Cells. *Thin Solid Films* **2003**, *431–432*, 477–482.
- (38) Berends, A. C.; Mangnus, M. J. J.; Xia, C.; Rabouw, F. T.; De Mello Donega, C. Optoelectronic Properties of Ternary I-III-VI₂ Semiconductor Nanocrystals: Bright Prospects with Elusive Origins. *J. Phys. Chem. Lett.* **2019**, *10*, 1600–1616.
- (39) Binsma, J. J. M.; Giling, L. J.; Bloem, J. Luminescence of CuInS₂. I. The Broad Band Emission and Its Dependence on the Defect Chemistry. *J. Lumin.* **1982**, *27*, 35–53.
- (40) Chen, H.; Wang, C.-Y.; Wang, J.-T.; Hu, X.-P.; Zhou, S.-X. First-Principles Study of Point Defects in Solar Cell Semiconductor CuInS₂. *J. Appl. Phys.* **2012**, *112*, 84513.
- (41) Ueng, H. Y.; Hwang, H. L. The Defect Structure of CuInS₂. Part I: Intrinsic Defects. *J. Phys. Chem. Solids* **1989**, *50*, 1297–1305.
- (42) Xia, C.; Winckelmans, N.; Prins, P. T.; Bals, S.; Gerritsen, H. C.; De Mello, C.; Donega, D. Near-Infrared-Emitting CuInS₂/ZnS Dot-in-Rod Colloidal Heteronanorods by Seeded Growth. *J. Am. Chem. Soc.* **2018**, *140*, 5755–5763.
- (43) Robinson, E. H.; Turo, M. J.; Macdonald, J. E. Controlled Surface Chemistry for the Directed Attachment of Copper(I) Sulfide Nanocrystals. *Chem. Mater.* **2017**, *29*, 3854–3857.
- (44) Coughlan, C.; Ibáñez, M.; Dobrozhan, O.; Singh, A.; Cabot, A.; Ryan, K. M. Compound Copper Chalcogenide Nanocrystals. *Chem. Rev.* **2017**, *117*, 5865–6109.
- (45) Tang, A.; Qu, S.; Li, K.; Hou, Y.; Teng, F.; Cao, J.; Wang, Y.; Wang, Z. One-Pot Synthesis and Self-Assembly of Colloidal Copper(I) Sulfide Nanocrystals. *Nanotechnology* **2010**, *21*, 285602.
- (46) Choi, S. H.; Kim, E. G.; Hyeon, T. One-Pot Synthesis of Copper-Indium Sulfide Nanocrystal Heterostructures with Acorn, Bottle, and Larva Shapes. *J. Am. Chem. Soc.* **2006**, *128*, 2520–2521.
- (47) Rivest, J. B.; Fong, L.-K.; Jain, P. K.; Toney, M. F.; Alivisatos, A. P. Size Dependence of a Temperature-Induced Solid-Solid Phase Transition in Copper(I) Sulfide. *J. Phys. Chem. Lett.* **2011**, *2*, 2402–2406.
- (48) Wang, L. W. High Chalcocite Cu₂S: A Solid-Liquid Hybrid Phase. *Phys. Rev. Lett.* **2012**, *108*, 1–5.
- (49) Chakrabarti, D. J.; Laughlin, D. E. The Cu-S (Copper-Sulfur) System. *Bull. Alloy Phase Diagrams* **1983**, *4*, 254–271.
- (50) ICDD (2019) PDF-4+ 2019 (Database). Edited by Dr. Soorya Kabekkodu. *Int. Cent. Diff. Data, Newt. Square, PA, USA*.

- (51) Van Der Stam, W.; Berends, A. C.; Rabouw, F. T.; Willhammar, T.; Ke, X.; Meeldijk, J. D.; Bals, S.; De Mello Donega, C. Luminescent CuInS₂ Quantum Dots by Partial Cation Exchange in Cu_{2-x}S Nanocrystals. *Chem. Mater.* **2015**, *27*, 621–628.
- (52) Van Der Stam, W.; Akkerman, Q. A.; Ke, X.; Van Huis, M. A.; Bals, S.; De, C.; Donega, M. Solution-Processable Ultrathin Size- and Shape-Controlled Colloidal Cu_{2-x}S Nanosheets. *Chem. Mater.* **2015**, *27*, 283–291.
- (53) Pearson, R. G. Absolute Electronegativity and Hardness: Application to Inorganic Chemistry. *Inorg. Chem.* **1988**, *27*, 734–740.
- (54) Xia, C.; Meeldijk, J. D.; Gerritsen, H. C.; De Mello Donega, C. Highly Luminescent Water-Dispersible NIR-Emitting Wurtzite CuInS₂/ZnS Core/Shell Colloidal Quantum Dots. *Chem. Mater.* **2017**, *29*, 4940–4951.
- (55) White, S. L.; Smith, J. G.; Behl, M.; Jain, P. K. Co-Operativity in a Nanocrystalline Solid-State Transition. *Nat. Commun.* **2013**, *4*, 1–8.
- (56) Routzahn, A. L.; Jain, P. K. Single-Nanocrystal Reaction Trajectories Reveal Sharp Cooperative Transitions. *Nano Lett.* **2014**, *14*, 987–992.
- (57) Xia, C.; Wu, W.; Yu, T.; Xie, X.; Van Oversteeg, C.; Gerritsen, H. C.; De Mello Donega, C. Size-Dependent Band-Gap and Molar Absorption Coefficients of Colloidal CuInS₂ Quantum Dots. *ACS Nano* **2018**, *12*, 8350–8361.

The synthesis and formation mechanism of $\text{Cu}_{2-x}\text{S}/\text{CuInS}_2$ heteronanocrystals



Chapter 4

The preparation of silica supported
 Cu_{2-x}S nanoparticles

Abstract *By depositing nanoparticles on a support material, their stability can be improved and their handling is made easier, making them more suitable for practical application. In this chapter we present a new method to prepare silica supported Cu_2S and CuS nanoparticles using copper nitrate as copper source, and 1-dodecanethiol or thioacetamide as sulfur source, respectively. Uniformly distributed Cu_2S nanoparticles with narrow size distribution were synthesized directly from 1-dodecanethiol and $\text{Cu}(\text{NO}_3)_2$ in the presence of silica. To prepare CuS nanoparticles of controlled size, that were uniformly distributed over the porous support, pre-synthesized CuO nanoparticles were converted into CuS using thioacetamide. With this method, the original size of the CuO nanoparticles was preserved upon sulfidation to CuS . In this way, well-established preparation methods of supported CuO nanoparticles can be extended to supported CuS nanoparticles.*

4.1 Introduction

When using nanoparticles in applications such as catalysis and energy conversion and storage, the stability of the nanoparticles is of crucial importance. Deposition of nanoparticles on a support material, such as silica or carbon, has several advantages.¹ For example, the support allows a uniform distribution of particles on the material and can prevent aggregation of the particles. In addition, supported nanoparticles are easier to handle in *e.g.*, separation of catalyst and product streams.

Silica is often used as catalyst support due to its inert nature, that does not influence most chemical reactions. Silica can be prepared with a high surface area and a variety of 3D pore structures. In this work, MCF (mesocellular foam) was chosen as support material. MCF is a silica support with a well-defined mesoporous network, consisting of large cages (~15-30 nm) connected by smaller windows (~10 nm).² MCF has been investigated as catalyst support in for example methanol synthesis using copper nanoparticles,³ the Fischer-Tropsch reaction using cobalt nanoparticles⁴ and the photocatalytic hydrogen evolution reaction using copper oxide nanoparticles.⁵

One method to obtain supported nanoparticles is by immobilization of pre-synthesized colloidal nanoparticles on a support material.⁶ This can be challenging, as pre-formed nanoparticles need to enter the small pores of the support material. In addition, the interactions between the nanoparticles and the support need to be favorable in order for the nanoparticles to stick to the support and remain there, also during the catalysis. Furthermore, as discussed in Chapter 2, the ligands stabilizing the nanoparticles prepared by colloidal methods complicate their use in applications, and consequently an additional ligand exchange step must be performed, either before or after the deposition. A more conventional manner to synthesize a supported nanoparticle catalyst is by directly growing the nanoparticles on the support. This can be done by methods such as incipient wetness impregnation or homogeneous deposition precipitation.¹

The synthesis of Cu_{2-x}S nanoparticles anchored on support materials has been studied before. For example, the preparation of carbon-supported Cu_{2-x}S nanostructures has been reported,⁷⁻¹² where often high temperatures (>150 °C) and long reaction times (>12 hours) were used.⁷⁻¹⁰ In addition, Hou *et al.*, reported the formation of sphere-like CuS particles with diameters ranging from 30-50 nm on TiO₂ fibers.¹³ Studies on the preparation of Cu_{2-x}S nanoparticles supported on silica are more scarce. One method was reported by Sohrabnezhad *et al.*, who found that by reacting thiourea and copper sulfate in water at 90 °C, mixed-phase CuS/Cu₂S nanoparticles supported on silica could be obtained.¹⁴ Synthesizing pure, single-phase CuS nanoparticles supported on silica proved to be more challenging and was realized by using ethylene glycol as the solvent and a high temperature of 250 °C.¹⁴

In this chapter we describe new strategies for the synthesis of pure, silica-supported Cu₂S- and CuS nanoparticles. Several approaches were investigated to obtain uniformly distributed and monodisperse nanoparticles. First, the direct deposition of Cu_{2-x}S nanoparticles onto the silica support was investigated, using copper nitrate as the copper precursor, and 1-dodecanethiol (DDT) and thioacetamide (TAA) as the sulfur source (Figure 4.1). As discussed in Chapter 2, DDT is an alkyl-thiol that is widely used as sulfur source and organic ligand in the synthesis of colloidal Cu_{2-x}S nanocrystals.¹⁵ TAA is an organic compound that has previously been used as H₂S and S²⁻ source in the synthesis of metal sulfides, such as NiS and CuS.¹⁶⁻¹⁹ Using these two different sulfur sources we were able to selectively form pure CuS or Cu₂S nanoparticles on silica.

Besides direct deposition of the nanoparticles on the support, the use of silica-supported CuO nanoparticles as precursor for supported Cu_{2-x}S nanoparticles was explored. This is an attractive route as it allows to further extend the elaborate experience and knowledge on the control of particle size in supported CuO and Cu₂O nanoparticles to supported Cu_{2-x}S nanoparticles.^{1,3,5,20}

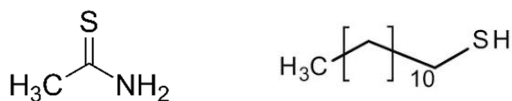


Figure 4.1 Molecular structures of **a**) thioacetamide (TAA) and **b**) 1-dodecanethiol (DDT).

4.2 Experimental methods

4.2.1 Materials

Pluronic P123, hydrochloric acid (HCl, 37%), nitric acid (HNO₃, 80%), 1,3,5-trimethylbenzene (TMB, 98%), tetraethyl orthosilicate (TEOS, 98%), ammonium fluoride (NH₄F, ≥98.0%), copper nitrate trihydrate (Cu(NO₃)₂ · 3 H₂O, 99%), 1-dodecanethiol (DDT, ≥98%), thioacetamide (TAA, ≥99.0%) ethanol and acetone were purchased from Sigma-Aldrich and used as received.

4.2.2 Synthesis of silica support

The synthesis of the MCF silica support was based on a method reported by Pompe *et al.*,³ The synthesis was performed in a 500 mL high-density polypropylene (HDPE) bottle. First, 4.0 g of triblock copolymer Pluronic P123 was added to 150 mL of a 1.6 M HCl aqueous solution (20 ml 37% HCl aqueous solution and 130 mL demi water). The mixture was stirred overnight at room temperature to dissolve the polymer. Subsequently, 4 g of 1,3,5-trimethylbenzene (TMB) was added dropwise and the mixture was left stirring for 4 hours. Then 8.5 g tetraethyl orthosilicate (TEOS) was added to the solution under vigorous stirring. After 5 minutes the stirring bar was removed and the mixture was kept at 39 °C under static conditions for 20 hours. Then 46 mg ammonium fluoride (NH₄F) was added while stirring the mixture. A hydrothermal treatment was performed at 80 °C for 24 hours in a Heraeus muffle oven, after which the solid product was collected by filtration. The solid was washed with 4 L demi water and subsequently dried at 60°C. Finally the solid was calcined at 550 °C in static air for 6 hours.

4.2.3 Synthesis of unsupported Cu_{2-x}S using different sulfidizing agents

First, unsupported Cu_{2-x}S nanoparticles were synthesized using Cu(NO₃)₂ and two different sulfidizing agents: DDT and TAA (Figure 4.1). For the synthesis using DDT, 0.12 mmol Cu(NO₃)₂ · 3 H₂O was dispersed in 5 mL DDT in a roundbottom flask and heated to 200 °C under stirring. The mixture was left to react for 2 hours and was subsequently cooled down to room temperature. The mixture was washed using ethanol and centrifugation.

For the synthesis using TAA, 0.12 mmol Cu(NO₃)₂ · 3 H₂O was dispersed in 13 mL demineralized water in a 100 mL roundbottom flask and heated to 110 °C under stirring. At a temperature of 90 °C 3 mL of a solution of 0.25 mmol TAA in demineralized water was added dropwise to the roundbottom flask. The mixture was left to reflux for 2 hours at 110 °C. After 2 hours the mixture was left to cool down and the samples were washed with demineralized water and acetone using vacuum filtration. Finally the samples were dried under vacuum at room temperature.

4.2.4 Direct deposition of Cu_{2-x}S on silica using different sulfidizing agents

Supported Cu_{2-x}S nanoparticles were prepared by direct deposition using Cu(NO₃)₂ with either DDT or TAA. For the deposition using DDT, 100 mg of silica and 0.12 mmol Cu(NO₃)₂ · 3 H₂O were dispersed in 5 mL DDT in a 100 mL roundbottom flask and heated to 200 °C under stirring. The mixture was left to react for 2 hours and was subsequently cooled down to room temperature. The mixture was washed using acetone and vacuum filtration and dried under vacuum at room temperature.

For the deposition using TAA, 100 mg of silica and 0.12 mmol Cu(NO₃)₂ · 3 H₂O were dispersed in 13 mL demineralized water in a 100 mL roundbottom flask and heated to 110 °C under stirring. At a temperature of 90 °C 3 mL of a solution of 0.25 mmol TAA in demineralized water was added dropwise to the roundbottom flask. The mixture was then left to reflux for 2 hours at 110 °C. After 2 hours, the mixture was left to cool down and the samples were washed with demineralized water and acetone using vacuum filtration. Finally the samples were dried under vacuum at room temperature.

4.2.5 Synthesis of supported CuO nanoparticles

Supported CuO nanoparticles on silica were prepared via incipient wetness impregnation followed by drying and heat treatment.²⁰ 500 mg of mesoporous silica was dried for 3 hours under vacuum at 120 °C. Then, the support was impregnated with an aqueous solution of Cu(NO₃)₂ · 3 H₂O in 0.1 M HNO₃. The volume used for impregnation corresponded to the total pore volume of the support, as determined using N₂-physisorption. After impregnation, the sample was dried overnight under vacuum at room temperature. Subsequently, the sample was transferred to a tubular reactor and heated to 350 °C (2 °C/min) under a gas flow of 375 ml/min of 5% NO/95% N₂ and kept at this temperature for 3 hours.

4.2.6 Subsequent sulfidation of CuO

The silica supported CuO nanoparticles were subsequently sulfidized using two different sulfidizing agents: TAA and DDT. For the sulfidation using TAA, 300 mg of silica supported CuO nanoparticles (10 wt% Cu) were dispersed in 40 mL demineralized water in a 100 mL roundbottom flask and heated to 110 °C under stirring. At a temperature of 90 °C 10 mL of a solution of TAA in demineralized water was gradually added to the silica-supported CuO nanoparticles, where a Cu:S molar ratio of 1:2 was used. The mixture was then left to reflux for 2 hours at 110 °C. After 2 hours, the mixture was left to cool down and the samples were washed with demineralized water and acetone using vacuum filtration. Finally the samples were dried under vacuum at room temperature.

For the sulfidation using DDT, 300 mg of silica-supported CuO nanoparticles (10 wt% Cu) were dispersed in 15 mL DDT in a 100 mL roundbottom flask and heated to 200 °C. The mixture was left to react for 2 hours and was subsequently cooled down

to room temperature. The mixture was washed using acetone and vacuum filtration and dried under vacuum at room temperature.

4.2.7 Characterization

N₂-physisorption was performed using a Micromeritics TriStar instrument at a temperature of -196 °C. Prior to the measurements the powders were dried under N₂ flow at 300 °C, for at least 16 hours. The pore diameter was determined using the Barrett-Joyner-Halenda (BJH) method and the pore volume was determined at $p/p_0=0.995$.

Transmission electron microscopy analysis was performed using a FEI Tecnai-12 microscope operating at 120 kV or a FEI Technai-20 microscope operating at 200 kV. MCF samples were microtomed by embedding the sample in a two component epoxy resin (EpoFix, EMS). 70 nm thick slices were cut with a Diatome 35° diamond knife mounted on a Reichert-Jung Ultracut E microtome. The slices were collected on a carbon-coated 200 mesh copper TEM grid. Carbon supported samples were suspended in ethanol and sonicated for 10 minutes. Subsequently the suspension was drop casted on a carbon-coated 200 mesh copper TEM grid.

X-ray diffraction measurements were performed on a Bruker D2 Phaser, equipped with a Co K α x-ray source with a wavelength of 1.79026 Å. The crystallite size of the copper sulfide nanoparticles was determined from the diffraction peak broadening using the Scherrer equation.²¹

4.3 Results and Discussion

4.3.1 The synthesis of Cu_{2-x}S nanoparticles in the absence of a support

In this work, Cu_{2-x}S nanoparticles were grown using $\text{Cu}(\text{NO}_3)_2 \cdot 3 \text{H}_2\text{O}$ as the copper precursor and DDT or TAA as sulfur source. To see if Cu_{2-x}S particles could be formed from these reagents at the chosen reaction conditions, the syntheses using $\text{Cu}(\text{NO}_3)_2$ and either DDT or TAA were first performed in the absence of silica. Figure 4.2 shows the XRD diffractograms of the two samples and the reference patterns of Cu_2S and CuS .²² The diffractograms show that when DDT is used as the sulfur source, Cu_2S nanoparticles are formed, whereas with TAA as the sulfur source CuS nanoparticles are formed.

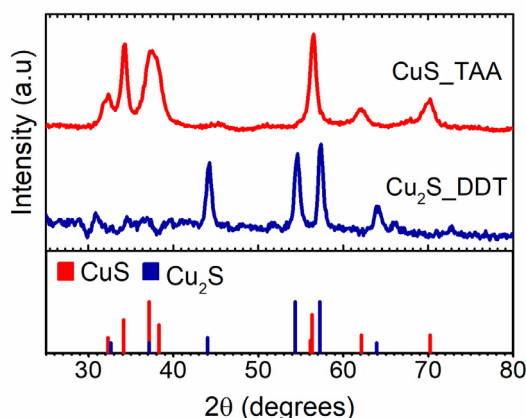


Figure 4.2 XRD patterns of the nanoparticles synthesized using DDT (blue line) and TAA (red line). The patterns match the reference patterns for Cu_2S (PDF card 00-053-0522) and of CuS (PDF card 00-006-0464), respectively.²²

The corresponding TEM images are shown in Figure 4.3 and indicate that nanoparticles were successfully grown from solution for both DDT and TAA. When using DDT, monodisperse, spherical Cu_2S nanoparticles with a size of 22.9 ± 2.2 nm were formed. When TAA was used as sulfur source, polydisperse platelets of CuS were formed with an average diameter of 45.1 ± 16.0 nm.

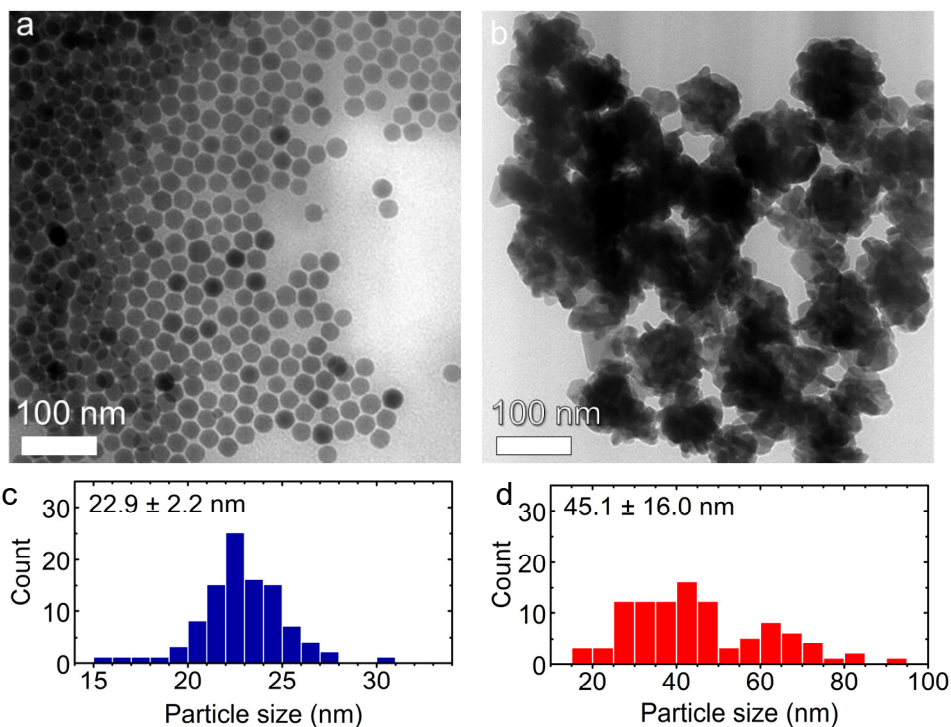


Figure 4.3 TEM images of unsupported Cu_{2-x}S nanoparticles prepared via direct synthesis with $\text{Cu}(\text{NO}_3)_2$ and a) DDT and b) TAA. c, d) Corresponding particle size histograms.

4.3.2 Characterization of the support material

Subsequently, the growth of Cu_2S and CuS nanoparticles on a silica support was investigated. First, MCF was synthesized and its textural properties were analyzed using N_2 -physorption. The large hysteresis observed in the isotherm (Figure 4.4a) indicates the presence of ink-bottle type pores, and is thus consistent with the presence of large cages with smaller windows. Figure 4.4b shows the pore size distribution obtained from N_2 -physorption. The adsorption branch (solid line) indicates a pore size of 12 nm for the cages, and the desorption branch (dashed line) gives a diameter 8 nm for the windows connecting the cages. The pore volume of the MCF was 1.36 mL/g and the support had a BET surface area of 690 m^2/g .

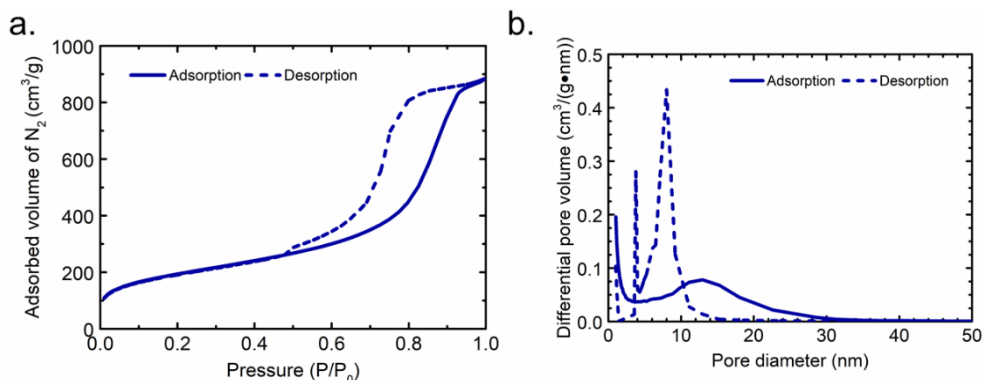


Figure 4.4 a) N_2 -physorption isotherms and b) pore size distributions of the silica (MCF) support. The solid lines represent the adsorption branch and the dashed lines from the desorption branch.

4.3.3 Direct deposition of Cu_{2-x}S on silica using different sulfidizing agents

Next, supported Cu_{2-x}S nanoparticles were prepared via the synthesis of Cu_{2-x}S in the presence of the MCF silica support. Figure 4.5 shows the XRD patterns of the $\text{Cu}_{2-x}\text{S}@\text{SiO}_2$ samples and shows that when DDT is used as the sulfur source, Cu_2S nanoparticles are formed, whereas with TAA as the sulfur source nanoparticles with a CuS phase are formed. The diffraction peaks at 57.5° and 56° were used to determine the crystallite size of the Cu_2S and CuS nanoparticles, respectively, using the Scherrer equation. The crystallite size was 14 nm for the Cu_2S nanoparticles and 17 nm for CuS nanoparticles. The broad diffraction peak around $25\text{-}30^\circ$, observed in the diffractograms of both samples, originates from the silica support.

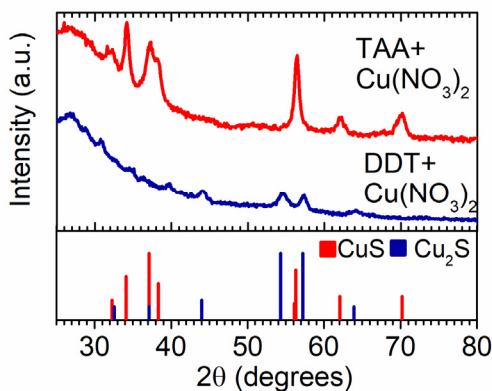


Figure 4.5 XRD patterns of silica supported nanoparticles prepared by DDT (blue line) and TAA (red line). The patterns match the reference patterns of Cu_2S (PDF card 00-053-0522) and CuS (PDF card 00-006-0464), respectively.²²

Figure 4.6 shows the TEM images of microtomed sections of the supported Cu_2S and CuS particles. Microtoming the samples into thin slices of 70 nm prior to TEM measurements facilitates the imaging of the particles inside the pores of the silica support. Figure 4.6a shows the TEM image of the Cu_2S sample, indicating a uniform distribution of the nanoparticles over the silica support. In addition, the particles are monodisperse with a particle size of 13.6 ± 2.8 nm. This is in good agreement with the crystallite size obtained from XRD, indicating that the particles are single crystalline. The uniform distribution of the Cu_2S nanoparticles over the support and the absence of particles that are separated from the support, suggest that the particles selectively nucleate on the silica support.

In contrast to the uniform distribution of the Cu_2S nanoparticles over the silica support, the CuS particles are aggregated and mostly present on the outside of the support or separate from the support (Figure 4.6b). The particles are polydisperse with an average particle diameter of 41.1 ± 13.3 nm. The formation of large particles outside the pores of the silica and separated from the silica indicates that the CuS nanoparticles nucleate in solution rather than on the support. To circumvent the fast nucleation of CuS outside the pores of the silica and obtain a more monodisperse particle size and better

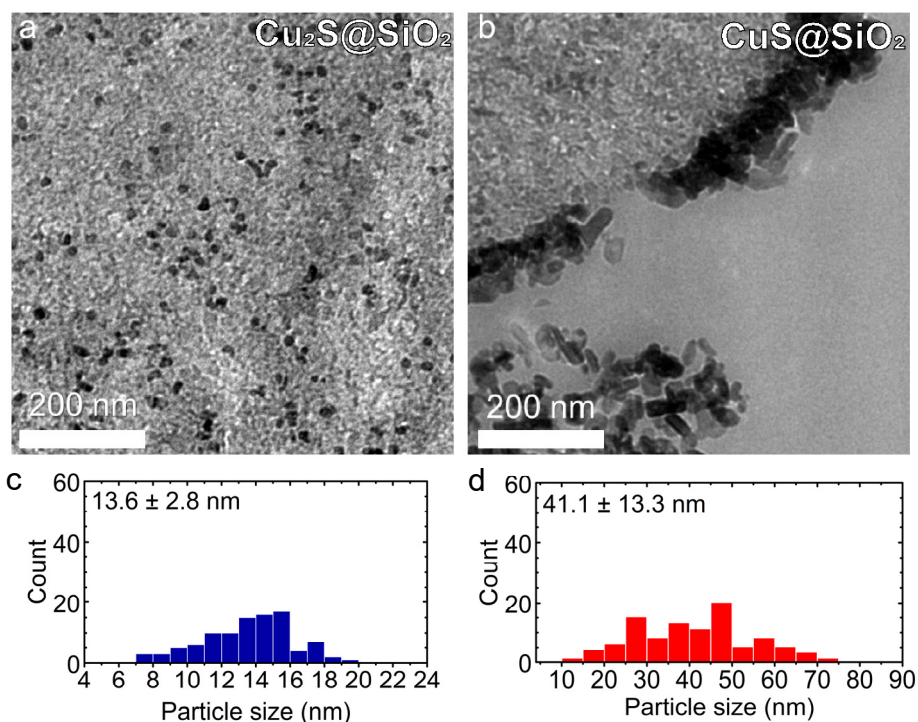


Figure 4.6 TEM images of silica-supported Cu_{2-x}S nanoparticles prepared via direct synthesis with $\text{Cu}(\text{NO}_3)_2$ and **a)** DDT and **b)** TAA. **c, d)** Corresponding particle size histograms. The images show that while the Cu_2S nanoparticles are uniformly distributed over the silica support (a), the CuS nanoparticles are clustered on the outside of the silica support (b).

distribution of the nanoparticles on the silica support, additional experiments were performed in which supported CuO particles were used as precursor for supported CuS particles.

4.3.4 Sulfidation of supported CuO nanoparticles using TAA

The preparation of uniformly distributed, silica supported CuO nanoparticles is well studied in our group and supported CuO nanoparticles can be synthesized with good control over particle size.^{3,20} Therefore, supported CuO nanoparticles were used as a precursor for the preparation of supported CuS nanoparticles. By using CuO nanoparticles that are already inside the pores of the silica as copper precursor, this method could facilitate the formation of CuS particles inside the pores of the support. Using the same reaction conditions as for the direct deposition with TAA described above, while replacing the $\text{Cu}(\text{NO}_3)_2$ by silica supported CuO nanoparticles, silica supported CuS nanoparticles were synthesized.

Figure 4.7 shows the XRD patterns of the $\text{CuO}@/\text{SiO}_2$ precursor and of the $\text{CuS}@/\text{SiO}_2$ sample obtained after sulfidation with TAA. The diffraction pattern after sulfidation matches a reference pattern of hexagonal CuS (PDF card 00-006-0464).²² In addition, no residual diffraction peaks of CuO are observed, indicating complete conversion of the CuO nanoparticles into CuS. The crystallite sizes of the samples were determined using the Scherrer equation and gave a crystallite size of 12 nm for both $\text{CuO}@/\text{SiO}_2$ and $\text{CuS}@/\text{SiO}_2$.

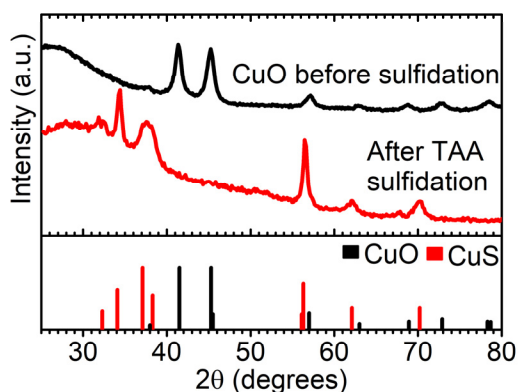


Figure 4.7 XRD patterns of silica supported CuO and of CuS nanoparticles prepared via the sulfidation of the CuO nanoparticles using TAA. The patterns match the reference patterns of CuO and CuS, respectively, indicating that the CuO nanoparticles are successfully converted to CuS nanoparticles.²²

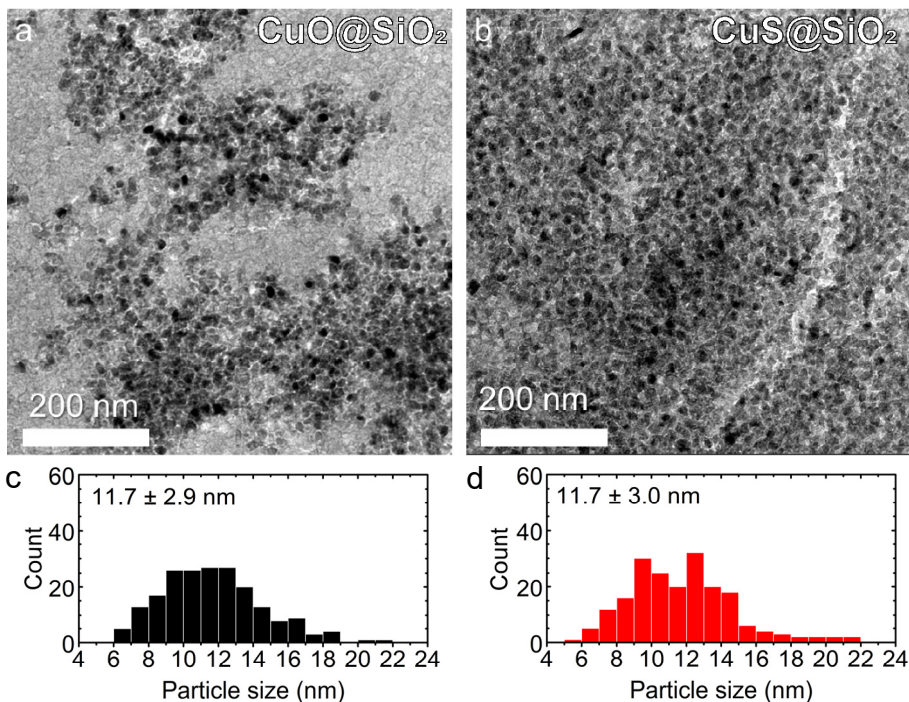


Figure 4.8 TEM images of **a)** supported CuO nanoparticles prepared via incipient wetness impregnation and heat treatment in 2% NO/98% N₂ and **b)** supported CuS nanoparticles prepared via liquid phase sulfidation of CuO nanoparticles with TAA and **c,d)** corresponding particle size histograms. The particle size histograms show that the particle size of the template CuO nanoparticles is preserved upon sulfidation to CuS.

Figure 4.8 shows the TEM images of microtomed sections of the silica supported CuO particles and the resulting CuS particles after sulfidation. In both samples, the nanoparticles are uniformly distributed in the pores of the silica support. The particle size obtained from TEM is 11.7 ± 2.9 nm for the supported CuO nanoparticles, and 11.7 ± 3.0 nm for the CuS particles upon TAA sulfidation. This is again in good agreement with the crystallite size obtained from XRD, indicating that the nanoparticles are single crystalline. In this case, the particle size of the CuS nanoparticles is similar to that of the precursor CuO nanoparticles. The histograms of the particle size of the CuO and CuS samples (Figure 4.8c,d) also clearly suggest that the particle size and the particle size distribution were preserved upon conversion of CuO to CuS.

To verify if the particle size was indeed preserved upon liquid phase sulfidation of CuO with TAA, silica supported CuO nanoparticles with different particle sizes were synthesized and used as template to prepare CuS nanoparticles. Small, well dispersed CuO nanoparticles were synthesized by changing the gas atmosphere during the heat treatment step from 2% NO/98% N₂ to 100% N₂.³ Upon sulfidation with TAA, CuS nanoparticles were formed, as was confirmed by XRD (Figure 4.9).

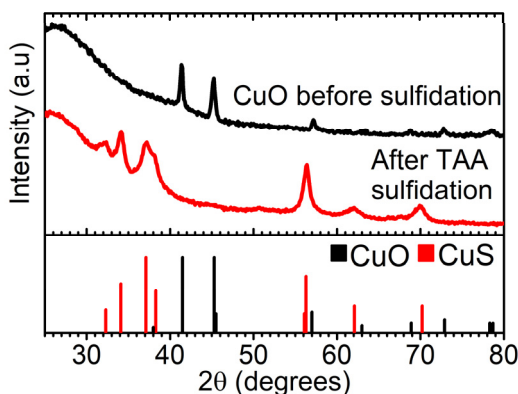


Figure 4.9 XRD patterns of silica supported CuO and of CuS nanoparticles prepared via the sulfidation of the CuO nanoparticles using TAA. The diffractograms match the reference patterns of CuO and CuS,²² respectively, indicating that the CuO nanoparticles were successfully converted to CuS nanoparticles upon sulfidation with TAA.

Figure 4.10a shows the overlay of the dark field STEM image with an EDX map of the precursor $\text{CuO}@SiO_2$, indicating the CuO is well dispersed over the silica and has a particle size smaller than 2 nm. In some areas larger CuO particles are also visible. Figure 4.10b shows the overlay of the dark field STEM image and EDX map of the supported CuS nanoparticles upon sulfidation with TAA, showing well dispersed CuS (particle size <2 nm) and also the presence of some larger CuS particles, similar to the $\text{CuO}@SiO_2$ precursor. Overall, the sulfidation method using TAA thus indeed allows to preserve the size of the precursor CuO nanoparticles. In addition, using silica-supported

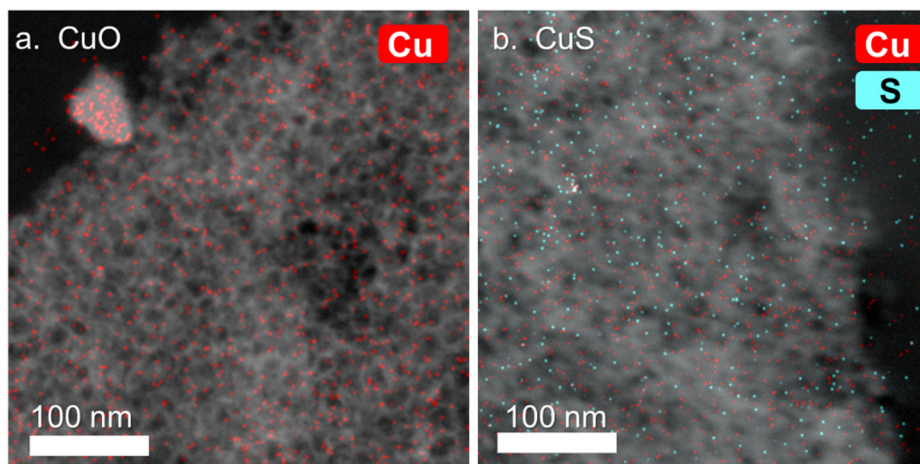


Figure 4.10 Overlay of HAADF-STEM images with EDX maps of well dispersed, silica supported **a)** CuO and **b)** CuS. The EDX signal of Cu is indicated in red, S in blue.

CuO particles as a template facilitates the formation CuS nanoparticles that are uniformly distributed over the silica support. The progress in the control over particle size of silica-supported CuO nanoparticles can in this way be extended to silica supported CuS nanoparticles.

4.3.5 Sulfidation of supported CuO nanoparticles using DDT

To verify if the control over particle size of CuS using CuO nanoparticles as precursor was also valid for the preparation of Cu₂S nanoparticles with different sizes, the method was extended to sulfidation using DDT as the sulfur source. The supported CuO was dispersed in DDT and left to react at 200°C for 2 hrs. Similar to the case of TAA discussed above, the ability to make particles with different sizes was investigated by using supported CuO nanoparticles with two different particle sizes, namely CuO with a particle size of 11.7 ± 2.9 nm, prepared via heat treatment in 2% NO/98% N₂, and the well dispersed CuO with a particle size <2 nm, prepared via heat treatment in 100% N₂. Figure 4.11 shows the XRD diffractograms of the samples prepared by sulfidation of supported CuO with DDT. For both the sample originating from the CuO particles with a size of about 11.7 nm and the sample originating from the well dispersed CuO particles, the CuO was completely converted to Cu₂S as no residual CuO reflections are observed.

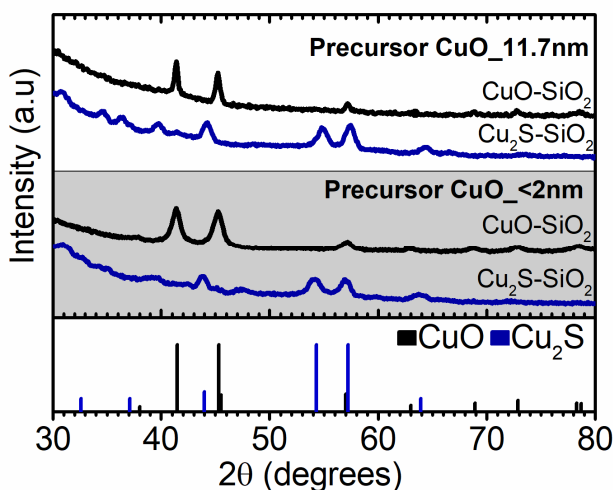


Figure 4.11 XRD patterns of silica supported Cu₂S nanoparticles prepared via the sulfidation of the CuO nanoparticles with a size of 11.7 nm (top) and of the well dispersed CuO of the well dispersed CuO (middle).

Figure 4.12 shows the TEM images of microtomed sections of the two samples. Both samples show homogeneously distributed nanoparticles on the silica support. The particles have a diameter of 13.8 ± 1.5 nm and 16.1 ± 1.7 nm for the samples originating from the well dispersed CuO sample with a particle size < 2 nm and the sample with

CuO particles of about 11.7 ± 2.9 nm, respectively. The increase in particle size observed for both samples indicates that in the case of DDT, the particle size was not preserved during the sulfidation step. Interestingly, the particle size of the Cu_2S sample prepared via direct synthesis using $\text{Cu}(\text{NO}_3)_2$ is fairly similar to the particle size of the Cu_2S samples prepared using CuO nanoparticles as template, suggesting a similar growth mechanism in all three cases.

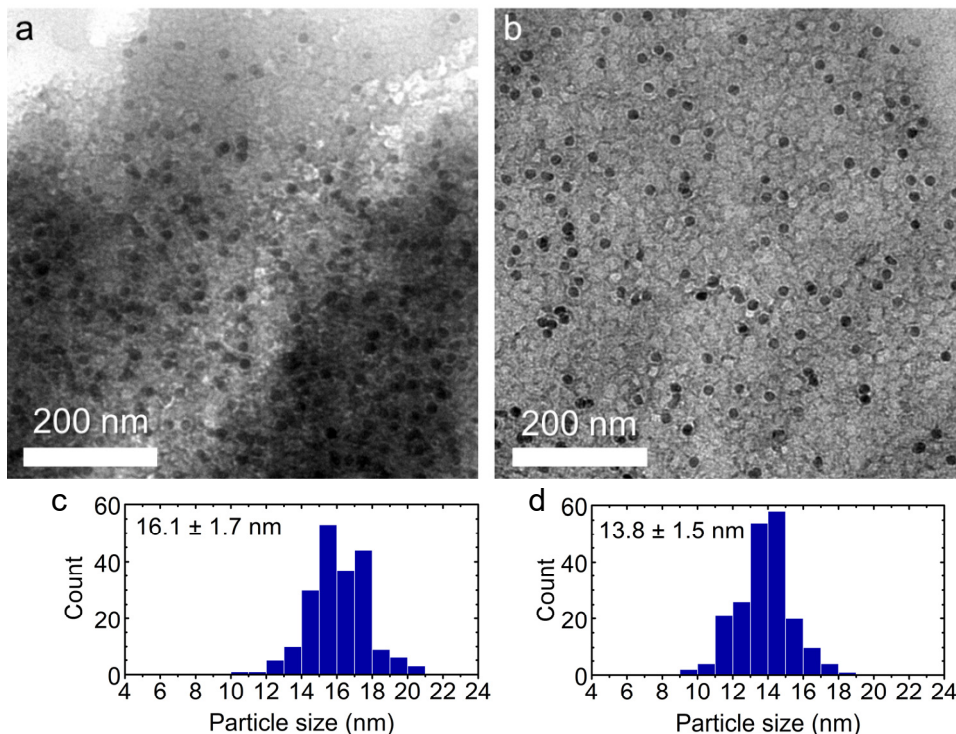


Figure 4.12 TEM images of supported Cu_2S nanoparticles prepared by sulfidation using DDT of **a)** supported CuO nanoparticles with a size of 11.7 ± 2.9 nm and **b)** supported, well dispersed CuO **c,d)** corresponding particle size histograms.

4.3.6 Mechanistic considerations

The results shown above indicate that when using DDT or TAA as the sulfur source in the synthesis of supported Cu_{2-x}S nanoparticles, two different mechanism for the growth of the nanoparticles play a role. Table 4.1 gives an overview of the average particle size of all samples discussed above.

Table 4.1 Overview of the particle sizes of the silica-supported Cu₂S and CuS samples, and the CuO@SiO₂ precursor they originate from. The particle sizes shown in this table were obtained from TEM measurements.

Sample:		Particle size of the CuO@SiO ₂ precursor (nm)	Particle size of supported Cu ₂ S or CuS (nm)
Cu ₂ S	direct deposition	-	22.9 ± 2.2
	direct deposition with MCF	-	13.6 ± 2.8
	CuO_NO/N ₂	11.7 ± 2.9	16.1 ± 1.7
	CuO_N ₂	<2 nm	13.8 ± 1.6
CuS	direct deposition	-	45 ± 16
	direct deposition with MCF	-	41 ± 13
	CuO_NO/N ₂	11.7 ± 2.9	11.7 ± 3.0
	CuO_N ₂	<2 nm	<2 nm

As can be seen from Table 4.1, the particle size of the Cu₂S@SiO₂ nanoparticles directly synthesized from Cu(NO₃)₂ in the presence of MCF have a very similar size as the Cu₂S@SiO₂ particles prepared from the synthesis using the two CuO@SiO₂ precursors with different CuO particle size. In addition, for all Cu₂S samples the nanoparticles were uniformly distributed inside the pores of the silica support. The common characteristic particle size and similar distribution of the nanoparticles over the support suggest a common growth mechanism. The existence of a common growth mechanism is further supported by the similar color changes observed during the reaction of DDT with either Cu(NO₃)₂ or the CuO@SiO₂ precursors, where the color of the reaction mixtures changed from turbid white-yellow, to clear yellow, clear orange and subsequently brown/black. These color changes are analogous to the color changes generally observed in colloidal synthesis of Cu_{2-x}S nanoparticles with DDT, where the yellow intermediate indicates the formation of Cu-thiolate complexes.^{15,24–26}

The common growth mechanism proposed for the formation of Cu₂S nanoparticles using DDT and either Cu(NO₃)₂ or CuO@SiO₂ precursors suggests that, rather than being directly converted to Cu₂S, the CuO particles dissolve and in this way act as a source of copper to form Cu₂S nanoparticles. To investigate if the CuO nanoparticles indeed dissolve during sulfidation with DDT, the yellow intermediate formed during reaction of DDT with the SiO₂-supported CuO nanoparticles of 11.7 nm was isolated and characterized. This was done by taking a sample of the suspension at the reaction stage in which the reaction mixture was yellow. Subsequently, the sample was centrifuged and the precipitate was dried and analyzed by TEM and XRD (Figure 4.13). TEM shows that at this stage of the reaction, particles are no longer present on the silica support, confirming that the CuO particles (partly) dissolve. In addition, XRD shows

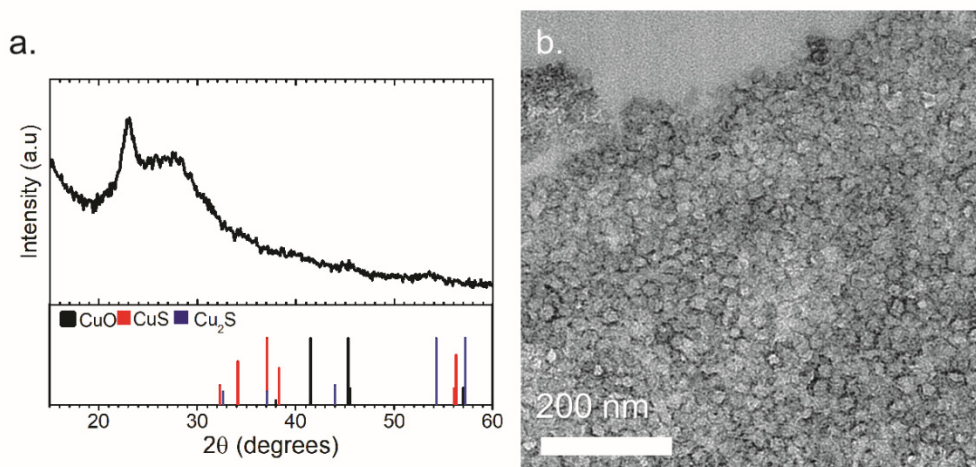


Figure 4.13 a) XRD pattern of the yellow intermediate during reaction of DDT with the silica-supported CuO nanoparticles of 11.7 nm and b) TEM image of this yellow intermediate. The intermediate was obtained from sampling of the suspension during the growth stage in which the reaction mixture is yellow.

that no crystalline CuO or Cu_{2-x}S phases were present in the yellow intermediate. There is a diffraction peak present at 21° , which possibly originates from Cu-thiolate complexes formed by the reaction of dissolved Cu with DDT.²³ The presence of Cu-thiolate complexes is supported by the yellow color of the intermediate.

The formation of the supported Cu_2S nanoparticles thus likely proceeded via the formation of Cu-thiolate complexes, which were subsequently decomposed by thermal cleavage of the C-S bond, resulting in Cu-S monomers for nucleation and growth of Cu_2S nanoparticles. The similarities to colloidal synthesis and the fact that DDT is a strong capping ligand for Cu_2S suggest that the resulting supported Cu_2S nanoparticles are likely capped with DDT.²⁷ To replace these ligands and make the nanoparticles more accessible for reactants, the ligand exchange procedures discussed in Chapter 2 can be used.

Supported CuS with different particle sizes could be synthesized using TAA. Direct synthesis using $\text{Cu}(\text{NO}_3)_2$ as the copper source resulted in large CuS particles outside the pores of the silica support. The size and shape of these CuS particles was similar to the CuS particles formed with the same synthesis method in the absence of silica. At these reaction conditions, the formation of CuS from $\text{Cu}(\text{NO}_3)_2$ and TAA has a low activation barrier and CuS particles thus readily nucleate in solution rather than on the silica support. By using silica-supported CuO particles as nuclei, copper is only present as CuO inside the pores of the silica. The absence of copper in solution allows the TAA to diffuse into the pores and subsequently react with the CuO particles inside the pores of the silica

to form CuS nanoparticles. The preservation of the particle size of the original CuO particle upon sulfidation with TAA suggests that here the oxygen of CuO is exchanged for sulfur from the TAA.

4.4 Conclusions

Silica-supported Cu₂S and CuS nanoparticles were successfully prepared by different methods. Supported Cu₂S nanoparticles can be formed by reaction of DDT with either Cu(NO₃)₂ or CuO nanoparticles at 200 °C. The resulting Cu₂S nanoparticles were monodisperse with a particle size ranging from 13.6 to 16.1 nm. In addition, the nanoparticles were uniformly distributed in the pores of the silica support. The particles were formed by a mechanism similar to colloidal Cu₂S synthesis, forming Cu-thiolate complexes that are thermally decomposed to Cu-S monomers for the formation of Cu₂S nanoparticles. Silica-supported CuS nanoparticles were formed by a new method, in which pre-synthesized, silica-supported CuO nanoparticles were sulfidized with TAA. The use of silica-supported CuO nanoparticles as precursor facilitates the preparation of uniformly distributed CuS nanoparticles inside the silica support. Using this TAA sulfidation method, the particle size of the template CuO particles was preserved, opening up a method to synthesize supported CuS with good control over particle size. The synthesis of supported Cu₂S and CuS nanoparticles facilitates the use of Cu₂S and CuS nanoparticles in catalytic applications. In Chapter 6, the methods presented in this chapter are further extended to carbon supports to prepare Cu₂S and CuS electrocatalyst.

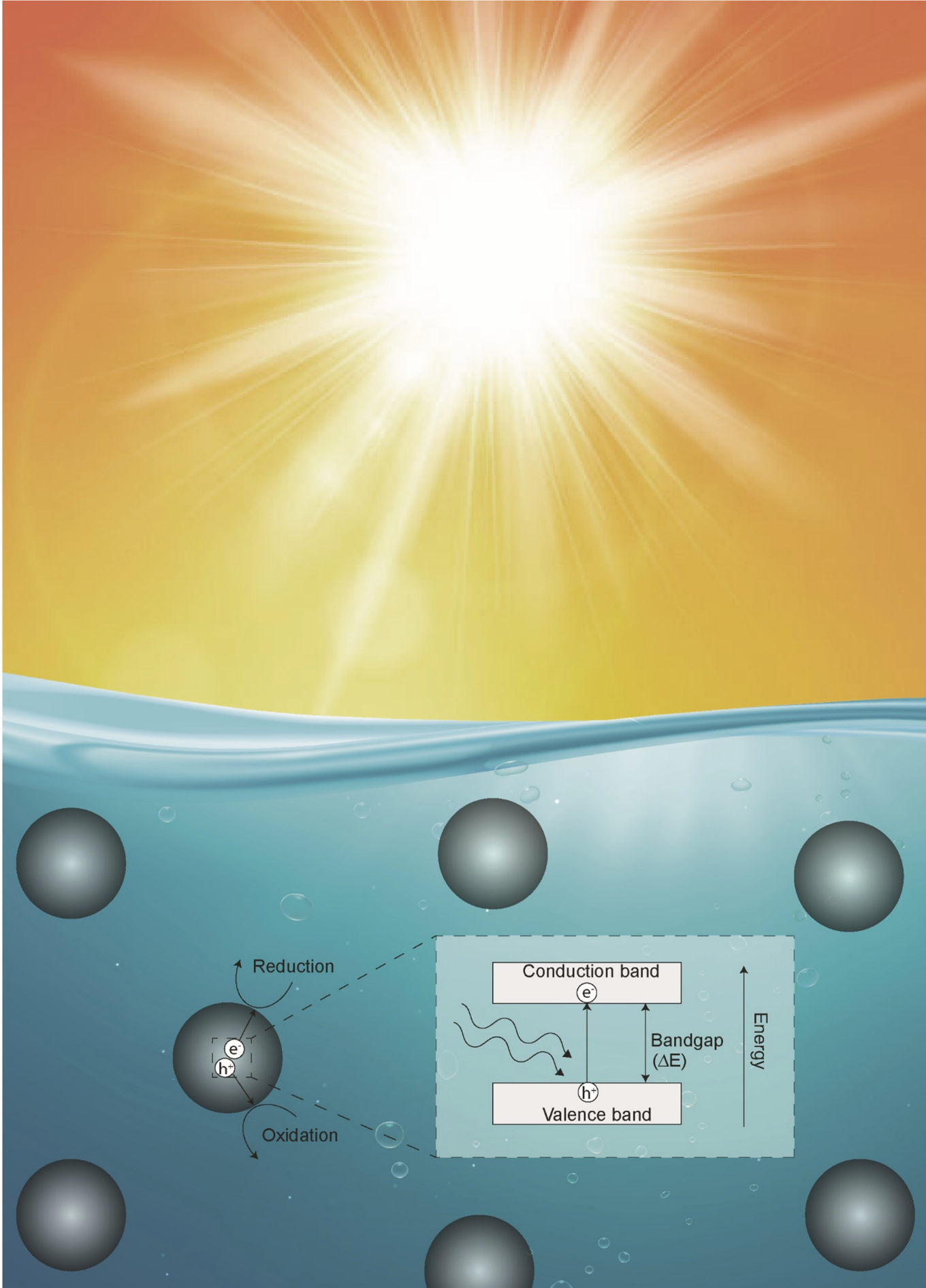
4.5 Acknowledgements

Lisette Pompe is thanked for providing the MCF supported CuO samples. Gang Wang and Koen Bossers are acknowledged for their help in the development of the sulfidation method. Lars van der Wal and Jogchum Oenema are acknowledged for microtoming the MCF samples. Nynke Krans is thanked for her help with measuring the STEM-EDX maps.

4.6 References

- (1) Munnik, P.; De Jongh, P. E.; De Jong, K. P. Recent Developments in the Synthesis of Supported Catalysts. *Chem. Rev.* **2015**, *115*, 6687–6718.
- (2) Schmidt-Winkel, P.; Lukens, W. W.; Zhao, D.; Yang, P.; Chmelka, B. F.; Stucky, G. D.; Beck, J. S.; Vartuli, J. C.; Roth, W. J.; Leonowicz, M. E.; et al., Mesocellular Siliceous Foams with Uniformly Sized Cells and Windows. *J. Am. Chem. Soc.* **1998**, *121*, 254–255.
- (3) Pompe, C. E.; van Uunen, D. L.; van der Wal, L. I.; van der Hoeven, J. E. S.; de Jong, K. P.; de Jongh, P. E. Stability of Mesocellular Foam Supported Copper Catalysts for Methanol Synthesis. *Catal. Today* **2019**, *334*, 79–89.
- (4) Ralston, W. T.; Melaet, G.; Saephan, T.; Somorjai, G. A. Evidence of Structure Sensitivity in the Fischer-Tropsch Reaction on Model Cobalt Nanoparticles by Time-Resolved Chemical Transient Kinetics. *Angew. Chemie Int. Ed.* **2017**, *56*, 7415–7419.
- (5) Wang, G.; van den Berg, R.; de Mello Donega, C.; de Jong, K. P.; de Jongh, P. E. Silica-Supported Cu₂O Nanoparticles with Tunable Size for Sustainable Hydrogen Generation. *Appl. Catal. B Environ.* **2016**, *192*, 199–207.
- (6) Rossi, L. M.; Fiorio, J. L.; Garcia, M. A. S.; Ferraz, C. P. The Role and Fate of Capping Ligands in Colloidally Prepared Metal Nanoparticle Catalysts. *Dalt. Trans.* **2018**, *47*, 5889–5915.
- (7) Saranya, M.; Ramachandran, R.; Kollu, P.; Kwan Jeong, S.; Nirmala Grace, A. A Template-Free Facile Approach for the Synthesis of CuS-RGO Nanocomposites towards Enhanced Photocatalytic Reduction of Organic Contaminants and Textile Effluents. *RSC Adv.* **2015**, *5*, 15831–15840.
- (8) Hu, X. S.; Shen, Y.; Zhang, Y. T.; Zhang, H. F.; Xu, L. H.; Xing, Y. J. Synthesis of Flower-like CuS/Reduced Graphene Oxide (RGO) Composites with Significantly Enhanced Photocatalytic Performance. *J. Alloys Compd.* **2017**, *695*, 1778–1785.
- (9) Zhang, Y.; Tian, J.; Li, H.; Wang, L.; Qin, X.; Asiri, A. M.; Al-Youbi, A. O.; Sun, X. Biomolecule-Assisted, Environmentally Friendly, One-Pot Synthesis of CuS/Reduced Graphene Oxide Nanocomposites with Enhanced Photocatalytic Performance. *Langmuir* **2012**, *28*, 12893–12900.
- (10) Nie, G.; Zhang, L.; Lu, X.; Bian, X.; Sun, W.; Wang, C. A One-Pot and in Situ Synthesis of CuS-Graphene Nanosheet Composites with Enhanced Peroxidase-like Catalytic Activity. *Dalt. Trans.* **2013**, *42*, 14006–14013.
- (11) Chen, T.-W.; Rajaji, U.; Chen, S.-M.; Govindasamy, M.; Paul Selvin, S. S.; Manavalan, S.; Arumugam, R. Sonochemical Synthesis of Graphene Oxide Sheets Supported Cu₂S Nanodots for High Sensitive Electrochemical Determination of Caffeic Acid in Red Wine and Soft Drinks. *Compos. Part B Eng.* **2019**, *158*, 419–427.
- (12) Shi, J.; Zhou, X.; Liu, Y.; Su, Q.; Zhang, J.; Du, G. Sonochemical Synthesis of CuS/Reduced Graphene Oxide Nanocomposites with Enhanced Absorption and Photocatalytic Performance. *Mater. Lett.* **2014**, *126*, 220–223.
- (13) Hou, G.; Cheng, Z.; Kang, L.; Xu, X.; Zhang, F.; Yang, H. Controllable Synthesis of CuS Decorated TiO₂ Nanofibers for Enhanced Photocatalysis. *CrystEngComm* **2015**, *17*, 5496–5501.
- (14) Sohrabnezhad, S.; Zanjanchi, M. A.; Hosseingholizadeh, S.; Rahnama, R. Facile and Low Temperature Route to Synthesis of CuS Nanostructure in Mesoporous Material by Solvothermal Method. *Spectrochim. Acta - Part A Mol. Biomol. Spectrosc.* **2014**, *123*, 142–150.
- (15) Chen, L.; Li, G. Functions of 1-Dodecanethiol in the Synthesis and Post-Treatment of Copper Sulfide Nanoparticles Relevant to Their Photocatalytic Applications. *ACS Appl. Nano Mater.* **2018**, *1*, 4587–4593.
- (16) Grau, J.; Akinc, M. Synthesis of Nickel Sulfide by Homogeneous Precipitation from Acidic Solutions of Thioacetamide. *J. Am. Ceram. Soc.* **1996**, *79*, 1073–1082.
- (17) Maheu, C.; Puzenat, E.; Geantet, C.; Cardenas, L.; Afanasiev, P. Titania - Supported Transition Metals Sulfides as Photocatalysts for Hydrogen Production from Propan-2-ol and Methanol. *Int. J. Hydrogen Energy* **2019**, *44*, 18038–18049.
- (18) Phuruangrat, A.; Thoonchalong, P.; Thongtem, S.; Thongtem, T. Synthesis of CuS with Different Morphologies by Refluxing Method: Nanoparticles in Clusters and Nanoflakes in Spongelike Clusters. *Chalcogenide Lett.* **2012**, *9*, 421–426.
- (19) Bai, L.; Ye, X.; Song, C.; Chen, H.; Cai, B.; Bai, Y.; Xu, C.; Li, Z. The Surfactant-Free Synthesis of Hollow CuS Nanospheres: Via Clean Cu₂O Templates and Their Catalytic Oxidation of Dye Molecules with H₂O₂. *RSC Adv.* **2016**, *6*, 83885–83889.
- (20) Munnik, P.; Wolters, M.; Gabriëlsson, A.; Pollington, S. D.; Headdock, G.; Bitter, J. H.; De Jongh, P. E.; De Jong, K. P. Copper Nitrate Redispersion to Arrive at Highly Active Silica-Supported

- Copper Catalysts. *J. Phys. Chem. C* **2011**, *115*, 14698–14706.
- (21) Patterson, A. L. The Scherrer Formula for X-Ray Particle Size Determination. *Phys. Rev.* **1939**, *56*, 978–982.
- (22) ICDD (2019) PDF-4+ 2019 (Database). Edited by Dr. Soorya Kabekkodu. *Int. Cent. Diffr. Data, Newt. Square, PA, USA*.
- (23) Van Der Stam, W.; Rabouw, F. T.; Geuchies, J. J.; Berends, A. C.; Hinterding, S. O. M.; Geitenbeek, R. G.; Van Der Lit, J.; Prévost, S.; Petukhov, A. V.; De Mello Donega, C. In Situ Probing of Stack-Templated Growth of Ultrathin Cu_{2-x}S Nanosheets. *Chem. Mater.* **2016**, *28*, 6381–6389.
- (24) Tang, A.; Qu, S.; Li, K.; Hou, Y.; Teng, F.; Cao, J.; Wang, Y.; Wang, Z. One-Pot Synthesis and Self-Assembly of Colloidal Copper(I) Sulfide Nanocrystals. *Nanotechnology* **2010**, *21*, 285602.
- (25) Han, W.; Yi, L.; Zhao, N.; Tang, A.; Gao, M.; Tang, Z. Synthesis and Shape-Tailoring of Copper Sulfide/Indium Sulfide-Based Nanocrystals. *J. Am. Chem. Soc.* **2008**, *130*, 13152–13161.
- (26) Kuzuya, T.; Tai, Y.; Yamamuro, S.; Sumiyama, K. Synthesis of Copper and Zinc Sulfide Nanocrystals via Thermolysis of the Polymetallic Thiolate Cage. *Sci. Technol. Adv. Mater.* **2005**, *6*, 84–90.
- (27) van Oversteeg, C. H. M.; Oropeza, F. E.; Hofmann, J. P.; Hensen, E. J. M.; de Jongh, P. E.; de Mello Donega, C. Water-Dispersible Copper Sulfide Nanocrystals via Ligand Exchange of 1-Dodecanethiol. *Chem. Mater.* **2018**, *31*, 541-552.



Chapter 5

Challenges and guidelines in
heterogeneous, liquid-phase
photocatalysis

Abstract *The original aim of this research was to study photocatalytic properties of Cu_{2-x}S nanoparticles. However, along the way we found that the Cu_{2-x}S nanoparticles showed only limited photocatalytic activity and that conducting photocatalytic experiments and interpreting results are not always straightforward due to the many variables influencing the reactions. In addition, results reported in literature were not always reproducible. In this chapter, we review various aspects of photocatalysis, including experimental techniques, data analysis, different variables influencing the reactions and the reporting of experimental results. The chapter provides practical guidelines on how to reliably conduct, interpret and report photocatalytic experiments, and is based on our own experience, as well as examples from literature.*

5.1 Introduction

Over the last decades, photocatalysis has attracted increasing interest for its use in environmental remediation (e.g., photocatalytic degradation of organic pollutants)^{1,2} and the generation of solar fuels (e.g., hydrogen evolution and CO_2 reduction).^{3,4} The field attracts researchers from several disciplines, most notably physics, materials science and catalysis. Figure 5.1 illustrates the growing importance by showing the increase in the number of publications on photocatalysis from 1992 to 2019 (Scopus database, February 2020).⁵ Model reactions are often used to probe the catalytic activity of novel materials. However, these reactions have complex mechanisms and are influenced by a variety of different parameters, which are often not taken into account when designing experiments and/or interpreting the results. It is a challenge to report all essential details of the experimental conditions, reference experiments and catalytic performance while including a clear discussion of the underlying mechanisms.

A few reviews and short communications address some common pitfalls and difficulties in photocatalytic experiments. For example, in 2006 Yan *et al.*, critically assessed the use of methylene blue as a reactant for photocatalytic activity tests and concluded that photosensitive dyes are less suitable probes for these tests.⁶ Several other researchers are also concerned with the use of dye degradation reactions as a method to assess photocatalytic activity.^{7,8} Nevertheless, dye degradation experiments remain a means of assessing the photocatalytic activity of a novel material (Figure 5.1). Guidelines for photocatalytic experiments, data interpretation and the reporting of results are offered in a few publications.⁹⁻¹⁸ However, many publications still lack essential details in the description of experimental conditions as well as control experiments, making it difficult to evaluate their value. In our own lab we have also found that performing and reproducing photocatalytic experiments is not always straightforward.

In this chapter, we provide an overview of the most important challenges in photocatalysis. We provide general guidelines for experimental techniques, data analysis and reporting of catalytic performance and include representative examples from our

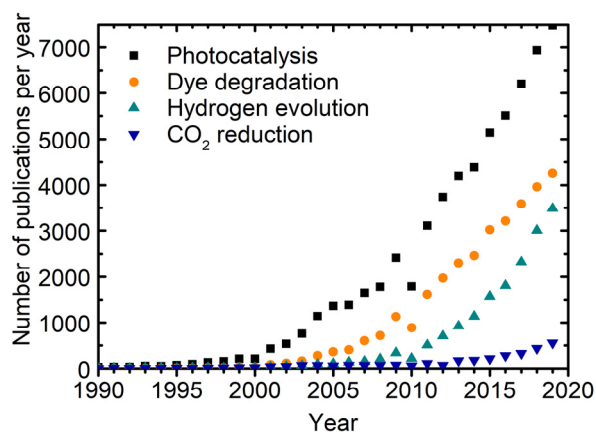


Figure 5.1 Evolution of the publications on photocatalysis from 1990 to 2019 and the share of papers on dye degradation, hydrogen evolution and CO₂ reduction within these numbers.⁵

own work, as well as some examples from literature. We hope that the practical guidelines are useful for researchers with backgrounds in physics, optics and materials science entering the field of catalysis, as well as for catalysis experts wanting to extend their work to photocatalysis.

5.2 Overview of common reactions, materials and experimental techniques

The term photocatalysis is used for reactions in which charge carriers are generated by the absorption of photons by a semiconductor material. These charge carriers can be used to drive chemical reactions at the surface of a photocatalyst. In general, two types of photocatalysis can be distinguished.^{16,19} Firstly, similar to ‘classical’ catalysis, a photocatalyst can reduce the activation energy of a chemical reaction and thereby accelerate a reaction that occurs spontaneously ($\Delta G < 0$). An example of this is the oxidative degradation of dye molecules. Dye degradation studies are often used to assess the performance of novel photocatalyst materials, typically motivated by the fact that dye degradation is a model reaction for the decomposition of organic pollutants in waste water. Frequently studied dyes in these types of reactions are methylene blue, methyl orange, malachite green and rhodamine B. These dyes are chosen due to their light absorption in the visible region, which makes it simple to follow their degradation using UV-Vis absorption spectroscopy.

In addition, the term photocatalysis is used for reactions that are thermodynamically uphill ($\Delta G > 0$), but can proceed with light in the presence of a photocatalyst. This includes hydrogen evolution from water or protons and CO₂ reduction. The interest in

hydrogen evolution is motivated by the need for solar fuels as an alternative for fossil fuels. However, the hydrogen evolution reaction is often studied in the presence of a sacrificial agent. This is not representative of true water splitting, for which oxygen evolution is typically the limiting reaction. Relating these studies to overall water splitting must be done with care, as the strong oxidants can have a large influence on the reaction, as will be discussed in more detail in section 5.3.5. In addition, large scale industrial implementation of hydrogen evolution using sacrificial agents that are valuable chemicals, *e.g.*, methanol, is not meaningful.²⁰ Similar to photocatalytic hydrogen evolution from water, photocatalytic CO₂ reduction, combined with proton or water reduction, allows for the production of a variety of chemicals and fuels in a sustainable way only if coupled to a meaningful oxidation counter reaction.^{21,22}

Although a detailed discussion of materials studied in photocatalysis is outside the scope of this chapter, a brief overview of the most studied materials is given below. Figure 5.2 gives an overview of the band edge positions and bandgaps of some commonly used semiconductors.^{23–29} One of the most investigated photocatalysts is TiO₂ due to its natural abundance, stability in aqueous solutions and capacity to both reduce and oxidize species.^{2,30} However, the relatively large bandgap of TiO₂ (3.2 eV) prevents the efficient use of visible light, and thus of sunlight. Other metal oxides, such as ZnO, Fe₃O₄, Cu₂O and especially bismuth-based metal oxides, such as BiVO₄, have also been extensively investigated.^{20,31} Photocatalysts based on perovskites, such as SrTiO₃, have shown good photocatalytic properties due to their excellent opto-electronic properties, good stability and tunable composition.^{32–34} Moreover, metal sulfides such as CdS and Cu_{2-x}S attract interest as their relatively small bandgaps allows them to efficiently utilize sunlight.^{35,36}

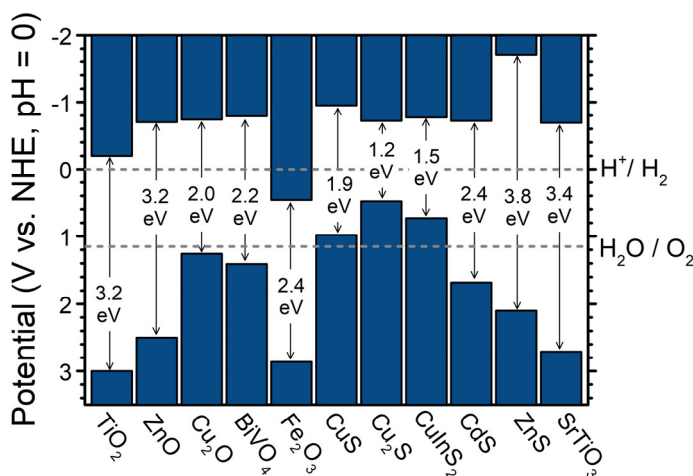


Figure 5.2 Schematic representation of the valence- and conduction band edge positions and band gap energies of semiconductors commonly used in photocatalysis. The band edge positions are obtained from refs [24–29].

The low stability of most metal sulfides and small-bandgap oxides due to photocorrosion is a downside. In laboratory studies, this low stability can be prevented by the addition of sacrificial agents such as S^{2-} .

Several experimental techniques can be used to follow the reactions mentioned above. Traditionally, the amount of hydrogen formed was evaluated volumetrically. A more sophisticated manner to quantify the amount of gasses evolved is gas chromatography (GC). Difficulties using this technique lie mainly in the practical implementation. Leaks in the system, dilution of the gas stream and calibration of the system can sometimes be challenging.

Upon CO_2 reduction, liquid phase products such as formic acid and methanol can form besides the gaseous products. Hence, it is important to analyze the liquid phase by *e.g.*, high-performance liquid chromatography (HPLC) or nuclear magnetic resonance (NMR) spectroscopy. As the products formed are usually present in low concentrations, it is helpful to minimize the volume of the liquid phase and in that way concentrate the formed products. In other photocatalytic reactions where the product of interest is not in the liquid phase, it is also useful to analyze the liquid phase. This gives for example information on any oxidation products of sacrificial agents or reaction intermediates in the case of dye degradation.

When studying dye degradation, the intensity of the light absorption at a fixed wavelength, followed by UV-Vis spectroscopy, is often taken as a quantitative measure of the dye concentration. This is experimentally straightforward as it is non-destructive, inexpensive and fast. However, although UV-Vis absorption spectroscopy is a powerful technique to follow the spectral changes of a reaction mixture, it does not give a complete picture of the dye degradation process. Decolorization of the reaction mixture can occur via different pathways, as will be discussed in more detail in section 5.3. Hence, additional analysis is needed to understand and quantify the photocatalytic performance. Furthermore, dye degradation experiments are generally motivated by the need to treat waste water and thus the efficiency of complete mineralization to non-toxic products like CO_2 , H_2O and N_2 is of interest. Consequently, additional experimental techniques are required to elucidate the reaction mechanisms, intermediate species and resulting products. Liquid chromatography - mass spectrometry (LC-MS) and GC-MS are powerful techniques to analyze also the colorless intermediates and reaction products. In addition, total organic carbon (TOC) analysis over time should be used to investigate the mineralization of the photocatalytic dye degradation.^{37,38}

5.3. Is the change in concentration of reactants and products really due to photocatalysis?

When performing photocatalytic experiments, data can sometimes be misleading as side reactions and processes can also occur and lead to changes in the concentration of the products or reactants. Therefore, it is important to have a thorough understanding of the photocatalytic process, and of possible side reactions and other parameters influencing the concentration.

5.3.1 Adsorption of reactants onto the catalyst

An important process occurring in a solution containing a solid catalyst and reactants is adsorption/desorption of the reactants on the catalyst surface. Adsorption brings the reactant in close proximity to the photocatalyst. In addition, adsorption of reactants leads to a decrease in reactant concentration in solution, which can be misinterpreted as degradation or conversion of reactants. This is especially apparent in dye degradation experiments. Before analyzing the outcome of a dye degradation experiment with UV-Vis spectroscopy, solid catalyst particles are often separated from the solution to prevent the light absorption of the catalyst itself interfering with the absorbance of the dye. This however means that all dye molecules adsorbed on the catalyst are also removed from solution, leading to a decrease in dye concentration that is not caused by catalysis.

5

The concept of adsorption is even more important when working with photocatalysts on support materials, such as silica or zeolites. Even though the support might be inactive as a photocatalyst, it can act as an adsorbent for the reactants, causing a strong decrease in the amount of 'free' reactants in solution. Additionally, the adsorption of a large amount of reactant on the catalyst support, *e.g.*, zeolites and various silica supports, can efficiently concentrate a large amount of reactant close to the photocatalyst, improving the photocatalytic conversion.³⁹⁻⁴² Although in many experiments the amount of dye adsorbed is quantified before starting the photocatalytic reaction, the amount of reactants adsorbed can change during reaction, as is discussed below.

The adsorption of reactant molecules is often due to electrostatic interaction and consequently depends on the surface properties of the photocatalyst (*e.g.*, charge, presence of capping ligands) and the charge of the reactant.⁴³ In turn, the charge of the catalyst surface and reactant depends on the pH of the solution. For example, working at a pH above the pK_a of the reactant molecule results in a negatively charged species that will be attracted to a positively charged photocatalyst surface, but repelled from a negatively charged catalyst surface. As pH changes usually occur upon reaction, it is very important to monitor the pH of the reaction solution and if necessary, use a buffer solution to control the pH. If adsorption of the reactant on the catalyst and/or catalyst support is significant, it is suggested to perform adsorption studies at different pH values to get a better understanding of the charge of both the reactants and the photocatalyst

and catalyst support. In addition, adsorption studies can provide valuable information on the surface coverage of photocatalyst by the reactant, and on how this influences the efficiency of the photocatalyst.

Figure 5.3 shows an example of such an adsorption study, where the amount of rhodamine B adsorbed onto a silica support material is plotted versus pH. At low pH the dye molecules adsorb on the silica support as there is no repulsion between the neutral silica support and the positively or negatively charged dye molecules. Increasing the pH above the point of zero charge of the silica (pH 2-4) and the pK_a of the dye molecule (3.7), will result in both species being negatively charged.⁴⁴ Consequently, with increasing pH, the negatively charged reactant and the negatively charged support surface repel each other and hence the adsorption decreases.

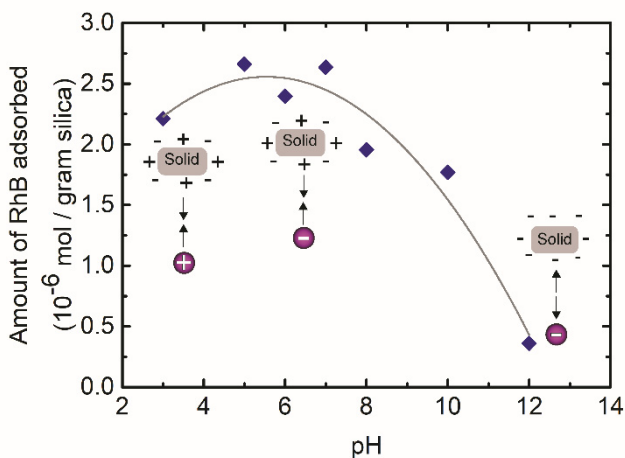


Figure 5.3 Influence of pH on the adsorption of rhodamine B on a silica support material (10 mg of silica support in 20 mL of 10 mg/L rhodamine B aqueous solution).

5.3.2 Interpretation of UV-Vis absorption spectra

When using absorption spectroscopy for the analysis of photocatalysis, several factors influence the absorption spectra of the reactants and/or products. This complicates the accurate determination of concentration, especially when monitoring a single wavelength. If the photocatalyst and dye absorb light in the same spectral region, overlap between the absorption of both species makes it difficult to obtain reliable kinetic data from the absorption spectra. This can be overcome by separating the solid catalyst from the solution by filtration or centrifugation. However, as discussed above, dye molecules are usually adsorbed on to the photocatalyst, which can lead to an overestimation of the amount of dye degraded. In addition, the adsorption of a dye on a catalyst or support can also change its optical absorption spectrum compared to 'free' dye molecules in

solution. For example, the absorption maxima of dyes adsorbed on TiO_2 have been found to shift to shorter wavelengths compared to those in solution and different hypotheses were formulated for the origin of this blue-shift, such as aggregation effects or deprotonation of functional groups.^{45–47}

Furthermore, both the position and the intensity of an absorption band can be affected by pH, which usually changes during photocatalyzed reaction.^{44,48–51} A clear example here is 4-nitrophenol, a reactant frequently used to study photocatalysis.^{52,53} Figure 5.4 shows the absorption spectra of 4-nitrophenol in aqueous solutions above and below its pK_a of 7.15.^{48,49,51} At a pH below the pK_a value, the molecule is protonated and has an intense absorption band at 316 nm. With increasing pH, the molecule is deprotonated and hence the intensity of the absorption band at 316 nm diminishes, while an absorption band at 398 nm appears, originating from the deprotonated form of 4-nitrophenol.

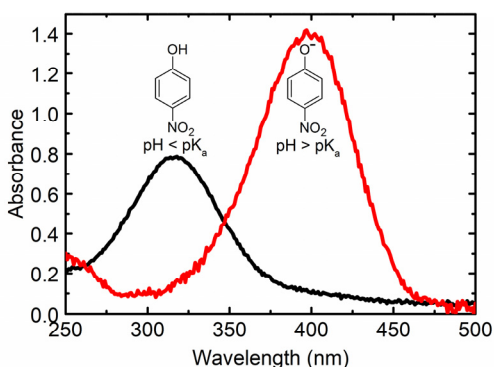


Figure 5.4 Absorption spectra of 4-nitrophenol in solutions with a pH below (black) and above (red) the pK_a (7.15) of 4-nitrophenol (0.005 M 4-nitrophenol in milliQ water ($\text{pH} < \text{pK}_a$, black line) and in a 0.1 M solution of NaBH_4 ($\text{pH} > \text{pK}_a$, red line).

Another challenge when using UV-Vis spectroscopy to follow the degradation of dye molecules is the optical absorption of reaction intermediates, especially if the absorption of these intermediates overlaps with the absorption of the dye. An example here is the N-deethylation of rhodamine B, a reaction often used in photocatalytic dye degradation. Upon N-deethylation of rhodamine B, several intermediates can be formed that absorb at slightly shorter wavelengths than rhodamine B.^{54,55} The absorption feature of the rhodamine B overlaps with that of the intermediate species and hence monitoring the absorption maximum of rhodamine B can be misleading. Due to the overlap between the absorption features of the intermediates and the different extinction coefficients of these intermediates and the dye molecule, it is challenging to determine the concentration of the dye in a reliable manner and hence to obtain reliable kinetic data.

5.3.3 The importance of reference experiments in the dark

The absorption of light leads to photogenerated or excited charge carriers that can subsequently drive redox reactions. However, some processes occur also in the absence of light, such as the establishment of an adsorption/desorption equilibrium of the reactant on the photocatalyst surface, heterogeneous catalysis or spontaneous degradation of the reactant. Hence it is vital to investigate the reaction mixture in the dark for a prolonged period of time prior to starting irradiation.

An interesting example of possible effects in the dark is based on our work on colloidal CuS photocatalysts. Figure 5.5 shows the absorption spectra over time of a rhodamine B solution in the dark and in the presence of S^{2-} -capped CuS nanoplatelets. The absorption peak of rhodamine B decreases in intensity and shifts to shorter wavelengths over time. This indicates that, even without light, degradation and deethylation of rhodamine B takes place. Control experiments on the influence of Na_2S , formamide and Cu^{2+} on rhodamine B show that this is caused by the CuS interacting with the rhodamine B rather than any other species that might be present in solution. Although the significant degradation of rhodamine B by CuS nanoparticles in dark in itself is an interesting subject for further study, it shows that this reaction is less suitable to assess the photocatalytic activity of this material.^{56,57}

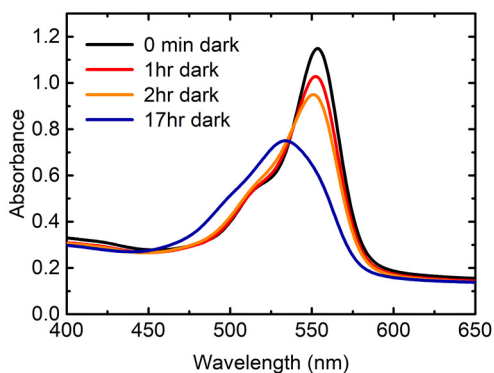


Figure 5.5 Absorption spectra of rhodamine B taken after different periods of time in dark in the presence of S^{2-} -capped CuS nanoplatelets. The absorption feature of rhodamine B clearly shifts over time, indicating that N-deethylation of rhodamine B by CuS nanoplatelets occurs even without illumination (40 mL 5 mg/L Rhodamine B with 0.13 mmol/L CuS nanoplatelets in the dark).

5.3.4 Potential side effects of illumination

Control experiments under illumination, but in the absence of the catalyst should also always be performed to investigate the stability of reactants upon light irradiation and the reactivity of additives such as sacrificial agents (section 5.3.5). However, they are rarely reported in literature. When testing the stability of some commonly used dyes upon light irradiation, we found that both methylene blue and malachite green slowly decompose upon light irradiation also in the absence of a photocatalyst (Figure 5.6). Even though the degradation of the dye can be more prominent in the presence of a photocatalyst, great care has to be taken when using these dyes as model compounds, as this photochemical degradation will influence the kinetics of the photocatalytic degradation. In contrast, rhodamine B is stable upon light irradiation under these conditions and is thus more suitable for photocatalytic activity tests.

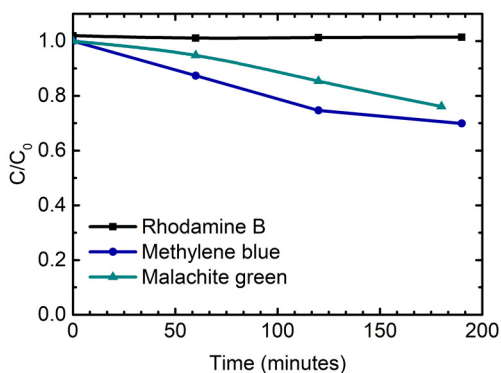


Figure 5.6 Concentration of three commonly used dyes as a function of time upon light irradiation in the absence of a photocatalyst. (20 mL 5 mg/L dye solution, constant $T=30\text{ }^{\circ}\text{C}$, irradiated with 75 W Xe lamp, $\lambda = 315\text{-}710\text{ nm}$, light intensity at reactor $100\text{ mW} \cdot \text{cm}^{-2}$).

In photocatalysis charge carriers are generated by the absorption of light and hence the reaction rate depends on the light intensity. A few studies reported the influence of light intensity on the reaction rate and show that generally two regimes exist.⁵⁸⁻⁶² At low light intensities, the reaction rate increases linearly with increasing light intensity. With increasing light intensities recombination of electrons and holes becomes more apparent, resulting typically in a dependence of the reaction rate on the square root of the intensity. At high light intensities, diffusion limitations might also play a role. Studying the dependence of the reaction rate on the light intensity can thus help to elucidate if a process is truly photocatalytic.

Another important factor that can influence photocatalytic reactions is temperature. During the experiment samples are irradiated with light, which might also comprise an IR component, and consequently the reaction mixture can heat up. For example, in our

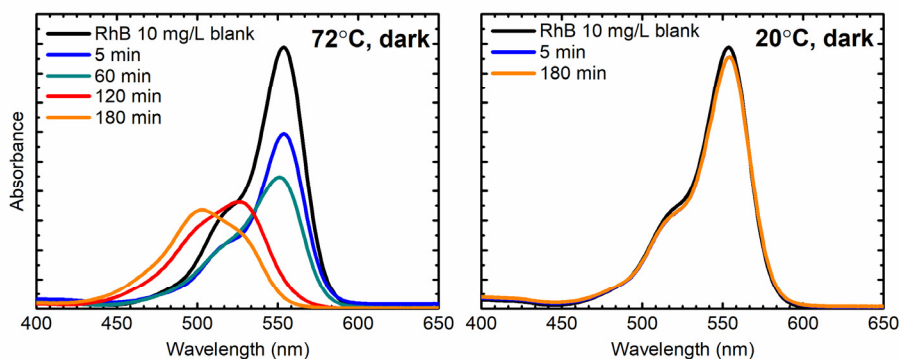


Figure 5.7 Absorption spectra of a rhodamine B solution over time for a control experiment in which a rhodamine B solution containing silica supported CuS nanocrystals is kept in dark at **a)** 72 °C and **b)** 20 °C. The clear decrease and shift of the rhodamine B absorption feature for the reaction mixture at 72 °C shows the temperature has a large influence on the degradation of the dye and hence the importance of temperature control during photocatalytic experiments. (Reaction conditions: 30 mL 10 mg/L rhodamine B solution with 20 mg of silica supported CuS (15 wt% Cu)).

studies, we found that upon irradiating a silica supported CuS photocatalyst in a glass reactor with 30 mL rhodamine B solution with a 150 W Xenon lamp without any filters,⁶³ the temperature of the solution increased up to 72 °C within 60 minutes. When performing a control experiment containing the silica supported CuS in a rhodamine B solution under dark conditions at a high temperature of 72 °C,⁶⁴ it was found that absorption feature of rhodamine B decreased and shifted towards shorter wavelengths as well, indicating N-deethylation in the dark at elevated temperatures. This control experiment demonstrates the importance of temperature control, for example by using a water-cooled reactor and IR filter.

Besides photocatalysis, the degradation of dyes can proceed via self-sensitization, as first described by Watanabe in 1977 for the N-deethylation of rhodamine B adsorbed onto cadmium sulfide.⁵⁴ In this process the dye molecules themselves are optically excited and transfer their photoexcited electrons to the conduction band of the photocatalyst (Figure 5.8). These electrons can then react with adsorbed species, such as O₂, to form radicals that can further degrade the destabilized dye cation radical. When irradiating the sample with light with an energy that can be absorbed by both the photocatalyst and the dye, it is not possible to determine if the dye is degraded via self-sensitization or via photocatalysis. This problem can be circumvented by using such a combination of dye and photocatalyst, that a wavelength can be selected at which only the photocatalyst is excited.

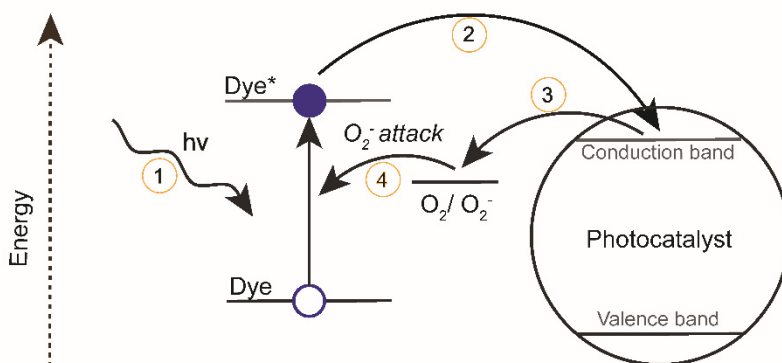


Figure 5.8 Schematic representation of the mechanism to degrade organic dyes upon light illumination via self-sensitization. In this process, the dye is excited upon photo illumination (1). The photogenerated electron can be transferred to the conduction band of the photocatalyst (2). Subsequently, the electron can react with adsorbed species, such as O_2 to form radicals (3) which can further degrade the destabilized dye cation radical (4).

5.3.5 The influence of additives and impurities

It is crucial to understand the role of impurities, additives and solvents in the reaction, especially if the reaction rates are relatively low. For example, in CO_2 reduction, other carbon-containing molecules present in solution can be involved in the reaction as they will react more readily than CO_2 molecules.^{65,66} Mul. *et al.*, used isotopic labeling experiments with a $^{13}CO_2$ gas feed to show that carbon residues on the catalyst surface could explain most of the reaction products reported in literature.⁶⁷ Similarly, impurities in *e.g.*, the gas feed or originating from the catalyst preparation can contribute to the formation of products. Besides isotopic labeling, reference experiments in the absence of the reactant are also crucial. In addition, keeping track of byproducts formed during the reaction can provide information on the catalytic cycle. For example, during water splitting, H_2 and O_2 should be formed in a two to one ratio. If a different ratio is observed, this means that other chemicals, *e.g.*, sacrificial agents or impurities, are involved in the reaction or that a subsequent reaction with one of the products occurs.

The role of additives should be investigated in the absence and the presence of light. In many reports on photocatalytic dye degradation H_2O_2 is added.⁶⁸⁻⁷³ However, in the presence of H_2O_2 , which is a strong oxidant, dyes can be degraded without photoexcitation. Several studies show the degradation of methylene blue and/or rhodamine B in the presence of a CuS catalyst and H_2O_2 , but in the dark.⁶⁸⁻⁷³ The reaction rate of the dye degradation in the presence of CuS and H_2O_2 is in many cases similar when comparing light and dark conditions, due to the formation of reactive hydroxyl radicals from H_2O_2 , which can oxidize the dye molecules.^{68,69,71,72} Hence, the use of H_2O_2 when studying the photocatalytic activity of materials is discouraged.

Sacrificial agents are often added in a photocatalytic reaction in order to selectively study either the oxidation or reduction reaction by overcoming the kinetic limitations of the other half reaction. Although the sacrificial agent often influences both half reactions, this is rarely discussed. When taking hydrogen evolution from water as an example, alcohols such as methanol or inorganic ions such as sulfides are typically used as sacrificial hole scavengers to circumvent the challenging water oxidation step and prevent photocorrosion of the photocatalyst by the photogenerated holes. However, the oxidation of alcohols such as methanol can lead to the formation of hydrogen and C1 products, and intermediates that can inject extra electrons into the valence band of the semiconductor.^{74,75} Similarly, when using $\text{Na}_2\text{S}/\text{Na}_2\text{SO}_3$ as sacrificial agent, hydrogen can be produced via protonation of S^{2-} and subsequent oxidation of SH^- by the photogenerated holes.¹¹ The oxidation of these sacrificial agents can thus contribute to the overall yield of hydrogen, leading to an overestimation of the photocatalytic activity. An example of this is shown in Figure 5.9, where an aqueous solution of 0.25 M $\text{Na}_2\text{S}/\text{Na}_2\text{SO}_3$ clearly produced hydrogen upon illumination with a 150 W Xenon lamp. A detailed analysis of the role of the sacrificial agent in both dark and light conditions is thus of great importance.

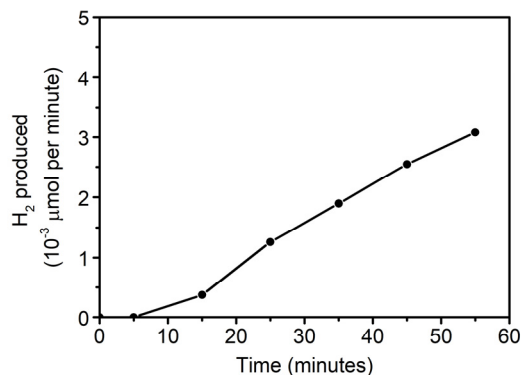


Figure 5.9 Formation of hydrogen upon illumination of an aqueous 0.25 M $\text{Na}_2\text{S}/\text{Na}_2\text{SO}_3$ solution irradiated with a 150 W Xenon lamp without the use of any filters and lenses. The evolved gas was transported by argon carrier gas (1 mL/min) and analyzed using a Shimadzu GC-2014, equipped with a thermal conductivity detector.

5.4. How to facilitate benchmarking results

When reporting the catalytic activity of new materials it is of great interest to compare these results to literature. However, this remains difficult as there is no standard manner to report quantitative results in photocatalysis. In this section we will highlight important factors to report the outcomes of photocatalytic experiments, also based on standard practice in 'classical' thermal catalysis.

5.4.1 Influence of the catalyst concentration

Whereas in ‘classical’ catalysis the reaction rate is typically proportional to the exposed active surface area, and hence the amount of catalyst, the reaction rate of a photocatalytic process can also be limited by the light intensity. This is illustrated in Figure 5.10, which compares the dependence of the conversion on the catalyst concentration for ‘classical’ catalysis and photocatalysis. In ‘classical’ catalysis, the conversion increases linearly with the catalyst concentration. This is not the case for a photocatalytic reaction, where the dependence of the conversion on the catalyst concentration can be split into two regimes. At low catalyst concentrations, in which only a small fraction of the incoming light is absorbed, the conversion increases with increasing catalyst concentration. However, at high catalyst concentrations a conversion plateau is reached, as the conversion is limited by the intensity of the incoming light.^{12,76,77}

In thermal catalysis the turn-over-frequency (TOF), the number of molecules converted per active catalyst *surface* site, is the standard measure for catalytic activity, although also activities per time unit per gram of catalyst are quite common.^{17,78–80} However, for photocatalytic activity, the reaction rate per amount of catalyst or number of active sites is meaningless if the illumination conditions are not known in detail. A more logical measure is the quantum efficiency or quantum yield of the system, as is discussed in more detail in the next section. However, it should be clear in which region of the dependence on the catalyst concentration this number is reported and hence, the catalyst concentration should be mentioned. In addition, as catalytic reactions proceed only at the surface of the catalyst, the total surface area of the photocatalyst is also an important parameter to report.

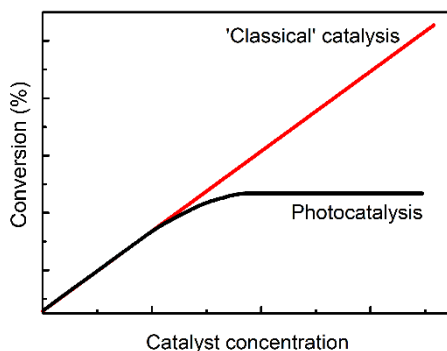


Figure 5.10 Schematic representation of the dependence of the reaction rate on the catalyst concentration for a ‘classical’ catalytic reaction (red) and of a photocatalytic reaction (black).

5.4.2 Reporting efficiencies in photocatalysis

The terminology used to describe photocatalytic efficiency is often confusing, originating from different fields of study using different words for the same concept. Table 5.1

summarizes the most important efficiency terms in photocatalysis. It is not very meaningful to stress only reaction rates per weight of catalyst. Therefore, the preferred way to report data is by quoting the quantum efficiencies or yields of the system.^{9,10,76,77} The term quantum yield is reserved for irradiation with a monochromatic light source, whereas the term quantum efficiency is used for irradiation with a broadband light source.^{12,76} Most meaningful is the internal quantum efficiency, which is defined as the amount of absorbed photons that are converted into reacting electron-hole pairs.

However, the measurement of the amount of absorbed photons is not always straightforward in heterogeneous reaction systems due to scattering and reflection of light by suspended particles.⁷⁷ The amount of incoming light is easier to determine. Hence, often the external quantum efficiency or photonic efficiency is reported, that is the fraction of *incoming* photons converted into electron-hole pairs that are used in the photocatalytic reaction. The external quantum efficiency gives a lower limit of the real internal quantum efficiency. Since the amount of absorbed photons depends on many factors (*e.g.*, the reactor used, energy of the photons), comparing external quantum efficiencies is not always meaningful, especially when comparing results between different experimental conditions.

Ultimately, when considering real applications in water treatment and solar fuel production, the energy efficiency and cost-effectiveness of the process are of importance. Especially in the field of solar fuels, where solar energy is converted into chemical energy, the energy efficiency of this conversion should be reported. The energy efficiency can be described by the energy input divided by the chemical energy stored in the product. Here, the energy input includes solar energy, but also all other energy used in the process, such as the feedstock energy and any operational energy, like energy to drive pumps and stirrers.

Table 5.1 Overview of various efficiency terms and their definitions used in the field of photocatalysis

Internal quantum efficiency	$\frac{\text{number of reacted electrons or holes}}{\text{number of absorbed photons (broadband light)}} \times 100$
Internal quantum yield	$\frac{\text{number of reacted electrons or holes}}{\text{number of absorbed photons (monochromatic light)}} \times 100$
External or apparent quantum efficiency (= photonic efficiency)	$\frac{\text{number of reacted electrons or holes}}{\text{number of incident photons (broadband light)}} \times 100$
External or apparent quantum yield	$\frac{\text{number of reacted electrons or holes}}{\text{number of incident photons (monochromatic light)}} \times 100$
Energy efficiency	$\frac{\text{energy input}}{\text{energy output of the products of interest}} \times 100$

5.4.3 Importance of elucidating the reaction mechanism

For more complicated reactions than hydrogen evolution, the determination of the internal and external quantum efficiencies is further complicated by the need for a detailed understanding of the reaction mechanism, as it determines the number of electron-hole pairs required for the reaction. This can be challenging in for example dye degradation experiments, where many different degradation pathways are possible. Using the degradation of rhodamine B as an example, the dye can be degraded via various pathways, such as N-deethylation, cleavage of the conjugated structure or ring opening. These degradation pathways can in turn be initiated by charge carriers from different origins: self-sensitization (as discussed in section 5.3.4), direct oxidation by the photogenerated hole or via an indirect oxidation by $\text{OH}\cdot$.^{54,81–84} These different mechanisms all use a different number of electron-hole pairs to degrade the rhodamine B molecule and will thus give different quantum efficiencies.

5.4.4 Experimental set-up and reproducibility

As each lab has its own set-up for photocatalytic testing, it is important to report all experimental conditions, such as reactor volume, catalyst, reactant and sacrificial agent concentrations, pH and temperature. In addition, we recommend to monitor and report variable reaction parameters such as pH and temperature before and after reaction. Furthermore, elaborate information on the excitation conditions should be reported, such as power and wavelengths of the light used (monochromatic or broadband), optical irradiance at the sample (mW cm^{-2}), reflection by the cell, amount of light absorbed in reactor and the use of filters and lenses.¹³ It is helpful to include experimental information like schemes or photographs of the set-up and the spectrum of the light source in the supporting information. In addition, the comparison of results between different research groups could be facilitated by including a reference measurement on a commercial catalyst (e.g., Degussa P-25 TiO_2 as photocatalyst), preferably after a standard pretreatment as is also routinely done in thermal catalysis.¹⁴ This will show the performance of a known material in a specific experimental set-up and hence allows for easier comparison.

Although thorough characterization of catalyst not only before reaction but also after use is a standard procedure in thermal catalysis, the characterization of the catalyst during or after reaction is rarely reported in photocatalysis. While *in situ* characterization techniques are often not easily accessed, characterization of the catalyst after reaction gives important information on the stability of the catalyst under reaction conditions. For example, transmission electron microscopy (TEM) and x-ray diffraction (XRD) techniques can give information on particle growth or a phase changes of the catalyst, and give a first indication of catalyst loss for instance by leaching. Performing elemental analysis, such as inductively coupled plasma optical emission spectroscopy (ICP-OES) or atomic absorption spectrometry (AAS), on the solution after catalysis can quantify dissolution of the catalyst under reaction conditions. If species do leach into solution, it

is important to investigate their influence on the catalytic reaction. This can be done by separating the solid photocatalyst from the solution and continuing the reaction with only the solution under the same conditions. If the leached species in solution are not contributing to the photocatalytic reaction, there should be no further conversion.

Recycling the catalyst by performing the same reaction several times, analogous to the “hot filtration test” in thermal catalysis, can give information on the stability and robustness of the material. As handling and/or storage between two subsequent reaction cycles can influence the material (*e.g.*, by oxidation), it is important to report the conditions that the material was exposed to in between subsequent reaction cycles. In addition, such recyclability tests should be performed at low conversions, to ensure the conversion is not limited by the availability of the substrate.¹⁷ This can be realized by using low catalyst concentrations or high reactant concentrations.

As in every experiment, checking the reproducibility is vital, even more so because often small quantities of product are formed and reactions are often run only for a short time. Experiments can be influenced by several factors, from the material preparation to measurement techniques and it is valuable to know what the standard deviation between experiments is. Hence, it is important to perform experiments multiple times, and at least for some hours.

5.5. Summary and compact series of experimental guidelines

The field of photocatalysis is an exciting, upcoming field with potential applications in environmental remediation and the production of solar fuels. However, the model reactions used to probe the photocatalytic performance of new materials often have complex mechanisms and are influenced by a variety of different parameters. To facilitate the execution, interpretation and reporting of photocatalytic experiments, we briefly summarize the above in the form of some practical guidelines:

The following reference experiments should always be performed:

- **Experiments with catalyst in the dark**, to study the effect of adsorption/desorption of reactants, possible side reactions in the dark by heterogeneous catalysis or spontaneous degradation of reactants and the effect of additives such as H₂O₂.
- **Experiments without catalyst under light illumination**, to study the stability of the reactants under light illumination and possible side reactions of for example the sacrificial agents.
- **Adsorption experiments with varying pH and reactant concentration**, since the adsorption/desorption can largely influence the catalytic performance by concentrating reactants close to the active sites.

- **Experiments with different catalyst concentrations**, to find the dependence of the conversion on catalyst concentration and the regime at which the conversion is independent of the catalyst concentration.
- **Experiments with different light intensities**, to show the reaction rate is proportional to the amount of light absorbed at sufficiently high catalyst concentrations.
- When using UV-Vis absorption spectroscopy to quantify reactants and products, **great care should be taken in the interpretation of data**, as this can be complicated by the of intermediate species or the catalyst itself, as well as the dependence of the position and intensity of an absorption band on the reaction conditions (*e.g.*, pH).

When reporting results, the following factors are important to include:

- **All performed reference experiments**
- **Extensive experimental details**, such as experimental set-up, light intensity, wavelength(s) of the light, amount of light absorbed in reactor, filters and lenses used, changes of pH and temperature upon reaction.
- **Quantum efficiencies of the reaction**, reported at the sufficiently high catalyst concentrations.
- **The stability of the catalyst**, including characterization of the catalyst after reaction, analyzing the reactivity of any leached species in solution and recyclability tests.
- An effort in understanding **the underlying reaction mechanism**, including identifying the rate-limiting step of the reaction. In addition, accompanying reactions of *e.g.*, sacrificial agents must also be discussed.
- **Experiments to verify the origin of the reaction products**, as other species (*e.g.*, carbon-containing precursors or sacrificial agents) in the reaction mixture can often contribute to the formation of products.
- **Reproducibility of the results**, as the photocatalytic process can be influenced by many factors (*e.g.*, light scattering, reactor design, catalyst preparation).

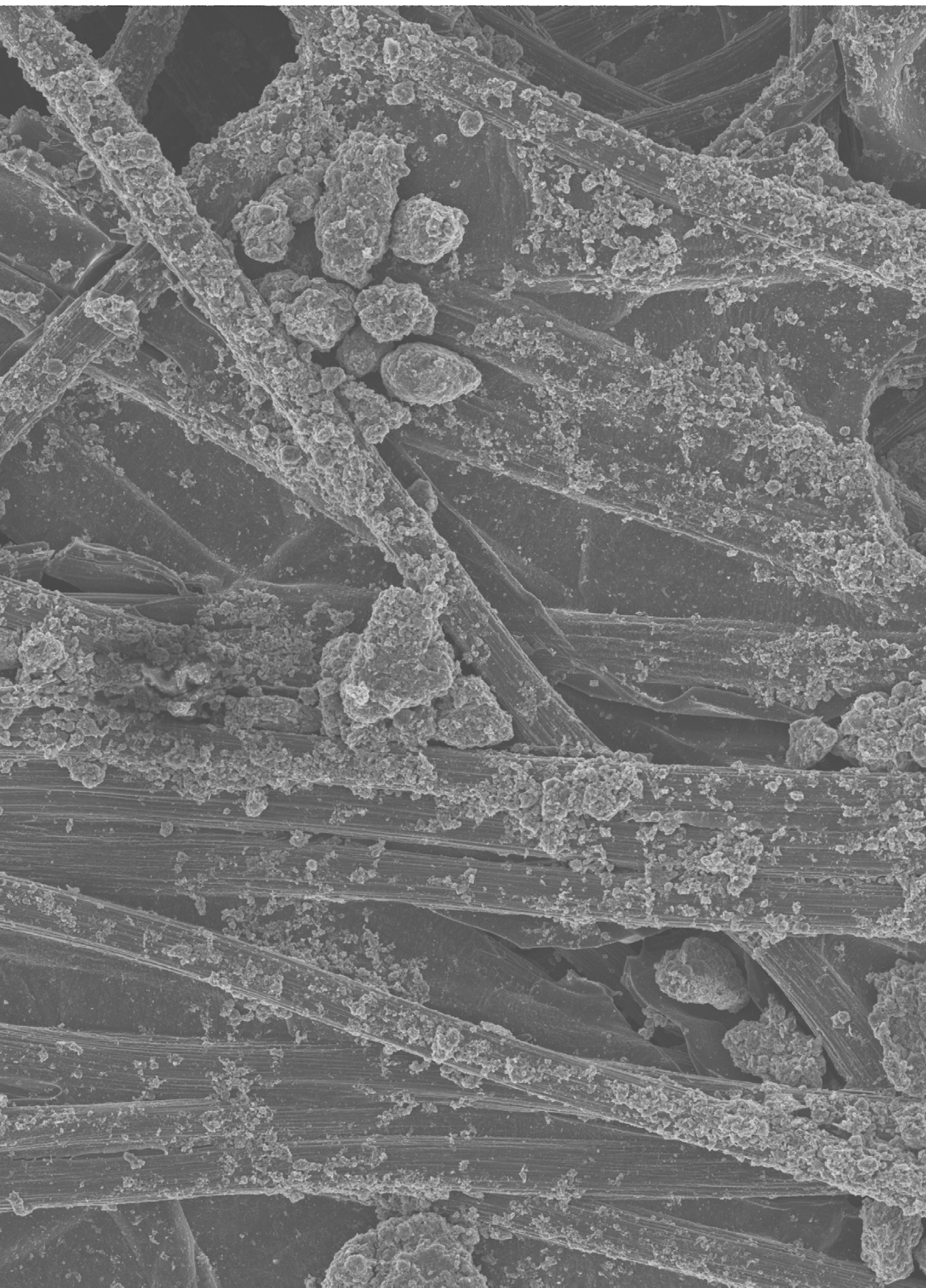
5.6 References

- (1) Byrne, C.; Subramanian, G.; Pillai, S. C. Recent Advances in Photocatalysis for Environmental Applications. *J. Environ. Chem. Eng.* **2018**, *6*, 3531–3555.
- (2) Pelaez, M.; Nolan, N. T.; Pillai, S. C.; Seery, M. K.; Falaras, P.; Kontos, A. G.; Dunlop, P. S. M.; Hamilton, J. W. J.; Byrne, J. A.; O’Shea, K.; et al. A Review on the Visible Light Active Titanium Dioxide Photocatalysts for Environmental Applications. *Appl. Catal. B Environ.* **2012**, *125*, 331–349.
- (3) Bhatt, M. D.; Lee, J. S. Nanomaterials for Photocatalytic Hydrogen Production: From Theoretical Perspectives. *RSC Adv.* **2017**, *7*, 34875–34885.
- (4) Joy, J.; Mathew, J.; George, S. C. Nanomaterials for Photoelectrochemical Water Splitting – Review. *Int. J. Hydrogen Energy* **2018**, *43*, 4804–4817.
- (5) Scopus database, February 2020, searched in “Article title, abstract and keywords”. Search terms: “photocatalysis”, “photocatalysis AND dye degradation”, “photocatalysis hydrogen evolution” and “photocatalysis and CO₂.”
- (6) Yan, X.; Ohno, T.; Nishijima, K.; Abe, R.; Ohtani, B. Is Methylene Blue an Appropriate Substrate for a Photocatalytic Activity Test? A Study with Visible-Light Responsive Titania. *Chem. Phys. Lett.* **2006**, *429*, 606–610.
- (7) Mitoraj, D.; Lamdab, U.; Kangwansupamonkon, W.; Pacia, M.; Macyk, W.; Wetchakun, N.; Beranek, R. Revisiting the Problem of Using Methylene Blue as a Model Pollutant in Photocatalysis: The Case of InVO₄/BiVO₄ Composites. *J. Photochem. Photobiol. A Chem.* **2018**, *366*, 103–110.
- (8) Rochkind, M.; Pasternak, S.; Paz, Y. Using Dyes for Evaluating Photocatalytic Properties: A Critical Review. *Molecules* **2015**, *20*, 88–110.
- (9) Parrino, F.; Loddo, V.; Augugliaro, V.; Camera-Roda, G.; Palmisano, G.; Palmisano, L.; Yurdakal, S. Heterogeneous Photocatalysis: Guidelines on Experimental Setup, Catalyst Characterization, Interpretation, and Assessment of Reactivity. *Catal. Rev. - Sci. Eng.* **2019**, *61*, 163–213.
- (10) Buriak, J. M.; Kamat, P. V.; Schanze, K. S. Best Practices for Reporting on Heterogeneous Photocatalysis. *ACS Appl. Mater. Interfaces* **2014**, *6*, 11815–11816.
- (11) Kamat, P. V.; Jin, S. Semiconductor Photocatalysis: “Tell Us the Complete Story!” *ACS Energy Lett.* **2018**, *3*, 622–623.
- (12) Hoque, M. A.; Guzman, M. I. Photocatalytic Activity: Experimental Features to Report in Heterogeneous Photocatalysis. *Materials*. **2018**, *11*, 1990.
- (13) Parkinson, B. On the Efficiency and Stability of Photoelectrochemical Devices. *Acc. Chem. Res.* **1984**, *17*, 431–437.
- (14) Serpone, N.; Salinaro, A. Terminology, Relative Photonic Efficiencies and Quantum Yields in Heterogeneous Photocatalysis. Part I: Suggested Protocol. *Pure Appl. Chem* **1999**, *71*, 1996–1999.
- (15) Ohtani, B. Revisiting the Fundamental Physical Chemistry in Heterogeneous Photocatalysis: Its Thermodynamics and Kinetics. *Phys. Chem. Chem. Phys.* **2014**, *16*, 1788.
- (16) Ohtani, B. Photocatalysis A to Z. What We Know and What We Do Not Know in a Scientific Sense. *J. Photochem. Photobiol. C Photochem. Rev.* **2011**, *11*, 157–178.
- (17) Kramm, U. I.; Marschall, R.; Rose, M. Pitfalls in Heterogeneous Thermal, Electro and Photocatalysis. *ChemCatChem* **2019**, *11*, 2563–2574.
- (18) Buriak, J. M.; Jones, C. W.; Kamat, P. V.; Schanze, K. S.; Schatz, G. C.; Scholes, G. D.; Weiss, P. S. Virtual Issue on Best Practices for Reporting the Properties of Materials and Devices. *Chem. Mater.* **2016**, *28*, 3525–3526.
- (19) Zhu, S.; Wang, D. Photocatalysis: Basic Principles, Diverse Forms of Implementations and Emerging Scientific Opportunities. *Adv. Energy Mater.* **2017**, *7*, 1700841.
- (20) Van De Krol, R.; Liang, Y.; Schoonman, J. Solar Hydrogen Production with Nanostructured Metal Oxides. *J. Mater. Chem.* **2008**, *18*, 2311–2320.
- (21) Li, K.; An, X.; Park, K. H.; Khraisheh, M.; Tang, J. A Critical Review of CO₂ Photoconversion: Catalysts and Reactors. *Catal. Today* **2014**, *224*, 3–12.
- (22) Kim, J.; Kwon, E. E. Photoconversion of Carbon Dioxide into Fuels Using Semiconductors. *J. CO₂ Util.* **2019**, *33*, 72–82.
- (23) Fresno, F.; Portela, R.; Suárez, S.; Coronado, J. M. Photocatalytic Materials: Recent Achievements and near Future Trends. *J. Mater. Chem. A* **2014**, *2*, 2863–2884.
- (24) Habisreutinger, S. N.; Schmidt-Mende, L.; Stolarczyk, J. K. Photocatalytic Reduction of CO₂ on TiO₂ and Other Semiconductors. *Angew. Chemie Int. Ed.* **2013**, *52*, 7372–7408.
- (25) White, J. L.; Baruch, M. F.; Pander, J. E.; Hu, Y.; Fortmeyer, I. C.; Park, J. E.; Zhang, T.; Liao, K.; Gu, J.; Yan, Y.; et al. Light-Driven Heterogeneous Reduction of Carbon Dioxide: Photocatalysts and Photoelectrodes. *Chem. Rev.* **2015**, *115*, 12888–12935.

- (26) Chen, S.; Wang, L. W. Thermodynamic Oxidation and Reduction Potentials of Photocatalytic Semiconductors in Aqueous Solution. *Chem. Mater.* **2012**, *24*, 3659–3666.
- (27) Hashimoto, Y.; Takeuchi, K.; Ito, K. Band Alignment at CdS/CuInS₂ Heterojunction. *Appl. Phys. Lett.* **1995**, *67*, 980.
- (28) Liu, G.; Schulmeyer, T.; Thissen, A.; Klein, A.; Jaegermann, W. In Situ Preparation and Interface Characterization of TiO₂/Cu₂S Heterointerface. *Appl. Phys. Lett.* **2003**, *82*, 2269–2271.
- (29) Liu, G.; Schulmeyer, T.; Brötz, J.; Klein, A.; Jaegermann, W. Interface Properties and Band Alignment of Cu₂S/CdS Thin Film Solar Cells. *Thin Solid Films* **2003**, *431–432*, 477–482.
- (30) Gaya, U. I.; Abdullah, A. H. Heterogeneous Photocatalytic Degradation of Organic Contaminants over Titanium Dioxide: A Review of Fundamentals, Progress and Problems. *J. Photochem. Photobiol. C Photochem. Rev.* **2008**, *9*, 1–12.
- (31) Malathi, A.; Madhavan, J.; Ashokkumar, M.; Arunachalam, P. A Review on BiVO₄ Photocatalyst: Activity Enhancement Methods for Solar Photocatalytic Applications. *Appl. Catal. A Gen.* **2018**, *555*, 47–74.
- (32) Vesborg, P. C. K. Photocatalysis: HI-Time for Perovskites. *Nat. Energy* **2017**, *2*.
- (33) Kanhere, P.; Chen, Z. A Review on Visible Light Active Perovskite-Based Photocatalysts. *Molecules* **2014**, *19*, 19995–20022.
- (34) Park, G. Do; Lee, C. W.; Nam, K. T. Recent Advances and Perspectives of Halide Perovskite Photocatalyst. *Curr. Opin. Electrochem.* **2018**, *11*, 98–104.
- (35) Hao, H.; Lang, X. Metal Sulfide Photocatalysis: Visible Light Induced Organic Transformations. *ChemCatChem* **2019**, *11*, 1378–1393.
- (36) Zhang, K.; Guo, L. Metal Sulphide Semiconductors for Photocatalytic Hydrogen Production. *Catal. Sci. Technol.* **2013**, *3*, 1672.
- (37) Ribbens, S.; Meynen, V.; Steert, K.; Augustyns, K.; Cool, P. The Use of Small Volume TOC Analysis as Complementary, Indispensable Tool in the Evaluation of Photocatalysts at Lab-Scale. *Stud. Surf. Sci. Catal.* **2010**, *175*, 321–324.
- (38) Kus, M.; Ribbens, S.; Meynen, V.; Cool, P. Microvolume TOC Analysis as Useful Tool in the Evaluation of Lab Scale Photocatalytic Processes. *Catalysts* **2013**, *3*, 74–87.
- (39) Tanaka, K.; Fukuyoshi, J.; Segawa, H.; Yoshida, K. Improved Photocatalytic Activity of Zeolite- and Silica-Incorporated TiO₂ Film. *J. Hazard. Mater.* **2006**, *137*, 947–951.
- (40) Yamaguchi, K.; Inumaru, K.; Oumi, Y.; Sano, T.; Yamanaka, S. Photocatalytic Decomposition of 2-Propanol in Air by Mechanical Mixtures of TiO₂ Crystalline Particles and Silicalite Adsorbent: The Complete Conversion of Organic Molecules Strongly Adsorbed within Zeolitic Channels. *Microporous Mesoporous Mater.* **2008**, *117*, 350–355.
- (41) Mahalakshmi, M.; Priya, S. V.; Arabindoo, B.; Palanichamy, M.; Murugesan, V. Photocatalytic Degradation of Aqueous Propoxur Solution Using TiO₂ and H Zeolite-Supported TiO₂. *J. Hazard. Mater.* **2009**, *161*, 336–343.
- (42) Zainudin, N. F.; Abdullah, A. Z.; Mohamed, A. R. Characteristics of Supported Nano-TiO₂/ZSM-5/Silica Gel (SNTZS): Photocatalytic Degradation of Phenol. *J. Hazard. Mater.* **2010**, *174*, 299–306.
- (43) Mishra, A. K.; Hussain, C. M. *Nanotechnology for Sustainable Water Resources*; Wiley, 2018.
- (44) Ramette, R. W.; Sandell Yol, E. B.; W Ramette, B. R.; Sandell, E. B. Rhodamine b Equilibria. *J. Am. Chem. Soc.* **1956**, *78*, 4872–4878.
- (45) Ducasse, L.; Castet, F.; Méreau, R.; Nénon, S.; Idé, J.; Toupance, T.; Olivier, C. Structure and Absorption Properties of the C212 Dye Chemisorbed onto the TiO₂ (1 0 1) Anatase Surface. *Chem. Phys. Lett.* **2013**, *556*, 151–157.
- (46) Karlsson, K. M.; Jiang, X.; Eriksson, S. K.; Gabriellson, E.; Rensmo, H.; Hagfeldt, A.; Sun, L. Phenoxazine Dyes for Dye-Sensitized Solar Cells: Relationship Between Molecular Structure and Electron Lifetime. *Chem. – A Eur. J.* **2011**, *17*, 6415–6424.
- (47) Hara, K.; Wang, Z. S.; Sato, T.; Furube, A.; Katoh, R.; Sugihara, H.; Dan-Oh, Y.; Kasada, C.; Shinpo, A.; Suga, S. Oligothiophene-Containing Coumarin Dyes for Efficient Dye-Sensitized Solar Cells. *J. Phys. Chem. B* **2005**, *109*, 15476–15482.
- (48) Patil, S.; Chaudhari, G.; Paradeshi, J.; Mahajan, R.; Chaudhari, B. L. Instant Green Synthesis of Silver-Based Herbo-Metallic Colloidal Nanosuspension in Terminalia Bellirica Fruit Aqueous Extract for Catalytic and Antibacterial Applications. *3 Biotech* **2017**, *7*, 1–12.
- (49) Saha, S.; Pal, A.; Kundu, S.; Basu, S.; Pal, T. Photochemical Green Synthesis of Calcium-Alginate-Stabilized Ag and Au Nanoparticles and Their Catalytic Application to 4-Nitrophenol Reduction. *Langmuir* **2010**, *26*, 2885–2893.
- (50) Moreno-Villoslada, I.; Jofré, M.; Miranda, V.; González, R.; Sotelo, T.; Hess, S.; Rivas, B. L. pH Dependence of the Interaction between Rhodamine B and the Water-Soluble Poly(Sodium 4-Styrenesulfonate). *J. Phys. Chem. B* **2006**, *110*, 11809–11812.

- (51) Biggs, A. I. A Spectrophotometric Determination of the Dissociation Constants of P-Nitrophenol and Papaverine. *Trans. Faraday Soc.* **1954**, *50*, 800.
- (52) Bhatkhande, D. S.; Pangarkar, V. G.; Beenackers, A. A. C. M. Photocatalytic Degradation for Environmental Applications - A Review. *J. Chem. Technol. Biotechnol.* **2002**, *77*, 102–116.
- (53) Fatima, R.; Afridi, M. N.; Kumar, V.; Lee, J.; Ali, I.; Kim, K. H.; Kim, J. O. Photocatalytic Degradation Performance of Various Types of Modified TiO₂ against Nitrophenols in Aqueous Systems. *J. Clean. Prod.* **2019**, *231*, 899–912.
- (54) Watanabe, T.; Takizawa, T.; Honda, K. Photocatalysis through Excitation Of Adsorbates. 1. Highly Efficient /V-Deethylation of Rhodamine B Adsorbed to CdS. *Bull. Chem. Soc. Jpn* **1977**, *81*, 1845–1851.
- (55) Chen, F.; Zhao, J.; Hidaka, H. Highly Selective Deethylation of Rhodamine B: Adsorption and Photooxidation Pathways of the Dye on the TiO₂/SiO₂ Composite Photocatalyst. *Int. J. Photoenergy* **2003**, *5*, 209–217.
- (56) Bai, L.; Ye, X.; Song, C.; Chen, H.; Cai, B.; Bai, Y.; Xu, C.; Li, Z. The Surfactant-Free Synthesis of Hollow CuS Nanospheres: Via Clean Cu₂O Templates and Their Catalytic Oxidation of Dye Molecules with H₂O₂. *RSC Adv.* **2016**, *6*, 83885–83889.
- (57) Srinivas, B.; Kumar, B. G.; Muralidharan, K. Stabilizer Free Copper Sulphide Nanostructures for Rapid Photocatalytic Decomposition of Rhodamine B. *J. Mol. Catal. A Chem.* **2015**, *410*, 8–18.
- (58) Tabata, S.; Ohnishi, H.; Yagasaki, E.; Ippommatsu, M.; Domen, K. Light-Intensity Dependence in Photocatalytic Decomposition of Water over K₄Nb₆O₁₇ Catalyst. *Catal. Letters* **1994**, *28*, 417–422.
- (59) Bell, S.; Will, G.; Bell, J. Light Intensity Effects on Photocatalytic Water Splitting with a Titania Catalyst. *Int. J. Hydrogen Energy* **2013**, *38*, 6938–6947.
- (60) Nogueira, R. F. P.; Jardim, W. F. TiO₂-Fixed-Bed Reactor for Water Decontamination Using Solar Light. *Sol. Energy* **1996**, *56*, 471–477.
- (61) Huang, A.; Cao, L.; Chen, J.; Spiess, F.-J.; Suib, S. L.; Obee, T. N.; Hay, S. O.; Freihaut, J. D. Photocatalytic Degradation of Triethylamine on Titanium Oxide Thin Films. *J. Catal.* **1999**, *188*, 40–47.
- (62) Ollis, D. F.; Pelizzetti, E. Destruction of Water Contaminants. *Environ. Sci. Technol.* **1991**, *25*, 1523–1529.
- (63) Experimental Conditions: 30 mL 10 mg/L rhodamine B solution with 18.5 mg silica supported CuS nanoparticles (15 wt% Cu). Reaction under light illumination with a Xe 150 Watt lamp. Light intensity at reactor was 100 mW·cm⁻². No wavelength filter was used.
- (64) Experimental Conditions: 30 mL 10 mg/L rhodamine B solution with 18.6 mg silica supported CuS nanoparticles (15 wt% Cu). To see the effect of temperature on the degradation of RhB, reactions were performed in the dark at a temperature of 72 °C and of 20 °C. Samples were centrifuged to remove the solid catalyst prior to UV-Vis measurements.
- (65) Moustakas, N. G.; Strunk, J. Photocatalytic CO₂ Reduction on TiO₂-Based Materials under Controlled Reaction Conditions: Systematic Insights from a Literature Study. *Chem. - A Eur. J.* **2018**, *24*, 12739–12746.
- (66) Sun, Z.; Talreja, N.; Tao, H.; Texter, J.; Muhler, M.; Strunk, J.; Chen, J. Catalysis of Carbon Dioxide Photoreduction on Nanosheets: Fundamentals and Challenges. *Angew. Chemie Int. Ed.* **2018**, *57*, 7610–7627.
- (67) Yang, C. C.; Yu, Y. H.; Van Der Linden, B.; Wu, J. C. S.; Mul, G. Artificial Photosynthesis over Crystalline TiO₂-Based Catalysts: Fact or Fiction? *J. Am. Chem. Soc.* **2010**, *132*, 8398–8406.
- (68) Kundu, J.; Pradhan, D. Controlled Synthesis and Catalytic Activity of Copper Sulfide Nanostructured Assemblies with Different Morphologies. *ACS Appl. Mater. Interfaces* **2014**, *6*, 1823–1834.
- (69) Islam, D. A.; Chakraborty, A.; Sarkar, U.; Acharya, H.; Bhattacharya, B. Tailored Synthesis of CuS Nanodisks from a New Macrocyclic Precursor and Their Efficient Catalytic Properties on Methylene Blue Dye Degradation. *J. Nanoparticle Res.* **2016**, *18*, 1–13.
- (70) Li, Z.; Mi, L.; Chen, W.; Hou, H.; Liu, C.; Wang, H.; Zheng, Z.; Shen, C. Three-Dimensional CuS Hierarchical Architectures as Recyclable Catalysts for Dye Decolorization. *CrystEngComm* **2012**, *14*, 3965–3971.
- (71) Shu, Q. W.; Lan, J.; Gao, M. X.; Wang, J.; Huang, C. Z. Controlled Synthesis of CuS Caved Superstructures and Their Application to the Catalysis of Organic Dye Degradation in the Absence of Light. *CrystEngComm* **2015**, *17*, 1374–1380.
- (72) Zhang, X.; Yang, F.; Cui, S.; Wei, W.; Chen, W.; Mi, L. Consecutive Reaction to Construct Hierarchical Nanocrystalline CuS “Branch” with Tunable Catalysis Properties. *Sci. Rep.* **2016**, *6*, 1–11.
- (73) Estrada, A. C.; Silva, F. M.; Soares, S. F.; Coutinho, J. A. P.; Trindade, T. An Ionic Liquid Route

- to Prepare Copper Sulphide Nanocrystals Aiming at Photocatalytic Applications. *RSC Adv.* **2016**, *6*, 34521–34528.
- (74) Schneider, J.; Bahnemann, D. W. Undesired Role of Sacrificial Reagents in Photocatalysis. *J. Phys. Chem. Lett.* **2013**, *4*, 3479–3483.
- (75) Kumaravel, V.; Imam, M.; Badreldin, A.; Chava, R.; Do, J.; Kang, M.; Abdel-Wahab, A.; Kumaravel, V.; Imam, M. D.; Badreldin, A.; et al. Photocatalytic Hydrogen Production: Role of Sacrificial Reagents on the Activity of Oxide, Carbon, and Sulfide Catalysts. *Catalysts* **2019**, *9*, 276.
- (76) Braslavsky, S. E.; Braun, A. M.; Cassano, A. E.; Emeline, A. V.; Litter, M. I.; Palmisano, L.; Parmon, V. N.; Serpone, N. Glossary of Terms Used in Photocatalysis and Radiation Catalysis (IUPAC Recommendations 2011). *Pure Appl. Chem* **2011**, *83*, 931–1014.
- (77) Kisch, H.; Bahnemann, D. Best Practice in Photocatalysis: Comparing Rates or Apparent Quantum Yields? *J. Phys. Chem. Lett.* **2015**, *6*, 1907–1910.
- (78) IUPAC. Compendium of Chemical Terminology -- The {IUPAC} Gold Book. 2nd ed. Blackwell Scientific Publications: Research Triangle Park, NC 2006.
- (79) Boudart, M. Turnover Rates in Heterogeneous Catalysis. *Chem. Rev.* **1995**, *95*, 661–666.
- (80) Bligaard, T.; Bullock, R. M.; Campbell, C. T.; Chen, J. G.; Gates, B. C.; Gorte, R. J.; Jones, C. W.; Jones, W. D.; Kitchin, J. R.; Scott, S. L. Toward Benchmarking in Catalysis Science: Best Practices, Challenges, and Opportunities. *ACS Catal.* **2016**, *6*, 2590–2602.
- (81) Zhao, J.; Wu, T.; Wu, K.; Oikawa, K.; Hidaka, H.; Serpone, N. Photoassisted Degradation of Dye Pollutants. 3. Degradation of the Cationic Dye Rhodamine B in Aqueous Anionic Surfactant/TiO₂ Dispersions under Visible Light Irradiation: Evidence for the Need of Substrate Adsorption on TiO₂ Particles. *Environ. Sci. Technol.* **1998**, *32*, 2394–2400.
- (82) Sundararajan, M.; Sailaja, V.; John Kennedy, L.; Judith Vijaya, J. Photocatalytic Degradation of Rhodamine B under Visible Light Using Nanostructured Zinc Doped Cobalt Ferrite: Kinetics and Mechanism. *Ceram. Int.* **2017**, *43*, 540–548.
- (83) Chen, C.; Ma, W.; Zhao, J. Semiconductor-Mediated Photodegradation of Pollutants under Visible-Light Irradiation. *Chem. Soc. Rev* **2010**, *39*, 4206–4219.
- (84) Merka, O.; Yarovsky, V.; Bahnemann, D. W.; Wark, M. pH-Control of the Photocatalytic Degradation Mechanism of Rhodamine B over Pb₃Nb₄O₁₃. *J. Phys. Chem. C* **2011**, *115*, 8014–8023.



Chapter 6

Cu_{2-x}S derived nanoparticles
supported on carbon for the
electrocatalytic reduction of CO_2

Abstract *The electrocatalytic reduction of CO₂ to produce sustainable fuels and chemicals is attracting great attention. Cu-based catalysts can lead to the production of a range of different molecules, and interestingly the product selectivity strongly depends on the preparation history, although it is not fully understood why. In this chapter, we describe an extension of the sulfidation methods discussed in Chapter 4 to carbon supports to prepare supported Cu nanoparticle catalysts with similar morphologies, but prepared by in situ reduction of either supported CuS, Cu₂S or CuO nanoparticles. For the first time the evolution of the Cu species was followed under CO₂ and H⁺ reduction conditions using in situ x-ray absorption spectroscopy. Excellent electrochemical contact between the Cu-based nanoparticles, the carbon support and the carbon-paper substrate was observed, resulting in metallic Cu as the predominant phase under typical electrochemical CO₂ reduction conditions. Even covering less than 4% of the H₂ producing carbon support with Cu-sulfide derived nanoparticles allowed to steer the selectivity to a maximum of 21 % for the production of formate. Clear differences between the catalysts derived from CuS, Cu₂S or CuO nanoparticles were observed, which was ascribed to the presence of residual sulfur in the catalysts.*

6.1 Introduction

When using renewable electricity, the electrochemical reduction of carbon dioxide (CO₂) provides a promising route to produce chemicals and fuels in a sustainable manner.^{1,2} The field of so-called “solar fuels” has triggered the interest of many researchers, focusing on the development and understanding of electrocatalysts that can promote electrochemical CO₂ reduction efficiently and with high selectivity to the targeted product.

The majority of electrocatalysts studied for the reduction of CO₂ are based on transition metals.^{3,4} As already described by Hori *et al.*, in 1985, the catalytic performance of a catalyst highly depends on the metal used.⁵ Metals such as gold,^{6,7} silver^{8,9} and zinc produce mainly CO, whereas metals such as platinum, nickel and iron reduce only small amounts of CO₂, instead leading to H₂ as the main product via the competing hydrogen evolution reaction.

Copper electrodes are extensively studied and stand out because of their unique ability to produce hydrocarbons and oxygenates, which is ascribed to their intermediate binding strength for the CO intermediate.^{1,5,10} Interestingly, Cu can lead to a range of different H⁺ and CO₂ reduction products, and much work is done in the field to obtain a better understanding of the catalytic activity of Cu and the selectivity of Cu electrodes. For example, the use of oxide-derived Cu electrodes promotes the production of CO and C₂₊ products at low overpotentials, even though the electrodes are operating at potentials where all oxide should be reduced to metallic copper.^{11,12} The exact explanation for the influence of the origin of the copper electrodes remains under debate: it might be attributed to the formation of specific surface structures of these oxide-derived electrodes¹, although some oxygen remaining in the material might also be a factor.¹³

More recently, several experimental and theoretical studies have demonstrated that the addition of sulfur modifies the performance of Cu catalysts.^{14–19} Even though copper sulfide is unstable under CO₂ and H⁺ reduction conditions, most studies show that some sulfur remains on the catalyst after reduction.^{14,15,17,18,20,21} Many of these studies observed an increased selectivity towards formate, that is often attributed to a change in the binding energy between the sulfur-containing catalyst and key intermediates in CO₂ reduction, such as *OCHO, *COOH and CO.¹⁹ Besides an increased production of formate, other studies indicate an increased production of CO and/or CH₄ at low overpotentials when using sulfur derived Cu electrodes.^{20,22} In addition, Zhuang *et al.*, reported the production of ethanol, propanol and ethylene at intermediate overpotential (-0.95 V vs. RHE) using Cu₂S-derived nanoparticles.²¹

Inspired by these studies, in this chapter we investigated the catalytic performance and stability of copper sulfide (Cu_{2-x}S) derived nanoparticles supported on carbon for electrochemical CO₂ reduction. Cu_{2-x}S can exist in a variety of different compositions and crystal structures, which have different chemical and physical properties and possibly also different catalytic performance.²³ Therefore, two Cu_{2-x}S catalysts with different starting compositions were studied, namely covellite (CuS) and chalcocite (Cu₂S).

The sulfidation method discussed in Chapter 4 was extended to carbon-supported CuO to prepare carbon-supported CuS (CuS@C) or Cu₂S (Cu₂S@C) nanoparticles. This resulted in a unique set of catalysts with very similar structural properties, that allowed us to investigate the influence of their chemical origin and of the presence of sulfur.

6.2 Experimental Methods

6.2.1 Chemicals

XGnP500® graphene nanoplatelets (GNP) were purchased from XG Sciences. Copper(II) nitrate hydrate ((CuNO₃)₂ · 3 H₂O, 99%), HNO₃ (70%), thioacetamide (TAA, ≥99.0%), Nafion® 117 solution, isopropanol (99.5%) Potassium bicarbonate (KHCO₃, ≥99%) and 1-dodecanethiol (DDT, ≥98%) were purchased from Sigma Aldrich. Nafion™ Membrane XL was obtained from Ion Power GmbH and carbon paper (TGP-H-060) was purchased from Toray.

6.2.2 Synthesis of carbon supported CuO nanoparticles

Carbon supported CuO (CuO@C) nanoparticles were prepared via incipient wetness impregnation followed by drying and heat treatment.^{24–27} 1 gram of graphite nanoplatelets (GNP500) was dried under vacuum at 120 °C for 2 hours and subsequently impregnated with an aqueous Cu(NO₃)₂ · 3 H₂O solution in 0.1 M HNO₃. The volume used for impregnation corresponded to the total pore volume of the support, as determined with N₂-physisorption. A weight loading of 20 wt% Cu was used for all samples. After impregnation, the sample was left to dry overnight at room temperature

under vacuum. Then the sample was transferred into a tubular reactor and heat treated at 230 °C for 2 hours under a N₂ flow (200 mL/min) to decompose the Cu(NO₃)₂ into CuO nanoparticles.

6.2.3 Liquid-phase sulfidation of carbon-supported CuO nanoparticles

To obtain carbon supported CuS (CuS@C) nanoparticles, 400 mg of carbon supported CuO was dispersed into 40 mL demineralized water in a 100 mL roundbottom flask and heated to 120 °C. At a temperature of 90 °C, 10 mL of an aqueous thioacetamide solution was gradually added to the mixture, using a Cu:S molar ratio of 1:1.5. The mixture was left to reflux for 2 hours at 120 °C. After 2 hours, the mixture was left to cool down and subsequently washed with demineralized water and acetone using vacuum filtration. The samples were then dried under vacuum for 2 hours.

To obtain carbon supported Cu₂S (Cu₂S@C) nanoparticles, 400 mg of carbon supported CuO was dispersed in 15 mL 1-dodecanethiol in a 100 mL roundbottom flask and subsequently heated to 200 °C. The mixture was left to react for 2 hours and then cooled down to room temperature. The sample was washed using toluene and acetone and subsequently dried under vacuum at room temperature.

6.2.4 Working electrode preparation

The working electrodes were prepared by spraying the CuO@C, CuS@C and Cu₂S@C on a carbon paper substrate (Toray TGP-H-060). Prior to deposition of the catalyst, the carbon paper substrate was washed in ethanol by sonication for 30 minutes and subsequently rinsed with milliQ (MQ) water. Then, a catalyst ink was prepared by mixing 11 mg of carbon supported catalyst, 1120 μL isopropanol, 4470 μL MQ water and 44.4 μL Nafion solution. The ink was sonicated for 30 minutes in an ultrasonic bath to ensure good dispersion of the catalyst powder. Subsequently the ink was sprayed onto a round carbon paper electrode with a surface area of 4.9 cm² using an Iwata HP-BP HI Performace Plus airbrush. A catalyst loading of 0.2 mg/cm² (with 20 wt% Cu) was intended for all electrodes. The electrodes were dried overnight before electrochemical testing.

6.2.5 Characterization of catalyst and electrodes

The GNP500 support was characterized using N₂-physisorption performed with a Micromeritics TriStar instrument at a temperature of -196 °C. Prior to the measurements the powder was dried at 300 °C under N₂-flow for 16 hours. The pore diameter was determined using the Barrett-Joyner-Halenda (BJH) method and the pore volume was determined at p/p₀=0.995.

Transmission electron microscopy (TEM) analysis was performed using a Thermo Fisher Scientific (formerly FEI) Tecnai12 microscope operating at 120 kV. The powder samples were suspended in ethanol and sonicated for 10 minutes. The suspension was then drop casted on a carbon coated 200 mesh copper TEM grid. Preparation of the

TEM grids of the used catalyst was done by rubbing a TEM grid over the used electrode. Prior to this, the used electrodes were extensively rinsed with MQ water. TEM-EDX measurements were performed with a Thermo Fisher Scientific TalosF200X microscope, operating at 200 keV. For EDX measurements, gold TEM grids were used.

The electrodes before and after reaction were analyzed using scanning electron microscopy with energy dispersive X-ray spectroscopy (SEM-EDX) on a Thermo Fisher Scientific XL30SFEG instrument.

X-ray diffraction (XRD) measurements were done on a Bruker D2 Phaser, equipped with a Co K α X-ray source with a wavelength of 1.79026 Å. The crystallite size of the copper sulfide nanoparticles was determined from the diffraction peak broadening using the Scherrer equation.²⁸

6.2.6 Electrochemical measurements

A custom built, H-type electrochemical cell with two compartments separated by a Nafion membrane was used for all electrochemical measurements (Figure 6.1). Each compartment of the electrochemical cell was filled with 11 mL electrolyte (0.5 M KHCO₃ or 0.5 M KHCO₃ + 0.5 M KCl). The anolyte was purged with argon and the catholyte was purged with CO₂ at 10 mL/min. All electrochemical measurements were performed on an Autolab PGSTAT204 Potentiostat, with a Pt disk as counter electrode and a Ag/AgCl 3M KCl reference electrode (Methrom). All potentials were converted to the reversible hydrogen electrode (RHE) potential using the equation:

$$E \text{ (vs. RHE)} = E \text{ (vs. Ag/AgCl)} + 0.209 + 0.059 \times \text{pH}$$

The catalyst supported on the carbon paper electrode was placed on a glassy carbon electrode for extra support and held in place by O-rings, leaving an electrode area of 3.8 cm² in contact with the electrolyte solution. Prior to all measurements, either CO₂ or argon was bubbled through the solution for 20 minutes.

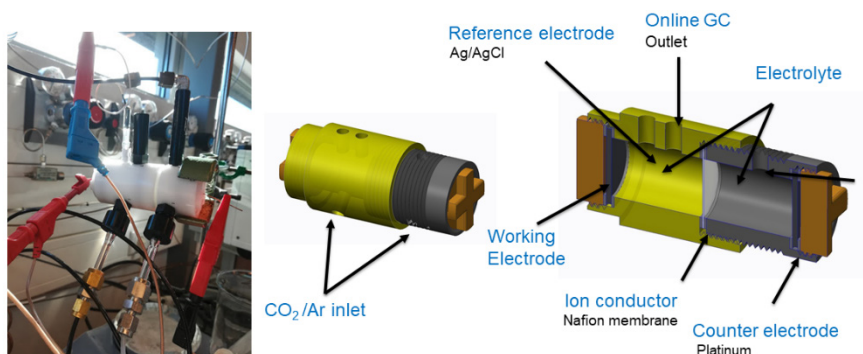


Figure 6.1 a) Photograph and b) schematic representation of the electrochemical cell used for CV and selectivity measurements.

Cyclic voltammetry was performed in a 0.5 M KHCO₃ electrolyte, a scanning rate of 10 mV/s and a constant Ar or CO₂ flow of 10 mL/min. The selectivity of the catalysts was determined using chronopotentiometry at different current densities for 5 hours (liquid products) or 1 hour (gaseous products). Gaseous products were analyzed by connecting the outlet of the cathode compartment to a Global Analysis Solutions Microcompact GC 4.0. The GC system was equipped with three channels: The first channel has a Rt-QBond (10 m*0.32 mm, Agilent) packed column and a FID detector for the detection of CH₄, C₂H₄ and C₂H₆, the second channel has Molecular Sieve 5A (10 m* 0.53 mm, Restek) packed column that separates small gaseous molecules such as CO, and CH₄. This channel has a FID detector with a methanizer to increase the detection sensitivity of CO. The third channel has a Carboxen 1010 (8 m*0.32 mm, Agilent) packed column which separates H₂ and CO₂ with a TCD. High purity nitrogen (N₂; 99.999%) was used as a carrier gas.

Liquid phase products were analyzed by analysis of the catholyte using a Varian HPLC equipped with a refractive index detector (RID) and a Bio-Rad Aminex HPX-87H column at 65 °C. 1 mM H₂SO₄ was used as the eluent with a flow rate of 0.55 mL/min. The retention time of formic acid was 15 min and the total analysis time was 20 minutes.

The Faradaic efficiency (FE) was calculated as:

$$FE(\%) = \frac{n_x \times F \times [\text{moles of product } x]}{Q} \times 100\%$$

In which n_x is the number of electrons needed to produce x (product) from CO₂ molecules and F is the Faradaic constant (96 485 s·A/mol).

For gaseous products ($x = \text{H}_2, \text{CO}, \text{CH}_4, \text{C}_2\text{H}_4, \text{or } \text{C}_2\text{H}_6$), the moles of product were determined via:

$$\text{moles of product} = \frac{C_x \times q \times p}{RT}$$

in which C_x is the volumetric concentration of product x in ppm extracted from the GC calibration curve, q is the gas flow rate, p is the pressure, R is the ideal gas constant (8.314 m³·Pa/K·mol), T is the temperature, n_x is the number of electrons needed to produce x (product) from CO₂ molecules and F is the Faradaic constant (96485 s·A/mol).

For liquid phase products ($x = \text{formate}$), the moles of product formed was determined via:

$$\text{moles of product} = \frac{C_x \times V_{\text{catholyte}}}{1000 \times M_w}$$

in which C_x is the volumetric concentration of product x in ppm extracted from the HPLC calibration curve, $V_{\text{catholyte}}$ is the volume of the catholyte (L) and M_w the molar weight of product x (g/mol).

6.2.7 XAS measurements

X-ray absorption measurements were performed at the Dutch-Belgian beamline DUBBLE, 26A at the European Synchrotron Radiation Facility (ESRF) in Grenoble, France. Spectra were recorded at the Copper K-edge (8978.9 eV). Reference spectra of CuS@C, Cu₂S@C and Cu foil were recorded in transmission mode. The Athena XAS data processing software was used for the analysis of data.

For the *in situ* XAS measurements, an electrochemical cell made by TU Delft was used (Figure 6.2).²⁹ All *in situ* experiments were performed in fluorescence mode, with an angle of 45° between the incoming x-rays and the sample. The time to acquire a spectrum was about 4.5 minutes and 2-5 scans were recorded at each potential. A CO₂-saturated 0.1 M KHCO₃ electrolyte was flown through the cell with a flowrate of 2 mL/min using a peristaltic pump. The Cu_{2-x}S@C electrodes were used as working electrode, a coiled platinum wire as counter electrode and a Ag/AgCl electrode as reference electrode. A BioLogic SP-240 potentiostat was used for all *in situ* XAS experiments.

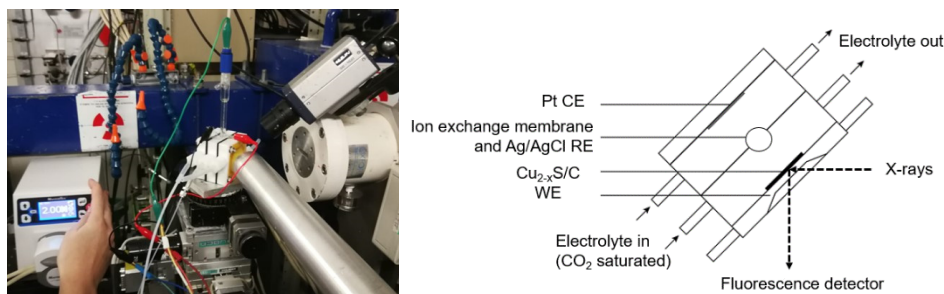


Figure 6.2 a) Photograph and b) schematic representation of the electrochemical cell used for *in situ* XAS experiments.

6.3 Results and Discussion

6.3.1 Structural properties of the catalyst and electrodes

Supported CuS and Cu₂S catalysts were prepared via a two-step synthesis route, based on the methods described in Chapter 4. In this method carbon supported CuO nanoparticles (CuO@C) were converted into carbon supported CuS (CuS@C) or Cu₂S (Cu₂S@C) nanoparticles. This approach was chosen in order to investigate whether the nanoparticle size of the CuO@C sample could be maintained in the CuS@C and Cu₂S@C samples. Figure 6.3 shows the x-ray diffractograms of CuO@C, CuS@C, Cu₂S@C and of bare carbon as a reference. For all four samples, diffraction lines are observed at 30.6° and 64.1°, which can be ascribed to the crystalline graphite support, which clearly was not damaged by the treatments. The CuO@C sample shows additional diffraction lines at 41.5°, 45.3° and 57.0°, which can be indexed with the monoclinic structure of CuO (PDF-01-070-6831 (ICDD, 2019)³⁰).

Upon conversion to CuS@C using thioacetamide, the diffraction pattern shows clear diffraction lines at 34.1°, 37.1°, 38.3° and 56.3°, which is consistent with the hexagonal CuS covellite structure (PDF-00-006-0464 (ICDD, 2019)³⁰). Upon conversion to Cu₂S@C using 1-dodecanethiol, the reflections at 44.0°, 54.3° and 57.2° demonstrate the presence of hexagonal Cu₂S chalcocite (PDF-00-053-0522 (ICDD, 2019)³⁰). For both the CuS@C and Cu₂S@C, no residual CuO reflections are observed, hence complete

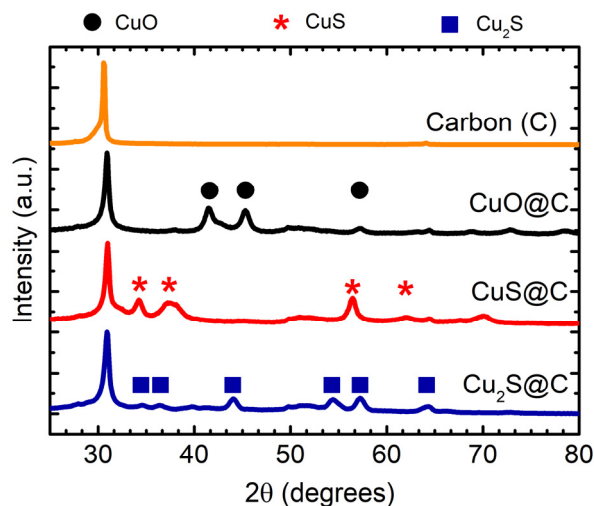


Figure 6.3 X-ray diffractograms of the bare GNP-500 carbon support (orange) and of the CuO@C (black), CuS@C (red) and Cu₂S@C (blue) nanoparticles on this carbon support. All samples have a loading of 20 wt% Cu. The symbols above the diffractograms represent reflections of CuO (black dot), CuS (red asterisk) and Cu₂S (blue square), obtained from the PDF reference cards PDF-01-070-6831 (ICDD, 2019), PDF-00-006-0464 (ICDD, 2019) and PDF-00-053-0522 (ICDD, 2019), respectively. [30]

conversion of CuO to either CuS or Cu₂S was achieved. The relative broad peaks in the CuO@C, CuS@C and Cu₂S@C samples prove the presence of nanocrystallites and the absence of macrocrystalline material. The Scherrer equation was used to determine the crystallite size of the particles, resulting in crystallite sizes of 13, 14 and 12 nm for the CuO@C, CuS@C and Cu₂S@C samples, respectively.

Figure 6.4 shows TEM images of the supported nanoparticles and the corresponding particle size histograms. Both the CuO@C and the Cu₂S@C samples show spherical particles with a particle size of 9 ± 3 nm for CuO and 17 ± 1 nm for Cu₂S. The supported CuS nanoparticles have a larger size of 25 ± 13 nm, with a few particles larger than 30 nm and a platelet-like morphology. The CuO@C nanoparticles can thus be successfully converted to nanoparticles of either CuS@C or Cu₂S@C. However, whereas for the silica supported CuO nanoparticles described in Chapter 4 the particle size and shape was preserved upon sulfidation to CuS@SiO₂, significant particle growth was observed upon sulfidation of the CuO@C to CuS@C.

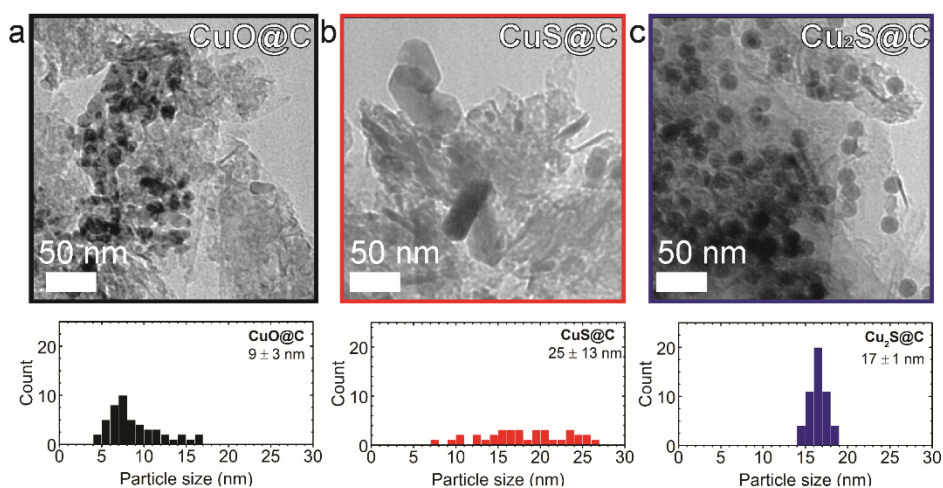


Figure 6.4 TEM images of a) CuO@C, b) CuS@C and c) Cu₂S@C nanoparticles and corresponding particle size histograms, indicating an average particle size of 9 ± 3 nm, 25 ± 13 nm and 17 ± 1 nm, respectively.

The working electrodes CuO@C, CuS@C or Cu₂S@C were prepared by spraying an ink containing the catalyst powder onto carbon paper substrates. Figure 6.5 shows representative scanning electron microscopy (SEM) images of the bare carbon paper substrate and of the Cu₂S@C nanoparticles and CuS@C nanoparticles sprayed onto the carbon paper substrate, illustrating the distribution over and adherence of the carbon supported nanoparticles to the carbon paper substrate.

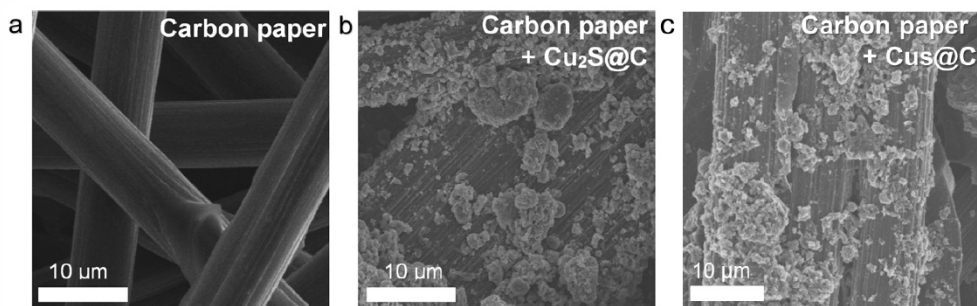


Figure 6.5 SEM images of the carbon paper substrate a) without any catalyst and with b) $\text{Cu}_2\text{S}@C$ or c) $\text{CuS}@C$ deposited on the carbon fibers by spraying.

6.3.2 Electrochemical characterization of the catalyst under eCO_2R reaction conditions

Figure 6.6 shows the cyclic voltammograms (CVs) of $\text{CuS}@C$ and $\text{Cu}_2\text{S}@C$ in a 0.5 M KHCO_3 electrolyte (pH=7.1) under argon flow, obtained with a scan rate of 10 mV/sec. For each sample, the first 5 cycles are shown. For $\text{CuS}@C$ (Figure 6.6a), two reduction peaks are observed in the first cathodic scan with onsets at potentials around -0.0 V and -0.4 V vs. RHE. Figure 6.6b shows the Pourbaix diagram of an aqueous Cu-S system at 25 °C with Cu and S concentrations of 1 M.³¹ The diagram shows that under these conditions, CuS is not thermodynamically stable at potentials more negative than -0.4 V vs. SHE (0.0 V vs. RHE) in aqueous solutions at pH 7, and can be reduced, via several copper rich Cu_{2-x}S phases, to metallic Cu. Relating this to the reduction peaks observed in the voltammogram of $\text{CuS}@C$, the first reduction peak can be attributed to a reduction of the CuS nanoparticles to more copper-rich copper sulfide phases, such as djurleite ($\text{Cu}_{1.94}\text{S}$) or chalcocite (Cu_2S). The second reduction peak can then be attributed to the reduction of the remaining Cu_{2-x}S phase to metallic Cu.

The voltammogram of the $\text{Cu}_2\text{S}@C$ sample (Figure 6.6c) also shows a reduction peak with an onset around -0.4 V vs. RHE, which corresponds to a reduction of the Cu_{2-x}S nanoparticles to metallic Cu. In addition, a reduction peak is observed here with an onset at a potential of -0.2 V. This reduction likely originates from a reduction of a more copper deficient Cu_{2-x}S phase or some CuO, which was formed during the storage of the electrode in air prior to the measurements. Figure 6.6d shows the voltammogram of the $\text{CuO}@C$ sample, showing two reduction peaks with onsets above 0 V vs. RHE and around -0.2 V vs. RHE in the first cathodic scan. These reduction peaks correspond to the ready reduction of CuO to Cu_2O and subsequently to metallic Cu.³²

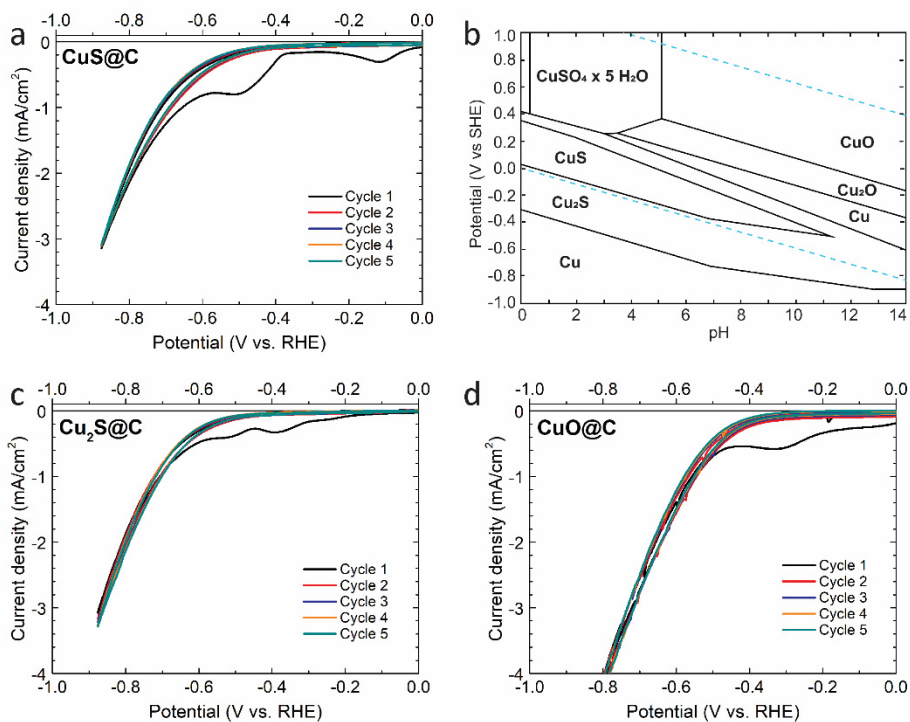


Figure 6.6 Voltammograms of **a)** CuS@C in a Ar-saturated 0.5 M KHCO₃ solution (pH=7.1). A scan rate of 10 mV/s was used for all measurements. The reduction of the Cu-based nanoparticles is clearly visible in the first cathodic scan. **b)** Pourbaix diagram of a Cu-S system in H₂O at 25°C. The molarities of Cu and S are 1 mol/liter H₂O. The diagram was constructed using the software HSC Chemistry.³¹ Voltammograms of **c)** Cu₂S@C and **d)** CuO@C in a Ar-saturated 0.5 M KHCO₃ solution (pH=7.1). A scan rate of 10 mV/s was used for all measurements. Again the reduction of the Cu-based nanoparticles is clearly visible in the first cathodic scan.

The CVs thus show that CuS@C and Cu₂S@C are reduced to metallic Cu when scanning to potentials more negative than -0.4 V vs. RHE. However, no oxidation peaks are observed in the anodic cycles of the CVs (Figure 6.6a,c), indicating the reduced phases do not oxidize back to the original CuS or Cu₂S phase in this potential range. During reduction, the sulfur will likely react with protons from solution to form SH_(aq) and H₂S_(g).¹⁵ The gaseous H₂S will escape from the cell, explaining the irreversibility of the reduction of CuS and Cu₂S.

X-ray absorption spectroscopy (XAS) was employed to probe the copper phases under operando reaction conditions. *In situ* techniques are invaluable as the characterization of catalysts after reaction is challenging due to the limited amount of catalyst used in reactions. In addition, the catalyst is often highly susceptible to changes when a potential is no longer applied, and the catalyst is removed from the electrolyte solution (*e.g.*, oxidation). XAS is a very suitable technique for *in situ* studies of electrocatalysts, as x-rays can easily penetrate through air and water due to their high energy.^{33–35}

Figure 6.7 shows the *ex situ* XAS spectra of the CuS@C and Cu₂S@C samples (dotted lines) and the *in situ* XAS spectra of these samples in the electrochemical cell, without applying a potential (solid lines). The conditions under which the samples were measured are different. The *ex situ* spectra were recorded using pellets of the as-synthesized powder samples. In contrast, the *in situ* spectra shown in Figure 6.7a are of the CuS@C and Cu₂S@C powders, deposited on the carbon paper substrate, in contact with a CO₂ saturated 0.1 M KHCO₃ electrolyte (pH=6.8), without applying a potential. However, for both CuS@C and Cu₂S@C, the *in situ* spectrum shows the same features as the corresponding sample measured under *ex situ* conditions. This demonstrates that the CuS@C and Cu₂S@C were stable upon deposition of the catalyst powder on the carbon paper substrate and subsequent contact with the CO₂ saturated electrolyte, and hence validates the *in situ* measurements.

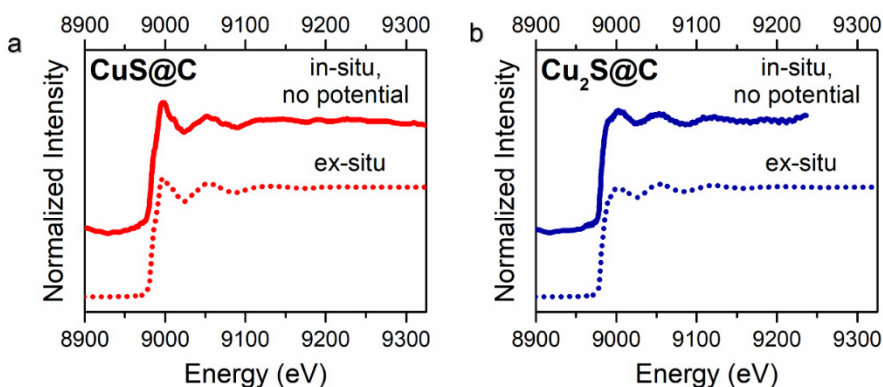


Figure 6.7 a) Normalized XAS spectra of a) CuS@C and b) Cu₂S@C, comparing an *ex situ* measurement (dotted lines) with that of the sample as electrode in the electrochemical cell, without applying a potential (solid lines).

Subsequently, the CuS@C and Cu₂S@C samples were analyzed under CO₂ and H⁺ reduction conditions. Figure 6.8a shows the *in situ* XAS spectra of the CuS@C sample upon applying increasingly negative potentials. Upon applying negative potentials, the spectra show clear changes. At potentials of -0.9 V vs. RHE, features start to appear at energies of 9025 eV and 9070 eV. When going to more negative potentials, such as -1.2 V and -1.6 V vs. RHE, these features become even more pronounced. As is shown by the *ex situ* XAS pattern of the Cu foil, the peaks at 9025 eV and 9070 eV are characteristic for metallic Cu. Although it is difficult to distinguish if the reduction occurs via any intermediate copper-rich Cu_{2-x}S phases, the *in situ* XAS data thus clearly show the reduction of the CuS nanoparticles to metallic Cu under reaction conditions.

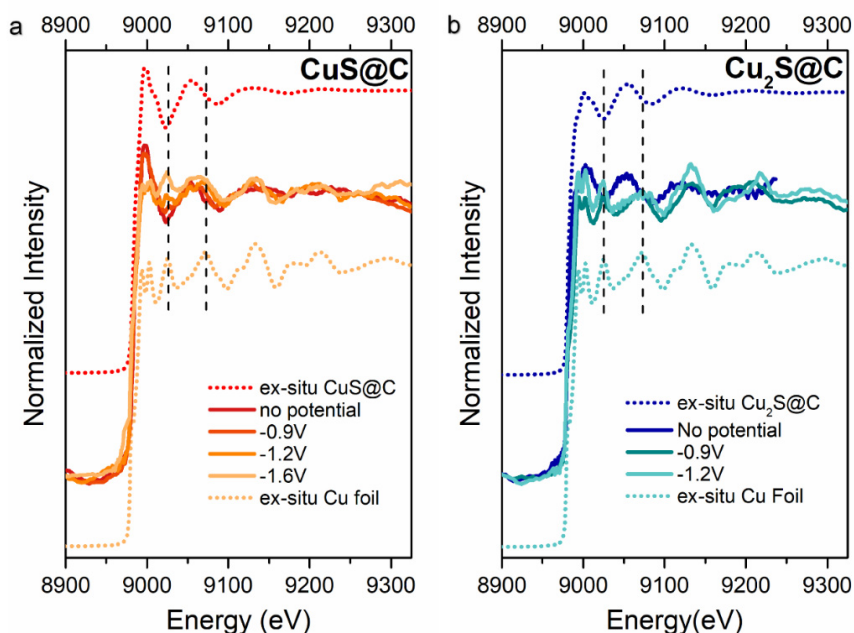


Figure 6.8 a) Normalized XAS spectra of CuS@C measured *in situ* during electrochemical CO₂ reduction at different potentials (solid lines), compared to *ex situ* reference spectra of CuS@C (dotted, red line) and Cu foil (dotted, orange line). Upon applying a more negative potential, the spectra resemble the Cu foil reference, indicating a reduction of the CuS to Cu. **b)** Normalized XAS spectra of Cu₂S@C measured *in situ* during CO₂ reduction at different potentials (solid lines), compared to *ex situ* reference spectra of Cu₂S@C (dotted, dark blue line) and Cu foil (dotted, light blue line). Upon applying a more negative potential, the spectra resemble the Cu foil reference, indicating a reduction of the Cu₂S to Cu.

Figure 6.8b shows the *in situ* XAS spectra of the Cu₂S@C sample under reaction conditions. Whereas for the CuS@C sample at -0.9 V vs. RHE the spectrum only showed minor changes compared to the as-prepared CuS@C spectrum, the spectrum of the Cu₂S@C sample at -0.9 V already clearly resembles the metallic Cu reference. This indicates a ready reduction of the Cu₂S nanoparticles to metallic Cu.

This technique thus allowed us to elucidate the chemical phase of the catalyst under electrochemical CO₂ reduction conditions. For both samples, the potential at which a reduction to Cu is observed by XAS (-0.9 V) is more negative than the potential of -0.5 V vs. RHE at which the reduction peak was observed in the CVs (Figure 6.6a,c). This is likely caused by the different experimental conditions used in the two experiments, such as the different cell geometries (see Figure 6.1, 6.2) leading to differences in ohmic resistance. In addition, an electrolyte concentration of 0.1 M KHCO₃ was used during the *in situ* XAS experiments, as compared to a concentration of 0.5 M KHCO₃ and the resulting lower conductivity and pH is expected to shift the reduction to slightly more negative potentials.

Most importantly, XAS is a bulk technique and from the fact that the spectra at potentials more negative than -0.9 V correspond to metallic Cu, with very little or none of the original *ex situ* spectrum remaining, it can be concluded that the vast majority of the nanoparticles are electrochemically active, and are in good electrochemical contact with the carbon support and carbon-paper substrate as well as with the electrolyte solution. To our knowledge, this is the first time that the chemical phases of CuS@C- and Cu₂S@C-derived catalysts were followed *in situ* under CO₂ and H⁺ reduction conditions, giving valuable insight in the active catalyst phase and on the electrochemical contact between the nanoparticles and support material.

6.3.3. Electrochemical CO₂ reduction

The product selectivity of the CuS@C and Cu₂S@C derived catalysts in electrochemical CO₂ reduction were compared to that of the CuO@C derived catalyst. For all three catalysts, the main CO₂ reduction product formed was formate. Table 6.1 shows the amount of formate produced for all three catalysts and a carbon reference, obtained from chronopotentiometry (CP) for 5 hrs in a 0.5 M KCl + 0.5 M KHCO₃ electrolyte saturated with CO₂ at current densities of -1.5 , -3.0 and -4.5 mA/cm². Here, the KCl was added as supporting electrolyte to increase the conductivity of the electrolyte and minimize ohmic resistances.

Table 6.1 The amount of formate and CO produced and Faradaic efficiency (FE) of formate and CO during CO₂ reduction using CuO@C, CuS@C and Cu₂S@C and a carbon reference at different currents applied. The data for formate is obtained by CP (5 hours for formate and 60 minutes for CO) with currents of -1.5 , -3 and -4.5 mA/cm², performed in a 0.5 M KCl + 0.5 M KHCO₃ electrolyte saturated with CO₂ (pH 7.5). The average potentials over 5 hours of CP are also shown (with standard deviation).

Applied current density (mA/cm ²)	Sample	Formate		CO		Resulting Potential (V vs. RHE)
		Production (μmol/hr)	FE (%)	Production (μmol/hr)	FE (%)	
-1.5	CuS@C	9	8	0.1	0.1	-0.77 ± 0.02
	Cu ₂ S@C	13	12	0.1	0.1	-0.78 ± 0.02
	CuO@C	3	3	0.6	0.6	-0.66 ± 0.04
	C	3	3	0.5	0.5	-0.82 ± 0.02
-3	CuS@C	14	7	0.4	0.2	-0.90 ± 0.08
	Cu ₂ S@C	21	10	2.4	1.1	-0.76 ± 0.01
	CuO@C	16	8	2.8	1.3	-0.88 ± 0.10
	C	4	2	0.3	0.2	-0.96 ± 0.01
-4.5	CuS@C	11	3	0.8	0.2	-1.05 ± 0.05
	Cu ₂ S@C	12	4	3.7	1.1	-0.87 ± 0.03
	CuO@C	19	6	4.3	1.3	-0.91 ± 0.02
	C	6	2	0	0	-1.65 ± 0.03

When a current density of -1.5 mA/cm² was applied, formate was produced with yields of 9, 13 and 3 μmol/hr for the CuS@C-, Cu₂S@C and CuO@C-derived catalysts, respectively. As the carbon support showed a similar production of formate (3 μmol/hr) as the CuO@C-derived catalyst, the production of formate on this catalyst is neglectable. The production of formate on the CuS@C- and Cu₂S@C-derived catalysts is however significantly higher, showing that the production of formate is promoted on the sulfide derived catalysts when compared to the oxide derived catalyst and the carbon support.

In addition, more formate is produced by the Cu₂S@C-derived catalyst than by the CuS@C-derived catalyst. This indicates that, even though both CuS@C and Cu₂S@C reduce to metallic Cu under reaction conditions, there is a difference between the two Cu-sulfide derived catalysts depending on whether they originate from CuS@C or Cu₂S@C. When applying more negative potentials, the formate production also on the oxide-derived catalyst increases, making the differences less pronounced, although in all cases the Cu₂S@C-derived catalyst produces more formate than the CuS@C-derived catalyst.

Besides formate, only small amounts of CO were produced with Faradaic efficiencies between 0-1.3% (Table 6.1). The differences between the measured CO concentrations on the different catalysts were close to the experimental error. No other CO₂ reduction products were found in the liquid or gaseous phase and hence the rest of the current led to the production of H₂. The production of H₂ readily occurred on the bare carbon reference sample. The surface coverage of the carbon support by the Cu-based nanoparticles was calculated using the surface area of the carbon support, the weight loading of the catalysts and by assuming spherical Cu-based particles, and was found to be less than 4% for all three catalysts. It is hence notable that CO₂ reduction products with Faradaic efficiencies ranging from 5-20% can be obtained with such a low coverage of the carbon surface, which so readily produced H₂ instead. This means that the Cu-based nanoparticles clearly introduce a preference for CO₂ rather than H⁺ reduction.

The enhanced selectivity for formate on the sulfide derived catalysts at current densities of -1.5 mA/cm² is consistent with previous studies and can be explained by the different pathways possible for CO₂ reduction.^{14,15,17,18} Norskov *et al.*,¹⁴ proposed that the reduction of CO₂ to HCOO⁻ occurs via a *OCHO intermediate, which is further reduced to formate (HCOO⁻).³⁶ On the other hand, other studies suggest the formation of formate occurs via a direct reaction of physisorbed CO₂ with adsorbed H⁺.^{18,37} In both mechanisms, CO and further reduced products are formed via a so-called CO pathway, in which CO₂ is reduced to *COOH, which can be further reduced to *CO, which in turn can desorb or be further reduced to various hydrocarbons and alcohols. Although no distinction can be made between the two mechanisms to form formate, the increased selectivity for formate observed for the sulfide derived catalysts at a current densities of -1.5 mA/cm² suggests that the HCOO⁻ pathway is favored over the CO pathway. Which pathway is preferred highly depends on the binding strength of important intermediates such as CO on the catalyst, suggesting that the binding affinity for the CO₂ reduction intermediates

is different on the sulfide-derived catalysts than on the oxide-derived catalyst. Nevertheless, elucidation of the exact role of sulfur on the CO₂ reduction mechanism will require additional studies.

6.3.4 Structure of catalysts after reaction

The increased formation of formate on Cu₂S@C-derived catalyst when compared to CuS@C-derived catalyst suggests a difference in the chemical composition between the two. Hence, additional characterization of the catalysts was performed after reaction. After being used in the CO₂ and H⁺ reduction for 5 hours at -3 mA/cm² in 0.5 M KCl + 0.5 M KHCO₃, the CuO@C-, CuS@C- and Cu₂S@C-derived catalysts were analyzed to see if any changes occurred upon reaction. Figure 6.9 shows TEM images of the CuO@C-, CuS@C- and Cu₂S@C-derived catalysts after being employed in the CO₂ reduction reaction. For CuO@C, the particle size increased from 9 ± 3 nm to 33 ± 14 nm and few particles with sizes over 50 nm were also observed. For the CuS@C-derived catalyst, no significant change in particle size is observed, whereas for the Cu₂S@C-derived catalyst, the particle size decreased from 17 ± 1 nm to 6 ± 2 nm upon reaction. Upon reaction, the CuO@C- and CuS@C-derived catalysts thus have a fairly similar particle size distribution, while the Cu₂S@C-derived catalyst has smaller and more monodisperse particles. This difference in particle size could play a role in the different catalytic behavior discussed in section 6.3.3.^{38,39}

In addition, TEM-EDX measurements were performed to analyze the presence of sulfur in the catalysts after reaction. The measurements showed remaining sulfur in the samples after reaction, where copper to sulfur ratios of 3:1 and 6:1 were found for the CuS@C-

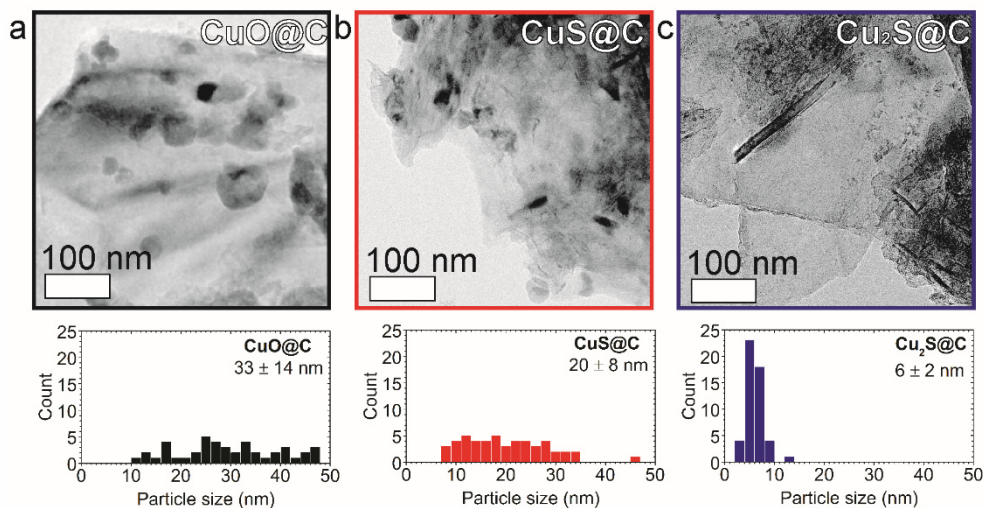


Figure 6.9 TEM figures of the a) CuO@C-, b) CuS@C-, and c) Cu₂S@C-derived catalysts after 5 hours of CO₂ and H⁺ reduction at -3mA/cm² in 0.5 M KCl +0.5 M KHCO₃. The lower panels show corresponding particle size histograms. For CuO@C, a few particles larger than 50 nm were also observed.

and Cu₂S@C-derived catalyst, respectively. This was much higher than the sulfur content detected in the CuO@C sample, with a Cu:S ratio of 32:1. This sample was used as a reference for the base sulfur content, as the Nafion binder used in the electrode preparation contains some sulfur as well. A small amount of sulfur, as well as K and Cl, can also be ascribed to incomplete removal of the electrolyte. Although precise quantification is thus not straightforward, it is clear that the sulfur content is higher for the CuS@C derived catalyst than for Cu₂S@C-derived catalyst, which can be explained by the higher initial sulfur content of CuS@C. The different sulfur content observed in all three catalysts is a plausible explanation for the different product selectivities discussed in section 6.3.3, as our preparation method allowed us to produce Cu-based catalysts otherwise very similar in morphology.

Table 6.2 Atomic% of Cu and S obtained from TEM-EDX on the CuS@C-, Cu₂S@C- and CuO@C-derived catalysts after 5 hours of CO₂ and H⁺ reduction at -3mA/cm² in 0.5 M KCl + 0.5 M KHCO₃. For the CuS@C and Cu₂S@C samples, EDX quantification was done at three different locations on the sample. The average of these three locations was used to determine to Cu to S ratio for each sample.

Sample	Atomic % Cu	Atomic % S
CuS@C (Location 1)	74.58 ± 0.16	25.41 ± 0.03
CuS@C (Location 2)	74.66 ± 0.20	25.33 ± 0.04
CuS@C (Location 3)	76.22 ± 0.16	23.77 ± 0.02
Cu ₂ S@C (Location 1)	82.99 ± 0.13	17.00 ± 0.03
Cu ₂ S@C (Location 2)	82.82 ± 0.10	17.17 ± 0.00
Cu ₂ S@C (Location 3)	89.88 ± 0.11	10.11 ± 0.01
CuO@C (Location 1)	97.27 ± 0.07	2.72 ± 0.00

6.4 Conclusions

In summary, carbon-supported, Cu_{2-x}S derived nanoparticles were studied for electrochemical CO₂ reduction in aqueous media. First, CuS@C and Cu₂S@C nanoparticles were successfully prepared via a liquid phase sulfidation of CuO@C nanoparticles. Subsequently the catalysts were deposited on carbon paper electrode substrates. Upon electrochemical CO₂ reduction, CuS@C and Cu₂S@C nanoparticles undergo a reduction to metallic Cu, as was verified by both CV and *in situ* XAS experiments. However, TEM-EDX measurements showed that some residual sulfur is left in both catalysts. The selectivity of the CuS@C- and Cu₂S@C-derived catalysts was tested and compared to that of a CuO@C-derived catalyst. On all three catalysts, formate was produced as the main CO₂ reduction product, next to H₂ mainly produced by the carbon support. At low current densities, the selectivity towards the production of formate was enhanced for the CuS@C- and Cu₂S@C-derived catalysts when compared to the CuO@C derived catalyst. It is remarkable that with less than 4% carbon surface coverage, a maximum of 21% overall selectivity to formate was achieved, showing the

effectiveness of Cu-sulfide derived catalysts to steer the selectivity to formate. In addition, the two Cu-sulfide derived catalysts showed clear differences in formate production, indicating the initial Cu-sulfide phase influences the product selectivity.

6.5 Acknowledgements

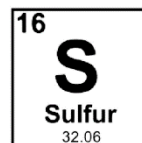
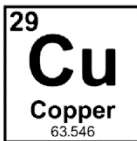
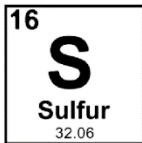
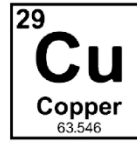
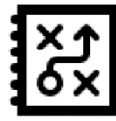
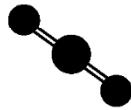
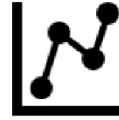
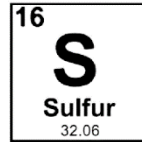
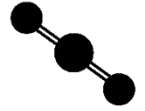
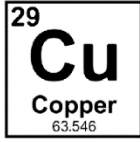
The work in this chapter was performed in collaboration with Marisol Tapia Rosales. Kristiaan Helfferich is thanked for the preliminary electrocatalytic experiments. Nienke Firt is acknowledged for providing the *in situ* XAS cell. Mahnaz Ghiasi Kalibiri is thanked for analysis and discussions of the XAS data. Hans Meeldijk is acknowledged for his help in performing the electron microscopy measurements. We are grateful to Alessandro Longo at the ESRF for providing assistance in using beamline 26 – The Dutch-Belgian Beam Line (DUBBLE). Fei Chang and Peter Ngene are thanked for their assistance and useful discussions during the XAS beamtime. Sneha Sameer is thanked for his help on the electrochemical cell design. Kai Han, Francesco Mattarozzi and Jan Willem de Rijk are acknowledged for useful discussions on the electrochemical set-up and measurements.

6.6 References

- (1) Nitopi, S.; Bertheussen, E.; Scott, S. B.; Liu, X.; Engstfeld, A. K.; Horch, S.; Seger, B.; Stephens, I. E. L.; Chan, K.; Hahn, C.; et al., Progress and Perspectives of Electrochemical CO₂ Reduction on Copper in Aqueous Electrolyte. *Chem. Rev.* **2019**, *119*, 7610–7672.
- (2) Appel, A. M.; Bercaw, J. E.; Bocarsly, A. B.; Dobbek, H.; Dubois, D. L.; Dupuis, M.; Ferry, J. G.; Fujita, E.; Hille, R.; Kenis, P. J. A.; et al., Frontiers, Opportunities, and Challenges in Biochemical and Chemical Catalysis of CO₂ Fixation. *Chem. Rev.* **2013**, *113*, 6621–6658.
- (3) Birdja, Y. Y.; Pérez-Gallent, E.; Figueiredo, M. C.; Göttle, A. J.; Calle-Vallejo, F.; Koper, M. T. M. Advances and Challenges in Understanding the Electrocatalytic Conversion of Carbon Dioxide to Fuels. *Nat. Energy* **2019**, *4*, 732–745.
- (4) Hori, Y.; Wakebe, H.; Tsukamoto, T.; Koga, O. Electrocatalytic Process of CO Selectivity in Electrochemical Reduction of CO₂ at Metal Electrodes in Aqueous Media. *Electrochim. Acta* **1994**, *39*, 1833–1839.
- (5) Hori, Y.; Kikuchi, K.; Suzuki, S. Production of CO and CH₄ in Electrochemical Reduction of CO₂ At Metal Electrodes in Aqueous Hydrogencarbonate Solution. *Chem. Lett.* **1985**, *14*, 1695–1698.
- (6) Cave, E. R.; Montoya, J. H.; Kuhl, K. P.; Abram, D. N.; Hatsukade, T.; Shi, C.; Hahn, C.; Nørskov, J. K.; Jaramillo, T. F. Electrochemical CO₂ Reduction on Au Surfaces: Mechanistic Aspects Regarding the Formation of Major and Minor Products. *Phys. Chem. Chem. Phys.* **2017**, *19*, 15856–15863.
- (7) Chen, Y.; Li, C. W.; Kanan, M. W. Aqueous CO₂ Reduction at Very Low Overpotential on Oxide-Derived Au Nanoparticles. *J. Am. Chem. Soc.* **2012**, *134*, 19969–19972.
- (8) Hatsukade, T.; Kuhl, K. P.; Cave, E. R.; Abram, D. N.; Jaramillo, T. F. Insights into the Electrocatalytic Reduction of CO₂ on Metallic Silver Surfaces. *Phys. Chem. Chem. Phys.* **2014**, *16*, 13814–13819.
- (9) Guntern, Y. T.; Pankhurst, J. R.; Vávra, J.; Mensi, M.; Mantella, V.; Schouwink, P.; Buonsanti, R. Nanocrystal/Metal–Organic Framework Hybrids as Electrocatalytic Platforms for CO₂ Conversion. *Angew. Chemie - Int. Ed.* **2019**, *58*, 12632–12639.
- (10) Kortlever, R.; Shen, J.; Schouten, K. J. P.; Calle-Vallejo, F.; Koper, M. T. M. Catalysts and Reaction Pathways for the Electrochemical Reduction of Carbon Dioxide. *J. Phys. Chem. Lett.* **2015**, *6*, 4073–4082.
- (11) Kas, R.; Kortlever, R.; Milbrat, A.; Koper, M. T. M.; Mul, G.; Baltrusaitis, J. Electrochemical CO₂ Reduction on Cu₂O-Derived Copper Nanoparticles: Controlling the Catalytic Selectivity of Hydrocarbons. *Phys. Chem. Chem. Phys.* **2014**, *16*, 12194–12201.
- (12) Lum, Y.; Yue, B.; Lobaccaro, P.; Bell, A. T.; Ager, J. W. Optimizing C-C Coupling on Oxide-Derived Copper Catalysts for Electrochemical CO₂ Reduction. *J. Phys. Chem. C* **2017**, *121*, 14191–14203.
- (13) Cavalca, F.; Ferragut, R.; Aghion, S.; Eilert, A.; Diaz-Morales, O.; Liu, C.; Koh, A. L.; Hansen, T. W.; Pettersson, L. G. M.; Nilsson, A. Nature and Distribution of Stable Subsurface Oxygen in Copper Electrodes during Electrochemical CO₂ Reduction. *J. Phys. Chem. C* **2017**, *121*, 31.
- (14) Deng, Y.; Huang, Y.; Ren, D.; Handoko, A. D.; Seh, Z. W.; Hirunsit, P.; Yeo, B. S. On the Role of Sulfur for the Selective Electrochemical Reduction of CO₂ to Formate on Cu_S Catalysts. *ACS Appl. Mater. Interfaces* **2018**, *10*, 28572–28581.
- (15) Shinagawa, T.; Larrazábal, G. O.; Martín, A. J.; Krumeich, F.; Pérez-Ramírez, J. Sulfur-Modified Copper Catalysts for the Electrochemical Reduction of Carbon Dioxide to Formate. *ACS Catal.* **2018**, *8*, 837–844.
- (16) Zhu, Q. G.; Sun, X. F.; Kang, X. C.; MA, J.; Qian, Q. L.; Han, B. X. Cu₂S on Cu Foam as Highly Efficient Electrocatalyst for Reduction of CO₂ to Formic Acid. *Acta Phys. - Chim. Sin.* **2016**, *32*, 261–266.
- (17) Huang, Y.; Deng, Y.; Handoko, A. D.; Goh, G. K. L.; Yeo, B. S. Rational Design of Sulfur-Doped Copper Catalysts for the Selective Electroreduction of Carbon Dioxide to Formate. *ChemSusChem* **2018**, *11*, 320–326.
- (18) Phillips, K. R.; Katayama, Y.; Hwang, J.; Shao-Horn, Y. Sulfide-Derived Copper for Electrochemical Conversion of CO₂ to Formic Acid. *J. Phys. Chem. Lett.* **2018**, *9*, 4407–4412.
- (19) Chen, Y.; Chen, K.; Fu, J.; Yamaguchi, A.; Li, H.; Pan, H.; Hu, J.; Miyauchi, M.; Liu, M. Recent Advances in the Utilization of Copper Sulfide Compounds for Electrochemical CO₂ Reduction. *Nano Mater. Sci.* **2019**, *In press*.
- (20) Zhao, Z.; Peng, X.; Liu, X.; Sun, X.; Shi, J.; Han, L.; Li, G.; Luo, J. Efficient and Stable Electroreduction of CO₂ to CH₄ on CuS Nanosheet Arrays. *J. Mater. Chem. A* **2017**, *5*, 20239–20243.

- (21) Zhuang, T. T.; Liang, Z. Q.; Seifitokaldani, A.; Li, Y.; De Luna, P.; Burdyny, T.; Che, F.; Meng, F.; Min, Y.; Quintero-Bermudez, R.; et al., Steering Post-C-C Coupling Selectivity Enables High Efficiency Electroreduction of Carbon Dioxide to Multi-Carbon Alcohols. *Nat. Catal.* **2018**, *1*, 421–428.
- (22) Shao, P.; Ci, S.; Yi, L.; Cai, P.; Huang, P.; Cao, C.; Wen, Z. Hollow CuS Microcube Electrocatalysts for CO₂ Reduction Reaction. *ChemElectroChem* **2017**, *4*, 2593–2598.
- (23) Van Der Stam, W.; Berends, A. C.; De Mello Donega, C. Prospects of Colloidal Copper Chalcogenide Nanocrystals. *ChemPhysChem* **2016**, *17*, 559–581.
- (24) Van Den Berg, R.; Prieto, G.; Korpershoek, G.; Van Der Wal, L. I.; Van Bunningen, A. J.; Lægsgaard-Jørgensen, S.; De Jongh, P. E.; De Jong, K. P. Structure Sensitivity of Cu and CuZn Catalysts Relevant to Industrial Methanol Synthesis. *Nat. Commun.* **2016**, *7*.
- (25) Munnik, P.; De Jongh, P. E.; De Jong, K. P. Recent Developments in the Synthesis of Supported Catalysts. *Chem. Rev.* **2015**, *115*, 6687–6718.
- (26) Munnik, P.; Wolters, M.; Gabriellson, A.; Pollington, S. D.; Headdock, G.; Bitter, J. H.; De Jongh, P. E.; De Jong, K. P. Copper Nitrate Redispersion to Arrive at Highly Active Silica-Supported Copper Catalysts. *J. Phys. Chem. C* **2011**, *115*, 14698–14706.
- (27) Wang, G.; van den Berg, R.; de Mello Donega, C.; de Jong, K. P.; de Jongh, P. E. Silica-Supported Cu₂O Nanoparticles with Tunable Size for Sustainable Hydrogen Generation. *Appl. Catal. B Environ.* **2016**, *192*, 199–207.
- (28) Patterson, A. L. The Scherrer Formula for X-Ray Particle Size Determination. *Phys. Rev.* **1939**, *56*, 978–982.
- (29) Li, J.; Che, F.; Pang, Y.; Zou, C.; Howe, J. Y.; Burdyny, T.; Edwards, J. P.; Wang, Y.; Li, F.; Wang, Z.; et al., Copper Adparticle Enabled Selective Electrosynthesis of N-Propanol. *Nat. Commun.* **2018**, *9*.
- (30) ICDD (2019) PDF-4+ 2019 (Database). Edited by Dr. Soorya Kabekkodu. *Int. Cent. Diff. Data, Newt. Square, PA, USA*.
- (31) A. Roine. HSC Chemistry® [Software], Outotec, Pori 2018. Software Available at www.Outotec.Com/HSC.
- (32) Tang, W.; Peterson, A. A.; Varela, A. S.; Jovanov, Z. P.; Bech, L.; Durand, W. J.; Dahl, S.; Nørskov, J. K.; Chorkendorff, I. The Importance of Surface Morphology in Controlling the Selectivity of Polycrystalline Copper for CO₂ Electroreduction. *Phys. Chem. Chem. Phys.* **2012**, *14*, 76–81.
- (33) Firet, N. J.; Blommaert, M. A.; Burdyny, T.; Venugopal, A.; Bohra, D.; Longo, A.; Smith, W. A. Operando EXAFS Study Reveals Presence of Oxygen in Oxide-Derived Silver Catalysts for Electrochemical CO₂ Reduction. *J. Mater. Chem. A* **2019**, *7*, 2597–2607.
- (34) Handoko, A. D.; Wei, F.; Jenndy, Yeo, B. S.; Seh, Z. W. Understanding Heterogeneous Electrocatalytic Carbon Dioxide Reduction through Operando Techniques. *Nat. Catal.* **2018**, *1*, 922–934.
- (35) Eilert, A.; Roberts, F. S.; Friebel, D.; Nilsson, A. Formation of Copper Catalysts for CO₂ Reduction with High Ethylene/Methane Product Ratio Investigated with in Situ X-Ray Absorption Spectroscopy. *J. Phys. Chem. Lett.* **2016**, *7*, 1466–1470.
- (36) Yoo, J. S.; Christensen, R.; Vegge, T.; Nørskov, J. K.; Studt, F. Theoretical Insight into the Trends That Guide the Electrochemical Reduction of Carbon Dioxide to Formic Acid. *ChemSusChem* **2016**, *9*, 358–363.
- (37) Cheng, T.; Xiao, H.; Iii, W. A. G. Reaction Mechanisms for the Electrochemical Reduction of CO₂ to CO and Formate on the Cu(100) Surface at 298 K from Quantum Mechanics Free Energy Calculations with Explicit Water. *J. Am. Chem. Soc.* **2016**, *138*, 25.
- (38) Loiudice, A.; Lobaccaro, P.; Kamali, E. A.; Thao, T.; Huang, B. H.; Ager, J. W.; Buonsanti, R. Tailoring Copper Nanocrystals towards C₂ Products in Electrochemical CO₂ Reduction. *Angew. Chemie - Int. Ed.* **2016**, *55*, 5789–5792.
- (39) Reske, R.; Mistry, H.; Behafarid, F.; Roldan Cuenya, B.; Strasser, P. Particle Size Effects in the Catalytic Electroreduction of CO₂ on Cu Nanoparticles. *J. Am. Chem. Soc.* **2014**, *136*, 6978–6986.

Cu_{2-x}S derived nanoparticles supported on carbon for the electrochemical reduction of CO₂



Chapter 7

Summary and outlook

In this thesis we focused on the preparation of Cu_{2-x}S nanoparticles suitable for catalytic applications, and explored their use in photo- and electrocatalysis. This chapter summarizes the results of the work and provides a brief outlook to follow-up work.

7.1 Summary

In **Chapter 1**, the topics discussed in the thesis were briefly introduced. First, the versatile and composition-dependent properties of Cu_{2-x}S were discussed, followed by an introduction to the unique properties of nanoparticles. The chapter also described the fundamentals of the synthesis of nanoparticles, focusing on colloidal synthesis methods and incipient wetness impregnation. Subsequently, the principles and relevance of photo- and electrocatalysis were explained.

The first part of the thesis (Chapters 2, 3 and 4) focused on the preparation Cu_{2-x}S nanoparticles that are suitable for catalytic applications. **Chapter 2** introduced a post-synthetic ligand exchange procedure for colloidal Cu_{2-x}S nanocrystals. The use of colloidal nanocrystals in catalytic applications is often complicated by the adverse effects of organic capping ligands. Consequently, ligand-exchange procedures are necessary to make these nanocrystals more suitable for (catalytic) applications. In colloidal Cu_{2-x}S nanocrystal synthesis, 1-dodecanethiol is often used as organic ligand and sulfur source, as this yield high-quality nanocrystals. We presented a facile and effective ligand-exchange procedure, in which native 1-dodecanethiol ligands on Cu_{2-x}S nanocrystals were replaced by 3-mercaptopropionic acid, 11-mercaptoundecanoic acid or S^{2-} in formamide under inert atmosphere. The resulting hydrophilic Cu_{2-x}S nanocrystals had excellent colloidal stability in formamide and their size, shape and optical properties were not significantly affected by the ligand exchange procedure. The Cu_{2-x}S nanocrystals were easily dispersed in water by precipitation of the nanocrystals from formamide and subsequent redispersion in water. Interestingly, the ligand-exchange rates depended on the synthesis method used to prepare the Cu_{2-x}S nanocrystals, where ligand-exchange on nanocrystals prepared by heating-up synthesis was much slower than on nanocrystals prepared by hot-injection synthesis. XPS studies revealed a less dense ligand layer for the nanocrystals prepared via hot-injection synthesis than via heating-up synthesis. The less dense ligand layer made the nanocrystal surface more accessible for the replacing ligands, thereby speeding up the ligand exchange rates. The facile ligand-exchange procedure presented in this chapter facilitates the use of colloidal Cu_{2-x}S nanocrystals in catalysis and can potentially be used for colloidal nanocrystals of other materials.

In **Chapter 3**, the synthesis and formation mechanism of $\text{Cu}_{2-x}\text{S}/\text{CuInS}_2$ heteronanocrystals was presented. Combining Cu_{2-x}S and CuInS_2 domains in one single nanocrystal can lead to improved spatial separation of photogenerated electrons and holes. This is expected to be beneficial in photocatalysis since it increases the lifetime of the photogenerated exciton, thereby kinetically favoring surface reactions involving the photogenerated charge carriers. The chapter presented a two-step synthesis route to prepare $\text{Cu}_{2-x}\text{S}/\text{CuInS}_2$ heteronanocrystals. First, Cu_{2-x}S seed nanocrystals were prepared, which were subsequently injected into a pre-heated solution of indium-oleate.

By characterization of the reaction intermediates, we proposed that the initial formation of the $\text{Cu}_{2-x}\text{S}/\text{CuInS}_2$ heteronanocrystals occurred via a single step, thiolate-mediated cation exchange of Cu^+ for In^{3+} . This was followed by CuInS_2 growth on the pre-formed CuInS_2 surface from solution. The size, shape and composition of the heteronanocrystals could be easily tuned by varying the reaction time.

In catalytic applications, the presence of a catalyst support, such as silica or carbon, can be beneficial as it improves the stability of the nanoparticles and allows for easier handling of the catalysts, making them more suitable for practical application. Therefore, **Chapter 4** describes the preparation of silica-supported CuS and Cu_2S nanoparticles via a novel method, using copper nitrate as the copper source and thioacetamide or 1-dodecanethiol as the sulfur source, respectively. Monodisperse Cu_2S nanoparticles with a uniform distribution over the silica support were prepared directly from 1-dodecanethiol and copper nitrate. To prepare CuS nanoparticles with control over particle size and a uniform distribution over the support, pre-synthesized CuO nanoparticles were converted into CuS nanoparticles using a liquid-phase sulfidation with thioacetamide. As the original size of the CuO nanoparticles was preserved upon sulfidation to CuS , this method allows for the extension of the good control over the particle size of silica-supported CuO nanoparticles to silica-supported CuS nanoparticles.

In the second part of this thesis (Chapters 5 and 6), the use of Cu_{2-x}S nanoparticles in photo- and electrocatalysis was explored. The initial focus was on the use of Cu_{2-x}S nanoparticles in photocatalysis. However, along the way we found that, in our experience, the Cu_{2-x}S nanoparticles showed only limited activity in photocatalytic dye degradation and H_2 evolution. Furthermore, conducting photocatalytic experiments and interpreting the data proved to not always be straightforward due to the many variables influencing the reactions. Therefore, in **Chapter 5** we reviewed the various aspects of photocatalysis, based on our own experience, as well as examples from literature. The chapter handled common pitfalls in photocatalysis, and gave practical guidelines on how to reliably conduct, interpret and report photocatalytic experiments.

Besides photocatalysis, the use of Cu_{2-x}S nanoparticles in electrocatalysis was studied. Recently, several experimental and theoretical studies have demonstrated that the addition of sulfur modifies the performance of Cu catalysts in the electrochemical reduction of CO_2 . Inspired by these studies, **Chapter 6** presented the use of Cu_{2-x}S derived nanoparticles supported on carbon for the electrocatalytic reduction of CO_2 . By extending the sulfidation method discussed in Chapter 4 to carbon supports, a set of three Cu nanoparticle catalysts with similar morphologies was prepared by *in situ* reduction of either supported CuS , Cu_2S or CuO nanoparticles. Subsequently, electrodes were prepared by spraying the carbon supported CuS , Cu_2S or CuO nanoparticles on a carbon-paper substrate. For the first time, the evolution of the Cu species was followed under typical CO_2 and H^+ reduction conditions using *in situ* x-ray absorption spectroscopy. Metallic Cu was observed as the predominant phase under reaction conditions, indicating an excellent electrochemical contact between the Cu -based nanoparticles, the carbon support and the carbon-paper substrate. On all three catalysts,

formate was produced as the main CO₂ reduction product, next to H₂ which was produced by the reduction of H⁺, mainly by the carbon support. At current densities of -1.5 mA/cm², the selectivity towards formate was enhanced for the CuS- and Cu₂S-derived catalysts when compared to the CuO-derived catalyst. Even though less than 4% of the carbon support was covered with Cu-based nanoparticles, a maximum Faradaic efficiency to formate of 21% was achieved. This showed the effectiveness of Cu_{2-x}S-derived catalysts to steer the selectivity of CO₂ reduction to formate.

7.2 Outlook

Photo- and electrocatalysis are promising strategies for the production of sustainable chemicals and fuels. Therefore, the development of good catalysts is important. To optimize catalysts, it is important to understand the origin of their catalytic performance, and gain insight into the influence of the catalyst composition, size and shape. Consequently, good quality, monodisperse samples are essential.

In this thesis, we discussed several methods to prepare Cu_{2-x}S nanoparticles, where colloidal Cu_{2-x}S (hetero)nanocrystals as well as supported Cu_{2-x}S nanoparticles were prepared with good control over size, shape and composition. Although the methods focused on Cu_{2-x}S, they can potentially be extended to other materials. For example, the adverse effects of ligands when using colloidal nanocrystals in catalytic applications is a well-known problem and consequently ligand-exchange procedures are also relevant for other materials. Although our method focused on strongly bound thiolate ligands on colloidal Cu_{2-x}S nanoparticles, it can likely be adapted to colloidal nanocrystals with other compositions. Similarly, the preservation of size when using pre-formed metal oxide nanoparticles as precursor for the preparation of metal sulfide nanoparticles could find use in the preparation of other metal sulfide nanoparticles.

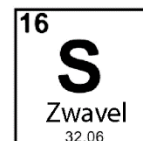
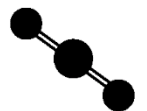
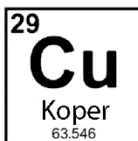
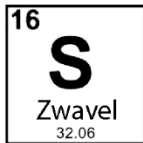
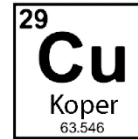
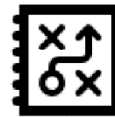
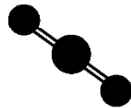
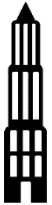
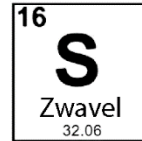
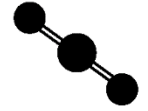
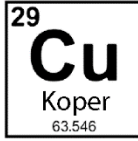
From our findings, Cu_{2-x}S nanoparticles have low potential to act as photocatalyst. However, several strategies to improve their performance could be investigated. For example, the addition of a co-catalyst, such as platinum, could facilitate separation and extraction of the photogenerated charge carriers and has been found to improve photocatalytic performance in *e.g.*, CdS, TiO₂ and Cu₂O. In addition, combining Cu_{2-x}S with other materials to create Type I^{1/2} or Type II heteronanocrystals can possibly improve the photocatalytic properties.

An important measure of catalyst performance is their selectivity to making the desired product. In Chapter 6, we showed that Cu_{2-x}S derived nanoparticles were effective in steering the selectivity of CO₂ reduction towards formate. Furthermore, even though both the CuS@C and Cu₂S@C catalyst were shown to be reduced to metallic Cu under CO₂ and H⁺ reduction conditions, a difference in selectivity between the two catalysts was observed. This difference was attributed to differences in residual sulfur on the catalyst, as identified by *ex situ* characterization after catalysis. To elucidate where the residual sulfur is located in or on the catalyst, additional *in situ* studies (*e.g.*, XAS at the

S edge) would be valuable. In addition, it would be very interesting to study the dependence of the product selectivity on the sulfur content in more detail. In order to do so, a broader range of Cu_{2-x}S compositions could be used as starting material, so that any trends in the dependence of product selectivity on sulfur content can be elucidated.

Besides formate, H_2 was produced by all catalysts, mainly on the carbon support. The formation of H_2 can likely be decreased by increasing the surface coverage of the carbon support by Cu_{2-x}S nanoparticles. This can be realized by using a carbon support with a lower surface area or by further increasing the catalyst loading. In addition, it would be interesting to further explore the use of colloidal Cu_{2-x}S nanocrystals, as these particles can be directly deposited on the carbon-paper substrate, thereby reducing the amount of carbon surface exposed. The challenge here would be to obtain monolayers of nanocrystals on the carbon-paper substrate to ensure a good electrochemical contact between the nanocrystals and the carbon-paper support. For this, the ligand-exchange procedure described in Chapter 2 could be used. This would not only improve the electrochemical contact between the nanocrystals and the carbon support, but also make the nanocrystal surface more accessible to reactants.

In this research we focused on Cu_{2-x}S nanoparticles for applications in catalysis. Due to their tunable properties, Cu_{2-x}S nanoparticles have also received attention for application in other fields, such as biomedical sensing, photothermal therapy and photovoltaic- and plasmonic devices. The methods discussed in this thesis can serve as a foundation for further research in these fields where the properties of Cu_{2-x}S are of interest.



Chapter 8

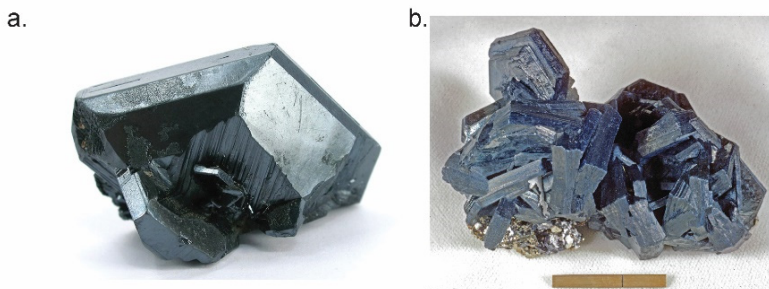
Nederlandse samenvatting

In dit proefschrift worden verschillende bereidingsmethoden van kopersulfide nanodeeltjes en hun toepassing in de foto- en elektrokatalyse besproken. Dit hoofdstuk geeft een korte uitleg over deze onderwerpen en sluit af met een korte samenvatting van de hoofdstukken in dit proefschrift.

8.1 Kopersulfide

Kopersulfiden zijn chemische verbindingen die bestaan uit koper en zwavel atomen. De meeste van deze kopersulfiden komen voor in de natuur als mineralen. Kopersulfide vertoont een grote verscheidenheid aan kristalstructuren met verschillende verhoudingen tussen koper en zwavel. De meest bekende kopersulfiden zijn chalcociet (Cu_2S) en covelliet (CuS) (Figuur 8.1). Dit zijn ook de twee kopersulfiden die in dit proefschrift het meest aan bod komen. Chalcociet is afgeleid van het Griekse woord *Chalkos*, dat koper betekent, en heeft een donker grijze tot zwarte kleur (Figuur 8.1a). Doordat chalcociet op veel plaatsen op de wereld voorkomt en een hoog kopergehalte heeft, is het een van de belangrijkste ertsen waaruit koper gewonnen wordt. Covelliet (CuS) is vernoemd naar Niccolo Covelli, die het mineraal als eerst ontdekte op de Vesuvius in Italië. In tegenstelling tot chalcociet komt covelliet maar in beperkte mate voor in de natuur. Covelliet heeft een indigoblauwe tot zwarte kleur met een regenboogkleurige gloed (Figuur 8.1b).

Kopersulfiden zijn interessant voor verschillende toepassingen door hun materiaaleigenschappen. Zo kunnen kopersulfiden bijvoorbeeld zichtbaar licht absorberen en stroom geleiden. De exacte materiaaleigenschappen variëren met de verschillende kopersulfide kristalstructuren en zijn sterk afhankelijk van de verhouding tussen koper en zwavel in de structuur. Door kopersulfide structuren met een specifieke koper/zwavel ratio te synthetiseren, kunnen bepaalde materiaaleigenschappen op een gecontroleerde wijze worden verkregen.

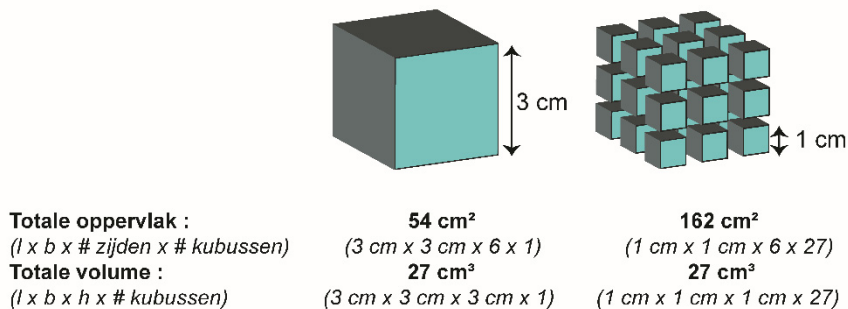


Figuur 8.1 a) Chalcociet (Cu_2S) kristallen en b) covelliet (CuS) kristallen.

8.2 Nanodeeltjes

In dit proefschrift is onderzoek gedaan naar kopersulfide nanodeeltjes. Nanodeeltjes zijn zeer kleine deeltjes met een grootte tussen de 1 en 100 nanometer (nm), waar 1 nm gelijk is aan 0.000000001 meter. Ter vergelijking, 1 nm is ongeveer 100.000 maal dunner dan de dikte van een vel papier. Een nanodeeltje bestaat uit ongeveer 100 tot 10.000 atomen.

Nanodeeltjes hebben door hun kleine formaat bijzondere eigenschappen en daarom worden ze veel gebruikt in producten zoals verf en zonnebrand. Ook worden nanodeeltjes gebruikt in de katalyse, waar de deeltjes fungeren als katalysator. Een katalysator is een materiaal dat een chemische reactie versnelt zonder daarbij zelf verbruikt te worden. Deze reacties vinden plaats aan het oppervlak van het katalysator deeltje. Het gebruik van nanodeeltjes heeft hier een voordeel, omdat in een klein deeltje naar verhouding meer atomen aan het oppervlak van het deeltje liggen dan in een groter deeltje. Dit is schematisch weergegeven in Figuur 8.2. Bij het gebruik van nanodeeltjes heb je dus minder materiaal nodig om hetzelfde actieve oppervlak te verkrijgen dan bij groter materiaal. Daarnaast hebben atomen aan het oppervlak minder chemische bindingen met buuratomen dan atomen in het binnenste van een deeltje. Hierdoor zijn de oppervlakte atomen meer reactief.



Figuur 8.2 Een schematische weergave van de snelle toename van het oppervlak bij het gebruik van kleine deeltjes ten opzichte van één groot deeltje, terwijl het totale volume in beide gevallen gelijk is. l geeft de lengte, b de breedte en h de hoogte van de (individuele) kubus(en) weer.

8.3 Het maken van nanodeeltjes

Nanodeeltjes kunnen in een laboratorium op verschillende manieren gemaakt worden. In dit proefschrift wordt er gebruik gemaakt van twee methoden: colloïdale synthese en de synthese van nanodeeltjes op een drager materiaal.

Colloïden zijn kleine deeltjes die verdeeld zijn in een vloeistof. Een voorbeeld van zo'n colloïdale dispersie is melk, waar vetdruppels en eiwitten gedispergeerd zijn in water. Colloïdale nanodeeltjes kunnen gevormd worden uit opgeloste precursors. Dit zijn

uitgangsstoffen die als voorloper dienen voor de nanodeeltjes, zoals bijvoorbeeld koperzouten en zwavelhoudende moleculen. Ook zijn zogenaamde liganden erg belangrijk tijdens en na de synthese van colloïdale nanodeeltjes. Liganden zijn grote moleculen die tijdens de synthese losjes aan de groeiende nanodeeltjes binden, en hierdoor de groei van de nanodeeltjes beïnvloeden. Deze liganden zijn ook na de synthese van de deeltjes van belang, omdat ze de nanodeeltjes in de suspensie stabiliseren en het samenklonteren van deeltjes voorkomen. De liganden zijn dus erg belangrijk voor de synthese van colloïdale nanodeeltjes, maar vormen een uitdaging bij het gebruik van colloïdale nanodeeltjes als katalysator. Dit komt doordat de liganden het oppervlak van de deeltjes blokkeren. Hierdoor is het katalytisch actieve oppervlak van colloïdale nanodeeltjes dus moeilijker te bereiken voor reactanten.

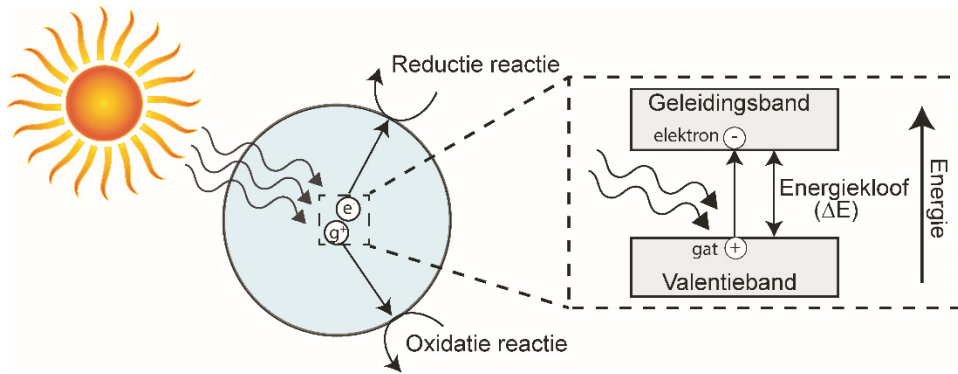
Een tweede methode om nanodeeltjes te maken is via synthese van nanodeeltjes op een dragermateriaal, zoals bijvoorbeeld silica of koolstof. Deze methode wordt veel gebruikt in de katalyse, omdat een drager zorgt voor extra stabiliteit van de nanodeeltjes. Ook maakt een dragermateriaal een katalysator beter hanteerbaar, omdat de katalysator zo uit minder kleine deeltjes bestaat en daardoor bijvoorbeeld gemakkelijker gescheiden kan worden van een reactiemengsel. De synthese van nanodeeltjes op een drager gaat vaak via impregnatie van een poreuze drager met een oplossing van een metaalprecursor. De metaalprecursors worden vervolgens door verschillende droog- en verwarmingsstappen omgezet in nanodeeltjes. Op deze manier kunnen met name metaaloxiden en metallische nanodeeltjes gemaakt worden (bijvoorbeeld koperoxide of koper). Om sulfide nanodeeltjes te maken is na deze impregnatie nog een extra sulfidatie stap nodig, waarin de koperoxide nanodeeltjes worden omgezet in kopersulfide.

8.4 Katalyse met kopersulfide nanodeeltjes

Kopersulfide nanodeeltjes zijn aantrekkelijk als katalysator door hun samenstelling-afhankelijke materiaaleigenschappen, geringe giftigheid en relatief lage kosten. In dit proefschrift hebben we gekeken naar de toepassing van deze nanodeeltjes in foto- en elektro-katalyse.

8.4.1 Fotokatalyse

Fotokatalyse is een proces geïnspireerd op de fotosynthese van planten. In dit proces nemen groene planten energie op uit zonlicht en zetten dit om in chemische energie, opgeslagen in moleculen zoals suikers. Een soortgelijk proces vindt plaats in fotokatalyse, waarin een halfgeleider materiaal (de fotokatalysator) door middel van het absorberen van zonne-energie chemische reacties kan aandrijven. Dit proces is schematisch weergegeven in Figuur 8.3. Een halfgeleider heeft een elektronische bandstructuur waar de valentie- en geleidingsband gescheiden zijn door een energiekloof. Als een halfgeleider wordt beschienen met licht met een energie hoog genoeg om deze kloof te overbruggen, kunnen negatief geladen elektronen van de valentieband naar de geleidingsband verplaatst worden. Dit laat vervolgens een positief



Figuur 8.3 Schematische weergave van een fotokatalysator. Het nanodeeltje kan (zon)licht absorberen met een energie gelijk aan of hoger dan de energieklouf. Door het absorberen van deze energie verandert de elektronische toestand van het deeltje, zoals weergegeven in het panel aan de rechterzijde. Een negatief geladen elektron kan van de valentieband naar de geleidingsband worden verplaatst. Er blijft dan een positief geladen gat over in de valentieband. Deze ladingsdragers, gecreëerd door het absorberen van licht, kunnen aan het oppervlak van het deeltje deelnemen aan reductie- en oxidatiereacties, zoals bijvoorbeeld het afbreken van moleculen of het produceren van waterstof.

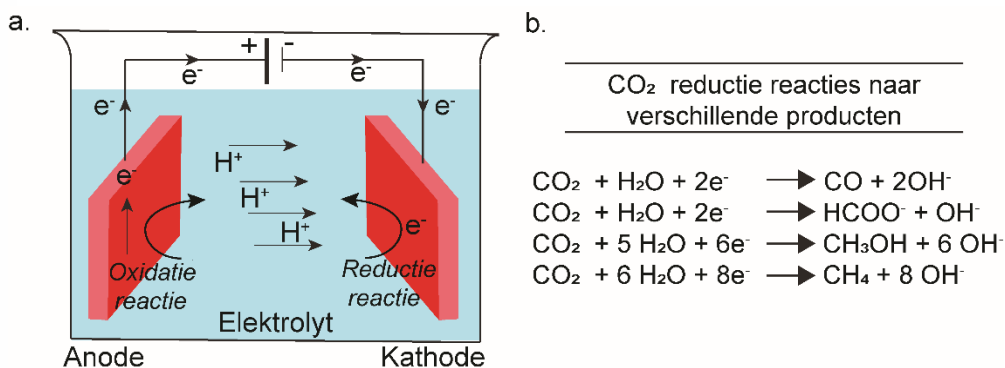
geladen gat achter in de valentieband. Als deze ladingsdragers het oppervlak van het deeltje kunnen bereiken, kunnen deze daar worden gebruikt om reductie- en oxidatiereacties aan te drijven. De energieklouf van een halfgeleider is dus een belangrijke eigenschap van een fotokatalysator. De energieklouf moet voldoende groot zijn om de energie benodigd voor de chemische reacties te kunnen opnemen. Aan de andere kant mag de energieklouf niet te groot zijn, omdat het zonlicht anders niet voldoende energie bevat om de energieklouf te overbruggen. De energieklouf van kopersulfide is afhankelijk van de hoeveelheid koper in de structuur en ligt tussen 1.2 eV voor Cu_2S en 1.9 eV voor CuS . Deze waarden maken kopersulfide geschikt als fotokatalysator, omdat kopersulfide hierdoor efficiënt zichtbaar licht (en dus zonlicht) kan absorberen.

Fotokatalyse kan gebruikt worden om verschillende chemische reacties te laten plaatsvinden. In dit proefschrift wordt het afbreken van organische kleurstofmoleculen besproken. In plaats van een het aandrijven van reacties die normaal gesproken niet zouden verlopen (zoals bij fotosynthese), gaat het in dit geval om het versnellen van reacties die normaal gesproken ook al zouden verlopen, maar dan langzamer. Dit soort reacties worden vaak gebruikt als modelstudie voor het afbreken van moleculen in afvalwater. Andere bekende reacties richten zich wel op fotosynthese, oftewel het produceren van zogenaamde 'solar fuels', waar zonne-energie kan worden omgezet in en opgeslagen als chemische energie. Een bekend voorbeeld hiervan is het fotokatalytisch produceren van waterstof en zuurstof uit water.

8.4.2 Elektrokatalyse

Een tweede vorm van katalyse die in dit proefschrift wordt behandeld is elektrokatalyse. Een reactie wordt dan aangedreven door een elektrische stroom en omvat de overdracht van lading van een elektrode aan moleculen of ionen in oplossing. Deze reactie kan worden versneld door gebruik van een elektrokatalysator. Deze katalysator kan de elektrode zelf zijn, maar kan ook worden aangebracht op een bestaande elektrode. In Figuur 8.4a is een elektrochemische cel weergegeven, bestaande uit drie hoofdcomponenten: de anode, de kathode en het elektrolyt. De anode is de elektrode waaraan oxidatie reacties plaatsvinden, *i.e.*, reacties waar elektronen worden afgestaan. De kathode is de elektrode waaraan reductie reacties plaatsvinden, *i.e.*, reacties waarin elektronen worden opgenomen. Het elektrolyt is een medium tussen de anode en kathode. Het geleidt geen elektrische stroom, maar wel ionen.

In dit onderzoek is gekeken naar de elektrochemische reductie van CO₂ met behulp van katalysatoren gebaseerd op kopersulfide. De reductie van CO₂ met behulp van duurzame elektriciteit is een veelbelovende manier om chemicaliën en brandstoffen te produceren. Voorbeelden van chemicaliën die op deze wijze geproduceerd kunnen worden zijn onder andere koolstofmonoxide (CO), formiaat (HCOO⁻), methanol (CH₃OH), en methaan (CH₄) (Figuur 8.4b). De laatste 10 jaar is er grote vooruitgang geboekt in de ontwikkeling van efficiënte elektrokatalysatoren voor de reductie van CO₂. De meeste van deze katalysatoren bestaan uit metalen, zoals bijvoorbeeld goud, zilver, koper of zink. Koper onderscheidt zich van de andere metalen omdat het als enige verschillende koolwaterstoffen en zuurstofhoudende verbindingen kan produceren. Het is echter een uitdaging om selectief een bepaald product te maken. Recente studies hebben laten zien dat het toevoegen van zwavel aan een koperkatalysator de selectiviteit van



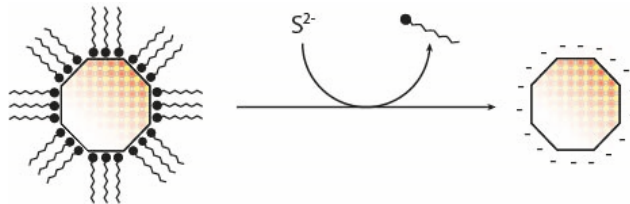
Figuur 8.4 a) Schematische weergave van een elektrochemische cel gebruikt in elektrokatalyse. Oxidatie reacties vinden plaats aan de anode en reductie reacties aan de kathode. Ionen kunnen zich verplaatsen door het elektrolyt, dat geen stroom geleidt. **b)** Voorbeelden van reductie reacties van CO₂, waarbij verschillende producten gevormd kunnen worden, zoals koolstofmonoxide (CO), formiaat (HCOO⁻), methanol (CH₃OH) en methaan (CH₄).

koperkatalysatoren naar bijvoorbeeld formiaat kan beïnvloeden. Geïnspireerd door deze studies hebben we gekeken naar het gebruik van kopersulfide als katalysator in de elektrochemische reductie van CO_2 .

8.5 Wat staat er in dit proefschrift?

Om katalysatoren te kunnen verbeteren, is het belangrijk om te begrijpen hoe een katalysator precies werkt, en wat de effecten van bijvoorbeeld de grootte, vorm en samenstelling van deeltjes zijn op de katalytische prestatie. Om dit goed te kunnen onderzoeken, is het belangrijk om uniforme monsters te maken, waarin alle deeltjes dezelfde samenstelling, grootte en vorm hebben. In het eerste deel van dit proefschrift (hoofdstuk 2, 3 en 4) zijn verschillende synthesemethoden voor het maken van uniforme kopersulfide nanodeeltjes beschreven. Het tweede deel (hoofdstuk 5 en hoofdstuk 6) beschrijft vervolgens de potentie van deze kopersulfide nanodeeltjes als foto- en elektrokatalysator.

Hoofdstuk 2 beschrijft een methode om colloïdale nanodeeltjes beter bruikbaar te maken voor toepassingen in de (foto)katalyse. Zoals hierboven beschreven zijn colloïden vaak omringd door een laag van liganden. Deze liganden zorgen onder andere voor de stabiliteit van de deeltjes in de oplossing. Als we deze nanodeeltjes willen gebruiken als katalysator, hebben deze liganden echter een nadelig effect. Dit komt onder andere doordat de ligand moleculen het oppervlak van het katalytisch actieve nanodeeltje blokkeren en reactanten dit oppervlak dus moeilijker kunnen bereiken. Een tweede uitdaging is dat liganden vaak apolair zijn, wat betekent dat de deeltjes niet makkelijk dispergeren in polaire vloeistoffen zoals water. Veel fotokatalytische reacties vinden echter wel plaats in water en daarom moeten deze colloïdale nanodeeltjes geoptimaliseerd worden voor gebruik in de katalyse. Dit kan door liganduitwisseling. Deze procedure vindt plaats na de synthese van de deeltjes en verwisselt de grote, apolaire ligandmoleculen voor kleinere, polaire liganden. Kopersulfide nanodeeltjes zijn vaak gestabiliseerd door een laag van zwavelhoudende thiol liganden, die erg sterk gebonden zijn aan het nanodeeltje. Dit maakt de uitwisseling van deze liganden lastig.



Figuur 8.5 Schematische weergave van een ligand uitwisseling. Een colloïdaal nanodeeltje is gestabiliseerd door lange, apolaire ligandmoleculen. Door middel van een ligand uitwisseling kunnen deze grote liganden verwisseld worden voor korte, polaire liganden. Hierdoor is het katalytisch actieve oppervlak van het nanodeeltje beter toegankelijk voor reactanten en kan het deeltje in polaire oplosmiddelen zoals water worden gebruikt.

In hoofdstuk 2 beschrijven we een methode om deze thiol liganden op kopersulfide nanodeeltjes toch te kunnen uitwisselen voor kleinere, polaire moleculen, door gebruik te maken van een sterk polair oplosmiddel en een zuurstofvrije omgeving.

Hoofdstuk 3 beschrijft de synthese en het groei mechanisme van heterogene nanodeeltjes, bestaande uit kopersulfide (Cu_2S) en koperindiumsulfide (CuInS_2). Het combineren van twee verschillende materialen in een enkel nanodeeltje kan van toegevoegde waarde zijn voor fotokatalysatoren, omdat op deze wijze de materiaaleigenschappen van beide materialen in een enkel deeltje samengevoegd kunnen worden. Bovendien kunnen er nieuwe materiaaleigenschappen ontstaan, zoals bijvoorbeeld een verlengde levensduur van de door licht opgewekte ladingsdragers. Hoofdstuk 3 beschrijft een synthese methode voor het maken van $\text{Cu}_2\text{S}/\text{CuInS}_2$ heteronanodeeltjes waarbij vooraf gevormde Cu_2S nanodeeltjes in een mengsel van oliezuur en indium-precursors worden geïnjecteerd. Door de reactietijd te variëren, kan de grootte, vorm en samenstelling van de deeltjes worden beïnvloed.

In katalyse wordt vaak gebruik gemaakt van een dragermateriaal om de stabiliteit van nanodeeltjes te vergroten. In **hoofdstuk 4** worden een methoden beschreven om kopersulfide nanodeeltjes op een silica dragermateriaal te maken. Chalcociet (Cu_2S) nanodeeltjes op silica werden bereid door een eenvoudige synthese methode in de aanwezigheid van silica. Deze methode resulteerde in Cu_2S nanodeeltjes van gelijke grootte die mooi verdeeld lagen over de silicadrager. Het maken van monodisperse, silica gedragen covelliet (CuS) nanodeeltjes bleek lastiger en daarom werd er een tweede methode ontwikkeld waarin silica gedragen koperoxide (CuO) deeltjes werden omgezet naar covelliet (CuS). Tijdens deze omzetting naar kopersulfide bleef de oorspronkelijke deeltjesgrootte van de koperoxide nanodeeltjes behouden. In eerder onderzoek van onze groep is al veel kennis opgedaan over het maken van silica gedragen koperoxide deeltjes met een goede controle over de deeltjesgrootte. Door deze koperoxide deeltjes vervolgens om te zetten naar kopersulfide, kan deze kennis gebruikt worden voor het maken van monodisperse, silica gedragen kopersulfide nanodeeltjes.

In het tweede deel van dit proefschrift (hoofdstuk 5 en hoofdstuk 6) verschuift de focus van de synthese naar de toepassing van kopersulfide nanodeeltjes in foto- en elektrokatalyse. Het oorspronkelijke plan was om de kopersulfide nanodeeltjes te gebruiken als fotokatalysator. Echter, gedurende het project bleek dat kopersulfide nanodeeltjes weinig actief waren, noch voor het fotokatalytisch afbreken van organische kleurstofmoleculen, noch voor de productie van waterstof en zuurstof uit water. Ook werd duidelijk dat het uitvoeren van fotokatalyse experimenten niet altijd eenvoudig en eenduidig is, en dat experimenten en resultaten gerapporteerd in literatuur niet altijd te reproduceren waren. In **hoofdstuk 5** wordt aan de hand van deze ervaringen een overzicht gegeven van de belangrijkste aspecten van fotokatalyse. Hierbij worden experimentele technieken, data analyse, verschillende mechanistische inzichten en het

rapporteren van katalytische data besproken aan de hand van onze eigen ervaringen met kopersulfide nanodeeltjes en door middel van voorbeelden uit de literatuur.

Naast fotokatalyse kunnen kopersulfide nanodeeltjes ook gebruikt worden in elektrokatalyse. In **hoofdstuk 6** wordt het gebruik van koolstof gedragen kopersulfide nanodeeltjes als katalysator voor de elektrochemische reductie van CO_2 onderzocht. De koolstof gedragen nanodeeltjes werden bereid met de methode besproken in hoofdstuk 4 en vervolgens op koolstof papier aangebracht. Op deze manier werden drie verschillende koolstof gedragen elektrodes bereid, namelijk met Cu_2S , CuS of CuO nanodeeltjes. Door gebruik te maken van een karakterisatiemethode gebaseerd op de absorptie van röntgenstraling, hebben we voor het eerst de chemische toestand van de katalysatoren tijdens reactie kunnen volgen. Hieruit bleek dat de kopersulfide nanodeeltjes onder reactie condities omgezet word naar metallisch koper. Ondanks deze reductie naar metallisch koper bevatten de gebruikte katalysatoren ook nog zwavel. Deze bevindingen toonden aan dat de actieve katalysatoren dus niet de kopersulfide nanodeeltjes zelf waren, maar metallisch koper met resten zwavel.

Door zowel de katalysatoren afgeleid van kopersulfide als van koperoxide werd formiaat gevormd door de reductie van CO_2 . Bij een stroomdichtheid van -1.5 mA/cm^2 produceerden de katalysatoren afgeleid van kopersulfide meer formiaat dan de katalysator afgeleid van koperoxide. De aanwezigheid van zwavel in de katalysatoren lijkt dus inderdaad de product selectiviteit naar formiaat te verhogen. Naast formiaat werd ook waterstof geproduceerd door de reductie van H^+ . Dit gebeurde voornamelijk op de koolstof drager. Opmerkelijk was dat, hoewel de kopersulfide nanodeeltjes maar 4% van het totale oppervlak van de koolstof elektrode bedekten, een elektron efficiëntie naar formiaat van 21% bereikt werd. Dit geeft aan dat het gebruik van katalysatoren afgeleid van kopersulfide nanodeeltjes een effectieve strategie is om de selectiviteit van CO_2 reductie naar formiaat te verhogen.

Al met al hebben we in dit proefschrift inzicht gegeven in verschillende methoden om monodisperse kopersulfide nanodeeltjes te maken, en hebben we laten zien dat met name hun toepassing in de elektrokatalyse interessante effecten geeft. De resultaten uit dit onderzoek kunnen ook in een breder perspectief geplaatst worden: zo kunnen ze bijvoorbeeld bijdragen aan de ontwikkeling van synthesemethoden voor nanodeeltjes bestaande uit andere materialen, of aan het gebruik van Cu_{2-x}S nanodeeltjes in toepassingen buiten de katalyse.

List of Publications

This thesis is based on the following publications:

- **van Oversteeg, C.H.M.**, Oropeza, F.E., Hofmann, J.P., Hensen, E.J.M., de Jongh, P.E. & de Mello-Donegá, C. (2019). Water-dispersible copper sulfide nanocrystals via ligand exchange of 1-dodecanethiol. *Chemistry of Materials*, 31, pp. 541-552 (Chapter 2)
- **van Oversteeg, C.H.M.**, Xia, C., Bogaards, V.C.L., Spanjersberg, T.H.M., Visser, N.L., Berends, A.C., Meeldijk, J.D., de Jongh, P.E. and de Mello Donegá, C. Synthesis and formation mechanism of $\text{Cu}_{2-x}\text{S}/\text{CuInS}_2$ heteronanocrystals via seeded-injection, *in preparation* (Chapter 3)
- **van Oversteeg, C.H.M.**, Kamarudheen, R., Baldi, A., de Mello Donegá, C. and de Jongh, P.E., Challenges and guidelines in heterogeneous, liquid-phase photo- and plasmon driven catalysis, *in preparation* (Chapter 5)
- **van Oversteeg, C.H.M.**, Tapia Rosales, M., Helfferich, K.H., Ghiasi, M., Meeldijk, J.D., Firet, N.J., Ngene, P., de Mello Donegá, C. & de Jongh, P.E., Cu_{2-x}S derived nanoparticles supported on carbon for the electrochemical reduction of CO_2 , *under review at Catalysis Today, 2020* (Chapter 6)

Other publications by the author:

- Raberg, J.H., Vatamanu, J., Harris, S.J., **van Oversteeg, C.H.M.**, Ramos, A., Borodin, O. and Cuk, T. (2019) Probing electric double-layer composition via in-situ vibrational spectroscopy and molecular simulations. *Journal of Physical Chemistry Letters*, 10, pp. 3381-3389
- Al Samarai, M., **van Oversteeg, C.H.M.**, Delgade-Jaime, M.U., Weng, T., Sokaras, D., Liu, B., van der Linden, M., van der Eerden, A.M.J., Vogt, E.T.C., Weckhuysen, B.M. & de Groot, F.M.F., (2019) Nature of cobalt species during the in situ reduction of $\text{Co}(\text{Ni})\text{Mo}/\text{Al}_2\text{O}_3$ hydrodesulfurization catalysts. *Journal of Synchrotron Radiation*, 26, pp. 811-818
- Xia, C., Wu, W., Yu, T., Xie, X., **van Oversteeg, C.H.M.** van, Gerritsen, H.C. & de Mello Donegá, C. (2018). Size-dependent band-gap and molar absorption coefficients of colloidal CuInS_2 quantum dots. *ACS Nano*, 12, pp. 8350-8361
- **van Oversteeg, C.H.M.**, Doan, H.Q., de Groot, F.M.F. & Cuk, T. (2016). In situ X-ray absorption spectroscopy of transition metal based water oxidation catalysts. *Chemical Society Reviews*, 46, pp. 102-125

Conference contributions

- Copper sulfide nanocrystals for photocatalysis at the **18th Netherlands Chemistry and Catalysis Conference, 2017** in Noordwijkerhout, The Netherlands (Poster)
- Water-dispersible copper sulfide nanocrystals at the **8th Nanoscience with Nanocrystals conference 2017** in Braga, Portugal (Poster)
- Water-dispersible copper sulfide nanocrystals at the **DPG Bad Honnef Physics school 2017** in Bad Honnef, Germany (Poster)
- Water-dispersible Cu_{2-x}S nanocrystals for photocatalytic applications at the **19th Netherlands Chemistry and Catalysis Conference 2018** in Noordwijkerhout, the Netherlands (Oral)
- Water-dispersible Cu_{2-x}S nanocrystals via ligand exchange at the **European Material Research Society Fall Meeting 2018** in Warsaw, Poland (Oral)
- Preparation methods of Cu_{2-x}S nanocrystals for photo- and electrocatalysis at **CHAINS 2018** in Veldhoven, The Netherlands (Oral)
- Water-dispersible Cu_{2-x}S nanocrystals via ligand exchange of 1-dodecanethiol at the **8th Molecular Aspects of Catalysis by Sulfides conference 2019** in Cabourg, France (Poster)
- Carbon-supported Cu_{2-x}S nanoparticles for the electroreduction of CO₂ at the **8th Molecular Aspects of Catalysis by Sulfides conference 2019** in Cabourg, France (Oral)
- Carbon-supported Cu_{2-x}S nanoparticles for the electrocatalytic reduction of CO₂ at the **1st electrochemical conversion and materials graduate school 2019** in Eerbeek, Netherlands (Poster)

Acknowledgements | Dankwoord

Na 4.5 jaar is mijn proefschrift af. Dit was niet gelukt zonder de hulp en steun van een heleboel mensen en daarom wil ik graag iedereen bedanken die heeft bijgedragen aan mijn onderzoek en de leuke tijd in Utrecht.

Allereerst wil ik mijn promotor Petra en copromotor Celso bedanken. Bedankt voor jullie fijne en goede begeleiding, flexibiliteit en jullie vertrouwen in mij. Petra, jouw optimisme en positieve kijk op dingen hebben mij altijd weer weten te motiveren en het was fijn dat ik altijd even binnen kon lopen met een vraag of nieuw resultaat. Celso, bedankt voor je enthousiasme en goede ideeën. Ik heb veel gehad aan onze (vaak urenlange) besprekingen en stapte jouw kantoor altijd uit vol nieuwe ideeën.

De experimenten in dit proefschrift zouden niet mogelijk zijn geweest zonder de technische staf van zowel CMI als ICC. Hans en Peter, bedankt voor jullie hulp met opstellingen en chemicaliën. Jan Willem, bedankt voor je hulp en geduld met de foto- en elektrolyse opstellingen. Stephan, Pascal, Ad, Dennie, Oscar, Herrick, Ramon, Fouad en Marjan, bedankt voor jullie technische ondersteuning. Ook wil ik graag Linda, Thea, Dymph en Ilonka bedanken voor jullie vriendelijke en goede assistentie aan de administratieve kant. Hans en Chris, ik wil ook jullie hartelijk bedanken voor jullie assistentie met de elektronenmicroscopen. Hans, ik vond de microscopie sessies op de Talos altijd erg gezellig en de resultaten hiervan hebben een groot aandeel gekregen in dit proefschrift. Bedankt voor je hulp en tijd.

Tijdens mijn onderzoek heb ik met veel verschillende mensen samengewerkt. Freddy, thank you for your help with the XPS measurements and sharing your expertise and enthusiasm. Chenghui, we had a nice collaboration that resulted in Chapter 3. I enjoyed running experiments together and learned a lot from you. Lisette, dankjewel voor het delen van je kennis over koper deeltjes op silica en je oude samples, ik heb er goed gebruik van gemaakt! Jogchum en Lars, bedankt voor jullie hulp met het microtomen van mijn samples. Jessi, het was fijn om jou als ervaringsdeskundige te hebben wat betreft het werken in twee groepen. Bedankt voor de fijne gesprekken. Marisol, I enjoyed working on electrocatalysis together and am happy that our collaboration resulted in Chapter 6. It was fun discussing science, but besides that also Mexican and Indian food and culture. I would also like to thank Kai and Francesco for your efforts on fixing and improving the electrocatalysis set-up and your patience when I was occupying the set-up during my last months at ICC. The XAS experiments in Chapter 6 could not have been done without Peter, Kristiaan, Fei and Alessandro. Thank you for your assistance and useful discussions prior and during the measurements. Nienke, bedankt voor het delen van jouw ervaringen met deze metingen en Mahnaz, thank you for your help with analyzing the XAS data.

Ook heb ik tijdens mijn PhD 3 studenten mogen begeleiden. Veerle, jij was mijn eerste student en jouw bijdrage aan de synthese van hetero-nanodeeltjes heeft een mooi plekje gekregen in dit proefschrift. Het was gezellig met je samen te werken, bedankt voor je inzet! Jelle, jij had een uitdagend project waarin je in 10 weken een hoop verschillende experimenten moest uitvoeren. Je enthousiasme en initiatiefrijkheid kwamen hier dus goed van pas en hebben tot mooie resultaten geleid. Ook heb ik, samen met Marisol, het master project van Kristiaan mogen begeleiden. Kristiaan, ik wil je bedanken voor je enthousiasme en harde werk. Je mocht mee met de XAS experimenten in Grenoble en hebt veel eigen initiatief laten zien. Daarnaast maakte je vrolijke persoonlijkheid het een plezier om met je samen te werken. Ik wens je veel succes met je eigen PhD!

Ik heb een leuke tijd gehad bij CMI en ICC en wil graag al mijn collega's van beide groepen bedanken. Anne, Kelly and Serena, thanks for the nice and peaceful atmosphere in our office at CMI and some fun office outings. Ilse en Maarten, we hadden een gezellig hoekje bij ICC en jullie nuchterheid, flauwe grappen en de broodjes Ben hebben de laatste stressvolle maanden zeker leuker gemaakt. I also want to thank all other colleagues of CMI and ICC for their help with experiments, discussions, good company on breaks, borrels and conference trips and the nice time I had over the past four years.

Anna, ik ben blij dat we na al die jaren nog zo goed bevriend zijn. Bedankt voor je interesse en luisterend oor en dat je mijn paranimf wilt zijn! Ellen, Anoenk en Ilse K., een groot deel van mijn tijd in Utrecht heb ik met jullie beleefd en ik ben blij dat we elkaar ook nu nog vaak zien. Bedankt voor alle goede gesprekken en gezellige avondjes in Utrecht en daarbuiten. Nynke, Ilse, Rens, Jogchum en Lars, bedankt voor alle gezelligheid en gekkigheid tijdens onze "Tapas"-uitjes. Nynke en Ilse, het was fijn om na onze master ook samen aan onze PhDs te beginnen en lief en leed met jullie te kunnen delen. Bedankt voor alle gezellige thee pauzes, sauna-avonden, etentjes, klaagsessies en goede gesprekken. Ik hoop dat er nog vele zullen volgen. Nynke, bedankt dat je na studiegenootje, collega en huisgenootje nu ook mijn paranimf wilt zijn!

Tot slot wil ik mijn lieve familie bedanken. Marrieke en Yaro, Katrien, Jan Willem en sinds kort ook Hanna, bedankt voor alle gezellige tijden de afgelopen jaren en jullie interesse en steun. Pap en Mam, jullie hebben me altijd de ruimte gegeven om het beste uit mezelf te halen. Bedankt voor alle goede zorgen en dat jullie er altijd voor me zijn.

Lieve Dhaval, met jou samen waren de afgelopen jaren avontuurlijker en leuker. Bedankt voor al je geduld, steun, liefde en vertrouwen. Ik kijk uit naar een mooie toekomst samen!

About the author

Christa van Oversteeg was born on the 2nd of May, 1992 in Muscat (Oman). After finishing high-school (VWO), she started the bachelor Chemistry at Utrecht University in 2010. She performed her bachelor project entitled 'Improving catalyst stability in the methanol synthesis reaction' in the Inorganic Chemistry and Catalysis group under supervision Prof. Petra de Jongh.



In 2013, she started her masters in 'Nanomaterials: Chemistry and Physics', where she focused on inorganic chemistry and catalysis. She performed her master research in the group of Inorganic Chemistry and Catalysis under supervision of Prof. Frank de Groot, where she investigated the reduction behavior of cobalt and nickel species in hydrodesulfurization catalysts using x-ray spectroscopy. In addition, she performed a 6 month research project at U.C. Berkeley (U.S.A) in the group of Tanja Cuk, where she studied the composition of the electric double layer in a battery electrolyte using advanced infrared spectroscopy techniques. As part of the Debye Honours program, she published a review article on x-ray absorption spectroscopy for the characterization of water-oxidation catalysts. She obtained her master's degree in 2015.

In November 2015 she started her PhD project in the Condensed Matter and Interfaces group and Inorganic Chemistry and Catalysis group under supervision of Dr. Celso de Mello Donegá and Prof. Dr. Petra de Jongh. Her research focused on the synthesis of Cu_{2-x}S nanoparticles and their application in catalysis. Part of the work discussed in this thesis is published in peer-reviewed journals and was presented on national and international conferences. Besides her scientific research, Christa taught practical courses to first year students and supervised several research projects of bachelor and master students. In her free time, she enjoys sailing, hiking and baking.